Ultrafast Transmission Electron Microscopy for Probing Light-Matter Interactions in Nanomaterials

Par

Rasool Doostkam

Thèse présentée pour l'obtention du grade de Philosophiae Doctor (Ph.D.)
en sciences de Énergie et Matériaux

Jury d'évaluation

Président du jury et examinateur interne	Prof. Sharif Sadaf
Examinateur interne	Prof. Sharif Sadaf
Examinateur externe	Prof. Germán Sciaini
Examinateur externe	Prof. Pablo Bianucci
Directeur de recherche	Prof. Aycan Yurtsever
Co-directeur de recherche	Prof. Kenneth R. Beyerlein
	INRS-ÉMT

ACKNOWLEDGEMENTS

I am profoundly grateful to Prof. Yurtsever for the invaluable experience I gained under his guidance in science and microscopy, as well as for his generous financial support throughout this research. My heartfelt thanks also go to Prof. Beyerlein, who offered me the opportunity to delve into crystallography and who supported me throughout the development and implementation of the algorithm. It has been both a privilege and a pleasure to work under the mentorship of two exceptional supervisors—each of you has taught me more than words can express.

I would also like to extend my sincere gratitude to INRS for its steadfast administrative, academic, and financial support during my doctoral studies. I am equally thankful for the financial assistance provided by the Canada Research Chair program, the NSERC Discovery Grant, the Fonds de recherche du Québec – Nature et technologies (FRQNT), and the Canada Foundation for Innovation (CFI).

I am also grateful to Prof. Andrei V. Rode, Prof. Ludovic Rapp, and Dr. Luca Gelisio for their insightful discussions and contributions to the crystallography project.

I extend my appreciation to the jury members—Prof. Sharif Sadaf, Prof. Germán Sciaini, and Prof. Pablo Bianucci—for generously dedicating their time to evaluating my thesis and providing valuable feedback.

I am deeply thankful to my wife, Sara, for her unwavering support and encouragement, which helped me remain focused and motivated during the challenges of my PhD. I also express heartfelt thanks to my parents and family, whose constant encouragement and belief in me sustained me through difficult times.

Finally, I would like to thank my research group members—Rezvan, Angel, and Wanting—for the time, knowledge, and camaraderie we shared throughout these years. Your support and collaboration were truly appreciated.

RÉSUMÉ

Comprendre les interactions lumière–matière à l'échelle nanométrique est essentiel pour le développement de la nanophotonique et de la recherche sur les nanomatériaux. Cette thèse regroupe deux investigations distinctes mais complémentaires. La première explore les réponses optiques en champ proche dans des nanoparticules plasmoniques à l'aide de la Microscopie électronique par champ proche induit par photons (PINEM). La seconde présente Poly, un algorithme informatique innovant fondé sur la diffraction, conçu pour identifier les polymorphes du silicium à haute pression dans des échantillons polycristallins.

Les interactions lumière–matière à l'échelle nanométrique sont étudiées à l'aide de la microscopie électronique en transmission ultrarapide (UTEM), offrant une résolution temporelle de l'ordre de la femtoseconde. Dans des expériences pompe-sonde, des nanoparticules plasmoniques d'or (Au) et d'argent (Ag) sont excitées optiquement par un laser femtoseconde, puis sondées par des photoélectrons. La technique PINEM, combinée à un filtrage énergétique, révèle que les orientations des dipôles induits dévient souvent de la direction fixe de polarisation linéaire du laser.

Des analyses statistiques montrent que les nanoparticules déposées sur des substrats de SiO présentent des écarts d'orientation dipolaire plus importants que celles sur des grilles en graphène. Pour plus de 100 nanoparticules d'or (Au NPs) sur SiO, l'histogramme des orientations dipolaires suit une distribution gaussienne avec une largeur à mi-hauteur (FWHM) de 19°, tandis que sur le graphène, cette largeur se réduit à 9°, illustrant un contraste significatif. Ces résultats suggèrent que le graphène constitue une plateforme plus stable et homogène pour les investigations en champ proche via PINEM. Par ailleurs, la rotation de la polarisation du laser pompe modifie les orientations dipolaires, faisant apparaître des motifs circulaires de champ proche à des angles de polarisation de 18°, 66°, 114° et 162°, ce qui révèle une périodicité d'environ π/4.

Dans le second projet, un algorithme informatique fondé sur la diffraction, nommé *Poly*, est développé pour effectuer une analyse quantitative de phase (QPA) ponctuelle de matériaux polymorphes à l'échelle nanométrique. Pour évaluer sa précision, des motifs de diffraction électronique en sélection d'aire (SAED) des phases de silicium à haute pression — notamment bt8-Si et st12-Si — sont simulés à partir de données cristallographiques. Ces simulations sont réalisées en Python en utilisant plusieurs bibliothèques scientifiques dédiées à la génération et à l'analyse des motifs de diffraction.

L’analyse des motifs simulés confirme que *Poly* identifie de manière fiable les polymorphes en comparant les positions des taches de diffraction selon des critères angulaires et d’espacement interréticulaire (distance d). Lorsqu’il est appliqué à des données SAED expérimentales issues d’échantillons de silicium soumis à un choc laser, l’algorithme démontre une identification robuste des phases. Les résultats confirment la présence de phases à haute pression jusqu’alors non rapportées, incluant t32-Si et *t32-Si**, comme structures dominantes dans les régions affectées par le laser. Alors que les travaux antérieurs de Rapp et al. [1] identifient plusieurs polymorphes tétragonaux et monoclinique du silicium sur la base des distances d uniquement, leur méthode manque de résolution spatiale. En revanche, l’approche à deux paramètres de *Poly* permet une attribution plus précise des phases à l’échelle individuelle de chaque tache.

Des données SAED résolues en temps, acquises à différents délais après exposition laser, révèlent que ces phases tétragonales métastables se détendent progressivement vers d’autres configurations à haute pression en environ 50 jours.

Ces deux investigations contribuent au développement des méthodologies de caractérisation optique et structurale à l’échelle nanométrique, avec des implications majeures pour la microscopie électronique ultrarapide et la science des matériaux.

La structure de cette thèse commence par une introduction générale à la microscopie électronique en transmission (TEM), accompagnée des concepts fondamentaux et des techniques pertinentes. Elle présente ensuite les deux projets de recherche principaux, chacun faisant l’objet d’un chapitre dédié suivant une structure cohérente comprenant : introduction, matériaux et méthodes, résultats et discussion, et conclusion.

Mots-clés : UTEM, Interaction Lumière-Matière, Plasmonique, Champs Proches Électriques, EELS, LSPRs, PINEM, Nanoparticules, Identification de Phase, Diffraction Électronique, Polymorphisme.

ABSTRACT

Understanding light–matter interactions at the nanoscale is pivotal for the advancement of nanophotonics and nanomaterials research. This dissertation encompasses two distinct yet complementary investigations. The first explores near-field optical responses in plasmonic nanoparticles through Photon-Induced Near-Field Electron Microscopy (PINEM). The second presents *Poly*, a novel diffraction-based computational algorithm designed to identify high-pressure silicon polymorphs in polycrystalline samples.

Light–matter interactions at the nanoscale are investigated using ultrafast transmission electron microscopy (UTEM) with femtosecond temporal resolution. In pump–probe experiments, plasmonic gold (Au) and silver (Ag) nanoparticles undergo optical excitation via a femtosecond laser and are subsequently probed by photoelectrons. Photon-Induced Near-Field Electron Microscopy (PINEM), augmented by energy filtering, reveals that the induced dipole orientations often deviate from the laser's fixed linear polarization direction.

Statistical analyses indicate that nanoparticles on SiO substrates exhibit greater deviations in dipole orientation than those on graphene grids. For over 100 gold nanoparticles (Au NPs) on SiO, the histogram of dipole orientations follows a Gaussian distribution with a full width at half maximum (FWHM) of 19°, whereas on graphene, the FWHM narrows to 9°, illustrating a significant contrast. These findings suggest that graphene provides a more stable and homogeneous platform for near-field investigations using PINEM. Furthermore, rotating the pump laser's polarization alters dipole orientations, with circular near-field patterns emerging at polarization angles of 18°, 66°, 114°, and 162°. This behavior demonstrates a periodicity of approximately π/4.

In the second project, a diffraction-based computational algorithm, *Poly*, is developed to perform spot-wise quantitative phase analysis (QPA) of nanoscale polymorphic materials. To assess its accuracy, selected area electron diffraction (SAED) patterns of high-pressure silicon phases—particularly bt8-Si and st12-Si—are simulated using crystallographic data. These simulations are implemented in Python, employing multiple scientific libraries for diffraction pattern generation and analysis.

Analysis of the simulated patterns confirms that *Poly* reliably identifies polymorphs by matching diffraction spot positions using both angular and interplanar spacing (d-spacing) criteria. When applied to experimental SAED data from laser-shocked silicon samples, the algorithm demonstrates robust phase identification. The results verify the presence of previously unreported

high-pressure phases, including t32-Si and t32*-Si, as dominant structures in laser-affected regions. While prior studies by Rapp et al. [1] identify several tetragonal and monoclinic silicon polymorphs based on d-spacing alone, their method lacks spatial resolution. In contrast, *Poly*'s dual-parameter approach enables more precise phase assignment at the individual spot level.

Time-resolved SAED data acquired at multiple delays post-laser exposure reveal that these metastable tetragonal phases progressively relax into other high-pressure configurations within approximately 50 days.

Together, these investigations advance methodologies for optical and structural characterization at the nanoscale, offering significant implications for ultrafast electron microscopy and materials science.

This thesis is structured to begin with a general introduction to transmission electron microscopy (TEM), along with foundational concepts and relevant techniques. It then presents the two primary research projects, each in a dedicated chapter following a consistent format that includes introduction, materials and methods, results and discussion, and conclusion.

Keywords: UTEM, Light-Matter Interaction, Plasmonics, Electric Near Fields, EELS, LSPRs, PINEM, Nanoparticles, Phase Identification, Electron Diffraction, Polymorphism.

SOMMAIRE RÉCAPITULATIF

Microscopie Électronique En Transmission Ultrarapide Pour Sonder Les Interactions Lumière-Matière Dans Les Nanomatériaux

Cette thèse porte sur deux projets principaux : l'analyse des signaux du champ proche autour de nanoparticules plasmoniques grâce à la Microscopie Électronique en Champ Proche induit par Photons (PINEM), et l'identification des phases à haute pression dans le silicium polycristallin à l'aide de l'algorithme diffractométrique Poly. Chaque chapitre suit une structure homogène : introduction, méthodes, résultats et conclusion.

Étude du comportement des champs proches et des dipôles des nanoparticules dans les images PINEM.

Introduction

Les domaines de la nanoscience, de la photonique et de la nanotechnologie convergent de plus en plus dans la compréhension des phénomènes complexes et le développement de technologies de pointe. La compréhension de l'interaction lumière–matière à l'échelle nanométrique est essentielle pour faire progresser la nanoplasmonique et la nanophtotonique. La technique PINEM permet de visualiser la réponse optique du champ proche dans des nanoparticules métalliques telles que l'or et l'argent, visibles lors d'excitations plasmoniques adéquates. Les champs électriques interagissant avec le laser linéaire se manifestent sous forme de dipôles dans les images PINEM, les polarisation circulaires étant également utilisées. Les recherches antérieures ont mis en évidence des motifs dipolaires en forme de croissant autour de nanoparticules sphériques, avec des comportements variant d'un individu à l'autre. Nous étudions l'influence de matériaux nanoparticulaires et de substrats variés sur le comportement dipolaire, afin de décrire les mécanismes régissant ces dynamiques de champ proche. Ces résultats sont utiles tant pour la compréhension fondamentale que pour la conception de nouveaux dispositifs photoniques et électroniques.

Microscopie Électronique en Transmission (TEM ou MET)

L'imagerie à haute résolution nécessite des longueurs d'onde plus courtes que la lumière visible. Les électrons, avec une longueur d'onde de De Broglie de l'ordre de l'ångström, répondent à ce critère. La TEM, mise au point pour la première fois par Ruska et Knoll en 1930, utilise des lentilles magnétiques (solénoïdes) pour contrôler le faisceau d'électrons. Les sources d'électrons

comprennent des émetteurs thermioniques (LaB_6), des émetteurs à champ, et des émetteurs Schottky.

Microscopie Électronique en Transmission Ultrarapide (METU ou UTEM)

L'étude de la dynamique des interactions lumière-matière, tout en offrant une haute résolution spatiale associée à une information temporelle et énergétique en temps réel, constitue un domaine de recherche avancé et complexe. La microscopie électronique en transmission ultrarapide (UTEM) combine les avantages en résolution spatiale de la microscopie électronique en transmission conventionnelle (TEM) avec une résolution temporelle ultrarapide afin d'explorer des phénomènes fondamentaux en physique, chimie, science des matériaux et biologie.

L'UTEM repose sur des expériences de type pompe-sonde, dans lesquelles un laser à impulsions ultrarapides excite l'échantillon pour initier des processus dynamiques tels que les transitions de phase, les vibrations du réseau cristallin ou les redistributions de charge. Un système de retard contrôle avec une grande précision le décalage temporel entre le laser de pompe et l'impulsion électronique de sonde, laquelle est générée par photoémission. En modulant ce délai, l'UTEM permet de reconstruire des images ou des motifs de diffraction à l'échelle femtoseconde, révélant ainsi l'évolution temporelle de la structure et de la dynamique de l'échantillon.

Les premières études pionnières menées à l'Université technique de Berlin, au Caltech et au Lawrence Livermore National Laboratory ont démontré la faisabilité d'expériences pompe-sonde en microscopie électronique, en utilisant soit des techniques stroboscopiques, soit des méthodes d'imagerie monocoup. Encouragée par ces avancées majeures révélant ses nombreuses applications potentielles, la microscopie électronique résolue en temps attire aujourd'hui un nombre croissant de groupes de recherche à travers le monde.

Pour étudier les phénomènes ultrarapides dans les régimes nanoscopiques hors équilibre, il devenait nécessaire de développer de nouveaux dispositifs. À la fin des années 1990 et au début des années 2000, Ahmed Zewail et son équipe ont fondé le domaine de la femtochimie, axé sur l'étude des réactions chimiques et des mouvements moléculaires à des échelles de temps ultrarapides. Ils ont cherché à combiner des impulsions laser femtoseconde avec la microscopie électronique afin d'accéder simultanément à l'information spatiale et temporelle des phénomènes ultrarapides. Plus tard, en 2008, Zewail et ses collaborateurs au Caltech ont perfectionné cette approche en développant la technique UTEM, permettant l'étude des mouvements moléculaires à l'échelle nanométrique avec une résolution temporelle femtoseconde. Cette avancée a permis

aux chercheurs d'examiner des phénomènes à l'échelle atomique avec une double résolution spatiale et temporelle. En 1999, Ahmed Zewail a reçu le prix Nobel pour ses travaux en femtochimie.

Dans un TEM conventionnel, la source électronique émet un faisceau d'électrons continu, typiquement par émission thermoïonique, fournissant une information spatiale bidimensionnelle. Le TEM peut fonctionner en mode image ou en mode diffraction, mais ces modes sont généralement utilisés dans un régime statique, capturant les propriétés stationnaires de l'échantillon. En revanche, dans un UTEM, un laser pulsé, d'une durée d'impulsion de l'ordre de quelques centaines de femtosecondes, est utilisé. À l'aide d'un dispositif optique, le faisceau laser initial est divisé en deux faisceaux. L'un est converti en une longueur d'onde UV par génération de la quatrième harmonique, tandis que l'autre est converti en une longueur d'onde spécifique, comme 515 nm. Le laser UV est dirigé à l'intérieur de la colonne du TEM vers le canon à électrons pour générer un faisceau d'électrons via un phénomène de photoémission. L'autre faisceau, appelé laser de pompe, est utilisé pour exciter l'échantillon et induire un état ultrarapide hors équilibre.

Interaction entre photoélectrons et nanomatériaux

Dans un microscope électronique en transmission conventionnel (TEM), les électrons sont émis par émission thermoïonique, produisant un faisceau électronique continu. En revanche, dans un microscope UTEM, les électrons sont générés par un processus de photoémission déclenché par un faisceau laser UV, aboutissant à un faisceau pulsé de photoélectrons. L'interaction entre les photoélectrons et les nanomatériaux donne lieu à des phénomènes uniques en raison des propriétés caractéristiques à l'échelle nanométrique, telles qu'un rapport surface/volume élevé et des effets de confinement quantique. Ces caractéristiques font que les nanomatériaux présentent des propriétés électroniques significativement différentes de celles de leurs équivalents massifs.

Par exemple, les boîtes quantiques (quantum dots), les nanofils et les nanofeuillets tels que le graphène possèdent des niveaux d'énergie électronique discrets et des états de surface proéminents, qui influencent fortement leur interaction avec les photoélectrons. Les techniques de spectroscopie des photoélectrons, telles que la spectroscopie des photoélectrons X (XPS) et la spectroscopie des photoélectrons UV (UPS), sont largement utilisées pour sonder les nanomatériaux. Ces techniques, intrinsèquement sensibles à la surface, sont idéales pour étudier les modifications de surface, les processus d'adsorption, ainsi que l'activité catalytique des nanomatériaux.

Spectroscopie de perte d'énergie des électrons (EELS)

La spectroscopie de perte d'énergie des électrons (EELS) désigne un ensemble de techniques dans lesquelles un faisceau d'électrons interagit avec un matériau (solide, liquide ou gaz), et les électrons diffusés résultants sont analysés afin de produire un spectre énergétique. Ce spectre reflète les pertes d'énergie subies par les électrons au cours de leur interaction inélastique avec l'échantillon. Le spectre EELS obtenu peut également être filtré, et les électrons sélectionnés peuvent être utilisés pour former une image de l'échantillon selon une méthode appelée imagerie spectroscopique électronique (ESI).

De manière générale, ces techniques relèvent de la spectroscopie d'absorption, car le faisceau électronique incident transfère de l'énergie au matériau et perd en intensité lors de l'interaction. La nature spécifique de cette perte énergétique dépend de la composition et de la structure électronique du matériau.

La technique a été initialement développée par James Hillier et R.F. Baker au milieu des années 1940. Cependant, elle est restée relativement peu exploitée pendant environ cinquante ans et n'a connu une adoption plus large dans la recherche qu'à partir des années 1990, grâce aux progrès significatifs dans l'instrumentation des microscopes et la technologie du vide.

Le microscope électronique en transmission JEOL JEM-2100 est équipé d'un système EELS, généralement intégré par des fabricants tels que Gatan (par exemple, le filtre d'imagerie Gatan, GIF). Lorsqu'un canon à électrons en LaB_6 est utilisé, la résolution énergétique du système EELS est d'environ 1,0 à 1,5 eV. La technique EELS est particulièrement bien développée pour une vingtaine d'éléments allant du carbone (Z = 6) au zinc (Z = 30), incluant les éléments légers et les métaux de transition de la série 3d.

Microscopie électronique par champ proche induit par photons (PINEM)

La microscopie électronique en transmission conventionnelle (TEM) repose sur les interactions élastiques entre les électrons et l'échantillon pour former des images ou des motifs de diffraction. À l'inverse, la spectroscopie électronique repose sur les pertes d'énergie associées aux interactions inélastiques entre les électrons de sonde et la matière. La microscopie électronique en transmission ultrarapide (UTEM) permet de réaliser des expériences de type pompe-sonde, où la sonde est constituée d'un faisceau pulsé de photoélectrons émis par le canon électronique, tandis que la pompe est un laser interagissant avec l'échantillon. Les électrons de valence ou de cœur de la matière sont excités par le laser pompe, puis les électrons de sonde interagissent avec cette matière excitée.

Grâce à ce dispositif complexe, l'une des techniques d'imagerie les plus avancées est la PINEM (Photon-Induced Near-field Electron Microscopy), qui permet la visualisation des champs électromagnétiques de proximité autour des nanomatériaux. Le laser pompe interagit avec le nanomatériau et génère des champs optiques de proximité évanescents et localisés. Les électrons de sonde traversant cette région interagissent avec ces champs et gagnent ou perdent une énergie quantifiée, correspondant à celle des photons. Ces échanges quantifiés d'énergie (les électrons libres échangeant des quanta d'énergie $\hbar\omega$ avec le champ plasmonique) apparaissent dans un spectre spécifique de spectroscopie appelé spectroscopie de perte d'énergie des électrons (EELS).

Le système UTEM est équipé d'un filtre énergétique fonctionnant comme un prisme pour les électrons, capable de séparer ces derniers selon leur énergie. Une fente permet alors de sélectionner une bande énergétique spécifique pour générer l'image. En filtrant tous les électrons sauf ceux ayant acquis l'énergie des champs de proximité, il devient possible de produire une image PINEM. Cette technique permet d'étudier les champs de proximité évanescents avec une résolution spatiale et temporelle à l'échelle de l'angström et de la femtoseconde, ainsi qu'une résolution énergétique correspondant aux quanta de photons. Elle trouve des applications prometteuses dans les domaines de la photonique, de la plasmonique et des nanostructures.

Nanoparticules plasmoniques

Les plasmons sont des oscillations collectives des électrons libres dans un matériau, généralement métallique. Les nanoparticules plasmoniques sont des nanoparticules métalliques dont les électrons de conduction peuvent osciller sous l'effet d'une lumière laser incidente, induisant des résonances plasmoniques. Ces résonances apparaissent à proximité de la surface de la nanostructure et sont appelées résonances plasmoniques de surface localisées (LSPR, *Localized Surface Plasmon Resonances*).

Grâce à ces LSPR, les nanomatériaux plasmoniques présentent des propriétés optiques uniques, telles qu'une absorption et une diffusion de lumière renforcées, ainsi qu'une intensification locale du champ électromagnétique. Ces propriétés leur confèrent une large gamme d'applications dans divers domaines.

Il existe trois types principaux de plasmons :

1. **Les plasmons de volume**, résultant des oscillations électroniques à l'intérieur même du matériau.

2. **Les plasmons de surface**, générés par l'interaction à l'interface entre un métal et un diélectrique, et confinés à la surface du matériau.
3. **Les plasmons de surface localisés (LSP)**, qui se produisent dans les nanostructures.

Les LSPR amplifient fortement le champ électromagnétique de proximité autour des nanoparticules et sont exploités dans des techniques telles que la spectroscopie Raman exaltée de surface (SERS), l'absorption infrarouge exaltée de surface (SEIRA), la biosensorique, la thérapie photothermique, l'optique non linéaire, ainsi que dans la technique PINEM elle-même.

MÉTHODOLOGIE

Synthèse des nanoparticules creuses

Les échantillons utilisés dans cette étude ont été synthétisés par des approches ascendantes (bottom-up) dans différentes entreprises spécialisées, telles que Nanocomposix, et sont généralement en suspension dans de l'eau distillée. Un exemple est constitué des NanoXact Gold Nanospheres, Bare (Citrate), 100 nm, à une concentration de 0.05 mg/mL dans une solution aqueuse de citrate de sodium à 2 mM. À l'aide d'une pipette, un petit volume de 5 mL a été transféré dans un récipient cylindrique en verre, puis dilué avec 10 mL d'eau distillée. Ensuite, une étape de sonication inférieure à 30 secondes a été réalisée afin de bien disperser les nanoparticules.

Par la suite, 100 µL de cette solution diluée ont été prélevés à l'aide d'une pipette, et deux gouttes ont été déposées sur un substrat (méthode du drop-casting) avant d'être séchées à température ambiante. Un autre échantillon consistait en des nanoparticules d'argent (Silver NPs), également synthétisées par la même entreprise. Leurs caractéristiques étaient : NanoXact Silver Nanospheres - Bare (Citrate), 100 nm, 0.02 mg/mL dans une solution de citrate de sodium à 2 mM. Le dernier type de nanoparticules étudié était constitué de nanoparticules de silice, avec les spécifications suivantes : NanoXact Silica Nanospheres, 100 nm, 10 mg/mL en suspension aqueuse.

Pour le dépôt de gouttelettes (drop-casting) des échantillons de nanoparticules, un grille TEM est nécessaire en tant que support. Il existe plusieurs types de grilles constituées de matériaux comme le cuivre, l'or, le nickel, le silicium, le carbone ou le graphène, avec des substrats tels que le carbone amorphe, le graphène, le carbone Lacey, ou encore le SiO. Les grilles utilisées dans cette expérience sont fournies par la société Graphene Laboratories Inc., qui propose des grilles en cuivre recouvertes d'un film de graphène (spécifications : CVD Graphene TEM grids, film de graphène CVD déposé sur des grilles en maille de cuivre ultrafine de 2000 mesh).

Les caractéristiques du graphène sont : conductivité électrique de 10^4 à 10^6 S/m, conductivité thermique de 2000 à 5000 W/mK, susceptibilité électrique négligeable (~0) et structure cristalline hexagonale à symétrie élevée. Le SiO, quant à lui, possède une conductivité électrique de l'ordre de 10^{-10} à 10^{-6} S/m, une conductivité thermique de 1 à 5 W/mK, et une susceptibilité électrique faible (~10^{-6}).

Synchronisation entre les impulsions photoélectroniques et le laser pompe (temps zéro)

Le point clé dans une expérience ultrarapide est la synchronisation entre les faisceaux pompe et sonde. Dans l'UTEM, l'alignement entre le faisceau de photoélectrons (sonde) et le laser pompe est assuré par un étage de retard mécanique, équipé d'un élément piézoélectrique permettant de raccourcir ou d'allonger le trajet optique du laser pompe. Un logiciel fourni par le fabricant permet de contrôler cet étage avec une précision temporelle de l'ordre de 1 ps.

Pour déterminer le moment où les deux faisceaux atteignent l'échantillon simultanément (temps zéro), le TEM est placé en mode EELS, et un spectre est acquis à chaque ajustement du retard. Étant donné que l'interaction entre le champ proche des nanoparticules et les photoélectrons se produit à l'échelle de la femtoseconde, si la sonde n'arrive pas en même temps que la pompe, le spectre EELS montre un comportement classique sans signatures d'interaction. Lorsque les impulsions sont synchronisées, le spectre révèle des pics de gain et de perte d'énergie, signe d'un transfert quantifié entre électrons et champ proche.

Filtrage énergétique

Pour capturer les images du champ proche autour des nanoparticules, il est nécessaire de filtrer les électrons de sonde, en ne sélectionnant que ceux ayant échangé une énergie multiple de $\hbar\omega$ (énergie d'un photon du laser pompe). Un système EELS peut être intégré dans un TEM soit avant (configuration in-column) soit après (configuration post-column) l'étage final d'agrandissement. Chaque méthode présente des avantages spécifiques, mais dans les deux cas, le principe repose sur la dispersion énergétique des électrons par un champ magnétique, à l'instar d'un prisme dispersant la lumière blanche.

Le spectre résultant peut être projeté sur un détecteur, ou bien filtré via une fente énergétique afin d'extraire une image filtrée en énergie (EFTEM). Ces deux techniques sont à la base de la majorité des analyses EELS.

Dans les expériences PINEM, on commence par régler la position du pic ZLP (Zéro-Loss Peak) pour obtenir la meilleure résolution énergétique (FWHM minimale). Ensuite, on passe en mode image et on applique la fente énergétique sur le spectre de gain. Par exemple, avec une dispersion énergétique de 0,05 eV et une largeur de fente de 6 eV, en centrant la fente à -6 eV, les électrons entre -9 et -3 eV participent à la formation de l'image PINEM.

Les étapes typiques pour capturer une image PINEM sont les suivantes :

L'échantillon est inséré dans le TEM et les nanoparticules sont localisées en mode champ clair.

On passe ensuite en mode photoémission, et en mode image, on focalise le faisceau de photoélectrons sur les nanoparticules pendant que le laser pompe est allumé.

On bascule en mode EELS pour ajuster la position du ZLP.

Enfin, on revient en mode image, on applique la fente énergétique, et on enregistre l'image PINEM des champs proches autour des nanoparticules.

Analyse des données pour les dipôles des nanoparticules

Pour l'analyse initiale des images acquises, nous avons utilisé le logiciel Gatan Microscopy Suite (GMS), également connu sous le nom de DigitalMicrograph, fourni par Gatan. Ce logiciel permet de piloter les caméras numériques et les composants associés, facilitant des applications clés telles que la tomographie, l'imagerie in situ, l'analyse spectrale, l'imagerie par diffraction, etc. (réf.).

Pour une analyse plus approfondie, nous avons utilisé MATLAB. Afin de déterminer l'angle de rotation des dipôles dans les nanoparticules (NPs), nous avons développé un programme qui intègre l'intensité de chaque structure en croissant des dipôles en coordonnées polaires. En ajustant le profil d'intensité avec une fonction gaussienne, nous avons pu identifier le centre de chaque croissant, ce qui nous a permis de déterminer l'angle associé. La comparaison de cet angle avec une ligne horizontale de référence (définie comme 0 degré) permet de calculer précisément l'angle de rotation des dipôles.

RÉSULTATS ET DISCUSSIONS

Le premier échantillon utilisé pour capturer les images PINEM et étudier les champs proches était constitué de nanoparticules d'or. Un ensemble de nanoparticules d'or (Au NPs) de 100 nm a été préparé par la méthode de dépôt par goutte (drop-casting) sur des grilles de SiO. Le laser pompe, d'une longueur d'onde de 515 nm et d'une puissance de 85 mW, illuminait une zone circulaire

d’environ 70 µm de diamètre à la surface de l’échantillon. La polarisation du laser était linéaire et orientée à 120°, comme indiqué par la ligne pointillée rouge dans le coin inférieur droit.

Étant donné cette polarisation linéaire, nous nous attendions à ce que les dipôles des nanoparticules s’alignent dans la même direction. Toutefois, les résultats ont montré que l’orientation des dipôles varie d’une nanoparticule à l’autre. Cette observation expérimentale est intéressante et suggère que d’autres facteurs peuvent influencer l’orientation des dipôles. Afin d’approfondir ce phénomène et de renforcer l’analyse statistique, l’expérience a été répétée plusieurs fois en utilisant différents ensembles de nanoparticules d’or déposées sur des grilles de SiO.

Pour explorer plus en détail ce comportement, nous avons étudié l’effet de la rotation de la polarisation du laser pompe, spécifiquement dans le sens antihoraire, sur l’orientation des dipôles. L’étude a été conduite par pas de 6° sur la lame demi-onde, ce qui correspond à des rotations de 12° de la polarisation. Une rotation complète de 180° de la lame demi-onde équivaut donc à une rotation complète de 360° de la polarisation.

De manière remarquable, lorsque la polarisation traverse certains angles spécifiques — tels que 18°, 66°, 114° et 162°, appelés ici angles transitoires, certaines nanoparticules présentent des signaux circulaires transitoires. Ces angles sont espacés d’environ 48° (proche de 45°), correspondant à des positions angulaires similaires à 0°, 90°, 180° et 270° sur le cercle trigonométrique, qui sont des points-clés de changement d’orientation directionnelle des vecteurs.

En résumé, au cours de la rotation de la polarisation du laser, l’orientation des dipôles commence dans une direction donnée, évolue progressivement à l’approche d’un angle transitoire, où un motif PINEM circulaire apparaît, puis se réaligne dans la direction opposée. Une autre observation importante est que l’angle transitoire varie légèrement d’une nanoparticule à l’autre, entraînant ainsi des orientations dipolaires différentes même sous la même direction de polarisation. Pour mieux examiner l’effet de la polarisation sur les dipôles, une expérience complémentaire a été menée avec une rotation de la polarisation dans le sens horaire. Comme auparavant, des motifs circulaires ont été observés près des angles transitoires, en particulier à 18° et 12° selon les particules étudiées.

Un autre test essentiel a porté sur l’effet de la puissance du laser pompe sur la réponse dipolaire PINEM des nanoparticules d’or. Afin de déterminer si des effets optiques non linéaires étaient responsables du comportement observé, la puissance du laser pompe a été réduite de 85 mW à

35 mW, puis à 21 mW. Il est important de noter que, bien que le processus PINEM soit intrinsèquement non linéaire, dans le sens où il implique l'absorption et l'émission de photons par les électrons, cette non-linéarité concerne l'échange d'énergie quantifié ($\hbar\omega$) et non la symétrie du champ.

Plus précisément, le laser pompe excite les modes plasmon de surface dans les nanoparticules, générant des champs électromagnétiques proches localisés. Les électrons de sonde qui traversent ces régions peuvent alors échanger de l'énergie sous forme de quanta $\hbar\omega$, donnant lieu à des bandes latérales dans le spectre d'énergie des électrons. Le filtrage de ces électrons, dont l'énergie a été modifiée, permet de former le signal PINEM. Cependant, cette non-linéarité fondamentale n'est pas à l'origine des motifs circulaires observés ni du désalignement des dipôles.

Le test suivant a consisté à bloquer le laser pompe pendant deux heures, puis à ajuster la lame demi-onde à un angle transitoire (par exemple 18°) pour commencer à capturer les signaux de champs proches. Lorsqu'on réajuste ensuite la polarisation à 12° ou 24°, l'image dipolaire attendue réapparaît, ce qui est conforme au comportement normal attendu lors d'une rotation continue. En outre, nous avons étudié l'effet de la puissance du laser pompe sur d'autres nanoparticules d'or et les résultats étaient similaires, quel que soit le niveau de puissance utilisé.

Le système UTEM comprend un étage de retard optique permettant d'ajuster avec précision le décalage temporel entre les impulsions d'électrons de sonde et les impulsions du laser pompe. Pour que le signal PINEM soit enregistré, les deux trains d'impulsions doivent être synchronisés au temps zéro. Une analyse approfondie a donc été menée autour du temps zéro pour déterminer si le comportement observé pouvait résulter d'un désalignement temporel ou d'une incertitude dans cette synchronisation. Il a été clairement établi que, sauf pour des variations d'intensité, le comportement des dipôles reste inchangé avant et après ce point de synchronisation.

Enfin, afin d'étudier l'influence du substrat sur l'orientation des dipôles, des nanoparticules d'or ont été déposées sur des grilles de graphène. De manière intéressante, sur le substrat de graphène, les variations dans l'orientation des dipôles sont moins fréquentes que celles observées sur les grilles de SiO. Les mêmes expériences ont été réalisées avec les Au NPs sur graphène, et bien que le phénomène général ait été confirmé, les désalignements dipolaires étaient nettement moins prononcés.

Quantification des directions des dipôles

Pour déterminer l'angle d'orientation des dipôles, la zone englobant la nanoparticule (NP) et le champ électromagnétique proche est segmentée en 36 secteurs polaires, chacun couvrant un angle de 10°, avec l'axe des abscisses (x) défini à 0°. L'intensité dans chaque secteur est ensuite intégrée et représentée en fonction de l'angle polaire. Étant donné que deux croissants lumineux apparaissent dans le profil à 360°, ces deux pics d'intensité dipolaire sont ajustés à l'aide de fonctions gaussiennes afin de localiser précisément leur centre.

L'angle dipolaire est défini comme la moyenne des positions centrales de ces deux pics. Dans le cas simulé, les deux pics sont situés à 135° et 315°, ce qui donne une séparation angulaire de 180° (315° − 135°). Après avoir validé cette méthode de localisation du centre, nous l'avons appliquée à l'analyse des nanoparticules d'or déposées sur des substrats de SiO et de graphène.

La distribution angulaire des dipôles dans un ensemble de 105 nanoparticules d'or (Au NPs) sur une grille de graphène a montré que 72 NPs présentaient un angle compris dans l'intervalle $120 \pm 5°$, avec une largeur à mi-hauteur (FWHM) de 9°. En comparaison, pour le substrat de SiO, 108 NPs ont été analysées et l'histogramme angulaire présentait une FWHM plus large de 19°, avec seulement 53 NPs dans la plage de $120 \pm 5°$, soit un nombre nettement inférieur à celui observé sur le graphène. Ces résultats indiquent que le substrat de SiO exerce une influence plus marquée sur l'orientation des dipôles que le substrat de graphène.

Cette différence peut s'expliquer par les propriétés thermiques contrastées des deux matériaux. La conductivité thermique de la grille de SiO est nettement inférieure (1 à 5 W/m·K) à celle du graphène (2000 à 5000 W/m·K). De plus, la grille de SiO est plus épaisse (~25 nm) que le substrat de graphène (~6 nm), ce qui réduit davantage la dissipation thermique. En conséquence, la chaleur induite par le laser se dissipe plus lentement dans le SiO, générant des températures locales plus élevées.

Ces températures accrues peuvent modifier les propriétés diélectriques tant du substrat que des nanoparticules d'or. Une augmentation locale de température peut influencer la fonction diélectrique du milieu environnant et du métal, affectant ainsi le comportement des oscillations plasmoniques. Ces altérations, causées par une accumulation thermique confinée, peuvent expliquer la distribution angulaire plus large des dipôles observée sur SiO.

Pour approfondir cette étude, des nanoparticules d'argent (Ag NPs) de 100 nm ont également été examinées sur un substrat de SiO, et des résultats similaires ont été obtenus, confirmant que l'effet observé n'est pas limité aux nanoparticules d'or.

Conclusion

Nous avons étudié l'interaction lumière–matière à l'échelle nanométrique avec une résolution temporelle femtoseconde. Plus précisément, nous avons analysé le comportement des champs proches autour de nanomatériaux à l'aide de la technique PINEM (Photon-Induced Near-field Electron Microscopy). Les résultats ont révélé que, bien que le laser pompe fût polarisé linéairement dans une direction fixe, les dipôles excités par le champ électrique du laser n'étaient pas toujours alignés avec cette direction. Certaines nanoparticules métalliques (NPs) d'or (Au) et d'argent (Ag) ont montré des orientations dipolaires déviant de la direction de polarisation du laser.

L'analyse statistique a montré que les nanoparticules déposées sur des substrats de SiO présentaient des déviations dipolaires plus marquées que celles déposées sur des grilles de graphène. Cette différence peut être attribuée à la conductivité thermique nettement plus faible du SiO (1 à 5 W/m·K) par rapport à celle du graphène (2000 à 5000 W/m·K). De plus, la grille de SiO est plus épaisse (~25 nm) que le substrat de graphène (~6 nm), ce qui en fait un substrat thermiquement isolant. Cette faible dissipation thermique peut perturber les oscillations plasmoniques à l'interface NP-substrat, entraînant ainsi des orientations dipolaires divergentes par rapport à la direction de polarisation du laser.

Nous avons également étudié des NPs d'argent et observé des déviations similaires. L'histogramme des angles dipolaires de plus de 100 NPs d'or sur un substrat de SiO a révélé une distribution gaussienne avec une largeur à mi-hauteur (FWHM) de 19°, tandis que sur des substrats de graphène, la FWHM n'était que de 9°, ce qui indique une différence significative. Ces résultats suggèrent que le graphène constitue un substrat plus adapté aux études de champs proches réalisées par la technique PINEM.

Enfin, nous avons examiné l'effet de la rotation de la polarisation du laser pompe sur l'orientation des dipôles. De manière intéressante, des motifs circulaires de champ proche ont été observés à des angles spécifiques tels que 18°, 66°, 114° et 162°, présentant une périodicité approximative de π/4.

Étude de la phase haute pression du silicium (Si) à l'aide de l'algorithme Poly

Introduction

L'évolution rapide des technologies exige le développement de nouveaux matériaux dotés de propriétés améliorées. Le silicium, matériau polyvalent, se distingue comme un candidat de choix en raison de ses nombreuses applications dans l'électronique et d'autres secteurs industriels. Les différentes phases du silicium présentent des propriétés uniques, ce qui motive d'importants efforts pour les synthétiser à l'aide de diverses techniques, avec un intérêt particulier pour l'application de hautes pressions.

Notre compréhension des structures et des propriétés des matériaux sous haute pression a été largement rendue possible grâce aux expériences menées avec des cellules à enclumes de diamant, lesquelles ont permis de révéler plusieurs transitions de phase ainsi que des états métastables. Cependant, ces dispositifs sont naturellement limités par la résistance du diamant, ce qui restreint la pression maximale atteignable à environ 640 GPa.

Récemment, une nouvelle approche a été développée pour exposer les matériaux à des pressions dépassant cette limite, tout en préservant les phases haute pression pour des études ultérieures. Cette méthode repose sur la focalisation de pulses laser ultracourts et de haute énergie à l'intérieur d'un matériau transparent, entraînant une micro-explosion confinée dans une géométrie restreinte. La formation de ces phases induit un défi majeur en matière d'identification structurale, car la région affectée contient souvent des nanomatériaux polymorphes dont les dimensions sont inférieures à la limite de résolution de la diffraction des rayons X (XRD).

Bien que la diffraction électronique en zone sélectionnée (SAED) permette d'obtenir des motifs de diffraction, l'information sur les distances interréticulaires (espacement ddd) peut s'avérer ambiguë pour la détermination de phase, car certains spots de Bragg peuvent correspondre à plusieurs phases. Ce chapitre présente un nouvel algorithme d'identification de phase, appelé Poly, destiné à l'analyse des motifs de diffraction ponctuels obtenus par SAED sur des nanomatériaux polymorphes. Nous avons développé cette approche afin de déterminer les phases haute pression prédominantes dans les régions du silicium affectées par des impulsions laser intenses.

L'identification de phase dans les nanomatériaux, en particulier pour les polymorphes, représente un défi complexe avec un fort potentiel d'erreurs. La méthode classique utilisée dans les laboratoires, l'analyse XRD, ne permet souvent pas d'obtenir des résultats fiables pour plusieurs raisons : les régions d'étude sont très petites et le signal de diffraction est moyenné sur l'ensemble

de l'échantillon. Dans les matériaux nanostructurés hétérogènes, où les polymorphes sont localisés, la diffraction X peut ne pas détecter ces variations locales. De plus, des polymorphes d'un même matériau peuvent présenter des structures cristallines très proches, entraînant un chevauchement des pics de diffraction.

L'amélioration de l'analyse quantitative de phase (QPA) des nanomatériaux polymorphes nécessite ainsi de nouveaux outils d'analyse des données de diffraction. Dans le cas du silicium irradié par laser, le volume proche de la surface de la cavité est polycristallin et contient un mélange de phases haute pression. Une approche simple consisterait à effectuer une moyenne azimutale du motif SAED et à introduire les positions des pics dans un logiciel de QPA pour PXRD. Toutefois, cette méthode réduit le contenu informationnel du motif de diffraction et ne permet pas de distinguer deux phases ayant des symétries de maille différentes mais des positions de pics similaires dans les diagrammes en poudre.

C'est dans cette optique que nous avons développé une nouvelle approche pour l'identification des phases polymorphes à partir de motifs de diffraction électronique en faisceau parallèle, tels que ceux obtenus en SAED. Cette méthode repose sur la corrélation des angles entre les spots de Bragg observés et ceux prédits pour une phase donnée. Elle attribue ensuite un score à cette corrélation de manière individuelle pour chaque spot, ce qui permet de réaliser une QPA sur des motifs issus d'échantillons polycristallins à phases multiples.

Le matériau : le silicium

Le silicium (Si) est le deuxième élément le plus abondant dans la croûte terrestre (environ 27,7 %), généralement présent sous forme de dioxyde de silicium (SiO_2) dans le sable et les roches. Il appartient au groupe 14 (IV-A) du tableau périodique, avec une configuration électronique $1s^2\ 2s^2\ 2p^6\ 3s^2\ 3p^2$. Le silicium est un métalloïde, ce qui signifie qu'il possède des propriétés intermédiaires entre les métaux et les non-métaux. Il se situe dans la période 3, entre le carbone (C) et le germanium (Ge). Son numéro atomique est 14, et il est reconnu pour ses propriétés semi-conductrices, ce qui en fait un matériau essentiel en électronique et en science des matériaux. Le silicium cristallise selon une structure cubique diamant, avec une constante de réseau d'environ 5,43 Å (angstroms).

Micro-explosion et autres méthodes pour créer les phases haute pression du silicium

Dans cette approche, l'énergie laser est déposée dans le volume intérieur d'un matériau transparent sur une échelle de temps très courte, inférieure à 1 picoseconde (ps) (1ps=10^{-12} s), soit plus rapidement que la dissipation par conduction électronique de la chaleur et le temps de collision électron-ion. La focalisation d'une énergie d'impulsion laser aussi faible que 1 µJ dans un volume focal sub-micronique conduit immédiatement à une densité d'énergie de l'ordre de 1 MJ/cm³ (soit 1 TPa), dépassant la résistance de tous les matériaux connus.

Cette déposition d'énergie entraîne une transformation rapide du plasma vers un état solide, favorisant la formation de phases métastables ne pouvant se former qu'à partir d'un état thermodynamiquement hors équilibre, à haute entropie, appelé matière dense chaude. Après un chauffage ultrarapide de ce volume confiné, une onde de choc extrêmement localisée se forme, qui se propage en dissipant son énergie dans le matériau. En tête de cette onde de choc, la pression peut atteindre environ 10 TPa et la température dépasser 10^5 K.

Cette micro-explosion est suivie d'un refroidissement ultra-rapide sous conditions très éloignées de l'équilibre, avec une détente de pression ultrarapide et des taux de refroidissement extrêmement élevés (~10^{14} K/s), ouvrant ainsi l'accès à de nouveaux états matériels correspondant à des minima locaux d'énergie libre très loin de l'équilibre. Ces nouvelles phases restent piégées dans une région localisée du cristal initial, ce qui permet leur caractérisation ultérieure. C'est ainsi que des zones affectées par le laser-choc sont créées, et que de nouvelles phases haute pression peuvent être étudiées.

Par exemple, de l'aluminium super-dense a été formé à partir de saphir, et des transformations de phase dans l'olivine $(Fe, Mg)_2SiO_4$ ont été rapportées en utilisant cette méthode.

En 2015, Rapp et al. ont produit de nouvelles phases de silicium en irradiant des échantillons avec des impulsions laser de 170 fs à une longueur d'onde de 790 nm. Le laser était focalisé sur une surface de silicium recouverte d'une couche amorphe transparente de dioxyde de silicium (SiO_2), qui confinait la micro-explosion. Les mesures de diffraction électronique en zone sélectionnée (SAED) réalisées sur la zone affectée ont montré que l'irradiation laser avait conduit à la formation de plusieurs polymorphes métastables du silicium. Des fluences laser de 48 et 95 J/cm² ont permis d'obtenir les phases métastables st12-Si et bt8-Si dans la zone affectée par le choc laser, ainsi qu'une indication de l'existence potentielle de deux autres structures nouvelles, t32-Si et t32*-Si.

Diffraction électronique en zone sélectionnée (SAED)

En mode diffraction dans un TEM (microscope électronique en transmission), les chercheurs s'intéressent souvent à l'analyse d'une région spécifique de l'échantillon. Pour ce faire, des diaphragmes circulaires de Diffraction Électronique en Zone Sélectionnée (SAED) sont utilisés afin de limiter le faisceau d'électrons transmis à une aire définie d'intérêt. Ces diaphragmes sont positionnés sous l'objectif, mais au-dessus des lentilles intermédiaires et projectrices, précisément dans le plan image de l'objectif.

Dans le TEM JEOL JEM-2100, on trouve généralement quatre diaphragmes SAED de diamètres 100, 50, 20 et 10 µm. Cependant, la zone réellement sélectionnée sur l'échantillon dépend également de la longueur de la caméra et du grossissement de l'objectif. Par conséquent, un même diaphragme peut correspondre à des zones physiques légèrement différentes selon les conditions d'imagerie.

Cristallographie et groupes de symétrie cristalline

L'étude des matériaux et la compréhension de la relation entre leurs propriétés et leur structure constituent depuis longtemps une quête centrale en science. Depuis plus d'un siècle, la cristallographie aux rayons X fournit des informations tridimensionnelles sur les mécanismes structuraux et les fonctions de nombreux matériaux et molécules biologiques importants. La cristallographie est devenue un outil essentiel, jouant un rôle clé dans diverses industries telles que l'exploitation minière, la pharmacie et l'aérospatiale.

En 1912, Max von Laue a démontré la diffraction des rayons X par les cristaux, apportant la preuve directe de leur structure périodique interne. À la même époque, W. H. Bragg et W. L. Bragg ont formulé la loi de Bragg, qui relie la longueur d'onde des rayons X à l'angle d'incidence et à la distance entre les plans atomiques dans un cristal. L'impact de cet outil puissant sur la biologie fut évident dans la découverte de la structure en double hélice de l'ADN par Watson et Crick dans les années 1950, basée sur des données de diffraction aux rayons X collectées par Rosalind Franklin et Maurice Wilkins. La cristallographie a aussi permis de déterminer les structures de protéines importantes comme la myoglobine et l'hémoglobine. Depuis le XXe siècle, des progrès significatifs ont été réalisés grâce au développement de techniques avancées telles que la diffraction aux neutrons, la diffraction électronique et la radiation synchrotron.

Lorsqu'un matériau est fragmenté en morceaux plus petits, il peut révéler une structure régulière et répétitive ou une organisation désordonnée de ses particules constitutives (atomes, ions,

molécules). Les matériaux à structure régulière sont dits cristallins, tandis que ceux à structure irrégulière sont qualifiés d'amorphes.

Pour étudier les cristaux, la cristallographie définit les éléments constitutifs du cristal comme le réseau (lattice) et la base (basis). Un réseau est un arrangement périodique tridimensionnel de points, qui indique où sont placées les bases pour construire la structure cristalline globale. La base est le groupe le plus simple d'atomes, ions ou molécules attaché à chaque point du réseau.

Pour analyser un cristal, on définit la maille élémentaire comme le plus petit volume répétitif qui, par répétition spatiale, décrit intégralement la structure cristalline. La maille élémentaire est caractérisée par les paramètres du réseau : a, b, et c, qui représentent les longueurs des arêtes le long des axes x, y, et z, respectivement, ainsi que par les angles α, β, et γ, qui sont les angles entre les arêtes (b & c, a & c, et a & b, respectivement).

Méthodes et algorithmes d'identification de phases dans les matériaux et nanomatériaux

Le principal défi de l'analyse quantitative de phases (QPA) des nanomatériaux polymorphes à partir de mesures SAED réside dans le fait que, dans de nombreux cas, les motifs contiennent des diffraction superposées issues de mélanges de phases nanocristallines. L'approche courante pour identifier les phases à partir des motifs SAED convient principalement aux monocristaux, car elle implique d'orienter les cristaux selon un axe de zone et de comparer le motif mesuré à celui calculé à partir des informations de maille élémentaire.

Une autre méthode fréquemment utilisée pour effectuer une QPA sur des matériaux nanocristallins consiste à effectuer une moyenne azimutale du motif SAED, puis à utiliser un logiciel conçu pour la diffraction sur poudre afin d'identifier les pics observés. Cependant, cette méthode réduit le contenu informationnel du motif et ne permet pas de distinguer les cas où deux phases ont des positions de pics qui se chevauchent.

D'autres approches rapportées pour réaliser la QPA sur des nanomatériaux en TEM incluent : l'étude de la transformée de Fourier locale des images à haute résolution, la corrélation avec l'imagerie en champ sombre pour éliminer les phases dominantes, ainsi que l'utilisation d'une série de mesures par diffraction en précession. Toutefois, chacune de ces méthodes présente des limitations liées à la cristallinité de l'échantillon ou requiert un équipement spécialisé.

Par ailleurs, les motifs SAED contiennent une richesse d'informations structurales qui peuvent être collectées avec n'importe quel TEM. De plus, la capacité à démêler les informations contenues dans des motifs de diffraction superposés issus de matériaux polycristallins a récemment été démontrée grâce au développement de multiples algorithmes d'indexation

cristalline pour les mesures de diffraction aux rayons X, tels que les méthodes triplets, Grainspotter et FELIX.

Les nanomatériaux sont des matériaux possédant au moins une dimension dans le domaine nanométrique. Ils présentent des propriétés physiques et chimiques uniques, résultant de leur taille de grain réduite et de leur surface spécifique accrue comparativement aux matériaux massifs. Des approches de type bottom-up (par exemple, synthèse chimique) ou top-down (par exemple, broyage, microexplosion) sont utilisées pour produire des nanomatériaux. La plupart de ces méthodes génèrent de nombreux petits grains cristallins aux orientations aléatoires. Par conséquent, ces nanomatériaux sont qualifiés de polycristallins, car ils sont composés de grains variés aux orientations nanocristallines différentes.

Détails de l'algorithme d'identification de phase spot-par-spot : Poly

Notre algorithme calcule un score pour chaque spot de diffraction observé, reflétant son niveau de correspondance avec une phase supposée connue. Sa logique et son organisation suivent l'approche d'accumulation décrite par Morawiec pour l'indexation et la détermination de l'orientation cristalline.

Étape 1 : Les spots sont détectés dans l'image de diffraction à l'aide d'une méthode de programmation Python, appelée Itseez.

Étape 2 : Le centre du motif est localisé, et la position de chaque spot est transformée en vecteur dans l'espace réciproque.

Étape 3 : Le jeu complet des vecteurs réciproques, noté ***h***, est calculé à partir d'une structure cristalline supposée. Les réflexions interdites sont éliminées de la liste en fonction du groupe d'espace de la phase associée. Dans notre cas, il n'était pas nécessaire d'inclure les spots dus à la diffraction dynamique, car nous étudions de petits domaines de phases de silicium à haute pression dans une zone déformée du substrat de silicium. Cependant, ce cadre permet d'intégrer les spots de diffraction dynamique lors de la génération de cette liste de vecteurs spot.

Étape 4 : La liste complète des vecteurs réciproques est regroupée selon des familles. Une famille est définie comme un ensemble de vecteurs réciproques reliés par les opérations de symétrie du groupe de Laue, indépendamment de leurs magnitudes.

Étape 5 *(implémentée implicitement)* : Identification des candidats vecteurs ***h*** potentiels pour un vecteur observé ***g*** en comparant leurs magnitudes.

Étape 6 : Une table de votes est générée avec les votes pour les vecteurs ***g*** organisés en lignes et les familles en colonnes. Si la condition de similarité est satisfaite, un vote est ajouté aux éléments de la table aux indices (i,m),(i,n),(j,m), et (j,n). Ainsi, les votes s'accumulent en considérant toutes les paires de vecteurs g\mathbf{g}g et les familles potentielles.

Étape 7 : Le score le plus élevé pour chaque vecteur ***g*** est sélectionné et enregistré pour une comparaison ultérieure. Cette étape identifie également les familles de réflexions qui corrèlent le plus avec le vecteur observé ***g***.

Étape 8 : Pour valider le score calculé, l'algorithme effectue un test d'hypothèse nulle afin de déterminer si le score est similaire à celui obtenu pour un ensemble de spots aléatoires sans relation cristallographique. Si le k-score d'un spot est supérieur à 2, l'hypothèse nulle est rejetée et le score est pris en compte pour l'analyse.

Étape 9 : Après application du filtre basé sur la valeur k à tous les scores, les scores finaux d'un spot pour différentes phases sont comparés. Cette comparaison spot-par-spot permet à l'algorithme Poly d'identifier des motifs de diffraction contenant plusieurs cristaux de phases différentes.

Méthodes de simulation des motifs de diffraction, en particulier pour le silicium
Pour évaluer la précision du programme d'identification de phases Poly, nous avons généré des motifs de diffraction simulés. Dans un premier temps, pour une phase spécifique du silicium, nous utilisons les conditions de réflexion du groupe de Laue afin d'identifier les indices de Miller (hkl) autorisés. Ensuite, en utilisant les paramètres cristallins de la phase considérée, nous calculons la norme des vecteurs de l'espace réciproque pour chaque valeur (hkl). Comme nous nous concentrons sur une région spécifique du motif de diffraction, si la norme d'un vecteur dépasse une valeur seuil déterminée, les indices correspondants sont retirés de la liste. Afin de garantir que le motif simulé ressemble à celui expérimental, nous appliquons ensuite les équations de rotation tridimensionnelle d'Euler pour faire tourner ces vecteurs, générant ainsi des motifs de diffraction le long de l'axe de zone, hors axe, ou selon d'autres orientations. Après avoir généré et sélectionné les vecteurs de l'espace réciproque, nous comparons leur norme au rayon de la sphère d'Ewald (1/λ), qui, dans notre cas, correspond à une longueur d'onde électronique de 0,0025 nm pour un faisceau électronique de 200 keV en TEM. Enfin, les spots de Bragg dont les vecteurs réciproques intersectent la sphère d'Ewald forment le motif de diffraction simulé.

Motifs SAED d'un échantillon de silicium irradié par laser (microexplosion)

Pour synthétiser des phases de silicium à haute pression, Rapp et al. ont utilisé la méthode de microexplosion, suivie d'un fraisage par faisceau d'ions focalisé (FIB) pour préparer les échantillons en vue d'une analyse par microscopie électronique en transmission (TEM). Des motifs de diffraction électronique à aire sélectionnée (SAED) ont alors été enregistrés par TEM.

Résultats et discussions

Test de l'algorithme Poly sur des motifs de diffraction simulés de silicium

Nous avons simulé des motifs SAED des phases bt8-Si et st12-Si, qui possèdent des cellules unitaires et groupes d'espace distincts, mais présentent de nombreuses similitudes dans les magnitudes des vecteurs de diffusion des pics de Bragg, rendant leur identification difficile par les méthodes existantes. Les motifs, comprenant plus de dix spots de Bragg, ont été conservés pour une analyse ultérieure. Les intensités des spots de Bragg n'ont pas été calculées, car elles ne sont pas prises en compte dans l'algorithme Poly. L'algorithme Poly décrit précédemment a d'abord été utilisé pour calculer des scores de similarité pour les spots, en supposant que les phases du silicium sont connues. En général, pour un motif de N spots, un spot peut former N-1 angles avec les autres ; le score maximal possible pour un spot est donc N-1, ce qui signifie que tous les angles avec les autres spots correspondent à la structure supposée. Pour le motif simulé contenant un mélange des phases Si-bt8 et Si-st12, Poly a pu identifier la phase de chaque spot. Ces résultats démontrent la bonne capacité de Poly à distinguer une phase spécifique de silicium parmi d'autres. De plus, l'algorithme fonctionne spot par spot et peut correctement classer les spots en différentes phases, ce qui est adapté aux échantillons polymorphes. Un inconvénient de Poly est qu'il nécessite une cellule unitaire prédéfinie. Cependant, nous avons constaté que de légères déviations, pouvant être causées par des défauts ou des contraintes, peuvent être tolérées en ajustant les paramètres de seuil ε_1 et ε_2. Enfin, l'algorithme ne fonctionne pas lorsque les phases ont des constantes de réseau et groupes d'espace similaires, car cela conduit à des scores proches en raison d'espacements interplans et de relations angulaires équivalentes. Des simulations comme celles présentées peuvent être utilisées pour tester si plusieurs phases dans la liste des candidats sont distinguables par l'algorithme. Toutefois, dans le cas où un spot obtient des scores élevés similaires pour plusieurs phases, il est préférable de considérer ce cas comme un sous-ensemble de correspondances potentielles et de comparer cette sous-liste avec la distribution des scores des autres spots du motif. Comme cela sera démontré, cette approche permet de réduire significativement la liste des candidats et d'identifier les phases dominantes dans un motif SAED.

Résultats du traitement des données pour l'échantillon de silicium irradié par laser

Pour analyser un motif de diffraction expérimental, le motif enregistré sur film a d'abord été numérisé, puis les spots ont été détectés dans le motif à l'aide de l'algorithme de détection de spots (Itseez, Python). Ensuite, via un programme MATLAB, les spots correspondant à un espacement interréticulaire (d-spacing) propre à la phase cubique du silicium ont été filtrés. L'algorithme Poly a alors été appliqué aux spots restants. Pour estimer l'incertitude sur la localisation des spots dans le motif SAED, un ajustement gaussien bidimensionnel a été réalisé sur chaque spot, la déviation standard du fit fournissant l'incertitude sur les coordonnées x et y.

Identification des phases du silicium avec Poly

Nous avons utilisé Poly pour analyser un ensemble de 10 motifs SAED mesurés dans différentes régions affectées autour de vides créés par des fluences laser incidentes de 48 ou 95 J/cm². Les échantillons ont été préparés par faisceau d'ions focalisé (FIB) afin de produire des coupes minces adaptées aux mesures en TEM. Le délai entre la préparation par FIB et la mesure SAED variait de 34 à 94 jours, que nous qualifierons de « délai de mesure ».

L'analyse a révélé que quatre motifs comportaient un nombre significatif de spots identifiables par l'algorithme. Les spots ayant obtenu un score inférieur au seuil de 2 ont été considérés comme des mauvaises correspondances, représentées par des cercles vides dans les motifs. Un tableau des paramètres expérimentaux et du nombre de spots correspondant à chaque phase de silicium haute pression est présenté. Les motifs mesurés avec un délai de moins de 50 jours (b901 et b679) contenaient majoritairement des spots présentant les scores de similarité les plus élevés avec les phases t32-Si et t32*-Si. Comme le montrent les distributions des scores, l'algorithme Poly attribue des scores similaires à ces deux phases, en raison de la grande similitude des paramètres de leurs cellules unitaires, ce qui complique leur distinction. Fait intéressant, un plus grand nombre de spots t32-Si et t32*-Si a été observé dans b679 que dans b901, ce qui semble corrélé à la fluence laser utilisée pour la création des vides, 95 J/cm² pour b679 contre 48 J/cm² pour b901.

Il apparaît donc qu'une fluence laser plus élevée favorise la formation des phases t32-Si dans la région affectée par le choc laser. Les spots correspondant à d'autres phases haute pression étaient significativement moins abondants. La phase r8-Si a été détectée dans les deux cas, tandis que les phases hd-Si et VIII-Si ont été attribuées à quelques spots uniquement lors de la mesure à fluence plus faible (b901). L'analyse initiale menée par Rapp et al., qui s'était concentrée sur les phases bt8-Si et st12-Si, n'a identifié que peu de spots correspondant à ces phases par l'algorithme Poly. Cette différence est compréhensible, car l'analyse initiale

considérait uniquement la magnitude des vecteurs de diffusion des spots sans tenir compte des corrélations angulaires comme dans notre approche. De plus, l'analyse originale s'est limitée aux spots proches du centre du motif, la reconnaissance des phases étant plus ambiguë pour les spots plus éloignés.

Les différents délais de mesure dans le jeu de données nous ont également permis d'étudier l'évolution de la stabilité des phases haute pression créées dans la région affectée par le choc laser. La préparation en coupe transversale et l'amincissement de l'échantillon près du vide entraînent la suppression des contraintes résiduelles, favorisant ainsi la relaxation des phases haute pression vers des phases de pression plus faible. Il est observé que le nombre de spots associés aux phases t32/t32*-Si, représentés en rouge et vert, diminue avec le temps. Cette diminution s'observe également pour la phase r8-Si, mais avec une pente moins prononcée. D'après ces analyses, le temps de relaxation des phases t32/t32*-Si et r8-Si est estimé entre 50 et 70 jours. En revanche, la phase XI-Si présente une évolution différente, avec une augmentation du nombre de spots attribués, passant de 0 % à 14 %, suggérant qu'elle est un sous-produit de la relaxation des phases t32/t32*-Si.

Il est à noter que la fréquence des spots considérés comme mauvaises correspondances augmente également avec le temps. La cause exacte reste incertaine, mais pourrait être liée à une phase non identifiée ou à un nombre insuffisant de spots détectés en diffraction dû à une petite taille cristalline. Une autre explication possible est une hétérogénéité accrue de la microstructure de l'échantillon. Dans l'algorithme Poly, le score des spots dépend du nombre total de spots (N) dans une phase donnée. Si la diversité des phases dans une région augmente, les scores diminuent et la probabilité de mauvaises correspondances croît. Pour approfondir ces cas, nous envisageons de réaliser des expériences de diffraction par nanofaisceau afin d'étudier les performances de Poly sur des volumes affectés plus petits, ce qui devrait réduire le nombre de phases présentes dans la zone et augmenter les scores relatifs.

Identification des limites de l'algorithme Poly à l'aide de mélanges de phases dans des motifs de diffraction polycristallins simulés

Les tests de Poly réalisés sur des motifs de diffraction simulés ont démontré son bon fonctionnement. Cependant, une question demeure : dans quelles conditions pourrait-il échouer ? Pour répondre à cela, nous avons conçu trois tests complémentaires, que nous classons en trois groupes.

Dans un premier temps, nous évaluons la précision de Poly lorsque le nombre de spots de Bragg d'une phase est réduit. Nous commençons par un mélange de deux phases puis, à chaque étape, nous supprimons certains spots d'une phase afin de déterminer si Poly peut toujours les identifier.

Ensuite, nous ajoutons au mélange des spots provenant de motifs simulés d'orientations différentes d'une autre phase, jusqu'au point où Poly ne peut plus différencier les phases.

Enfin, nous ajoutons à chaque étape un motif de diffraction simulé issu de différentes phases du silicium afin de définir le seuil où Poly échoue dans l'identification des phases.

Limite du nombre de spots

Pour ce premier test, nous avons utilisé la procédure de simulation décrite précédemment pour générer des spots de Bragg correspondant à la phase Si-t32. Lors de la dernière étape, seuls quatre spots Si-t32 subsistaient. Fait remarquable, Poly a pu distinguer ces quelques spots des spots de la phase Si-st12. Les scores associés aux spots Si-st12 restaient dans la même fourchette, indiquant une identification stable des phases. Nous concluons donc que Poly est capable de gérer des cas où le nombre de spots d'une phase spécifique est très limité.

Limite liée à l'orientation cristalline

Pour évaluer l'impact des différentes orientations sur les résultats de Poly, nous avons réalisé un test débutant avec un motif Si-t32, auquel nous avons ajouté des motifs de la phase Si-st12 dans différentes orientations. Ce test reflète la situation expérimentale où différents grains présentent la même phase mais des orientations variées.

Pour un motif contenant 120 spots, la phase Si-t32 reste identifiable avec un score moyen d'environ 28. Au fur et à mesure que le nombre de spots Si-st12 augmente, un effet mixte apparaît : certains spots Si-st12 voient leur score augmenter, tandis que l'ambiguïté s'accroît pour d'autres spots de cette phase.

Cette analyse démontre que Poly peut identifier correctement des phases dans un mélange de motifs comportant des orientations variées, bien que le nombre total de spots puisse influencer les scores et donc l'identification finale des phases.

Limite liée au mélange de phases

Dans cette dernière partie, nous étudions les résultats de Poly sur des mélanges de motifs de diffraction issus de différentes phases de silicium. Plusieurs motifs SAED simulés de diverses phases ont été générés et analysés avec l'algorithme en considérant onze phases possibles de silicium.

Il est important de noter que l'ambiguïté apparaît pour la plupart des spots lorsque le motif comprend environ 66 spots. Au-delà d'un certain nombre de spots, la probabilité d'ambiguïté augmente. La raison pour laquelle la phase Si-t32 reste identifiable est que la probabilité de correspondance de ses spots avec d'autres phases reste faible.

Conclusion

Nous avons développé l'algorithme Poly afin d'effectuer une analyse quantitative de phase (QPA) ponctuelle sur des matériaux polymorphes à l'échelle nanométrique. Des motifs de diffraction simulés des phases bt8-Si et st12-Si ont été utilisés pour tester cet algorithme.

Nous avons exploité les informations cristallographiques des différentes phases du silicium pour simuler des motifs SAED. Ces simulations ont été réalisées en Python, en s'appuyant sur diverses bibliothèques dédiées au traitement. Les phases de silicium à haute pression étudiées comprenaient notamment Si-bt8, Si-st12, Si-bc8, Si-r8, Si-hd, Si-IX, Si-VIII, Si-m32, Si-m32*, Si-t32, et Si-t32*.

L'analyse de ces motifs simulés avec Poly a démontré la forte capacité de l'algorithme à identifier avec précision les phases présentes.

Les résultats montrent que l'algorithme Poly peut associer de manière fiable les spots de diffraction détectés lors d'expériences de microexplosion avec des phases de silicium à haute pression connues. Par ailleurs, nous avons analysé des motifs SAED expérimentaux issus d'échantillons de silicium affectés par des chocs laser, révélant la présence de nouvelles phases de haute pression. Une étude antérieure menée par Rapp et al. avait rapporté que les microexplosions dans le silicium généraient plusieurs phases tétragonales et monoclinique ; cependant, leur identification reposait uniquement sur les distances interplans (d-spacing) et manquait de précision à l'échelle des spots individuels. Notre analyse avec Poly, qui intègre à la fois les informations angulaires et les distances interplans, a permis d'identifier les phases t32-Si et t32*-Si comme composantes dominantes des régions affectées par le choc laser, ce qui est rapporté ici pour la première fois.

De plus, l'analyse d'une série de motifs obtenus avec différents délais de mesure indique que ces phases se relâchent progressivement vers d'autres phases de haute pression en environ 50 jours. Des travaux en cours visent à évaluer plus en détail les capacités de cette approche d'identification ponctuelle dans d'autres systèmes matériels et à l'appliquer à de nouveaux motifs obtenus par diffraction en nano-faisceau. Par ailleurs, Poly est également applicable aux motifs de diffraction sensibles à la position collectés via la technique 4D-STEM. Cependant, dans de nombreux cas, ces motifs tendent à être très diffus. Lorsque des spots de Bragg nets et bien définis sont présents, Poly peut grandement faciliter une identification précise des phases.

Les procédures d'identification de phase, allant des plus simples aux plus complexes, comportent toujours une certaine incertitude due aux erreurs instrumentales, à la qualité des données, aux spécificités des échantillons, aux erreurs d'analyse et aux imprécisions dans les données de référence. Dans le cas de Poly, nous utilisons la magnitude des vecteurs et leurs angles dans le motif SAED, en les comparant à la base de données du matériau étudié, ici le silicium. Il est donc crucial d'identifier les faiblesses de l'algorithme en utilisant des motifs SAED simulés idéaux. Ces simulations minimisent les erreurs liées aux instruments et aux expériences tout en fournissant les données de base nécessaires à l'évaluation de l'algorithme.

Table of Contents

List of Tables

List of Figures

List of Equations

$$P = \varepsilon_0 \chi^{(1)} E \tag{1.1}$$

$$\Gamma_{i\to f} = \frac{2\pi}{\hbar} \left| \langle f | \hat{H}_{int} | i \rangle \right|^2 \rho_f \tag{1.2}$$

$$\Lambda = \frac{1}{N\sigma} \tag{1.3}$$

$$\mathrm{P(n)} = \left(\frac{1}{n!}\right) \left(\frac{x}{\Lambda}\right)^n \exp\left(-\frac{x}{\Lambda}\right) \tag{1.4}$$

$$\lambda = \frac{h}{p} = \frac{hc}{\sqrt{E_k^2 + 2E_k mc^2}} \tag{1.5}$$

$$n\lambda = 2d\sin\theta \tag{1.6}$$

$$\mathrm{d} = \frac{0.612\lambda}{\mathrm{n}\sin\alpha} \tag{2.1}$$

$$\lambda = \frac{\mathrm{h}}{\mathrm{p}} = \frac{\mathrm{h}}{\mathrm{mv}\sqrt{1 - \mathrm{v}^2/\mathrm{c}^2}} \tag{2.2}$$

$$P = \frac{U}{t} \tag{2.3}$$

$$E_z(x, y, z, t) \approx E_0 a^3 \chi(\omega) \frac{3xz}{r^5} e^{-i\omega t} \tag{2.4}$$

$$F(x, y) \approx \int_{-\infty}^{+\infty} E_z(x, y, z)\, e^{-i\left(\frac{\omega}{v}\right)z} dz \tag{2.5}$$

$$\beta = (e/\hbar\omega)F \tag{2.6}$$

$$P_n = J_n^2(2|\beta|) \tag{2.7}$$

$$P_{\pm 1} \approx |\beta|^2 \tag{2.8}$$

$$E_z(x, y, z; t) = E_0 a^3 \frac{(\vec{p}.\,\vec{r})z}{r^5} e^{-iwt} \tag{2.9}$$

$$E_z(x, y, z; t) = \frac{(p_x x + p_y y)z}{r^5} e^{-iwt} \tag{2.10}$$

$$\begin{bmatrix} p_x \\ p_y \end{bmatrix} = \begin{bmatrix} \chi_{xx} & \chi_{xy} \\ \chi_{yx} & \chi_{yy} \end{bmatrix} \begin{bmatrix} E_x \\ E_y \end{bmatrix} \tag{2.11}$$

$$\begin{bmatrix} p_x \\ p_y \end{bmatrix} = \begin{bmatrix} \chi_{xx} & \chi_{xy} \\ \chi_{yx} & \chi_{yy} \end{bmatrix} \begin{bmatrix} cos(\varphi) \\ sin\,(\varphi) \end{bmatrix} \tag{2.12}$$

$$p_x = \chi_{xx}\cos(\varphi) + \chi_{xy}\sin(\varphi)\ ,\ p_y = \chi_{yx}\cos(\varphi) + \chi_{yy}\sin(\varphi) \tag{2.13}$$

$$\chi = \begin{bmatrix} \chi_{xx} & \chi_{xy} \\ \chi_{yx} & \chi_{yy} \end{bmatrix} = \chi_0 \begin{bmatrix} 1 & i \\ -i & -1 \end{bmatrix} \tag{2.14}$$

$$p_x = \chi_0 \cos(\varphi) + i\chi_0 \sin(\varphi),\ p_y = -i\chi_0 \cos(\varphi) - \chi_0 \sin(\varphi) \tag{2.15}$$

$$\boldsymbol{g_i} = [x_i/d,\ y_i/d,\ 0], \tag{3.1}$$

$$\boldsymbol{h} = h\boldsymbol{a}^* + k\boldsymbol{b}^* + l\boldsymbol{c}^*. \tag{3.2}$$

$$\boldsymbol{a}^* = \frac{\boldsymbol{b}\times\boldsymbol{c}}{\boldsymbol{a}\cdot(\boldsymbol{b}\times\boldsymbol{c})};\ \boldsymbol{b}^* = \frac{\boldsymbol{c}\times\boldsymbol{a}}{\boldsymbol{a}\cdot(\boldsymbol{b}\times\boldsymbol{c})};\ \boldsymbol{c}^* = \frac{\boldsymbol{a}\times\boldsymbol{b}}{\boldsymbol{a}\cdot(\boldsymbol{b}\times\boldsymbol{c})}, \tag{3.3}$$

$$|h - g| < \varepsilon_1, \tag{3.4}$$

$$\left|\eta_{mn} - \gamma_{ij}\right| < \varepsilon_2, \tag{3.5}$$

$$k = \frac{|\bar{x} - M|}{\Delta}, \tag{3.6}$$

$$\begin{gathered} hkl: h + k + l = 2n \\ 0kl: k + l = 2n \\ h0l: h + l = 2n \\ hk0: h, k = 2n \\ h00: h = 2n \\ 0k0: k = 2n \\ 00l: l = 4n \end{gathered} \tag{3.7}$$

$$R_x = \begin{bmatrix} 1 & 0 & 0 \\ 0 & \cos\theta & -sin\theta \\ 0 & \sin\theta & cos\theta \end{bmatrix},$$

$$R_y = \begin{bmatrix} cos\varphi & 0 & sin\varphi \\ 0 & 1 & 0 \\ -sin\varphi & 0 & cos\varphi \end{bmatrix} \tag{3.8}$$

$$R_z = \begin{bmatrix} cos\psi & 0 & cos\psi \\ cos\psi & -sin\psi & 0 \\ 0 & 0 & 1 \end{bmatrix}$$

$$I = \sum_i I_i, \tag{3.9}$$

$$\boldsymbol{p}_c = \sum_i I_i \boldsymbol{p}_i \tag{3.10}$$

$$k_c = \sum_i I_i\ \ \|\boldsymbol{p}_i - \boldsymbol{p}_c\|^2, \tag{3.11}$$

$$\gamma = 1 - \frac{\sum_{i\notin C} I_i}{\sum_{i\in C} I_i} \tag{3.12}$$

$$\boldsymbol{p}_O = \frac{\sum_n w_n \overline{\boldsymbol{p}_n}}{\sum_n w_n}. \tag{3.13}$$

$$|S - 1/\lambda| < \varepsilon_3, \tag{3.14}$$

$$g d_{hkl} = L\lambda \tag{A.1}$$

$$d_{hkl} = \frac{1}{g} = \frac{0.543}{\sqrt{h^2+k^2+l^2}} \tag{A.2}$$

List of Abbreviations

Ag	Silver
Al	Aluminum
Au	Gold
C	Carbon
CB-UEM	Convergent Beam Ultrafast Electron Microscopy
CCD	Charge-Coupled Device
Cu	Copper
DFT	Discrete Fourier Transform
EELS	Electron energy loss spectroscopy
EFTEM	Energy-Filtered Transmission Electron Microscopy
ESI	Electron Spectroscopic Imaging
FHG	Fourth Harmonic Generation
FWHM	Full Width at Half Maximum
Ge	Germanium
GMS	Gatan Microscopy Suite
LaB_6	Lnthanum Hexaboride
LSPR	Localized Surface Plasmon Resonances
NBD	Nano Beam Diffraction
NP	Nanoparticle
OAPM	Off-Axis Parabolic Mirror
PINEM	Photon-Induced Near-Field Electron Microscopy
Platinum	Pt
PXRD QPA	Powder X-ray Diffraction Quantitative Phase Analysis
QPA	Quantitative phase analysis
SAED	Selected area electron diffraction

Sc	Scandium
SEM	Scanning Electron Microscope
SHG	Second Harmonic Generation
Si	Silicon
SNOM	Scanning Near-field Optical Microscopy
TEM	Transmission Electron Microscopy
TiO_2	Titanium Dioxide
UED	Ultrafast electron diffraction
UPS	Ultraviolet Photoelectron Spectroscopy
UTEM	Ultrafast Transmission Electron Microscopy
XPS	X-ray Photoelectron Spectroscopy
XRD	X-ray Diffraction
ZLP	Zero-Loss Peak
Zn	Zinc

List of Publications, Conferences

Publications

- R. Doostkam, L. Gelisio, A. Yurtsever, L. Rapp, A. V. Rode, and K. R. Beyerlein, "*Studying novel high-pressure phases in laser-shock-affected silicon using poly: an algorithm for spot-wise phase identification*."

  J. Appl. Crystallogr, vol. 58, no. 1, pp. 128–137, (2025).

- Uriel Bruno-Mota, Ingrid Nayeli Rodriguez-Hernández, Rasool Doostkam, Patrick Soucy, Fabiola Navarro-Pardo, German Orozco, Aycan Yurtsever, and Ana Tavares, "*Steady-state voltammetric characterization and simulation-aided study of the mass transfer enhancement at conical W/WO2 ultramicroelectrodes*."

  Electrochimica Acta, 402, 139524, (2022).

In Preparation

- Rasool Doostkam et al, "*Substrate-Dependent Orientation of Near-Field Dipoles in Plasmonic Nanoparticles Observed with Ultrafast Transmission Electron Microscopy*."
- Rasool Doostkam et al, "*Observation of Induced Chirality in Metallic Nanoparticles*."

Conferences

- Rasool Doostkam, Kenneth Beyerlein, Aycan Yurtsever. "*Overcoming Phase Identification Ambiguity in the Analysis of SAED Patterns from Polymorphic Nanomaterials*.", *IUMAS8 Conference* (2023).
- Rezvan Haji Hashemi, Wanting He, Rasool Doostkam, Roberto Morandotti, Aycan Yurtsever, "*Thermal Dynamics of Single Titanium Nitride Nanoparticles Using UTEM*." *MSC·SMC Meeting*, Ottawa, Canada (2024).
- Uriel Bruno-Mota, Ingrid Nayeli Rodriguez-Hernández, Rasool Doostkam, Patrick Soucy, Fabiola Navarro-Pardo, German Orozco, Aycan Yurtsever and Ana Tavares, "*Effect of the Geometry on the Mass Transfer Enhancement at Conical W/WO2 Ultramicroelectrodes*."
  ECS Meeting Abstracts, vol. MA2022-01, no. Z01, p. 2328, (2022).

1 Introduction

This chapter provides an overview of Transmission Electron Microscopy (TEM), covering its fundamental principles, commonly used methodologies, key applications, and essential concepts. Detailed introductory discussions related to the two main research projects are presented independently in Chapters 2 and 3.

1.1 Fundamentals of light-matter interactions

Light–matter interactions refer to the fundamental processes through which photons couple to electronic, vibrational, and other quasiparticle excitations in condensed matter systems. At the nanoscale, these interactions give rise to phenomena that classical optics cannot adequately describe. This regime—commonly referred to as nanophotonics or nano-optics—leverages sub-wavelength field confinement and resonant modes to manipulate light beyond the diffraction limit [2].

Nanoscale architectures enable the localization of electromagnetic fields within extremely small volumes, thereby significantly enhancing the strength of light–matter coupling relative to that in bulk materials. This enhanced interaction lies at the core of numerous emerging technologies; for instance, plasmonic and photonic nanostructures support applications in ultra-sensitive detection, high-speed optical communication, and efficient light harvesting for solar energy conversion.

Mastering the control of light–matter coupling at the nanoscale thus represents not only a compelling frontier in fundamental science but also a foundation for the development of next-generation optical and quantum devices.

In the macroscopic and microscopic regimes, Maxwell's equations govern the interaction between electromagnetic fields and matter, predicting the induced polarization response

$$P = \varepsilon_0 \chi^{(1)} E \tag{1.1}$$

where $\chi^{(1)}$ denotes the linear electric susceptibility, ε_0 is vacuum permittivity, and E is the electric field [3]. The real component of the complex electric susceptibility describes the material's refractive properties, while the imaginary component describes its optical absorption. Scattering phenomena arise from spatial variations in the dielectric function ε(ω), manifesting as Rayleigh scattering in the elastic limit or Mie scattering when the scatterer size is comparable to the wavelength.

These classical electrodynamic models provide accurate descriptions of bulk optical responses, including light transmission through dielectric media, metallic reflectivity, and the colorimetry of colloidal nanoparticle suspensions—provided that the system dimensions remain larger than those associated with quantum confinement effects.

At atomic and molecular length scales, energy levels are quantized. Photons with energy $\hbar\omega$ can induce transitions between quantum states $|i\rangle$ and $|f\rangle$ when the energy difference $\Delta E = E_x - E_i$ satisfies the resonance condition $\Delta E=\hbar\omega$. Time-dependent perturbation theory yields the Fermi golden rule, which describes the transition rate as

$$\Gamma_{i\to f} = \frac{2\pi}{\hbar}\left|\langle f|\hat{H}_{int}|i\rangle\right|^2\rho_f \qquad (1.2)$$

where $\hat{H}_{int}=-\boldsymbol{d}\cdot\boldsymbol{E}$ in the electric-dipole approximation, and ρ_f denotes the density of final states. This theoretical framework encompasses the fundamental processes of optical absorption, spontaneous emission (arising from vacuum field fluctuations), and stimulated emission—the latter forming the physical basis for laser operation [4,5].

Key quantum mechanical phenomena such as coherence, dephasing, and population inversion play essential roles in the design and performance of modern photonic and optoelectronic systems. Light–matter interactions encompass a variety of mechanisms that give rise to distinct physical outcomes and underpin numerous optical technologies. Absorption occurs when photon energy is transferred to internal excitations within the material, such as electronic, vibrational, or phononic modes—an essential process in applications like solar cells and UV–Vis spectroscopy. Emission involves the release of photons from an excited state; this can be either spontaneous, resulting in incoherent light (as in LEDs), or stimulated, which produces coherent photons and is fundamental to lasers and single-photon sources. In elastic scattering, the direction of photon propagation changes while its energy remains conserved, a principle exploited in Lidar systems, optical tweezers, and the manifestation of structural color. In contrast, inelastic scattering involves an exchange of energy between photons and matter, as seen in processes such as Raman and Brillouin scattering, which enable chemical fingerprinting and temperature mapping. Finally, nonlinear optical processes arise when the material polarization includes higher-order susceptibility terms (e.g., $\chi^{(2)}$, $\chi^{(3)}$), allowing for phenomena such as frequency conversion, second-harmonic generation, and optical Kerr gating, which are pivotal in ultrafast optics and signal processing [6, 7].

Light–matter interactions can be classified into distinct coupling regimes depending on the strength and spatial nature of the interaction. In the weak coupling regime, light perturbs matter

without significantly modifying its intrinsic eigenstates; most conventional spectroscopies, including absorption and fluorescence measurements, operate within this regime. In contrast, strong coupling occurs when the interaction between light and matter is sufficient to create hybridized states known as polaritons, leading to a characteristic splitting of energy levels into upper and lower branches—an effect observable as Rabi splitting. Finally, near-field coupling arises when evanescent or non-propagating electromagnetic field components dominate the interaction, enabling spatial confinement well below the diffraction limit. This regime is harnessed in techniques such as scanning near-field optical microscopy (SNOM) and photon-induced near-field electron microscopy (PINEM), allowing nanoscale resolution and access to localized optical phenomena [8-10] .

1.2 Fundamentals of electron-matter interactions, electron scattering, and diffraction

In electron microscopy, electrons interact with the sample to produce images or signals that reveal its characteristics. Understanding the fundamentals of electron–matter interactions is therefore essential. The probability of scattering is described by the cross section, σ, or mean free path, Λ. The cross section is the effective area over which a particle can interact with the electron beam [11]. For a specimen with N particles per unit volume, the probability of scattering a single electron passing dx thickness of the sample is Nσdx. The mean free path is the average distance that an electron can travel through the sample before scattering

$$\Lambda = \frac{1}{N\sigma} \tag{1.3}$$

If the specimen is thin (typically <100 nm), electrons are more likely to undergo single or no scattering events. However, in thicker samples, electrons may scatter multiple times, a phenomenon known as dynamical scattering. When an electron passes x distance in a specimen, the probability of n-times scattering is described by Poisson statistics:

$$\mathrm{P(n)} = \left(\frac{1}{n!}\right)\left(\frac{x}{\Lambda}\right)^{n} \exp\left(-\frac{x}{\Lambda}\right) \tag{1.4}$$

In cases involving multiple scattering events with different mechanisms, computational averaging methods such as Monte Carlo simulations are particularly useful [11].

As an electron beam passes through a thin specimen, it can undergo various interactions. Inelastic interactions include ionization, secondary emission, and energy-loss excitation. Additionally, electrons may be elastically scattered by atomic nuclei and electron clouds, changing

direction without any loss of energy. A portion of the electrons are backscattered, while the remaining ones undergo scattering by atomic nuclei and electron clouds through Rutherford scattering.

In elastic interactions, although the electron retains its energy, its direction can change significantly. These electrons play a major role in the formation of images and diffraction patterns in electron microscopes. Elastic scattering can be classified into two types, one of which is large-angle scattering (typically >5°), also known as Rutherford scattering, which arises from interactions between electrons and atomic nuclei. The second type is known as small-angle scattering (typically between 0.5° and 5°), which occurs when primary electrons are scattered by the screened nuclear field, as a result of the shielding effect of the atom's electron cloud. As the scattering angle increases, elastic scattering can begin to lose coherence, and in some cases, like 180° collisions, it may result in a slight energy change - for example, a 100 keV electron may lose approximately 1 eV. Elastic scattering probability scales approximately with the square of the atomic number (Z^2), while inelastic scattering tends to scale linearly with Z [11,12].

There are many inelastic processes involved in electron–matter interactions, but four well-known ones include phonon excitation, plasmon excitation, single-electron excitation, and inner-shell ionization (radiative transitions). Phonon excitation occurs when the electron beam interacts with lattice vibrations in the sample, transferring energy to phonons-quanta of atomic vibrations-which can locally increase the temperature. The energy loss in this process is typically less than 1 eV, and the scattering angle is relatively large, on the order of ~10°, with a mean free path of approximately 1 μm. Plasmon excitation involves the inelastic scattering of primary electrons that resonantly excite collective oscillations of valence electrons, known as plasmons. These oscillations are described by the Drude–Lorentz model, where the valence electrons behave like a free electron gas. The energy loss associated with plasmon excitation typically ranges from 5 to 30 eV, and the corresponding mean free path is relatively short, around 100 nm. This short mean free path makes plasmon scattering one of the most frequent inelastic interactions. As a result, to observe other, less dominant inelastic processes, plasmon contributions often need to be removed from the spectrum. The third process, known as single-electron excitation, occurs when the incident electron beam transfers energy to a valence or core electron in the sample, causing ionization. If the excited electron escapes the sample surface, it can contribute to secondary electron imaging. The typical energy loss for valence electron excitation is up to ~50 eV, but for core-level excitations, the energy loss can be significantly higher. For instance, the carbon K-edge appears at approximately 284 eV, while the zirconium L-edge is around

2200 eV [11,13]. As the energy of the primary electrons increases, the probability of single-electron (inelastic) scattering events generally decreases. The fourth major inelastic process is direct radiation loss, also known as bremsstrahlung (braking radiation). It originates from the deceleration or deflection of high-energy electrons as they pass through the electric fields of atomic nuclei in a solid, resulting in the emission of photons. The energy loss in bremsstrahlung can range from near zero to the full energy of the primary electron. When the high-energy electrons pass through a sample, all inelastic processes can occur till the electron stops or leaves the sample. Figure 1.1 shows the schematic of some of the interactions between the electron beam and the sample.

Figure removed due to copyrights issues

Figure 1-1 Schematic diagram of different processes for electron-matter interaction in a thin sample. BSE stands for back-scattered electrons. EELS stands for electron energy loss spectroscopy [11]**.**

Electron diffraction is a powerful technique used in electron microscopy and crystallography to study the structural properties of materials at the atomic scale. By exploiting the wave-like nature of electrons, electron diffraction enables the investigation of the arrangement of atoms in solids, the identification of crystal structures, and the measurement of interplanar spacings within materials. This technique is particularly valuable in the study of nanomaterials, thin films, and complex materials that cannot be easily analyzed using traditional X-ray diffraction.

When an electron beam interacts elastically with a crystalline material, the electrons undergo diffraction due to the periodic arrangement of atoms in the crystal lattice. This interaction is governed by the wave-particle duality of electrons, where the electrons behave as both particles

and waves. The wavelength of the electrons is inversely proportional to their momentum, which is determined by their accelerating voltage. According to de Broglie's hypothesis, the wavelength

$$\lambda = \frac{h}{p} = \frac{hc}{\sqrt{E_k^2 + 2E_k mc^2}} \tag{1.5}$$

where h is Planck's constant, m is the rest mass of the electron, and E_k is the kinetic energy of the electron. At high accelerating voltages, the electron wavelength becomes sufficiently small to resolve atomic-scale features, typically in the range of picometers, making electron diffraction a high-resolution technique.

As the electron beam passes through the crystal, the atoms scatter the incident electrons. This scattering leads to interference, resulting in diffraction patterns that are characteristic of the crystal's structure. Diffraction patterns typically appear as concentric rings for amorphous materials, a combination of discrete spots arranged in ring-like formations for polycrystalline materials, and sharp, isolated spots for single crystals. These patterns are commonly observed using selected area electron diffraction (SAED), microbeam, or nanobeam diffraction techniques. The spacing and intensity of these spots or rings can provide valuable information about the crystallographic structure of the material.

For diffraction to occur, the incident electron beam must satisfy the Bragg's law condition, which relates the diffraction angle to the wavelength of the electrons and the spacing between crystal planes:

$$n\lambda = 2dsin\theta \tag{1.6}$$

where n is the diffraction order, λ is the wavelength of the electron, d is the interplanar spacing of the crystal planes, and θ is the angle of diffraction [14].

The diffraction pattern can be analyzed using the concept of the reciprocal lattice, which is a mathematical construct used to represent the diffraction conditions for a given crystal. The reciprocal lattice vectors are related to the real-space lattice vectors, and the diffraction spots in the electron diffraction pattern correspond to the reciprocal lattice points. This relationship allows the determination of crystal symmetry, unit cell parameters, and orientation.

1.3 Transmission electron microscopy (TEM)

The pursuit of high-resolution imaging capabilities, constrained by the diffraction limit inherent to optical microscopy due to the comparatively large wavelengths of visible light, prompted the development of alternative techniques. Electrons, possessing de Broglie wavelengths on the order of picometers—several orders of magnitude shorter than visible light—emerged as a compelling probe for achieving enhanced spatial resolution. This conceptual advance culminated in the design and construction of the first transmission electron microscope (TEM) by Ernst Ruska and Max Knoll in Berlin in 1930, laying the foundation for modern electron microscopy [15,16]. Due to their charge and mass, electrons are susceptible to Lorentz forces when subjected to magnetic fields. Consequently, electron beam manipulation in transmission electron microscopes (TEMs) is achieved using magnetic lenses, typically implemented as solenoid-generated fields. Figure 1.2 presents a schematic diagram of a conventional TEM, which is vertically configured—from the electron source at the top to the imaging detector at the bottom.

At the apex of the column resides the electron emitter, or filament, which serves as the primary electron source. This component is commonly fabricated from materials with low work functions, such as tungsten, tantalum, or lanthanum hexaboride (LaB_6), and is positioned within a Wehnelt cylinder—an electrostatic element that functions as a focusing electrode. Electron emission within TEMs can occur through various mechanisms, including thermionic emission, field emission, or a hybrid approach known as Schottky emission. In the latter case, thermal energy assists field emission by lowering the potential energy barrier at the emitter surface, thereby enhancing electron yield while maintaining spatial coherence [17].

Figure removed due to copyrights issues

Figure 1-2 Schematic of the main parts of TEM with a ray diagram in the center of the column [18]**.**

Electrons are accelerated toward the anode by an applied voltage, typically in the range of 100 keV to 400 keV, giving them high kinetic energy. The electron beam then passes through a series of magnetic condenser lenses, which demagnify and focus the beam to a spot size on the order of a few microns to nanometers, depending on the type of electron source used. The C1 lens (or spot size control lens) adjusts the demagnification of the electron source, effectively controlling the beam convergence. The C2 lens (also called the intensity lens) further focuses the beam and determines the spot size on the sample. The specimen is typically 100 nm thick or thinner to allow sufficient electron transmission. The objective lens is the next critical component; it forms the initial real-space image of the specimen at the image plane and simultaneously produces the reciprocal space (diffraction) pattern at its back focal plane. At this stage in the TEM imaging process, the magnification is typically around 50X to 100X, as determined by the objective lens. Objective apertures, with diameters ranging from 10 to 100 microns, can be inserted to limit beam divergence and enhance image contrast by blocking scattered electrons. Following the objective lens, the projector lens system—including the intermediate lens (often referred to as the first projector lens)—can be adjusted to focus the electron beam either on the image plane to form a real-space image, or on the back focal plane to produce the diffraction pattern of the specimen. A series of projector lenses further magnifies the image or diffraction pattern formed by the objective lens. In diffraction mode, a selected area electron diffraction (SAED) aperture is used to isolate a specific region of the specimen for analysis. The final component of the TEM is the

fluorescent screen, which allows direct visualization of the image or diffraction pattern. This screen is often coupled with a camera system to digitally capture and record the data. There are two important angles mentioned by α and β, which are convergence and collection semi-angles. The angle α determines how tightly the electron beam is focused onto the sample, and the angle β defines the range of scattered electrons that are collected to form the image or diffraction pattern. A TEM can produce images with magnifications exceeding one million times, allowing visualization of structures at the atomic scale [19,20].

1.4 Ultrafast transmission electron microscopy (UTEM)

Investigating the ultrafast dynamics of light–matter interactions—while simultaneously achieving high spatial resolution and real-time access to temporal and energy-resolved information—represents a frontier challenge in modern science. Ultrafast Transmission Electron Microscopy (UTEM) addresses this by integrating the high spatial resolution capabilities of conventional TEM with femtosecond temporal resolution of ultrafast lasers, enabling the exploration of transient phenomena across disciplines including physics, chemistry, materials science, and biology.

UTEM operates on the principle of pump–probe methodology, wherein an ultrafast pulsed laser (pump) initiates dynamic processes in the specimen—such as phase transitions, lattice vibrations, or charge redistributions—and an electron pulse (probe), generated via photoemission, interrogates the evolving state of the system. A precisely controlled optical delay stage adjusts the temporal offset between the pump and probe pulses, allowing for systematic reconstruction of time-resolved images or diffraction patterns on the femtosecond timescale. This technique enables direct visualization of the structural and electronic evolution of materials with spatiotemporal resolution sufficient to capture the fundamental mechanisms driving ultrafast phenomena.

Initial groundbreaking studies at Caltech, the Technical University of Berlin in Stefan Eisebitt's group, the Max Born Institute (MBI) under Thomas Elsässer's leadership, and Lawrence Livermore National Laboratory established the viability of conducting pump-probe experiments within electron microscopy, employing either stroboscopic techniques or single-shot imaging methods. Encouraged by significant individual achievements demonstrating its wide-ranging

applications, time-resolved electron microscopy is now being actively pursued by an increasing number of research groups around the world [21,22].

The experimental work presented in Chapter 2 was carried out using the UTEM, and the current explanation refers to that project. Further technical details about the UTEM are also provided in Chapter 2.

1.5 Photoelectrons and nanomaterials interactions

In conventional transmission electron microscopy (TEM), electrons are typically generated through thermionic emission, producing a continuous electron beam. In contrast, ultrafast TEM (UTEM) utilizes photoemission triggered by ultraviolet (UV) laser pulses, generating a pulsed electron beam via the photoelectric effect at the electron gun. This enables time-resolved imaging and diffraction studies of ultrafast phenomena on femtosecond timescales. Here, photoelectrons refer to the electrons emitted via the photoelectric effect at the electron gun, triggered by ultraviolet (UV) laser illumination, which subsequently probe the sample

The interaction between photoelectrons and nanomaterials gives rise to distinct physical effects, driven by the inherent characteristics of nanoscale systems—most notably, their high surface-to-volume ratios and quantum confinement. To probe these phenomena, photoelectron spectroscopy techniques—including X-ray Photoelectron Spectroscopy (XPS) and Ultraviolet Photoelectron Spectroscopy (UPS)—are widely employed. These methods provide valuable insights into the electronic structure, chemical composition, and surface states of nanomaterials, thereby complementing the time-resolved imaging capabilities of UTEM [23,24]. These techniques are inherently surface-sensitive, making them ideal for studying surface modifications, adsorption processes, and catalytic activity of nanomaterials.

The reduced dimensionality, pronounced surface-to-volume ratio, and quantum confinement effects impart electronic properties to nanomaterials that differ markedly from those of their bulk analogues. For instance, nanoparticles, quantum dots, nanowires, and two-dimensional materials such as graphene exhibit quantized electronic energy levels and prominent surface states—features that significantly influence their interactions with incident photoelectrons and modulate their electronic response [25-27].

Furthermore, elucidating the interactions between photoelectrons and nanomaterials is critical for advancing a range of high-performance technologies, including photovoltaic cells, photocatalysts, and photoelectron-based sensors. In the context of photocatalysis, for example, electrons

generated through photon absorption facilitate redox reactions at the surface of semiconductor nanostructures. These processes underpin key applications such as the conversion of solar energy into chemical fuels and the degradation of environmental pollutants. A comprehensive understanding of the mechanisms governing photoelectron generation, transport, and their interactions at the nanoscale is essential for optimizing the efficiency and functionality of these technologies [28-31].

In ultrafast transmission electron microscopy (UTEM), a critical aspect of photoelectron-nanoparticle interactions involves the generation of localized electromagnetic fields surrounding metallic nanoparticles, such as gold or silver. These near fields can be directly visualized using Photon-Induced Near-Field Electron Microscopy (PINEM), a technique that leverages electron energy-loss spectroscopy (EELS) to spectrally filter electrons based on energy exchange. This enables the formation of images composed solely of electrons that have interacted with the optical near fields. Another key application of UTEM is the investigation of nanoparticle thermodynamics via ultrafast electron diffraction (UED). In this modality, selected area electron diffraction (SAED) patterns are acquired at successive time delays, allowing temporal resolution of structural dynamics. By quantifying changes in Bragg reflection intensities and invoking the Debye–Waller formalism, atomic vibrations can be extracted, enabling the determination of transient lattice temperatures with high spatial and temporal precision [32-38].

1.6 Electron energy loss spectroscopy (EELS) and Photon-Induced Near-field Electron Microscopy (PINEM)

Electron energy-loss spectroscopy (EELS) encompasses techniques wherein a beam of high-energy electrons interacts with a material—whether solid or liquid—and the scattered electrons are analyzed to yield an energy-loss spectrum. This spectrum captures the inelastic scattering events and reflects the energy transferred from the electrons to the specimen. A subset of EELS, known as electron spectroscopic imaging (ESI), enables spatially resolved analysis by filtering electrons based on their energy losses to generate images formed exclusively from inelastically scattered electrons. Another technique is energy-filtered transmission electron microscopy (EFTEM), which enables the filtering of the electron beam based on its energy. These techniques are broadly categorized under electron energy-loss and gain spectroscopy, as the incident electron beam may lose or gain energy and undergo changes in intensity upon interacting with the sample. The characteristics of the recorded energy-loss spectrum are susceptible to the

material's elemental composition and electronic structure, thereby providing valuable insights into both chemical and physical properties at the nanoscale.[11].

The phenomenon of electron energy loss was first explored by James Chadwick and Charles Ellis in the 1920s–1930s, who measured energy loss of electrons passing through thin foils and gases. The technique was later developed for practical use in the transmission electron microscope by James Hillier and R. F. Baker in the mid-1940s. However, it remained relatively underutilized for the next five decades and only gained broader adoption in research during the 1990s, largely due to significant advancements in microscope instrumentation and vacuum technology [39].

The JEOL JEM-2100 transmission electron microscope (TEM) is equipped with an EELS system, typically integrated from manufacturers such as Gatan (e.g., Gatan Imaging Filter – GIF). When using a LaB_6 electron gun, the energy resolution of the EELS system is approximately 1.0–1.5 eV. EELS is particularly well developed for around 25 elements ranging from carbon (Z=6) to zinc (Z=30), including light elements and the 3d transition metals [40].

For example, light elements such as carbon (C), nitrogen (N), and oxygen (O) are commonly analyzed via their K-edges, which typically lie in the 280–540 eV range. The 3d transition metals—from scandium (Sc) to zinc (Zn), including Sc, Ti, V, Cr, Mn, Fe, Co, Ni, Cu, and Zn—are analyzed using their $L_{2,3}$-edges, generally located between 400 and 1000 eV [11].

There are certain limitations to EELS, such as overlapping edges, which occur when different elements have core-loss edges at similar energy levels—for example, distinguishing the N K-edge from the Ti L-edge. Additionally, limited energy resolution and beam-induced damage pose further challenges for this technique [17].

The integration of UTEM with plasmonics offers a uniquely powerful platform for directly probing plasmonic near-fields and dynamics at the nanoscale. A prominent example of this synergy is PINEM. In PINEM, an ultrafast optical pump pulse excites localized or propagating surface plasmons, while a time-synchronized electron pulse interacts with the resulting near-fields [32], [41].

As electrons traverse optically induced near-fields, they can absorb or emit discrete energy quanta corresponding to integer multiples of the plasmon energy, resulting in the emergence of sidebands within the electron energy-loss spectrum. Through the application of energy-filtered imaging, one can construct spatially resolved maps of the near-field intensity, thereby enabling

direct visualization of plasmonic field distributions with a spatial resolution dictated by the electron probe itself.

Critically, the precise temporal synchronization between the optical excitation pulse and the electron probe confers femtosecond-scale temporal resolution. Time-resolved photon-induced near-field electron microscopy (PINEM), for instance, has been employed to image the propagation and interference of surface plasmon polaritons (SPPs) along buried metal–dielectric interfaces, revealing spatiotemporal dynamics with sub-10-nanometer spatial and approximately 100-femtosecond temporal resolution. These capabilities highlight the power of ultrafast transmission electron microscopy (UTEM) as a tool for capturing the real-space and real-time evolution of optically excited plasmonic phenomena [42,43].

1.7 Selected area electron diffraction (SAED)

In transmission electron microscopy (TEM) operating in diffraction mode, precise analysis of localized sample regions is often required. This is achieved through the use of circular Selected Area Electron Diffraction (SAED) apertures, which confine the transmitted electron beam to a designated area of interest. These apertures are strategically positioned at the image plane of the objective lens, situated between the objective lens and the intermediate and projector lenses. By isolating specific regions, SAED facilitates the acquisition of diffraction patterns that are representative of targeted crystallographic domains within the specimen.

In the JEOL JEM-2100 TEM, there are typically four SAED apertures with diameters of 100, 50, 20, and 10 μm [19]. However, the actual area selected on the sample also depends on the objective lens magnification. As a result, the same aperture may correspond to slightly different physical areas under different imaging conditions. Figure 1.3 shows an example of a SAED pattern acquired from a selected region using one of the apertures.

Figure removed due to copyrights issues

Figure 1-3 An example of SAED. Part a shows the selected area in the real-space image mode, and part b represents the captured diffraction pattern [19]**.**

The lattice spacing limit that can typically be analyzed using Selected Area Electron Diffraction (SAED) is on the order of 0.1 to 1 nm. However, this limit can be extended to approximately 10 nm or more when employing high-dispersion electron diffraction, enabling the resolution of much larger lattice spacings such as those found in superlattices or moiré patterns. According to Bragg's law, a larger lattice spacing d corresponds to a smaller diffraction angle θ, causing the resulting diffraction spots to appear very close to the central (transmitted) beam. This proximity makes them difficult to distinguish in standard SAED mode. In high-dispersion mode, the diffraction pattern is magnified—typically by increasing the camera length—thereby spreading out small-angle features and allowing large d-spacings to be resolved more clearly. This information about SAED forms the basis for the measurements done in the study of laser-induced high-pressure phases of silicon presented in Chapter 3.

1.8 Crystallography and crystal symmetry groups

The investigation of materials and the elucidation of the relationship between their properties and underlying structures has remained a fundamental objective across scientific disciplines. For over a century, X-ray crystallography has served as a cornerstone technique, offering three-dimensional insights into the structural mechanisms and functional behavior of a diverse array of materials and biological macromolecules. As a result, crystallography has evolved into an

indispensable analytical tool, underpinning advancements in a broad spectrum of industries, including mining, pharmaceuticals, and aerospace engineering [44].

In 1912, Max von Laue demonstrated the diffraction of X-rays by crystals, providing direct evidence of their periodic internal structure. Around the same time, W. H. Bragg and W. L. Bragg formulated Bragg's Law, which relates the wavelength of X-rays to the angle of incidence and the distance between atomic planes in a crystal. The impact of this powerful new tool on biology was evident in the discovery of the double-helix structure of Deoxyribonucleic acid (DNA) by Watson and Crick in the 1950s, which was based on X-ray diffraction data collected by Rosalind Franklin and Maurice Wilkins. It also enabled the determination of the structures of important proteins, such as myoglobin and hemoglobin. Since the 20th century, there has been significant progress in crystallography through the development of advanced techniques such as neutron diffraction, electron diffraction, and synchrotron radiation [45,46].

When a material is subdivided into increasingly smaller components, its internal structure may reveal either a periodic, ordered arrangement or a disordered configuration of its constituent particles—such as atoms, ions, or molecules. Materials exhibiting long-range order are classified as crystalline, whereas those lacking such periodicity are termed amorphous. The field of crystallography provides a systematic framework for studying crystalline materials by defining two fundamental concepts: the lattice and the basis. A lattice is a three-dimensional, periodically repeating array of points that delineates the spatial arrangement for placing the basis. The basis represents the simplest assembly of atoms, ions, or molecules associated with each lattice point. Together, these elements construct the overall crystal structure. To facilitate structural analysis, a unit cell is identified as the smallest representative volume that, through translational symmetry, can reproduce the entire crystal lattice. A unit cell of a crystal is defined by the lattice parameters: a, b, and c, which represent the lengths of the cell edges and the angles α, β, and γ, which are the angles between the edges (b & c, a & c, and a & b, respectively).

The pursuit of symmetry in nature and materials—and the effort to simplify its understanding—has been a longstanding human endeavor. While many attempts have been made to document aspects of symmetry, the foundation of its modern scientific study is largely attributed to the Abbé Haüy. By examining the way calcite crystals fractured, Haüy noticed that the resulting fragments consistently exhibited specific angles between their faces. This led him to conclude that crystals are built from repeating, identical units. In 1815, he expanded his research to numerous other crystals and formalized his findings in what he termed the Loi de symétrie (Law of Symmetry).

During the 19th century, the study of symmetry advanced considerably with the introduction of key concepts such as point groups, Bravais lattices, and space groups [47].

A point group is a collection of symmetry operations centered around a point that collectively fulfill the conditions of a mathematical group. In crystallography, point groups must also be compatible with a space lattice. Only a limited number of such symmetry combinations are found in actual crystals. The classification of the 32 crystallographic point groups was first introduced by Hessel in 1830, though his work went largely unrecognized until Gadolin independently rediscovered the same groups in 1869. The 32 crystallographic point groups are distributed among seven crystal systems as follows: 2 in triclinic, 3 in monoclinic, 3 in orthorhombic, 7 in tetragonal, 5 in trigonal, 7 in hexagonal, and 5 in cubic systems [45].

Another important class of symmetry groups arises from considering translational symmetry operations. If we examine the internal structure of a crystal, we find that it consists of a vast number of atoms or molecules arranged in a highly regular pattern. Within this structure, there exists a set of points that are indistinguishable in terms of their surroundings—the crystal appears identical when viewed from any of these points. This set of equivalent points forms what mathematicians refer to as a lattice. It can be mathematically demonstrated that there are only a limited number of fundamentally different ways to arrange such points in space so that each one has the same environment. This classification was established by Bravais in 1850, who proved that in three-dimensional space, only 14 distinct lattice types exist. These are now known as the Bravais lattices.

A point group describes the symmetry of a finite object and, in the case of natural crystals, only 32 distinct point groups exist. In contrast, a Bravais lattice focuses on the spatial arrangement of a set of mathematical points. However, to fully understand the internal structure of a crystal—specifically, the precise arrangement of atoms within its unit cell—one must go beyond point groups and Bravais lattices to a more advanced symmetry concept: the space group.

A space group accounts for the symmetry of a structure made up of repeating units, where each unit is not just a point but a finite object or a cluster of atoms, potentially possessing its internal symmetry. Space groups include all the symmetry operations found in point groups, such as rotations, reflections, inversions, and roto-inversions (or roto-reflections). In addition, space groups incorporate translational symmetry operations, such as: screw axes (a combination of rotation and translation along the axis), and glide planes (a combination of reflection and translation parallel to the plane). These operations involve a displacement of the crystal's structure along with the rotational or reflective transformation, making space groups essential for describing

the full symmetry of three-dimensional crystalline materials. The 230 crystallographic space groups are classified into seven crystal systems as follows: 2 in triclinic, 13 in monoclinic, 59 in orthorhombic, 68 in tetragonal, 25 in trigonal, 27 in hexagonal, and 36 in cubic systems.

A Laue group is a type of point group that characterizes the symmetry of a crystal's diffraction pattern, rather than the symmetry of the crystal structure itself. These groups include all point group operations that preserve the direction of the incident X-ray or electron beam and always contain inversion symmetry, reflecting the inherent centrosymmetric nature of diffraction patterns. Since multiple crystallographic point groups can produce identical diffraction symmetries, the 32 crystallographic point groups reduce to only 11 distinct Laue groups. The 11 Laue groups are distributed among the seven crystal systems as follows: 1 in triclinic, 1 in monoclinic, 3 in orthorhombic, 2 in tetragonal, 1 in trigonal, 2 in hexagonal, and 1 in cubic systems [48].

2 Studying the behavior of near fields and dipoles of nanoparticles using the PINEM technique

2.1 Introduction

2.1.1 Background and Motivation

In the modern era, the fields of electronics, photonics, nanomaterials, and nanotechnology are increasingly intertwined in the pursuit of advanced phenomena and high-tech fabrication processes aimed at addressing evolving human needs. The rapid growth of nanomaterials science and the nanophotonics industry demands a profound understanding of light–matter interactions at the nanoscale. A key avenue of exploration in this context is the investigation of the electric fields surrounding nanostructures—an essential step in deepening our knowledge of nanoplasmonic and nanophotonic behavior. Photon-Induced Near-Field Electron Microscopy (PINEM) has emerged as a powerful technique for probing the near-field optical response of nanostructures. This method is widely employed to visualize the optical near-fields of metallic nanoparticles, particularly those composed of noble metals such as gold and silver, which exhibit pronounced surface plasmonic resonances when excited with appropriately tuned photon energies.

PINEM images frequently reveal dipolar field distributions around spherical nanoparticles, typically aligned with the linear polarization axis of the incident pump laser; in certain studies, circular polarization has also been employed to investigate alternative field configurations. These dipolar fields often manifest as crescent-shaped features, indicative of the localized plasmonic response. In systems comprising ensembles of nanoparticles, the near-field behavior may vary significantly between individual particles under uniform excitation, reflecting differences in particle morphology, spacing, material composition, and substrate interactions. Our research focuses on elucidating these variations by systematically studying the dipolar response of nanoparticles under diverse conditions—including different nanomaterial types and substrate compositions—in order to uncover the physical mechanisms governing these interactions. The resulting insights aim to inform the development of next-generation nanophotonic and nanoelectronic devices through an improved understanding of the evanescent electromagnetic fields that arise at the nanoscale.

2.1.2 Problem Statement and Research Objectives

The Photon-Induced Near-Field Electron Microscopy (PINEM) technique has yielded valuable spatio-temporal insights into the optical near-field responses of various nanoparticles. In particular, studies focused on spherical gold nanoparticles (Au NPs) have demonstrated the generation of dipolar field distributions upon excitation by a pump laser. In most experimental configurations, linearly polarized pump lasers are employed, with polarization angles rotated orthogonally using a half-wave plate to induce and visualize dipolar modes along multiple directions. These interactions between the incident electromagnetic fields and the nanoparticles give rise to evanescent fields, whose characterization is essential for deepening our understanding of the underlying plasmonic behavior.

To systematically investigate these interactions, we analyzed the dependence of PINEM signal dipole behavior on several experimental parameters, including the polarization direction of the pump laser, substrate composition, and the temporal synchronization between the pump pulse and the probe photoelectrons. This study aims to elucidate how such factors influence the formation and orientation of dipolar near-fields, thereby contributing to a more comprehensive understanding of nanoparticle-light interactions at the nanoscale.

2-1-3 Literature review

2.1.3.1 Pump-probe experiments

Pump–probe techniques are widely employed in light–matter interaction experiments to investigate ultrafast electronic dynamics in response to laser excitation. By monitoring variations in the optical response as a function of the time delay between the pump and probe pulses, one can extract temporal information about underlying physical, chemical, or biological processes. A typical pump–probe setup comprises a high-intensity pump laser used to initiate a specific excitation—such as electronic transitions, molecular vibrations, or phase changes—followed by a lower-power probe pulse that interrogates the system at predefined temporal delays. The delay is controlled via an optical delay stage, enabling precise synchronization between the two beams. By systematically varying this delay, the transient evolution of the system can be temporally

resolved, allowing for detailed insights into its dynamic behavior on femtosecond to picosecond timescales [49], [50], [51]

The classification of pump-probe experiments depends on the nature of the probe employed. Common configurations include optical pump-optical probe, optical pump–electron probe, and optical pump–X-ray probe techniques, among others [52], [53]. Pump–probe experiments are generally categorized into two main classes: pump–probe spectroscopy and pump–probe microscopy. In pump–probe spectroscopy, an ultrafast pump laser pulse excites a molecule from its ground state to an excited state, initiating relaxation dynamics on a femtosecond to picosecond timescale. A time-delayed probe pulse subsequently interrogates the population of the excited state at various temporal delays relative to the excitation, enabling the investigation of ultrafast dynamic processes.

Pump–probe microscopy, on the other hand, is an advanced imaging modality that extends this concept by spatially resolving the excited-state dynamics. It generates a sequence of time-resolved images that map the temporal evolution of the system, offering a visual representation of ultrafast phenomena.

A landmark development in this field was introduced by Ahmed Zewail, who pioneered the use of a transmission electron microscope coupled with a pulsed laser to probe dynamic processes in nanomaterials at ultrafast timescales. This technique, known as four-dimensional (4D) electron microscopy, integrates spatial, temporal, and energy resolution, providing comprehensive insight into nanoscale dynamics in both time and space [53,54].

2.1.3.2 UTEM and its capability for material characterization

Until 1931, the investigation of microscopic structures relied exclusively on optical microscopy, which was fundamentally constrained by the diffraction limit, as described by Ernest Abbe's equation (2.1), which imposes a spatial resolution limit of approximately 200 nm for light with a wavelength of 400 nm [55], [56].

$$\mathrm{d} = \frac{0.612\lambda}{\mathrm{n}\sin\alpha} \tag{2.1}$$

where d is the minimum resolvable distance (spatial resolution limit), λ is the wavelength of the light used, n is the refractive index of the medium between the objective lens and the sample, and α is the half-angle of the maximum cone of light collected by the objective lens (also known as the angular aperture)

De Broglie had already shown in 1924 that electrons can behave as a wave with a relevant

wavelength

$$\lambda = \frac{h}{p} = \frac{h}{mv\sqrt{1-v^2/c^2}} \tag{2.2}$$

where h is Planck's constant (6.626×10^{-34} J·s), m and v are the rest mass and the velocity of the object. The wavelength of an electron with a speed close to the light ($c = 3 \times 10^8$ m/s) is much shorter than the optical wavelengths. To overcome the resolution limits of optical microscopes, scientists turned to electron beams, which significantly enhance spatial resolution down to the angstrom scale.. In 1931, Ernst Ruska and Max Knoll started to develop the first electron microscope to show its capability of spatial resolution, which resulted in the first TEM in 1933 [16]. After that, scientists tried to boost its accuracy by adjusting the tools, such as additional lenses, aberration correction, and so on. To study the ultrafast phenomena in nanoscale regimes that are happening in nonequilibrium conditions, there was a need for devices. In the late 1990s and early 2000s, Ahmed Zewail and his team developed the field of femtochemistry, which focuses on studying chemical reactions and molecular motions on ultrafast timescales [53,57]. They combined femtosecond laser pulses with electron microscopy to achieve the spatial and temporal information of ultrafast phenomena. Later, in 2008, Zewail and his collaborators at Caltech advanced this research by developing the ultrafast transmission electron microscopy (UTEM) technique, which enables the study of structural dynamics occurring on the femtosecond timescale within localized nanoregions [38,58]. Using this new development, researchers were able to investigate phenomena with near-atomic spatial resolution and hundreds of femtoseconds temporal precision. In 1999, Ahmed Zewail won the Nobel Prize for his work in femtochemistry.

In conventional transmission electron microscopy (TEM), a continuous electron beam is emitted from an electron source, typically operating in the thermionic emission mode. This enables the acquisition of two-dimensional spatial information. TEM can function in both imaging and diffraction modes; however, these modes are generally employed in a static regime, capturing the steady-state structural and crystallographic properties of a sample.

In contrast, ultrafast transmission electron microscopy (UTEM) incorporates a pulsed laser, often with pulse durations on the order of hundreds of femtoseconds. Using a specialized optical setup, the initial laser beam is split into two distinct beams. One beam undergoes fourth harmonic generation to produce ultraviolet (UV) light, which is then directed into the TEM column and focused on the electron gun. This UV light initiates photoemission, generating ultrashort electron pulses. The second beam, commonly referred to as the pump laser, is converted to a desired wavelength (e.g., 515 nm) and used to excite the sample, thereby inducing an ultrafast, non-

equilibrium state. The delayed electron pulses subsequently probe the sample, allowing time-resolved investigation of dynamic processes at the nanoscale. Figure 2.1 shows a typical UTEM configuration with a UV and pump laser.

Figure removed due to copyrights issues

Figure 2-1 A schematic of a UTEM with UV and pump lasers. The pump and UV lasers are generated by the second (SHG) and fourth harmonic generation (FHG) processes, respectively. UV laser generates photoelectron pulses with a pulse duration in the order of 220 fs, and the pump laser excites the sample with the same pulse duration [59]**.**

Once temporal synchronization is achieved between the arrival of photoelectrons emitted from the electron gun and the excitation induced by the pump laser at the sample, UTEM measurements can be performed. In UTEM, each electron pulse contains a relatively small number of electrons. This low electron population minimizes Coulomb repulsion (also known as space-charge effects) among the electrons, which in turn leads to improved temporal and energy resolution in the measurement [22,60]. In contrast, Dynamic Transmission Electron Microscopy (DTEM) utilizes electron pulses containing a significantly larger number of electrons—typically on the order of millions—within a single pulse. This high-charge configuration is particularly well-suited for investigating irreversible phenomena, where a single excitation event induces permanent structural or phase changes in the sample [61,62]. In stroboscopic observation, ultrafast phenomena initiated by periodic excitations—such as pump laser interactions—are recorded as a series of discrete snapshots using synchronized electron pulses at well-defined

temporal intervals. This technique enables the reconstruction of time-resolved dynamics by effectively “freezing” successive stages of a transient event.

By applying stroboscopic techniques to the investigation of nanomaterials, researchers can capture a sequence of time-resolved snapshots that reveal intermediate states and transient structural transformations occurring during complex, non-equilibrium processes—prior to the attainment of thermodynamic equilibrium. This methodological approach significantly advances our understanding of the underlying mechanisms driving ultrafast phenomena at the nanoscale.

A pivotal contribution to this field came in 2003, when Ramesh Srinivasan, working in Ahmed Zewail’s research group, introduced a major development in time-resolved structural analysis through the publication titled “Ultrafast Electron Diffraction (UED): A New Development for the 4D Determination of Transient Molecular Structures.” This work laid the groundwork for capturing molecular dynamics in both space and time, enabling researchers to directly observe structural rearrangements with femtosecond temporal resolution [63]. These advancements enabled the imaging of complex molecular structures with spatial and temporal resolutions reaching 0.01 Angstrom and 1 picosecond, respectively—providing unprecedented insight into atomic-scale dynamics. Notably, it was not an electron microscope.

In 2009, researchers in Zewail’s group further expanded the frontier of ultrafast electron microscopy by reporting the development of Convergent Beam Ultrafast Electron Microscopy (CB-UEM). This technique was specifically applied to study the structural dynamics, atomic vibration amplitudes, and temperature distributions of atoms within a crystalline silicon slab. CB-UEM provided enhanced spatiotemporal resolution and sensitivity to subtle lattice changes, offering a powerful approach for probing thermally induced phenomena at the nanoscale [38].

In 2012, Zewail’s group introduced a single-nanoparticle probing technique that achieved simultaneous high spatial, temporal, and spectral resolution. This method marked a significant advancement in nanoscale imaging and spectroscopy, enabling precise characterization of dynamic phenomena within individual nanoparticles across multiple dimensions of measurement [41]. They successfully captured spectral images of nanoscale dielectric fields in systems such as silver nanoparticles and the metallic copper–vacuum interface, achieving a resolution governed by photon interactions despite the use of electron-based imaging. This breakthrough illustrated the possibility of probing electromagnetic near-fields beyond conventional spatial limits.

In a related study published in 2012, they investigated the near-field dynamics of ensembles of silver nanoparticles. Utilizing ultrafast electron microscopy, they visualized the space–time evolution of photon-induced electric fields, offering unprecedented insight into light–matter interactions at the nanoscale [41] . In another significant study, they published "Entangled Nanoparticles: Discovery by Visualization in 4D Electron Microscopy", demonstrating the capability of ultrafast transmission electron microscopy (UTEM) to directly visualize the coupled near-field interactions [43]. This pioneering work highlighted the potential of 4D electron microscopy in exploring nanoscale optical phenomena with high spatiotemporal precision. Subsequent efforts to enhance the resolution and accuracy of UTEM and related ultrafast electron microscopy (UEM) techniques have yielded remarkable milestones [64]. For instance, in 2017, researchers reported record-setting pulse characteristics, including a focused beam diameter of 9 Angstroms, a pulse duration of 200 femtoseconds, and an energy spread of 0.6 eV [22]. Further advancements have explored the integration of attosecond spectroscopy and quantum optics into electron microscopy frameworks [65,66], offering novel avenues for probing electronic dynamics at previously inaccessible time scales. Additionally, innovative methods such as all-optical control, compression, and characterization of electron pulses using single-cycle terahertz laser fields have been introduced to significantly improve temporal resolution and beam manipulation within a TEM environment [67,68]. These developments continue to expand the frontiers of UTEM, enabling applications across nanoscience, quantum materials, and ultrafast photonics.

2.1.3.3 Photon-Induced Near-field Electron Microscopy (PINEM)

In conventional TEM, image formation and diffraction patterns result from elastic interactions between incident electrons and the sample’s atomic structure. These interactions preserve the kinetic energy of the electrons and provide high-resolution structural information in both real and reciprocal space. In contrast, electron energy-loss spectroscopy (EELS) relies on inelastic scattering events, where probe electrons transfer energy to the specimen—such as by exciting vibrational, electronic, or plasmonic modes—resulting in a measurable energy loss that yields valuable insights into the material’s electronic structure, bonding environment, and composition.

Ultrafast transmission electron microscopy (UTEM) integrates these concepts within a pump–probe framework, wherein the probe consists of ultrashort photoelectron pulses generated via photoemission at the electron gun, and the pump is a synchronized femtosecond laser pulse that interacts with the sample. The pump laser induces electronic excitation—typically promoting valence or core electrons to higher energy states—and initiates transient non-equilibrium

dynamics within the material. The subsequent probe electron pulses interact with this excited state, enabling time-resolved investigation of ultrafast processes with atomic-scale spatial and temporal resolution.[32].

Among the advanced imaging techniques enabled by this sophisticated experimental setup is Photon-Induced Near-Field Electron Microscopy (PINEM), again observed in Zewail's group, which facilitates the visualization of electromagnetic near fields surrounding nanomaterials. In this method, the pump laser interacts with the nanostructure, generating evanescent optical near fields localized around the material's surface. As probe electrons traverse this region, they couple with the oscillating electromagnetic fields and undergo inelastic scattering events, whereby they gain or lose quantized amounts of energy corresponding to the energy of the interacting photons. This photon–electron energy exchange is manifested as sidebands in the electron energy spectrum and provides a direct mechanism for mapping localized optical fields at ultrafast timescales and nanometer spatial resolution.

Figure removed due to copyrights issues

Figure 2-2 EELS spectrum at time zero (t = 0) showing distinct PINEM sidebands symmetrically around the zero-loss peak (ZLP), indicating pump–probe synchronization on the specimen. The energy of a photon is given by $\hbar\omega$, where $\hbar$ is the reduced Planck constant and ω is the angular frequency of the photon [69]**.**

These quantized energy gains or losses (free electrons exchange energy quanta ħω with the plasmonic field) appear in a specific spectroscopy spectrum called EELS, which is shown in Figure 2.2. UTEM enjoys an energy filter part that works as a prism for electrons and can separate electrons from each other based on the energy, and a slit can allow to desired energy band to pass and create the image. Using these facilities, it is feasible to filter out all electrons except those with the gain energy of near-field quanta interaction, which results in a PINEM image. Since PINEM enables the study of evanescent near fields with spatial resolution at the angstrom scale

and temporal resolution in femtoseconds. It also provides energy-resolved information at the level of photon quanta, offering a powerful tool for fundamental investigations in photonics, plasmonics, and nanostructured materials [33], [69], [70]. PINEM can increase our understanding of surface plasmon polaritons (SPPs) and localized surface plasmons by visualizing the details of their spatial distribution and temporal evolutions [42,71-73]. This advanced microscopy can reveal the optical properties of the dielectric nanomaterials and help to design new nano-optical components. PINEM enables real-time tracking of charge carrier motion and excitations in complex materials. In addition, PINEM provides unique information on the light-matter interaction, which can aid quantum optics investigations such as quantum coherence, photon-electron entanglement, and ultrafast nonlinear optics [74-77].

In the UTEM setup, a pulsed laser system is employed to generate two beams: a UV beam used to generate photoelectrons via photoemission, and a pump beam that excites the sample. This raises the question of how the system would behave if either the probe electron beam or the pump laser were continuous rather than pulsed. To understand the implications, a quantitative analysis is necessary. Consider a representative laser configuration operating at a repetition rate of 400 kHz, with a pulse duration of 220 femtoseconds and an average power of 10 mW. Dividing one second by the repetition rate yields a 2.5 microsecond interval between consecutive pulses, while the actual duration of each pulse remains on the order of 220 femtoseconds. This highlights the stark temporal separation between excitation and probing events, allowing ultrafast dynamics to be temporally resolved.

If either the electron beam or the pump were continuous, the overlap of excitation and probing would become uncontrolled and temporally indistinct, thereby blurring the ultrafast time resolution crucial for pump–probe measurements. Figure 2.3 schematically illustrates two consecutive pulses within the relevant temporal framework, emphasizing the necessity of pulse synchronization in UTEM experiments.

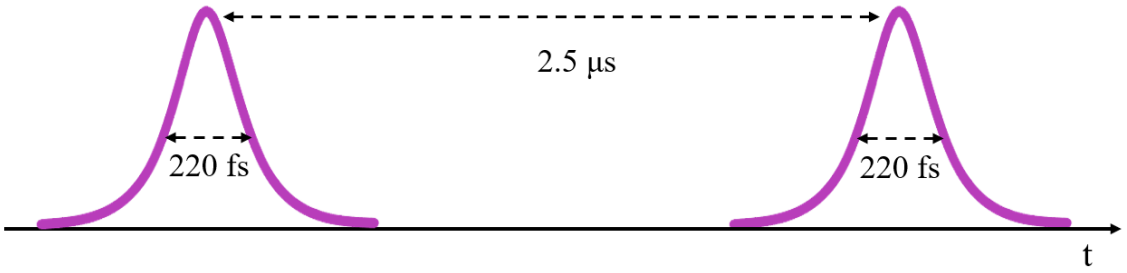

Figure 2.3 A schematic of two photon pulses with 220-fs pulse durations. A repetition rate of 400 kHz results in a 2.5 μs time interval between the two pulses.

In a system operating at a repetition rate of 400 kHz with a pulse duration of 220 femtoseconds, a total of 400,000 pulses are delivered per second. This results in a cumulative interaction time of only 400,000 × 220 fs = 0.88 ns within each one-second interval. Consequently, only 0.88 ns out of every second corresponds to moments when the sample is both excited by the pump laser and probed by the photoelectron pulse. Electrons interacting with the sample during this narrow temporal window carry the meaningful signal, while those outside this window contribute primarily to background noise. Given that the vast majority of electrons fall outside the synchronized interaction window (i.e., during the remaining 1 second – 0.88 ns), the signal-to-noise ratio (SNR) becomes extremely low—approaching zero in practice—making it exceedingly difficult to detect meaningful data without precise synchronization techniques or gating strategies.

This analysis underscores the necessity of employing a pulsed probe electron beam in ultrafast transmission electron microscopy (UTEM). However, an important complementary question arises: why must the pump laser also operate in pulsed mode?

To address this, we begin by examining the parameters associated with the typical pulsed laser used in UTEM experiments and then compare these to the requirements of a hypothetical continuous-wave (CW) laser delivering an equivalent effect. In standard UTEM configurations, the pump laser irradiating the sample typically operates with an average power between 10 and 100 mW, with 10 mW considered the minimum effective threshold for inducing observable ultrafast dynamics.. Using the following equation, we can calculate the power of the laser.

$$P = \frac{U}{t} \tag{2.3}$$

where u is energy and t is time. The equation for t=1s gives U= 10 mJ, and dividing the energy by the repetition rate 400 kHz gives the pulse energy of the laser, which is 25 nJ. To deliver 25 nJ in each 220-fs pulse continuously over 1 second, one would need to match this energy across

approximately 1s/220 fs: 5×10^{12} pulses. This results in a total energy demand of: 25 nJ × 5×10^{12}= 125 kJ, which equates to 125 kW of continuous power. Such an enormous power requirement is impractical. Therefore, both the electron probe beam and the pump laser must operate in a pulsed regime to enable ultrafast measurements efficiently and effectively.

Moreover, capturing ultrafast dynamics necessitates the use of short pump and probe pulses. A brief excitation pulse is essential not only for initiating coherent evolution within the ensemble, but also for shaping the nature of the system's response—both temporally and spectrally.

2.1.3.4 Plasmonic nanoparticles and their optical properties

Plasmons are collective oscillations of free electrons in a material, typically metals. Plasmonic nanoparticles are metallic nanoparticles whose conduction electrons can oscillate in response to incident laser light, leading to plasmon resonances. These resonances are created near the surface of the nanostructure and are called localized surface plasmon resonances (LSPR). Due to these LSPRs, plasmonic nanomaterials exhibit unique optical properties—such as enhanced light absorption, scattering, and local field intensification—and find widespread applications across various fields [78-84].

There are three types of plasmons: the first one, bulk plasmons, which are the result of electrons' oscillations inside the material. The second one, surface plasmons, which are created when the interaction happens at the interface of a metal and a dielectric, and they are bound to the surface of the material. The third one is Localized Surface Plasmons (LSPs), which occur in nanomaterials. LSPRs enhance the strength of the electromagnetic near field of nanoparticles and have applications in surface-enhanced Raman spectroscopy (SERS) surface-enhanced infrared absorption (SEIRA), biosensing, photothermal therapy, nonlinear optics, and PINEM technique [85-89]. The plasmon mode structure (dipole, quadrupole, etc.) and particle geometry determine how the near-field interacts with probe electrons. Plasmons can have different spatial distributions that depend on the excitation wavelength, size, and shape of the particle. The fundamental mode is a dipole mode, so that free electrons in the nanoparticle oscillate collectively in one direction. In a quadrupole mode, electron oscillations create two dipoles, in a hexapole mode, three dipoles, and so on for higher-order modes. By increasing the size of the nanoparticle in comparison to the wavelength of the exciting laser, the role of higher-order poles increases (Mie theory). Moreover, if the shape of NP becomes less symmetric, the dipolar modes can have

different frequencies along three axes, and also higher multipolar charge distributions can exist in the interaction [82,84,86].

For spherical nanoparticles, dipole mode and, in some cases, quadrupoles are dominant. If a particle has sharp edges, the plasmonic effect at the edges is more effective. Some examples of plasmonic nanoparticles that are of interest in different applications from industry to medicine, are Gold (Au) in the visible range 520-580 nm with biocompatibility in medical applications, Silver (Ag) in the range of 400-450 nm with strong plasmonic resonances [84]. Other ones are like copper (Cu), Platinum (Pt), Aluminum (Al), and core-shell nanoparticles [86], with applications such as sensing and catalysis, electrocatalysis, semiconductor-based plasmonic materials, optical sensors, photonic, and SERS [80,85,86].

2.1.3-5 Near field of metallic nanoparticles and their dipoles in PINEM images

This section presents a review of selected studies involving PINEM as applied to the imaging and characterization of nanoparticles. To gain insight into the dipolar response of spherical nanoparticles, I begin by employing the approximated analytical equation [43] to calculate and simulate the dipole fields of a spherical gold nanoparticle, which is valid under the dipole approximation ($a \ll \lambda$), which assumes the particle is much smaller than the wavelength of light.

$$E_z(x,y,z,t) \approx E_0 a^3 \chi(\omega) \frac{3xz}{r^5} e^{-i\omega t} \tag{2.4}$$

where polarization is in the x plane, $r = \sqrt{x^2 + y^2 + z^2}$, E_0 is the amplitude of the incident field, and a is the radius of the spherical NP. $\chi(\omega)$ is the susceptibility of the material, which is

$\chi(\omega) = [\varepsilon(\omega) - 1]/[\varepsilon(\omega) + 2]$ and ε is a complex dielectric function of the material. Using this equation and MATLAB, the PINEM signals for gold nanoparticles are simulated and plotted as dipolar patterns, as shown in Figure 2.4.

To calculate the PINEM interaction field, we integrate the longitudinal electric field component E_z along the electron's trajectory near the nanoparticle (NP), accounting for the electron's transit time $t = z/v$, where v is the electron velocity. The resulting field amplitude is given by:

$$F(x,y) \approx \int_{-\infty}^{+\infty} E_z(x,y,z)\, e^{-i\left(\frac{\omega}{v}\right)z} dz \tag{2.5}$$

The dimensionless electron–field coupling parameter, β is then defined as:

$$\beta = (e/\hbar\omega)F \tag{2.6}$$

When an electron interacts with the optical near field, it can absorb or emit integer multiples of photon energy $\hbar\omega$. The probability P_n of electrons occupying the n-th energy sideband (gain or loss) in the EELS spectrum is given by [32]:

$$P_n = J_n^2(2|\beta|) \tag{2.7}$$

where J_n is the Bessel function of the first kind of order n, and β quantifies the strength of the electron–field interaction. The total sideband intensity increases with $|\beta|$, which is proportional to the integrated field amplitude along the electron's path. In the weak-field regime ($|\beta| \ll 1$), the first-order sideband intensities scale quadratically:

$$P_{\pm 1} \approx |\beta|^2 \tag{2.8}$$

For stronger fields, higher-order sidebands emerge, and the full Bessel-function distribution must be fitted to accurately extract $|\beta|$.

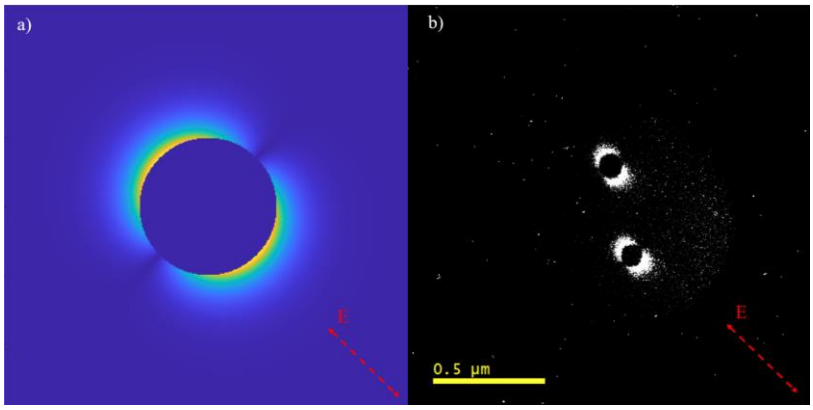

Figure 2-3 a) Theoretical calculations, b) experimental PINEM of near fields for Au nanoparticles. The exciting photon propagation is along z (perpendicular to the page). E indicates that the laser's electric field is linearly polarized at 45°. The particle size is 100 nm.

In 2012, Zewail's group conducted pioneering experiments at the California Institute of Technology utilizing a state-of-the-art Ultrafast Electron Microscopy (UEM) system to visualize PINEM signatures from silver nanoparticles [69]. A femtosecond laser operating at a central wavelength of 520 nm, with a pulse duration of 220 fs and an average power of 20 mW at a repetition rate of 200 kHz, was employed as the optical pump source. This configuration delivered photon energy of approximately 2.4 eV, enabling efficient plasmon excitation. Concurrently, the electron probe pulses were accelerated to 200 keV, and the resulting PINEM images were

acquired via energy-filtered detection of scattered electrons using a post-column energy spectrometer. Figure 2.5 presents the structural morphology of the silver nanoparticles along with their associated PINEM spectral features [41].

Figure 2-4 PINEM images of an Ag NPs ensemble for two linear polarizations, a) Ep1 and b) Ep2. c) The sum image of Ep1 and Ep2. d) depicts the bright field transmission electron microscope image of the same area. Arrows at the upper right corner denote the linear polarization direction of the excitation laser pulse. The scale bar is 500 nm, and the images are shown in colors for enhancement of contrast. The white circle is to guide the eye for the polarization effect of a single particle [41]**.**

Figure 2.5 illustrates the dipolar field distributions of a representative ensemble of silver (Ag) nanoparticles under two orthogonal linear polarization states of the excitation laser. Due to the linear nature of the pump polarization, the resulting plasmon-induced near-fields exhibit crescent-shaped patterns, spatially aligned along the direction of the incident electric field. This anisotropic field distribution reflects the symmetry of the excitation geometry. When the two polarization-resolved images (Figures 2.5a and 2.5b) are superimposed, the composite near-field pattern manifests as a circularly symmetric distribution, closely resembling the expected response under circularly polarized excitation.

In a separate study, the authors explored the interparticle dipole-dipole interactions that arise when silver nanoparticles are positioned in close spatial proximity. These near-field interactions

significantly influence the collective optical response of the ensemble, leading to modified plasmonic coupling effects and anisotropic field distributions [43]. To investigate these interparticle interactions, the authors examined silver nanoparticles with a nominal diameter of 70 nm and characterized the formation of entangled plasmonic channels between neighboring particles at varying center-to-center separations of 32, 47, and 250 nm, as depicted in Figure 2.6. These observations provide insight into the distance-dependent coupling dynamics and the evolution of near-field plasmon modes within nanoparticle assemblies.

Figure removed due to copyrights issues

Figure 2-5 Entangled particles by dipolar fields and nanometer-scale void-channels. Shown are the near-fields of a nanoparticle pair with an edge-to-edge distance of 32 nm (A), 47 nm (B), and 250 nm (C) with false-color mapping [43]**.**

Figure 2.6A illustrates the distance-dependent evolution of near-field coupling between two silver nanoparticles. At a center-to-center separation of 32 nm, a pronounced interaction is observed, indicating strong plasmonic coupling between their evanescent fields. As the interparticle distance increases to 47 nm, the interaction becomes noticeably weaker, reflecting a reduction in dipole-dipole coupling strength. At a separation of 250 nm, the near-field interaction is no longer discernible, suggesting the absence of significant plasmonic coupling at this scale.

In 2010, Sang Tae and Zewail conducted both theoretical and experimental investigations into PINEM, providing an analytical framework that elucidated the key parameters governing the generation and interpretation of PINEM signals [32]. Figure 2.7 presents both simulated and experimental PINEM signals from a single protein vesicle with a radius of 150 nm, as reported by the authors. Their analysis began with energy–momentum conservation principles governing photoelectron–plasmon interactions and extended to analytical formulations for cylindrical and spherical geometries. They compared the calculated PINEM field amplitudes with experimental

data, highlighting the influence of nanoparticle size, material composition, polarization, fluence, and temporal dynamics on the evanescent field. The study concluded that when nanoparticle dimensions are comparable to or smaller than the pump laser wavelength, Rayleigh or Mie scattering theories can effectively describe near-field behavior, while electron–field interactions require treatment via the time-dependent Schrödinger equation [32,34].

Figure removed due to copyrights issues

Figure 2-6 Theoretical, and b) experimental PINEM polarization dependences in a semi-spherical NP. The sample is a single protein vesicle with a 150 nm radius [32]**.**

The trajectory of PINEM research continued in 2020, when Wang et al. demonstrated coherent interaction between free electrons and a photonic cavity, pushing the boundaries of electron–photon coupling. Their work highlighted the critical role of engineered near-field environments in shaping electron wavefunctions, marking a shift from passive imaging to active quantum control. These studies underscore the evolution of PINEM from a diagnostic tool into a versatile platform for quantum manipulation and ultrafast field mapping [90].

More recently, advances in phased-locked ultrafast transmission electron microscopy (UTEM) have expanded the scope of PINEM applications. UTEM now enables spectral mapping of near-field distributions around plasmonic structures such as silver nanowires, nanoparticles, nanotips, and gold nanostars. By leveraging its high temporal resolution and synchronized electron–photon interactions, UTEM achieves superior spatial and energy-resolved insights compared to conventional electron energy-loss spectroscopy (EELS) [91].

Building on this trajectory, the emerging technique known as Lorentz-PINEM allows for full-field, phase-resolved imaging of complex near-field distributions with nanometric precision. By combining energy-filtered sideband imaging with Fresnel-mode phase contrast, researchers have

successfully reconstructed spatially varying field phases on plasmonic nanotips—revealing both the amplitude and phase of the coherent optical near field [92].

2.2 Materials and Methods

2.2.1 Nanoparticle synthesis

To conduct the nanomaterial experiments, synthesized nanoparticle samples were required. Synthesis methods are broadly categorized into top-down and bottom-up approaches. The top-down approach involves reducing bulk materials to the nanoscale using techniques such as etching, sputtering, ball milling, laser ablation, and lithography. In contrast, the bottom-up approach forms nanoparticles from atoms or molecules via chemical or physical processes.

In this study, samples were synthesized via bottom-up methods by commercial providers such as Nanocomposix. One such sample consisted of NanoXact Gold Nanospheres – Bare (Citrate), 100 nm in diameter, with a concentration of 0.05 mg/mL in 2 mM sodium citrate aqueous solution. A 5 mL aliquot was transferred to a cylindrical glass vial, diluted with 10 mL of distilled water, and sonicated for 30 seconds to disperse the nanoparticles. Subsequently, 10 µL of the diluted solution was drop-cast onto a substrate and allowed to dry under ambient conditions.

Figure 2.8a–c shows the Au nanoparticle suspension, the substrate drying process, and related tools. TEM bright-field images of the dried Au nanoparticles are displayed in Figure 2.8d–f.

Additional samples included NanoXact Silver Nanospheres – Bare (Citrate), 100 nm, 0.02 mg/mL in 2 mM sodium citrate, and NanoXact Silica Nanospheres, 100 nm, at 10 mg/mL in water (Appendix A4).

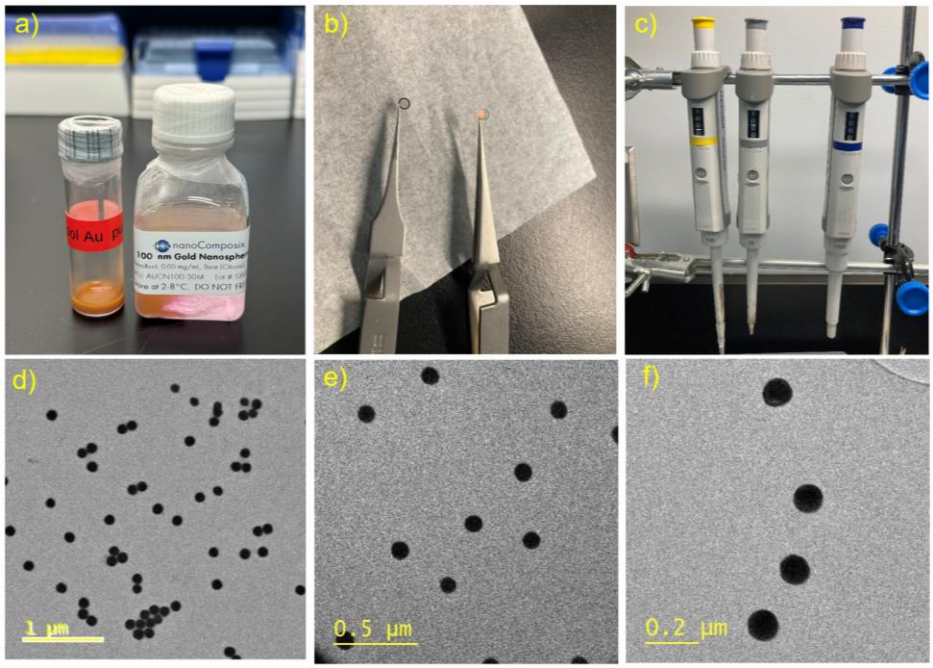

Figure 2-7 a) Gold nanoparticles dispersed in aqueous solution.b) TEM grids and tweezers used for sample preparation. c) Micropipettes with different volume ranges: 0.5–10 µL, 10–100 µL, and 100–1000 µL. d–f) TEM images of selected gold nanoparticles.

2.2.2 Different substrates and their properties (grids of TEM)

To prepare nanoparticle samples for imaging, drop-casting was performed onto transmission electron microscopy (TEM) grids, which serve as substrates supporting the nanoparticles. These grids are available in various material compositions, including copper, gold, nickel, silicon, carbon, and graphene, combined with support films such as amorphous carbon, graphene, Lacey carbon, and SiO. In this work, copper TEM grids coated with chemical vapor deposition (CVD) graphene films were used, supplied by Graphene Laboratories Inc. These grids consist of ultrafine 2000-mesh copper with a monolayer graphene coating. Figure 2.9 displays two types of TEM grids utilized in the experiments. Graphene's high frequency-dependent electrical conductivity (on the order of several hundred S/m), exceptional thermal conductivity (around 2000–5000 W/m·K), negligible electric susceptibility (~0), and hexagonal lattice symmetry make it an ideal support material for high-resolution electron microscopy.[93], [94], [95]. Silicon monoxide (SiO), a suboxide of silicon, demonstrates very low electrical conductivity (~1 S/m), moderate thermal conductivity (1–5 W/m·K), and low electric susceptibility (~0) reflecting its insulating and weakly

polarizable nature [96], [97]. For SiO, the nonlinear optical susceptibility is generally low, though it can exhibit weak second-order or third-order nonlinear effects [98], [99].

Figure removed due to copyrights issues

Figure 2-8 a) Graphene grid. CVD Graphene film deposited on Copper TEM grids (2000 Mesh). The thickness of Graphene film: 0.3-2 nm (1-6 monolayers). Typical graphene coverage: 60-90% b) SiO grid. A thin film of pure silicon monoxide (15 – 30 nm) is deposited directly on the Copper grid with 400 mesh. C) A typical TEM holder. The grid is put in the tip of the holder and is fixed by a ring and a screw [100], [101].

Based on the experimental requirements, TEM operators select a grid with the appropriate mesh size. After the drop-casting step, the grid is mounted onto the TEM holder, as illustrated in the Figure 2.9c.

2.2.3 EELS system in TEM

In light–matter interaction studies, spectroscopy is a powerful technique for characterizing materials and determining their chemical, optical, and electronic properties. When applied in a transmission electron microscope (TEM), spectroscopy adds an additional capability to electron microscopy, offering deeper insights into the investigation of nanomaterials. Electron energy loss spectroscopy (EELS) is a TEM technique that measures the energy difference of electrons before and after interacting with the sample, thereby providing atomic and chemical information about

the material. EELS is a powerful method that can reveal the type and quantity of atoms in the sample, determine their chemical state, and provide insights into the optical and vibrational (acoustic) properties of the nanomaterial.

EELS utilizes the energy distribution of electrons transmitted through a sufficiently thin sample, typically less than 100 nm thick, when using a 200 keV probe electron beam. As electrons pass through the sample, they can interact either elastically (without energy exchange) or inelastically (with energy exchange). EELS specifically analyzes inelastic interactions to extract valuable information about the sample's composition and electronic structure. The resulting EELS spectrum displays the distribution of electrons according to their energy loss. The central peak in the spectrum, known as the zero-loss peak (ZLP), corresponds to electrons that have not exchanged energy with the sample. Notably, the full width at half maximum (FWHM) of the ZLP indicates the energy resolution of the technique (Appendix A5). This resolution is critical in applications such as PINEM imaging, which relies on near-field–modulated electrons. In ultrafast TEM (UTEM), the ZLP FWHM can typically range from approximately 1.1 eV to 1.8 eV, depending on experimental conditions. Other peaks in the spectrum correspond to the ionization edges of the sample, and detailed analysis of these features can reveal valuable information about the material. EELS extracts a wealth of information about the material, such as specimen thickness, valence or conduction electron density, the complex dielectric function in the low-loss region, band structure, interband transitions (using near-zero-loss features), and elemental composition (using core-loss edges).

Figure 2.10 shows a typical EELS spectrum with the ZLP peak located at the left of the diagram. There is a standardized EELS atlas and data library available for peak identification, allowing comparison between observed spectral features and known reference data to determine the elemental composition of a sample. Additionally, EELS can be used to generate elemental maps—images showing the spatial distribution of elements—through energy-filtered transmission electron microscopy (EFTEM), which integrates the intensity around specific ionization edges. For the purpose of capturing a PINEM image, the EELS spectrum is used to verify the synchronization between the probe and pump beams, as well as to filter electrons based on their energy loss, selecting those that have interacted with the near fields of the nanoparticles.

Figure removed due to copyrights issues

Figure 2-9 A typical EELS spectrum achieved by TEM. The high peak on the left side represents the ZLP, and the lower peak on the right side shows the bulk plasmon peak. By adjusting the desired interval of energy and zooming in, one can see the details of the edges to identify the present elements in the sample [102]**.**

2.2.4 Optical setup of UTEM

To upgrade the transmission electron microscope (TEM) into an ultrafast TEM (UTEM), a Ytterbium-based laser system was integrated, operating at a repetition rate of 400 kHz with 220 fs pulse duration and 17 W output power at a central wavelength of 1028 nm. An external harmonic generation unit (HIRO box), supplied by Light Conversion alongside the Pharos laser system, was used to produce ultraviolet (UV) and the pump beam. The HIRO unit utilizes fixed optical elements to split the fundamental beam and generate its harmonics, specifically producing fourth harmonic generation (FHG) at 257 nm and second harmonic generation (SHG) at 514 nm.

Figure 2.11 illustrates the main optical setup of the UTEM. Following the HIRO unit, two motorized polarizers and half-wave plates are used to control the power of the UV and pump lasers. Off-axis parabolic mirrors (OAPMs) are employed to focus or collimate the laser beams with minimal optical aberrations.

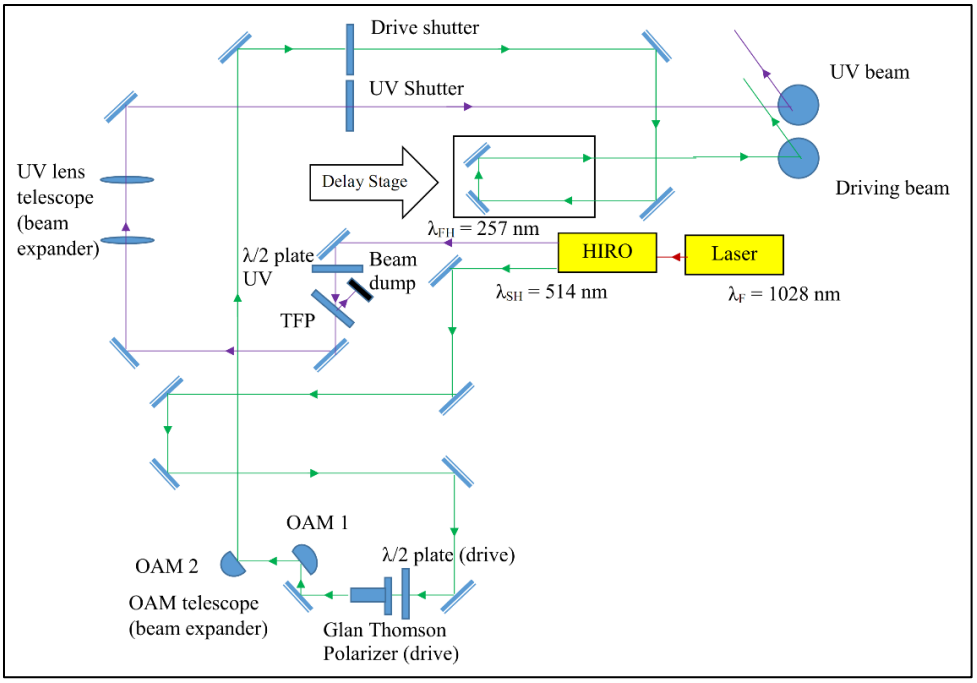

Figure 2-10 Schematic of the main optical setup of the UTEM. The system begins with a 1028 nm laser beam, which is converted by the HIRO unit into two beams: a UV laser at 257 nm and a pump laser at 514 nm. These beams are subsequently directed to the vertical setup located before the TEM column, as illustrated in Figure 2.12.

Figure 2.12 depicts the vertical configuration of the ultrafast transmission electron microscope (UTEM) setup positioned directly beside the TEM column, designed to guide and manipulate the laser beams. A beam splitter (BS) is employed to divide the incoming laser beam into two paths, with one path directed toward CCD cameras for real-time monitoring and alignment of the beam position. The ultraviolet (UV) beam is guided into the column and reflected upward toward the electron source, where it triggers electron emission via the photoelectric effect. Simultaneously, the pump laser is redirected by an internal mirror to illuminate and interact with the specimen.

It is worth noting that in the experimental setup, beam expanders are employed to ensure that the pump laser irradiates the sample with an adequately sized and uniform beam profile. To minimize optical aberrations and maintain beam quality, mirrors are used in the pump laser path. For the ultraviolet (UV) beam, lenses are incorporated to achieve precise focusing and spatial control.

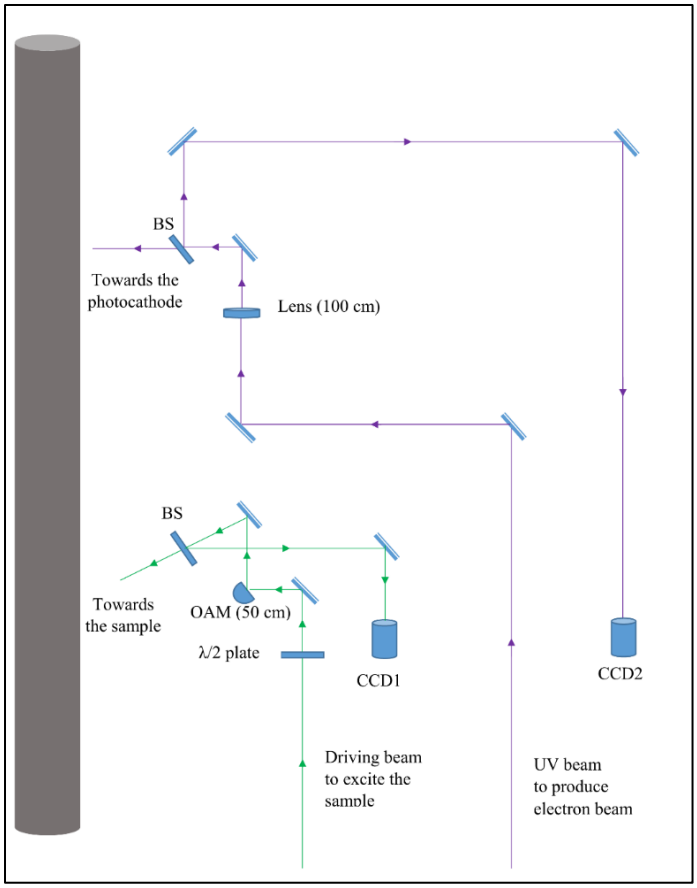

Figure 2-11 Schematic of the vertical setup of the UTEM. The UV and pump laser beams are directed toward the TEM column, with the UV beam entering from the top and the pump laser beam entering from the bottom near the specimen region.

2.2.5 Synchronization between photoelectron and pump laser pulses (time zero)

A critical aspect of ultrafast experiments in UTEM is the precise temporal synchronization between the pump laser and the photoelectron probe beams. To achieve this, a mechanical delay stage equipped with a piezoelectric actuator is employed to vary the optical path length of the pump beam with sub-picosecond precision. This stage is controlled via dedicated software provided by the laser system manufacturer, enabling temporal adjustments with a resolution of approximately 50 fs.

Determination of the temporal overlap—referred to as the "time zero"—is conducted with the TEM operating in electron energy loss spectroscopy (EELS) mode. Spectra are acquired for each incremental adjustment of the delay stage. Given that energy exchange between the nanoparticle

near-field and the probe electrons occurs on a femtosecond timescale, a misalignment in timing results in a conventional EELS spectrum devoid of excitation features, as illustrated in Figure 2.13a. When the optical path is correctly aligned, the pump beam excites the sample concurrently with electron probing, leading to the emergence of characteristic energy gain and loss features in the EELS spectrum, as shown in Figure 2.13b.

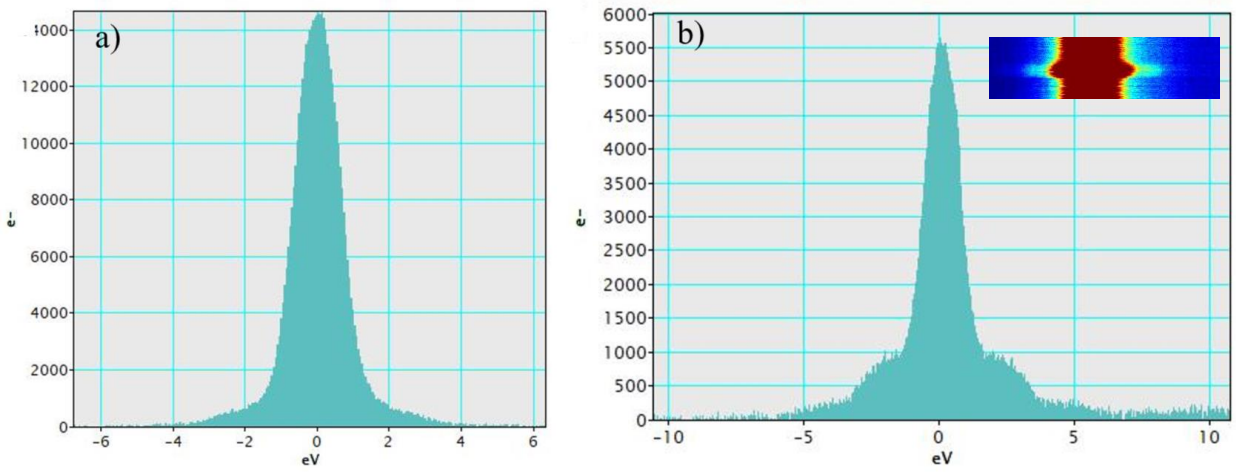

Figure 2-12 (a) EELS spectrum of Au nanoparticles at a delay time far from time zero. (b) EELS spectrum at time zero. The inset shows a top-view map of EELS spectra as a function of time delay (vertical axis) and energy loss (horizontal axis, in eV), matching the main spectra.

By defining the temporal overlap point as time zero, the delay stage can be adjusted to negative values (probing the sample before pump excitation) or positive values (probing after excitation). Sequential acquisition of frames across this temporal window enables the reconstruction of a time-resolved image sequence, effectively capturing the dynamical evolution of the interaction in a movie-like format.

2.2.6 Filtering system in UTEM for electrons with different energies

To image the near-field interactions surrounding nanoparticles, probe electrons must be energy-filtered to isolate those that have undergone inelastic scattering involving energy exchange in integer multiples of the pump laser photon energy ($\hbar\omega$). This energy selection is achieved using an electron energy loss spectroscopy (EELS) system, which can be integrated into the transmission electron microscope (TEM) either before or after the final image magnification stage—referred to as in-column and post-column configurations, respectively. These two configurations are schematically illustrated in Figure 2.14, with the post-column arrangement shown on the left and the in-column setup on the right [40].

Figure removed due to copyrights issues

Figure 2-13 Schematic of TEM and energy selecting system for EELS. There are two approaches to embedding the energy selecting slit in a TEM, called in-column (right figure) or post-column (left figure) configurations [103]**.**

Each method presents distinct advantages and limitations; however, both rely on the fundamental principle of using a magnetic field to disperse electrons according to their energy, akin to the dispersion of white light into its constituent wavelengths by a glass prism. The resulting energy-dispersed electron spectrum can be projected onto a detector to generate an electron energy loss spectrum. Alternatively, an energy-selecting slit can be applied to isolate a specific energy range from the spectrum, allowing the reconstruction of spatially resolved, energy-filtered transmission electron microscopy (EFTEM) images. These two techniques form the cornerstone of electron energy loss spectroscopy (EELS) analysis.

For PINEM imaging, the procedure begins in EELS mode by optimizing the zero-loss peak (ZLP) to achieve the narrowest possible full width at half maximum (FWHM), thereby maximizing energy resolution. Once optimized, the system is switched to image mode, and an energy slit is applied to isolate the electron gain side of the spectrum. The energy dispersion is set to 0.05 eV, with a slit width of 6 eV. By centering the slit at –6 eV, for instance, electrons within the energy range of –9 to –3 eV are selected, forming the basis of the resulting PINEM image.

2.2.7 Capturing PINEM signals using UTEM

The procedure for capturing near-field interactions and photoelectron probe signals involves several sequential steps. Initially, the sample is inserted into the transmission electron microscope (TEM), and bright-field imaging is performed to locate target nanoparticles, whose positions are saved for further analysis. The system is then switched to photoemission mode, and the photoelectron beam is focused on the selected nanoparticles while the pump laser simultaneously irradiates the sample. Next, the TEM is set to electron energy loss spectroscopy (EELS) mode to optimize the zero-loss peak (ZLP) width, ensuring high energy resolution. The setup is then returned to image mode, where an energy slit is applied to record the PINEM image, selectively capturing electrons that interacted with the near fields around the nanoparticles.

Figure 2.15 illustrates this procedure using 100 nm gold nanoparticles (Au NPs) deposited on a graphene grid. Figure 2.15a displays the bright-field TEM image; Figure 2.15b shows the corresponding PINEM image revealing induced dipoles, with the pump laser polarization oriented along the northwest direction, indicated by a red arrow. In Figure 2.15c, the laser polarization has been rotated by 90° using a half-wave plate, resulting in a reoriented dipolar field distribution.

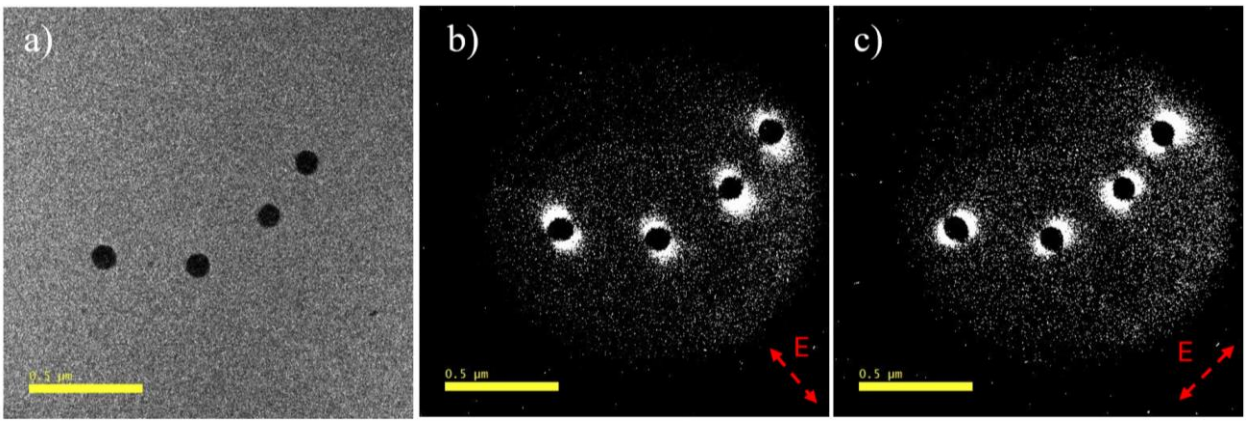

Figure 2-14 a) Gold nanoparticles with 100 nm size in the bright field image b) PINEM image of AU NPs where the pump laser polarization is shown with a red arrow, c) PINEM image as in (b), but with the laser polarization rotated by 90° using a half-wave plate.

2.2.8 Data analysis for dipoles of nanoparticles

Initial image analysis was conducted using the Gatan Microscopy Suite (GMS), also known as DigitalMicrograph, which supports a range of functionalities including tomography, in-situ imaging,

spectral analysis, and diffraction imaging through the operation of digital cameras and associated hardware. For more advanced quantitative analysis, MATLAB was employed. To extract the dipole rotation angles in the nanoparticles (NPs), a custom algorithm was developed that integrates the intensity distribution of each crescent-shaped dipolar feature in polar coordinates. A Gaussian function was then fitted to the resulting intensity profiles to determine the central orientation of each feature. These orientations were compared to a fixed horizontal reference (defined as 0°) to calculate the corresponding dipole rotation angles.

2.3 Results and Discussions

2.3.1 The PINEM and dipolar behavior of Au nanoparticles on SiO grids

2.3.1.1 The difference in the directions of dipoles

The first sample used to capture PINEM images and study the near fields consisted of gold nanoparticles. An ensemble of 100 nm Au NPs was prepared by a drop-casting method onto SiO grids. The pump laser, with a wavelength of 515 nm and a power of 85 mW, illuminated a circular area on the sample with a diameter of approximately 70 µm.

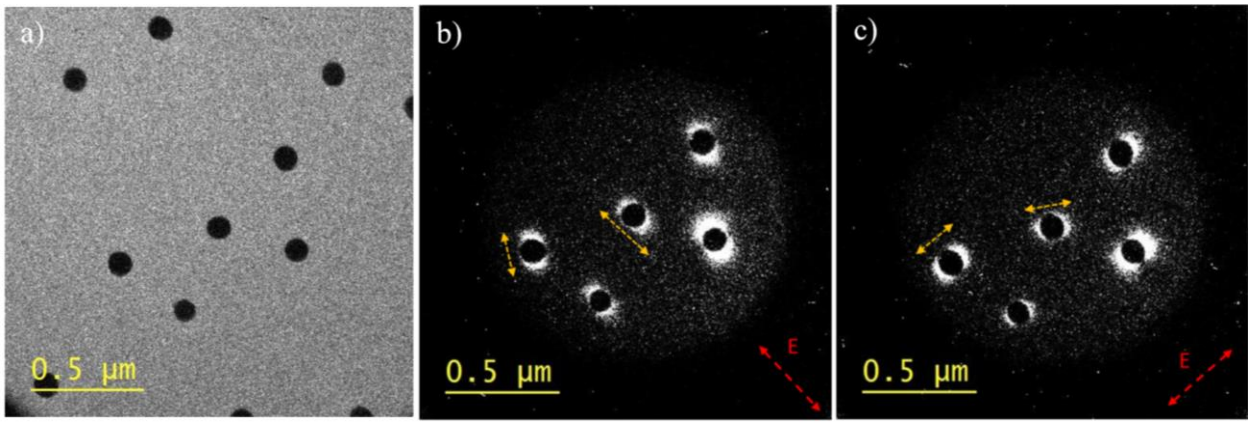

Figure 2-15 a) TEM bright field image of the gold nanoparticles with a size of 100 nm drop-casted on the SiO grid. b) PINEM images of the near fields of the Au NPs ensemble due to a linear polarization of the pump laser indicated by a red dashed line in the right lower corner. c) near fields of Au NPs for the case in which the polarization of the pump laser is rotated 90 degrees.

Figure 2.16a shows a TEM bright-field image of Au nanoparticles deposited on a SiO grid using the drop-cast method. Figure 2.16b presents the near-field distribution of the same Au NPs under illumination by the pump laser, captured using the PINEM technique. The pump laser has linear

polarization oriented at 120°, as indicated by the red dashed line in the lower right corner. Given the linear polarization (Appendix A6), we expected the dipole orientations of the nanoparticles to align accordingly. However, it is evident that the dipole directions vary among the NPs—for example, the two yellow dashed lines highlight different dipole orientations.

In Figure 2.16c, the laser polarization has been rotated by 90° using a half-wave plate in the optical setup. Again, the dipole directions of the two marked NPs differ from each other. This experimental observation is intriguing and suggests that additional factors may influence dipole orientation. To further investigate this phenomenon and obtain statistical support, we repeated the experiment multiple times using different sets of Au NPs on SiO grids.

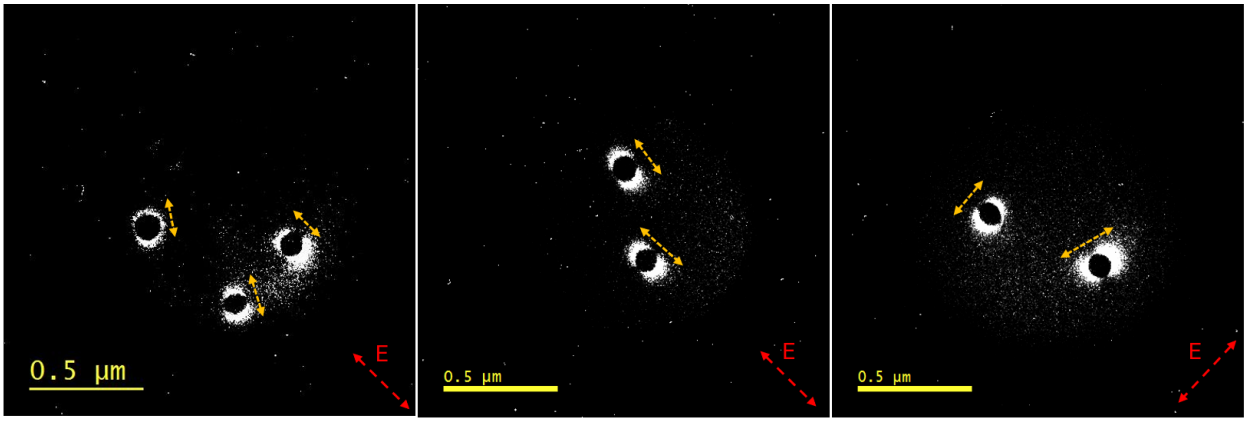

Figure 2-16 PINEM images of the near fields of the Au NPs applied by the pump laser with a linear polarization indicated by a red dashed line in the right lower corner. The dipoles are not aligned in the same direction.

Figure 2.17 presents additional PINEM images of the near fields surrounding Au nanoparticles, where the dipole directions are clearly not uniform. By analyzing more than 100 nanoparticles, we observed that approximately more than 20% exhibited misaligned dipoles when deposited on a SiO substrate. More details of this analysis are presented in section 2.3.3.

To explore this phenomenon in greater detail, we investigated how rotating the polarization of the pump laser, specifically in a counterclockwise direction, affects the dipole orientations. The study was conducted using incremental steps of 6° on the half-wave plate, corresponding to 12° rotations in polarization. Thus, a full 180° rotation of the wave plate results in a complete 360° polarization rotation.

Figure 2.18 shows the evolution of dipole orientation in Au NPs as a function of the pump laser polarization angle. The rotation angle is labeled in yellow in the upper right corner of each image,

while the red dashed lines indicate the polarization direction at key angles: 0°, 48°, 90°, 138°, and 180°.

Interestingly, when the polarization passes through certain angles, such as 18°, 66°, 114°, and 162°, referred to here as transient angles, some nanoparticles exhibit transient circular signals. These transient angles are separated by approximately 48° (close to 45°), corresponding to angular positions similar to 0°, 90°, 180°, and 270° in the trigonometric circle, which represent key boundaries for directional changes in vector orientation.

In summary, during the rotation of the laser polarization, the dipole orientation initially points in one direction, gradually shifts as it approaches a transient angle, where a circular PINEM signal appears, and eventually realigns in the opposite direction.

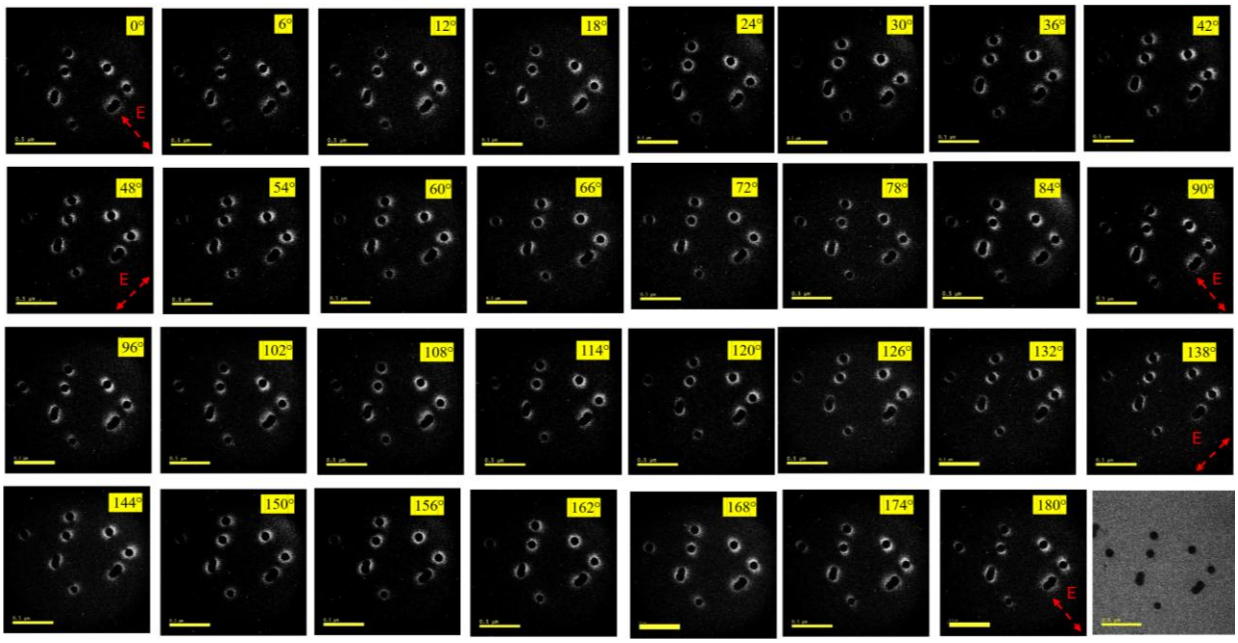

Figure 2-17 Dipoles of near fields in Au NPs as a function of the polarization rotation of the pump laser, captured by the PINEM technique. The rotation angle is shown in yellow color on the right upper corner and the red dashed line indicates polarization direction for the angles 0°, 48°, 90°, 138°, and 180°. NPs show circular signals for the transient angles, which change the direction of the laser polarizations in a vertical or horizontal situation.

Another important observation is that the transient angle varies slightly between individual nanoparticles, resulting in different dipole orientations even under the same polarization direction. Figure 2.19 shows the dipole responses of three additional Au NPs under the influence of the near fields. At 0° and 6°, the dipole orientations differ among the NPs. As the polarization is rotated to 12°, the upper nanoparticle begins to exhibit a circular signal. At 18°, it transitions toward a

dipolar shape, and by 24°, the dipole direction becomes clearly defined. In contrast, the two lower nanoparticles require further rotation, up to 30° and 36°, respectively, before displaying distinct dipolar signals.

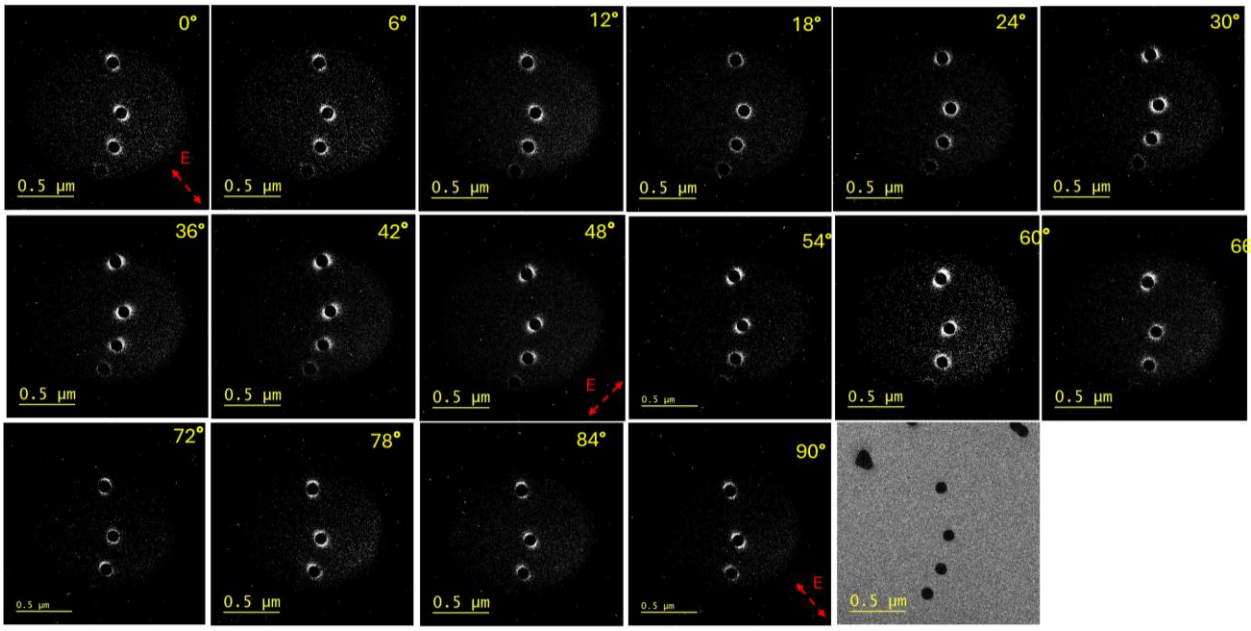

Figure 2-18 Near-field signals in three Au NPs as a function of the polarization rotation of the pump laser, captured by the PINEM technique. The rotation angle is shown in yellow color on the right upper corner, and the red dashed line indicates polarization direction for the angles 0°, 48°, and 90°.

To examine the effect of laser polarization on the dipoles, we conducted an additional experiment in which the polarization was rotated in the opposite (clockwise) direction, as shown in Figure 2.20, where circular signals appeared in the dipole patterns of the nanoparticles during this rotation. For the upper nanoparticle, the circular response began at 72° and transitioned to a dipolar shape by 66°, while for the others, it started at 66° and ended at 54°. As before, circular features were observed near the transient angles, specifically at 18° and 12° for the respective particles.

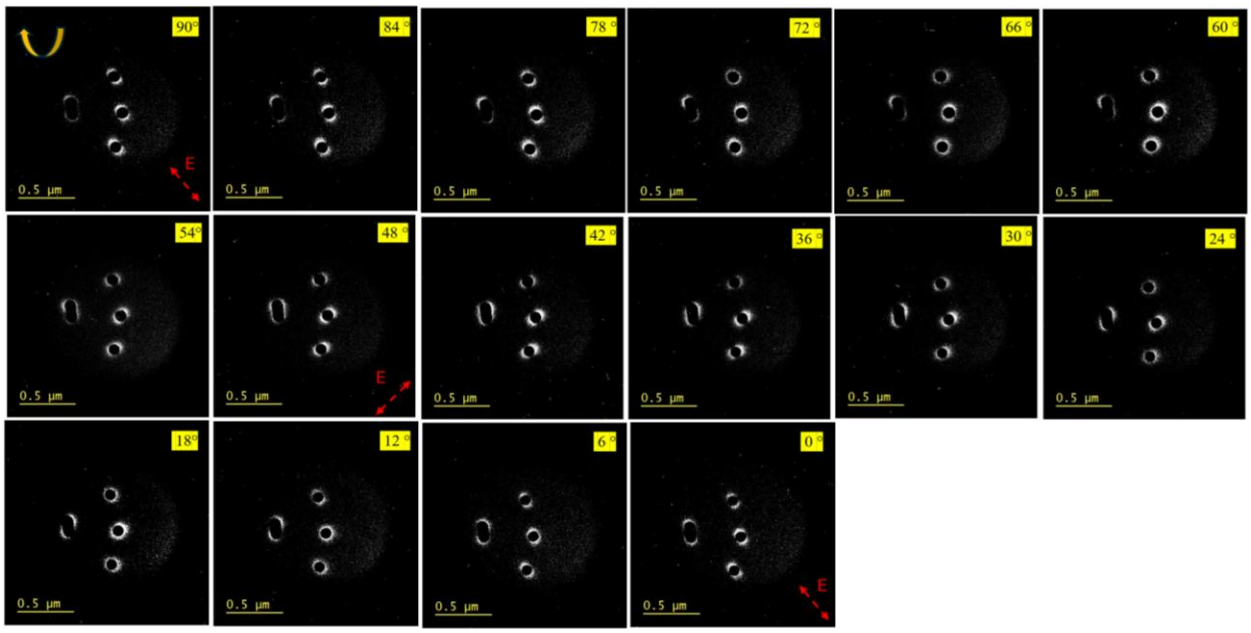

Figure 2-19 Near field signals in some Au NPs as a function of the polarization rotation of the pump laser, captured by the PINEM technique. The rotation angle is shown in yellow color on the right upper corner, and the red dashed line indicates the polarization direction for the angles. The rotation is in the clockwise direction.

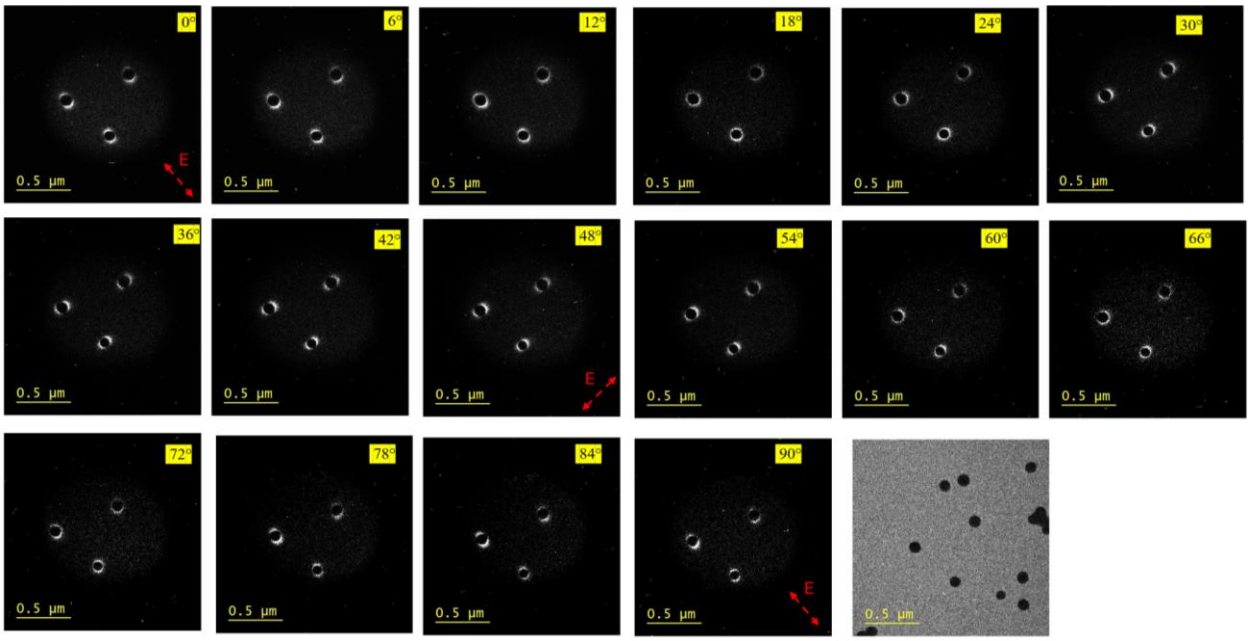

Figure 2-20 PINEM signals of three Au NPs as a function of the polarization rotation of the pump laser. The rotation angle is shown in yellow color on the right upper corner, and the red dashed line indicates the polarization direction for the angles. The rotation is in the counterclockwise direction. The last image shows the bright-field TEM image of the particles. The photoemission beam was focused on three NPs to increase the signal and to observe only three NPs.

To address potential skepticism, it is important to investigate whether the history of laser polarization exposure affects the sample's dipole response. One control test involved repeating the experiment after a two-hour interval. Figure 2.21 shows PINEM signals from three Au nanoparticles, highlighting the rotation angles and the appearance of circular signals at transient angles.

After capturing the initial set of images, the pump laser was blocked for two hours. The experiment was then repeated for polarization angles ranging from 0° to 24°. In Figure 2.22, the first row displays the initial results, while the second row presents the data collected after the two-hour delay. The results demonstrate consistent behavior across both sets, indicating that blocking the laser for an extended period does not affect the observed dipole responses.

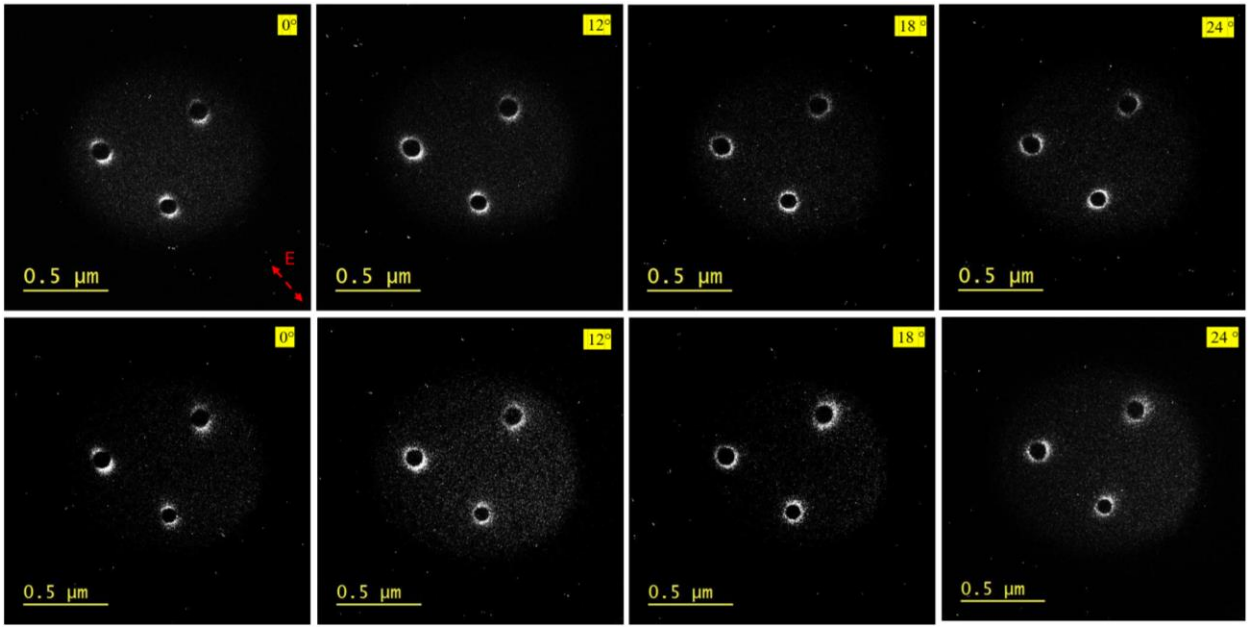

Figure 2-21 PINEM signals of three Au NPs as a function of the polarization rotation of the pump laser. First row images correspond to the initial experiment, and the second row images are captured after a 2-hour gap. The rotation angle is shown in yellow color on the right upper corner, and the red dashed line indicates the polarization direction for the angles. The rotation is in the counterclockwise direction.

So far, it has been shown that the variation in dipole directions and their circular transient behavior is not caused by the history of the applied polarization on the nanoparticles. Moreover, the observed phenomenon persists even when the pump laser polarization is rotated in the opposite (clockwise) direction.

2.3.1.2 Checking the effect of the power of the pump laser on the behaviors of the dipoles

Another essential test concerns the effect of pump laser power on the PINEM dipole responses of Au nanoparticles. To investigate whether nonlinear optical effects are responsible for the observed dipole behavior, we reduced the pump laser power from 85 mW to 35 mW and then to 21 mW. It is important to clarify that while PINEM is inherently a nonlinear process—in the sense that it involves photon absorption and emission by electrons—this nonlinearity pertains to quantized energy exchange rather than field symmetry.

Specifically, the pump laser excites surface plasmon modes in the nanoparticles, generating localized near fields. The passing probe electrons can then exchange energy in discrete units of $\hbar\omega$, leading to sidebands in the electron energy spectrum. Filtering these energy-shifted electrons yields the PINEM signal. However, this intrinsic nonlinearity is not responsible for the observed circular features or the misalignment of dipole directions.

Figure 2.23 shows PINEM images captured with the pump laser power reduced to 35 mW, across polarization rotation angles from 0° to 30°, focusing on the emergence of circular features around 18°.

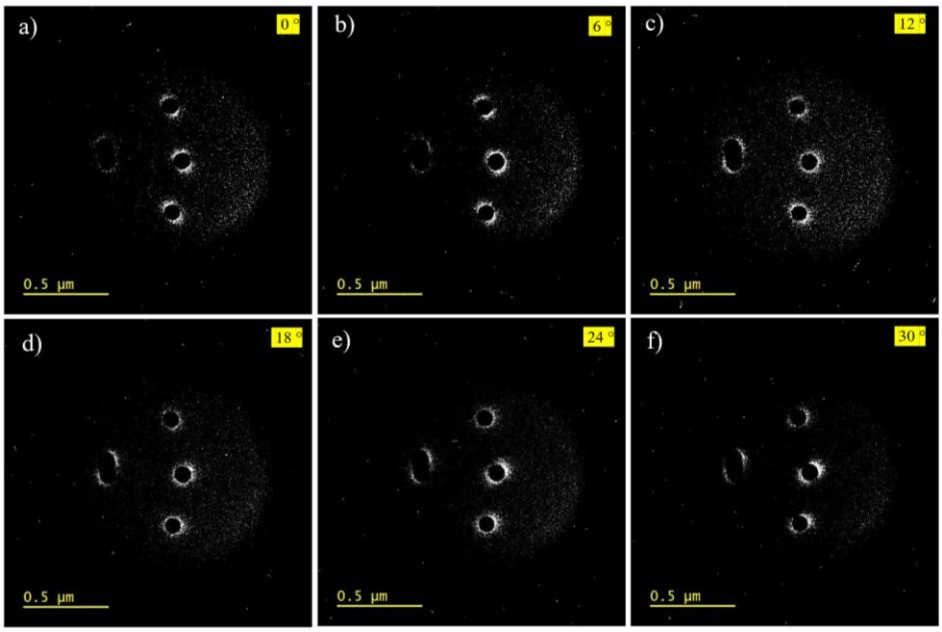

Figure 2-22 PINEM signals of three Au NPs as a function of the polarization rotation of the pump laser with a power of 35 mW. The rotation angle is indicated in yellow in the upper-right corner.

The pump laser was then blocked for 2 hours, and the experiment was repeated at 21 mW. The new PINEM images, also shown in Figure 2.24, demonstrate that even with a significant decrease in laser power, the dipole behavior remains consistent. The only noticeable effect is that lower power may require a longer acquisition time to accumulate enough electrons for a clear signal.

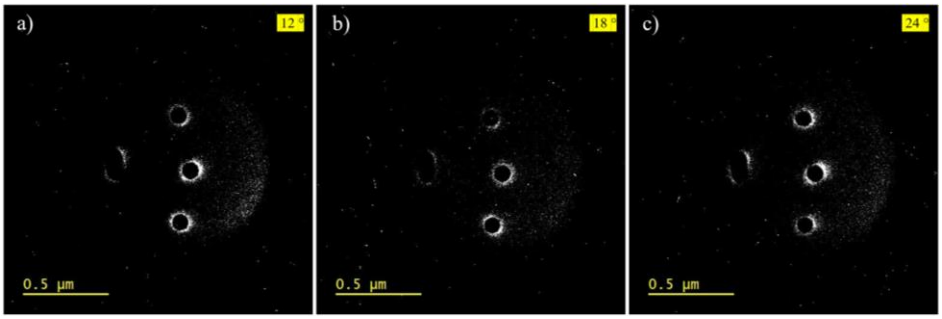

Figure 2-23 PINEM signals of three Au NPs as a function of the polarization rotation of the pump laser with a power of 21 mW. The rotation angle is indicated in yellow in the upper-right corner.

The next test we performed involved blocking the pump laser on the specimen for 2 hours, then adjusting the half-wave plate to a transient angle, such as 18°, and beginning to capture the near-field signals. Figure 2.25 shows that even under these conditions, the signal initially appears as a circular shape. When the polarization is subsequently adjusted to 12° or 24°, the expected dipolar image is recovered, consistent with normal rotation.

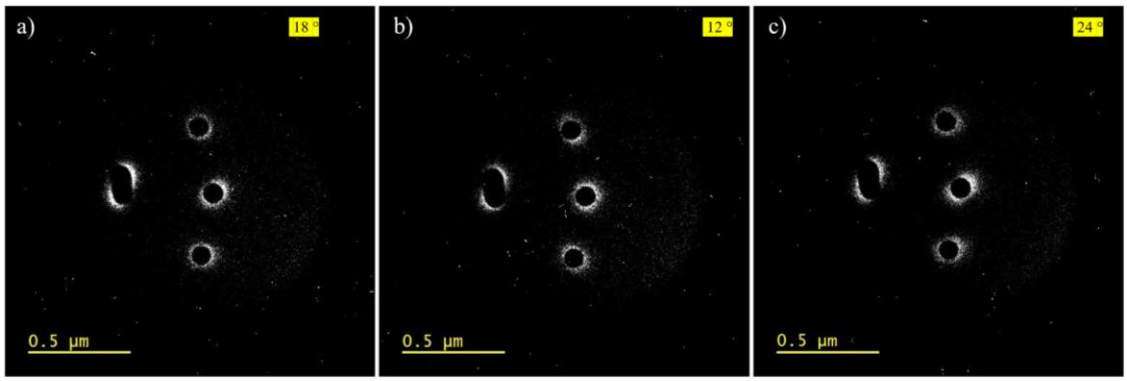

Figure 2-24 PINEM signals of Au NPs as a function of the polarization rotation of the pump laser. The images are captured after a 2-hour delay and start directly using an 18° polarization angle.

Additionally, we examined the effect of pump laser power on the PINEM signal behavior of other Au nanoparticles. Figure 2.26 shows the near-field images generated by pump laser powers of 22 mW (first row) and 37.3 mW (second row).

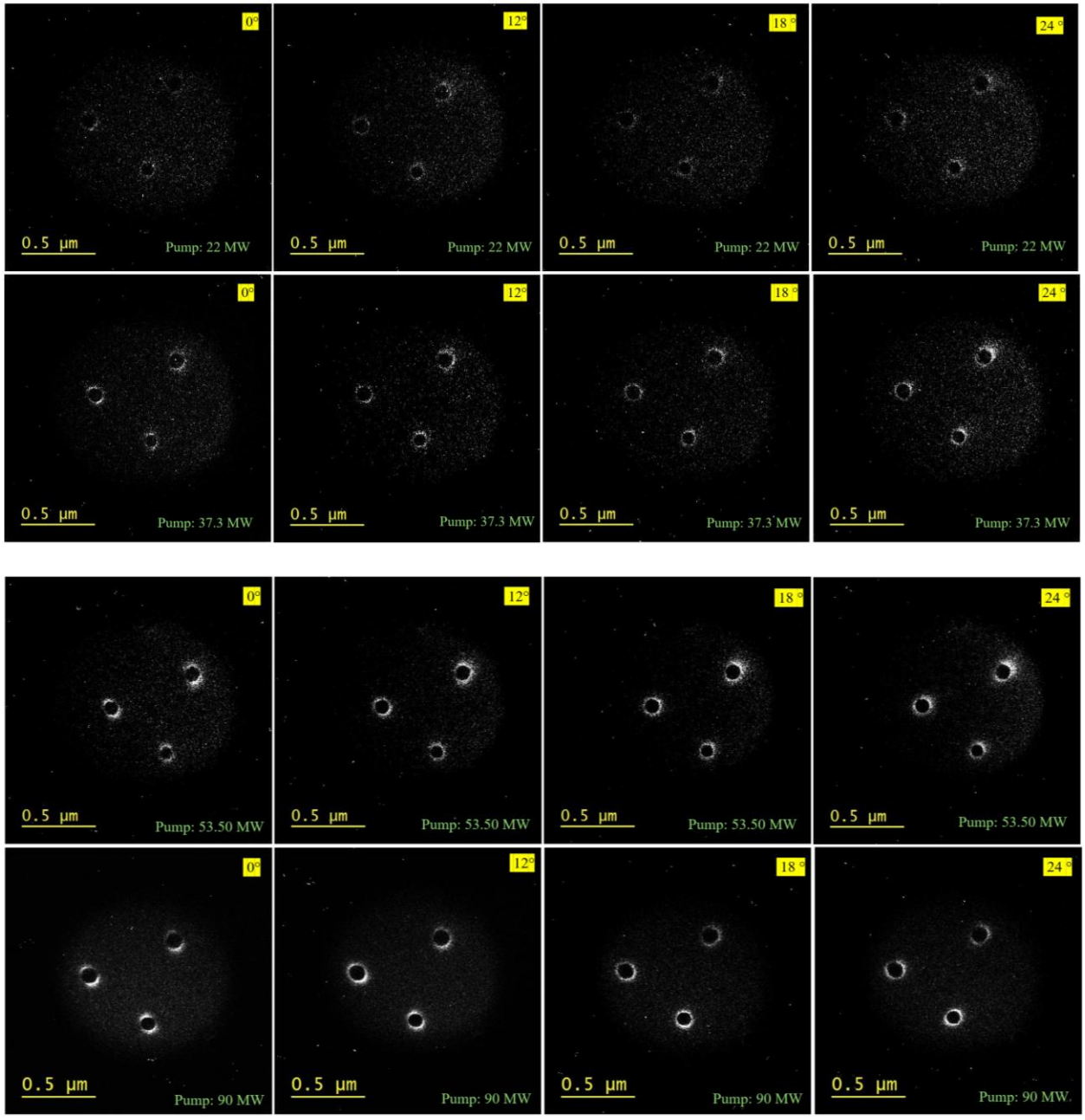

Figure 2-25 PINEM signals of Au NPs as a function of the polarization rotation of the pump laser in four different laser powers. The first row corresponds to 22 mW, the second one to 37.3 mW, the third row to 53.50 mW, and the fourth one to 90 mW. The rotation angle is indicated in yellow in the upper-right corner.

The experiment was also performed at two higher powers, 53.5 mW and 90 mW, shown in the third and fourth rows, respectively. These additional experiments confirm that varying the pump laser power does not significantly affect the dipole behavior of the Au nanoparticles.

As discussed, UTEM includes a delay stage in the optical setup to precisely adjust the time delay between the electron probe pulses and the pump laser pulses. To capture the PINEM signal, these two pulse trains must be synchronized at time zero. The next critical investigation is to study the PINEM signals around time zero to determine whether the observed behavior arises from any misalignment or uncertainty in this temporal synchronization.

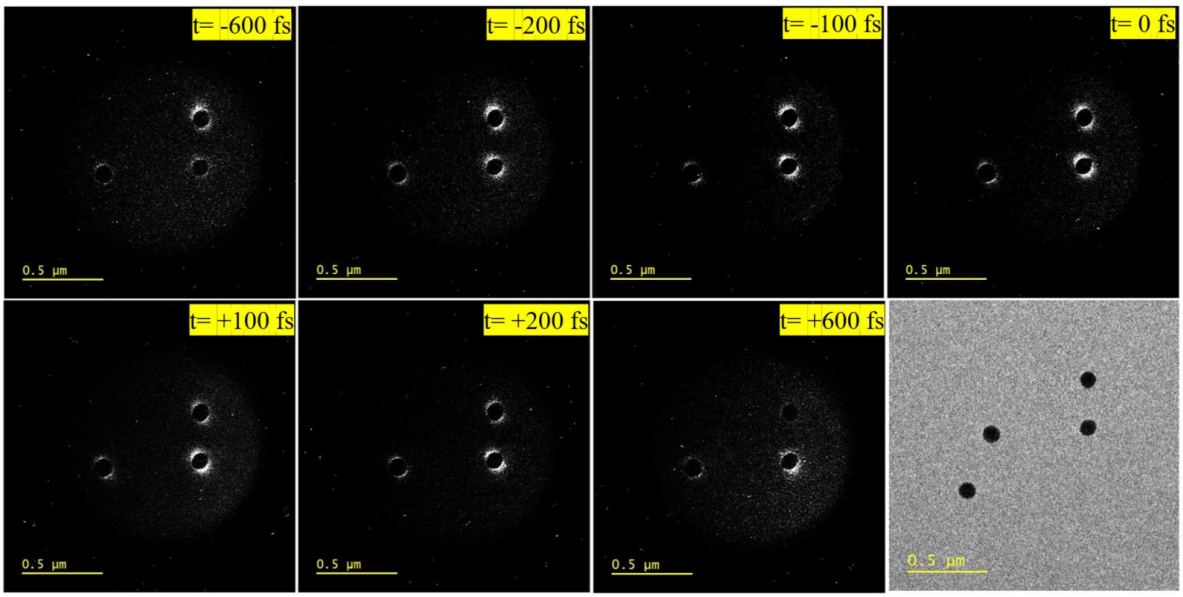

Figure 2-26 PINEM images as a function of the time delay between electron probe and pump laser pulses with steps of 100 fs. Relative t=0 fs is the time zero, and the times less than 0 fs are the negative times, meaning the electron pulse probes before the laser.

Figure 2.27 shows PINEM images of the Au NP dipoles captured at different time delays with 0.1 ps steps. As shown in Figure 2.27, the determined time zero occurs at a relative time of 0 fs. It is clear that before and after this point, the dipole behavior remains unchanged, although the intensities vary. Time delays less than 0 fs correspond to negative delays, where the probe electron pulses reach the sample before the pump laser pulses. Conversely, time delays greater than 0 fs are positive delays, meaning the probe pulses arrive after the pump laser. Figure 2.28 also presents the same experiment with larger time delay steps of 400 fs to observe the behavior at delays further from time zero.

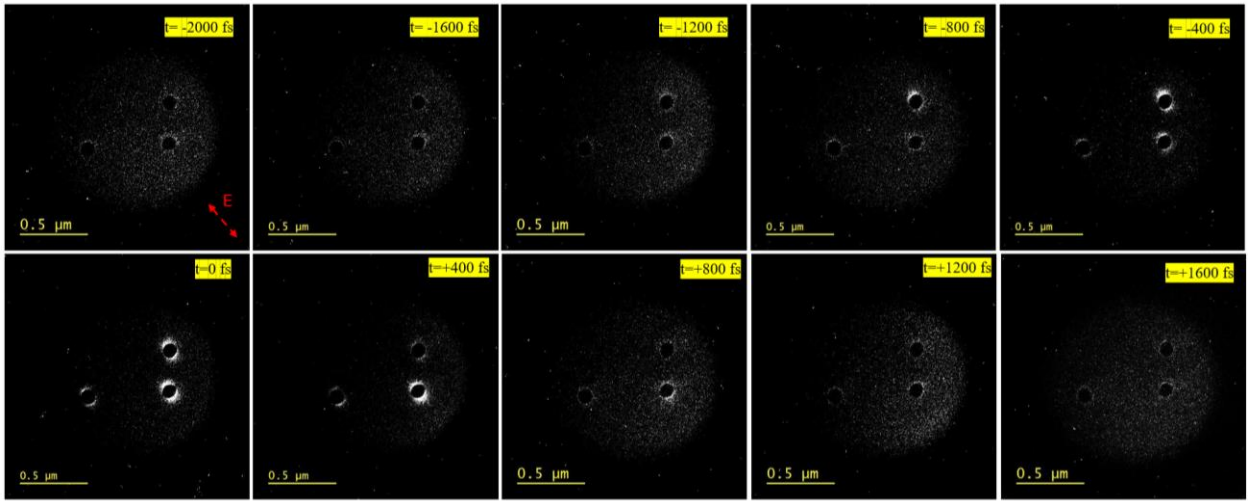

Figure 2-27 PINEM images as a function of the time delay between electron probe and pump laser pulses with a step of 400 fs. Relative t=0 fs is the time zero, showing the strong signal.

Another similar test, shown in Figure 2.29, was performed using 100 fs time delay steps to capture more detailed dynamics. The results demonstrate that the signal strengthens around a relative time of t = 0 fs and gradually diminishes as the delay moves away from time zero. These experiments indicate that the observed misaligned dipoles and circular signals are not caused by timing misalignment between the pump and probe pulses.

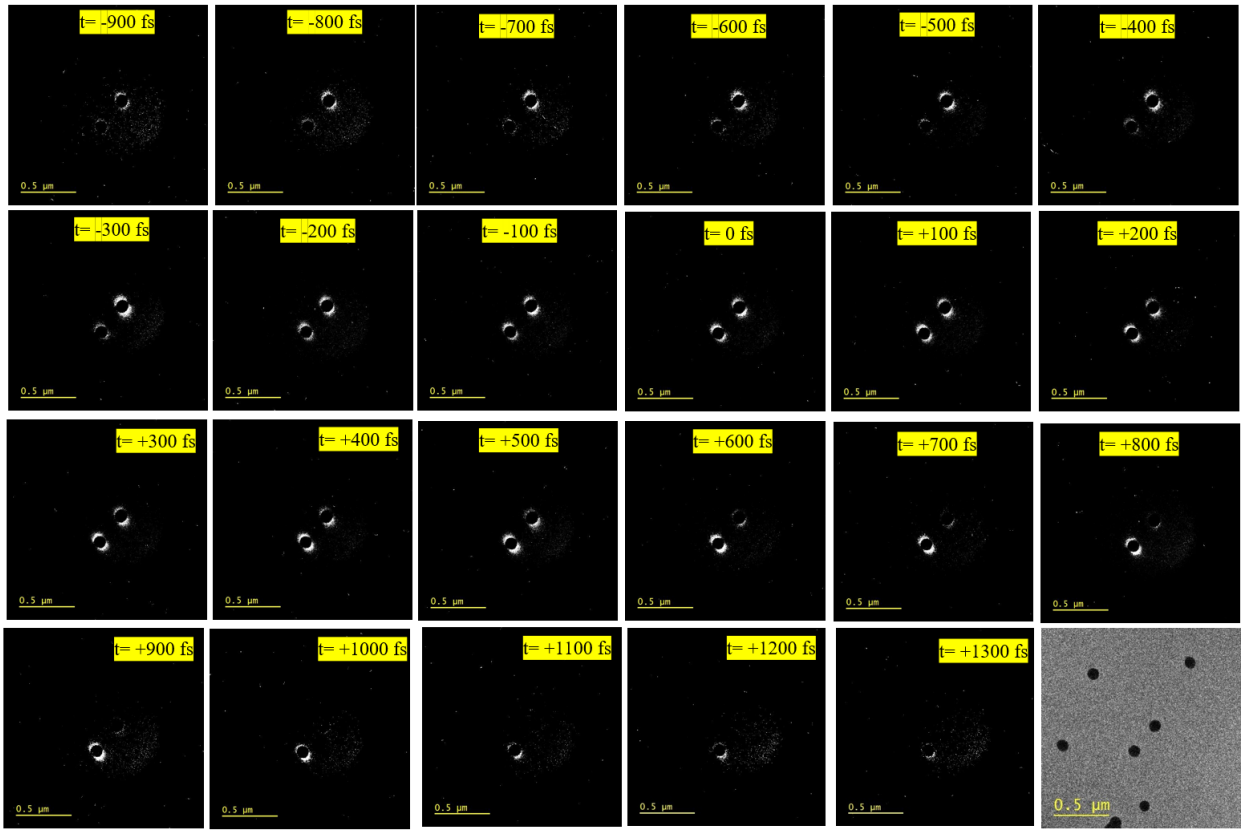

Figure 2-28 PINEM images of two Au NPs as a function of the time delay between electron probe and pump laser pulses, with the steps of 100 fs. Relative t=0 ps is the time zero, showing the strong signal.

2.3.2 The PINEM and dipolar behavior of Au nanoparticles on the Graphene grids

To investigate whether different substrates influence the dipole orientation, we used graphene grids for the Au nanoparticles. Figure 2.30 shows the TEM image of the gold nanoparticles and their corresponding PINEM images under two different linear polarization directions of the pump laser. Interestingly, on the graphene substrate, variations in dipole orientation are less frequent compared to those observed on the SiO substrate.

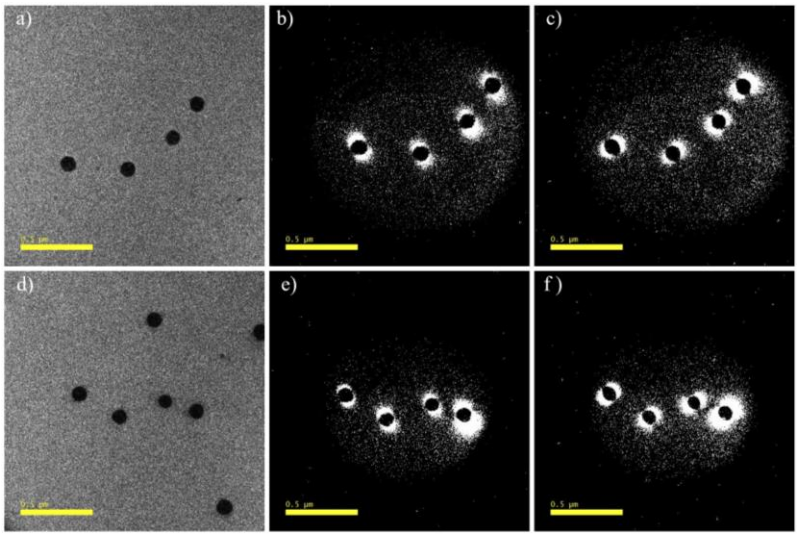

Figure 2-29 a) TEM bright field and b,c) PINEM images of four Au NPs on the Graphene grids. d) the same image for different particles of Au NPs and their e,f) PINEM signals. The size of the Au NPs is 100 nm.

Figure 2.31 shows another set of Au nanoparticles on a graphene grid, where parts a and d present the TEM bright-field images of the sample. The corresponding PINEM images of the nanoparticles in part a are shown in b and c, captured under two different linear polarization directions of the pump laser, indicated by red dashed lines. Similarly, the PINEM images of the nanoparticles in part d are shown in e and f. As observed in parts b, c, e, and f, the near fields around the particles do not exhibit distinctly misaligned dipoles.

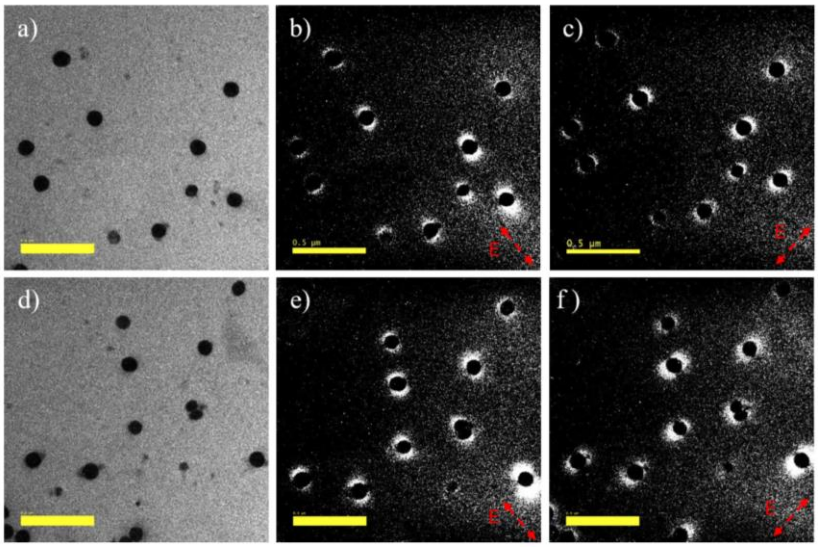

Figure 2-30 a) TEM bright field and b,c) PINEM images of some Au NPs on the Graphene grids. d) the same TEM image for other particles of Au NPs and their e,f) PINEM signals. The size of the Au NPs is 100 nm. Red dashed lines show the direction of the polarization of the pump laser rotated 90° in the c and f.

Although misaligned dipoles are less frequently observed on the graphene substrate, repeated experiments revealed some occurrences. Figure 2.32a shows a TEM bright-field image of several Au nanoparticles, each approximately 100 nm in size. Figures 2.32b and 2.32c display the corresponding near fields of these particles under two different linear polarization directions of the pump laser, indicated in red. A similar set of images for another ensemble of Au nanoparticles is shown in Figures 2.32d, e, and f. In Figure 2.32e, two nanoparticles exhibit differing dipole orientations, marked by yellow vectors. After rotating the laser polarization by 90° relative to the initial direction, the PINEM image in Figure 2.32f confirms that these two nanoparticles remain misaligned.

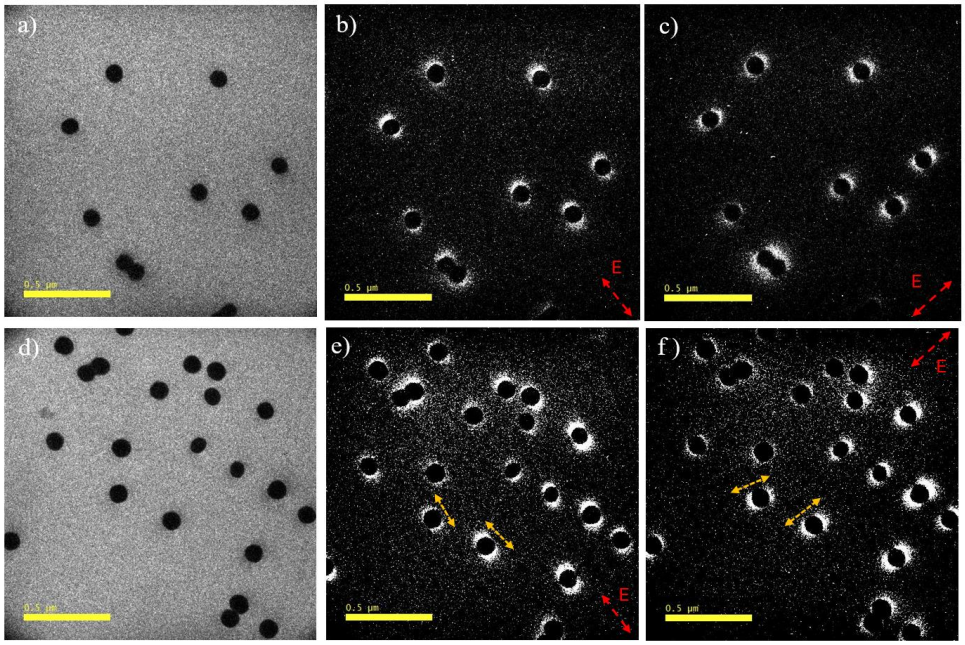

Figure 2-31 a) TEM bright field and b,c) PINEM images of some Au NPs on the Graphene grids. d) the same TEM image for other particles of Au NPs and their e,f) PINEM signals. Red dashed lines show the direction of the polarization of the pump laser, and yellow dashed lines show the dipole directions for the two NPS, which are different.

To compare the results of Au NPs on the Grephane grids to those on the SiO grids, we captured PINEM signals of Au on the Grephane substrates as a function of the polarization rotation of the pump laser. The resulting images are shown in Figure 2.33 and Figure 2.34. These results show that Au NPs on the graphene substrate behave similarly to the polarization rotation, where at transient angles the near fields transform to circular signals.

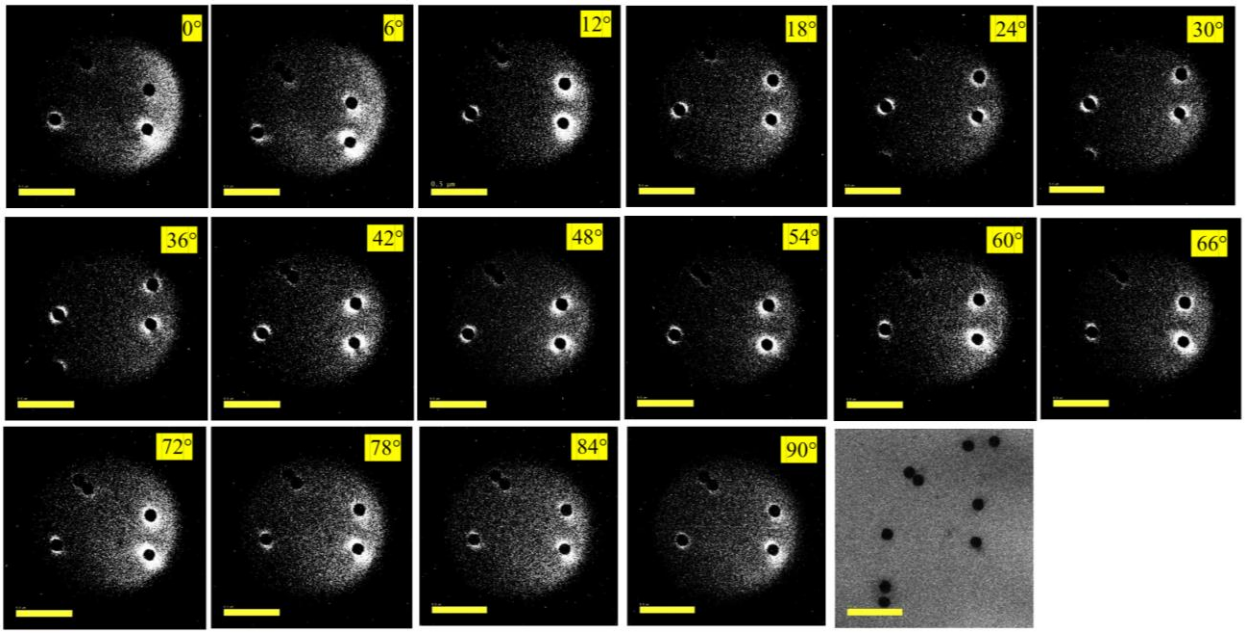

Figure 2-32 Near-field signals in three Au NPs on the graphene substrate as a function of the polarization rotation of the pump laser, captured by the PINEM technique. The rotation angle is shown in yellow color on the right upper corner, and the red dashed line indicates polarization direction for the angles 0°, 48°, and 90°.

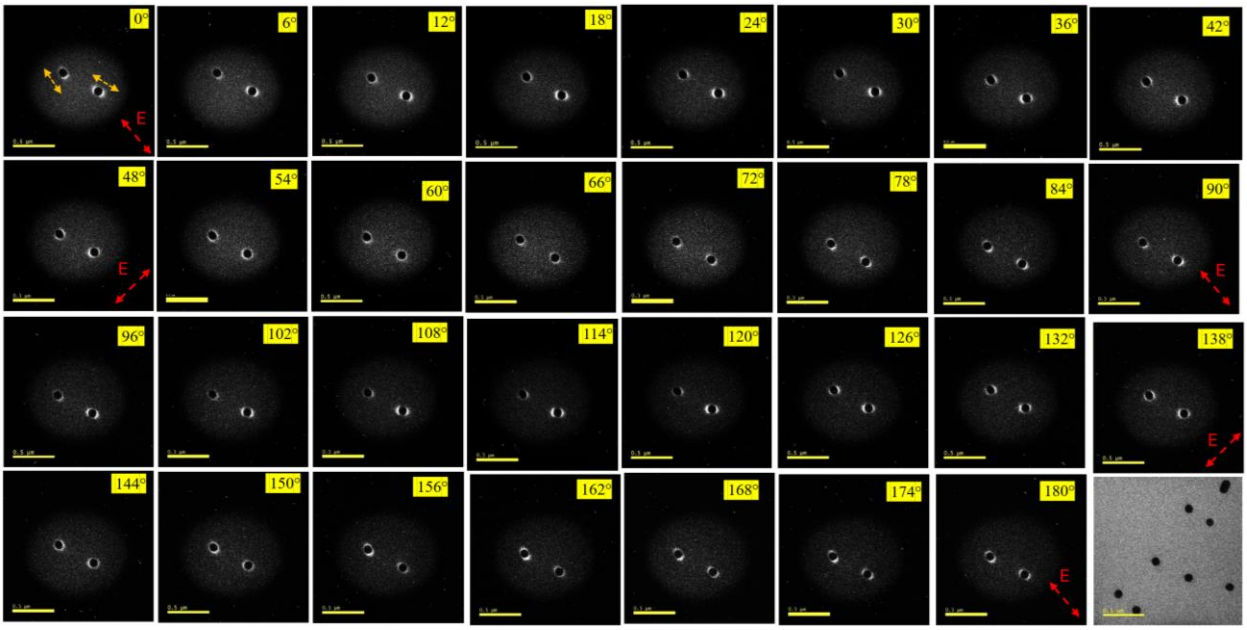

Figure 2-33 Near-field signals in three Au NPs on the graphene substrate as a function of the polarization rotation of the pump laser, captured by the PINEM technique. The rotation angles are 0° to 180°.

2.3.2 Quantification of the directions of the dipoles

Using Equation (2.4) and similar to Figure (2.4), a simulated dipole of Au NPs is created and shown in Figure 2.35. To calculate the direction angle of the dipole, the area of NP and the electromagnetic near field is segmented into 36 slices with the polar angle of 10°, where the direction of the x-axis is at 0°. Then, the intensity of each slice is integrated and plotted as a function of polar angle. Because there are two bright crescent-shaped features, the plot in Figure 2.35c shows two peaks labeled left and right peaks. Then, these two peaks of dipole data are fitted with Gaussian functions to find their centers, shown in Figure 2.35c. The defined center is the average of these two peak centers. For the simulated case, the angles are exact and 135° and 315°, which gives 315-135=180°.

Figure 2.35d shows the experimental near fields of Au NPs, where Figure 2.35b shows the slicing process and Figure 2.35d shows the calculation process for the experimental dipoles, which resulted in 44° and 234° for left and right peaks. The average of these peaks is 49° and 229°, which gives 229-49=180°.

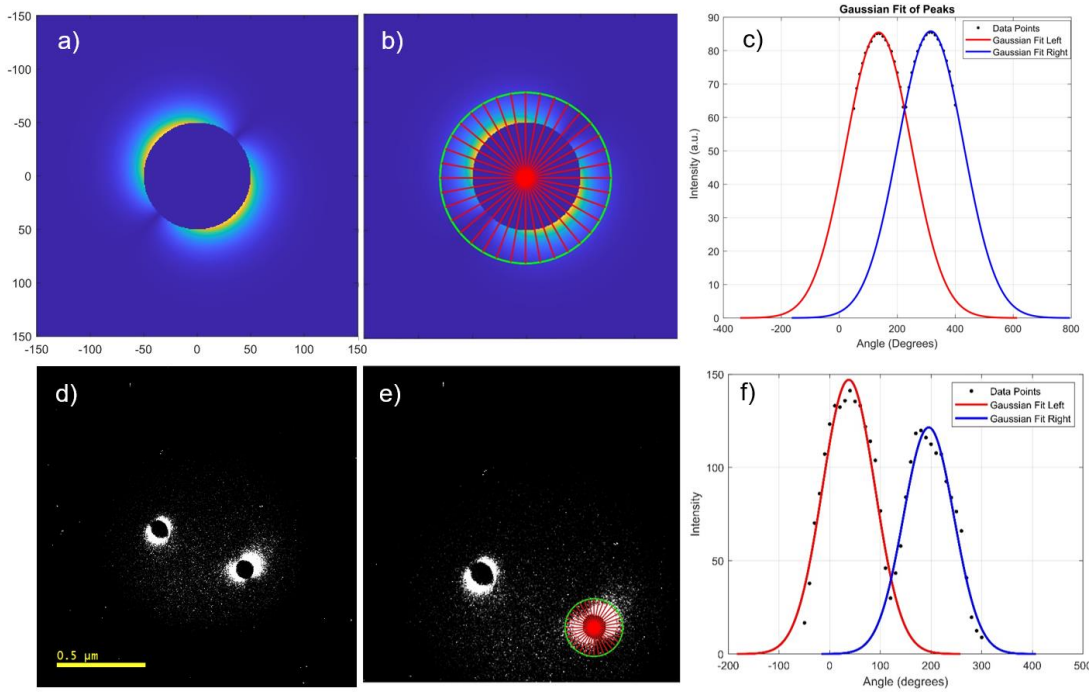

Figure 2-34 a) The simulated near fields of Au. b) Slices in polar coordinates to calculate the intensity as a function of angle to apply c) a Gaussian fit, and then, finding the center of dipoles.

Using this approach, fitting a Gaussian function yields an uncertainty on the order of approximately 2–3 degrees.

After testing the capability of the center-finding approach in Figure 2.35, we used this fitting approach to calculate the angle of direction for the nanoparticles of Au on the SiO and Graphene substrate. Figure 2.36 shows the dipoles of Au NPs on the SiO grids for different regions. In Figure 2.36b, four NPs are present with the angles of 111°, 117°, 134°, and 137°. In Figure 2.36d, the angles are 118°, 121°, 130°, and 137°.

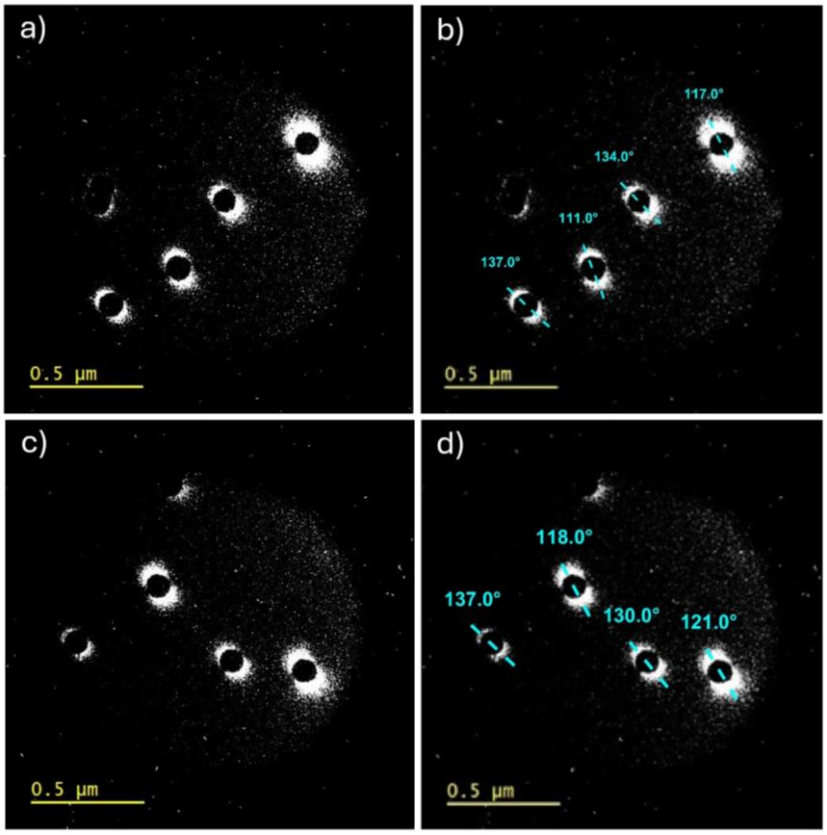

Figure 2-35 a) and c) The PINEM images of near fields around Au NPs on the SiO substrates and b,d) their calculated directions. The angles are calculated in a way that the direction of the x-axis is at 0°.

By applying the same approach to quantify the dipole directions in the captured PINEM images for both SiO and graphene grids, the corresponding angles were determined. Figure 2.37 presents an example of Au nanoparticles on the SiO grid, while Figure 2.38 shows the results for Au nanoparticles on the graphene grid.

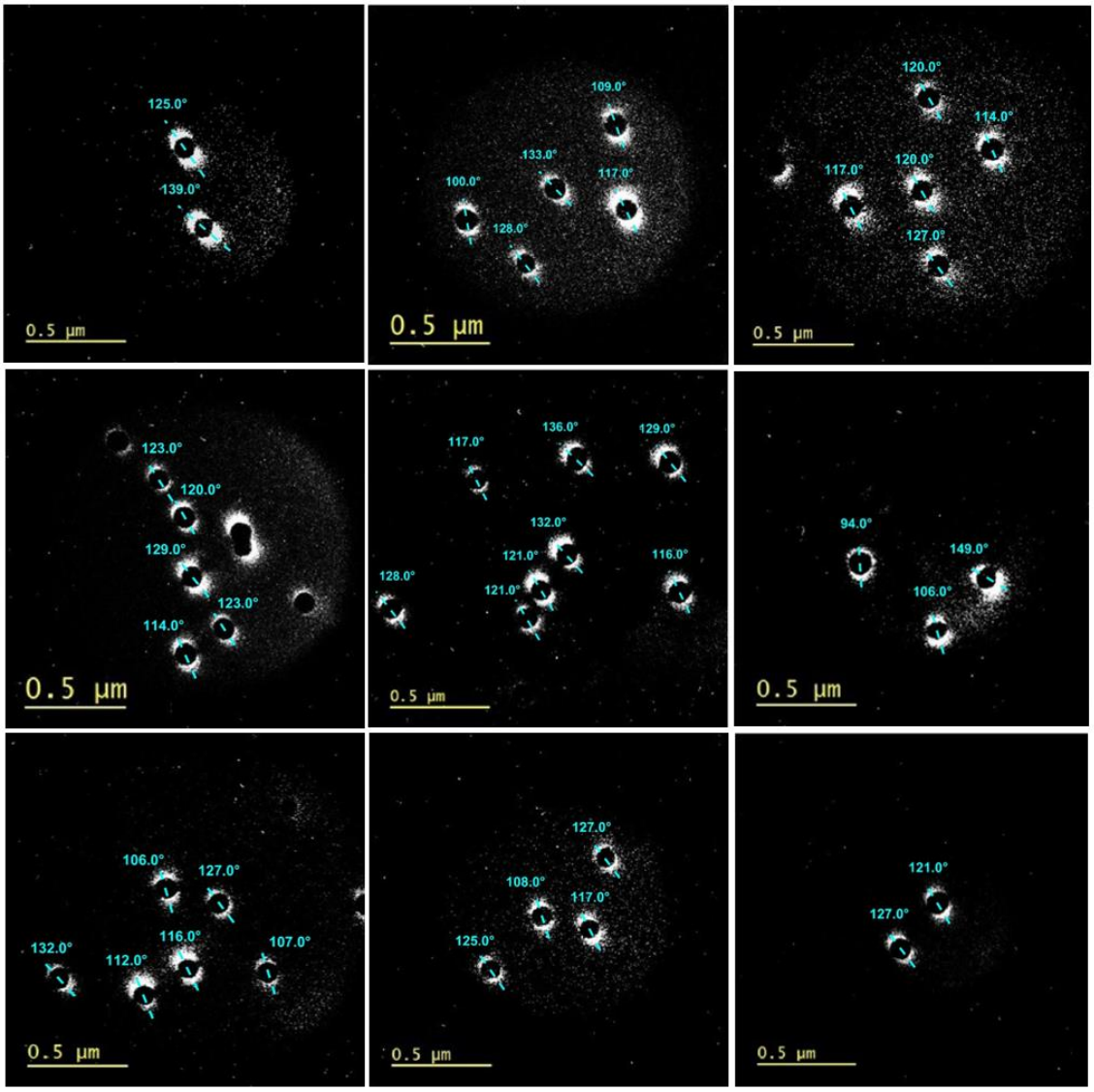

Figure 2-36 a) and c) The PINEM images of near fields around Au NPs on the SiO substrates and b,d) their calculated directions. The angles are calculated in a way that the direction of the x-axis is at 0°.

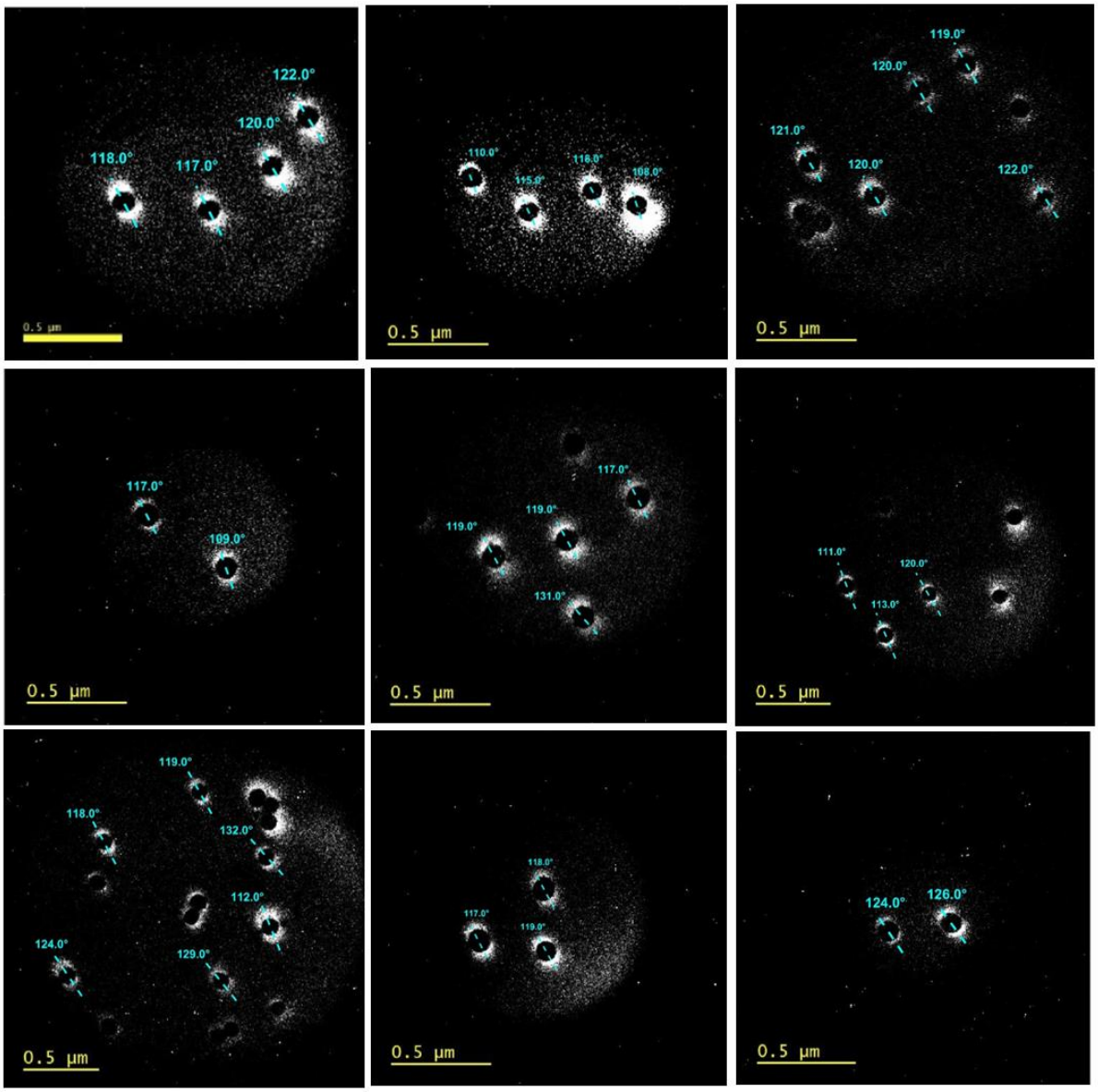

Figure 2-37 a) and c) The PINEM images of near fields around Au NPs on the graphene substrates, and b,d) their calculated directions. The angles are calculated in a way that the direction of the x-axis is at 0°.

2.3.3 Comparison of dipole directions of Au NPs on the SiO and Graphene grids

We used the approach explained in the previous section (2.3.2) to find the directions of the Au NPs in graphene and SiO grids to make a comparison. Figure 2.39a shows the distribution of dipole angles in 105 Au nanoparticles (NPs) on the graphene grid. Among them, 72 NPs have angles within $120 \pm 5°$, with a full width at half maximum (FWHM) of 9°. For the SiO substrate, 108 Au NPs were analyzed, and the angle histogram in Figure 2.39b shows a broader FWHM of 19°, with only 53 NPs falling within the $120 \pm 5°$ range, fewer than on graphene. This broader angular distribution is more evident in Figure 2.39c, which compares both grids. These results indicate that the SiO substrate has a stronger influence on the orientation of dipoles in Au NPs compared to the graphene substrate.

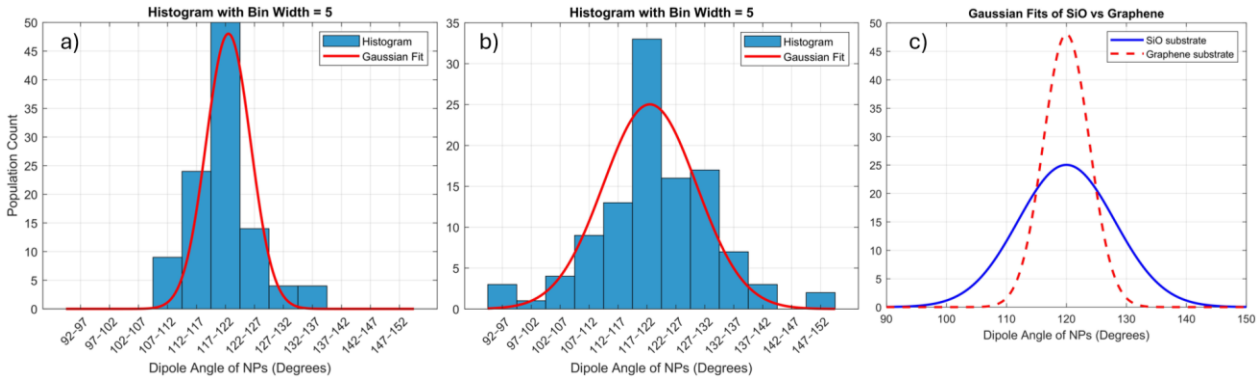

Figure 2-38 Distribution of direction angles of Au NPs on the a) Graphene, b) SiO substrates. The red fitted curve is a Gaussian fit with a center of 120°. C) The Gaussian fits are plotted together for comparison.

Defect-rich SiO substrates exhibit localized surface charges that can electrostatically couple with the surface charges of nanoparticles, influencing adhesion and charge transfer. These interactions are highly sensitive to the nature and distribution of substrate defects. Additionally, the crystallographic facets of nanoparticles—each with distinct atomic arrangements and surface energies—can modulate particle–substrate coupling. Facet-dependent interactions may lead to selective binding and anisotropic behavior. Together, defect coupling and facet orientation govern the overall particle–substrate dynamics, leading to plasmon–phonon–polariton coupling [104] and potentially inducing dipole misalignment in the near field. This, in turn, results in modified plasmon oscillation behavior and a broader dipole orientation distribution observed on SiO.

2.3.4 The PINEM and dipolar behavior of Ag nanoparticles

In the preceding sections, dipole orientations derived from PINEM signals of gold (Au) nanoparticles on SiO and graphene substrates were examined. Notably, a subset of nanoparticles—particularly those on the SiO support—exhibited dipole alignments deviating from the dominant polarization direction. In the current section, we extend this analysis to silver (Ag) nanoparticles on the SiO substrate to investigate whether similar deviations in dipole orientation are also present.

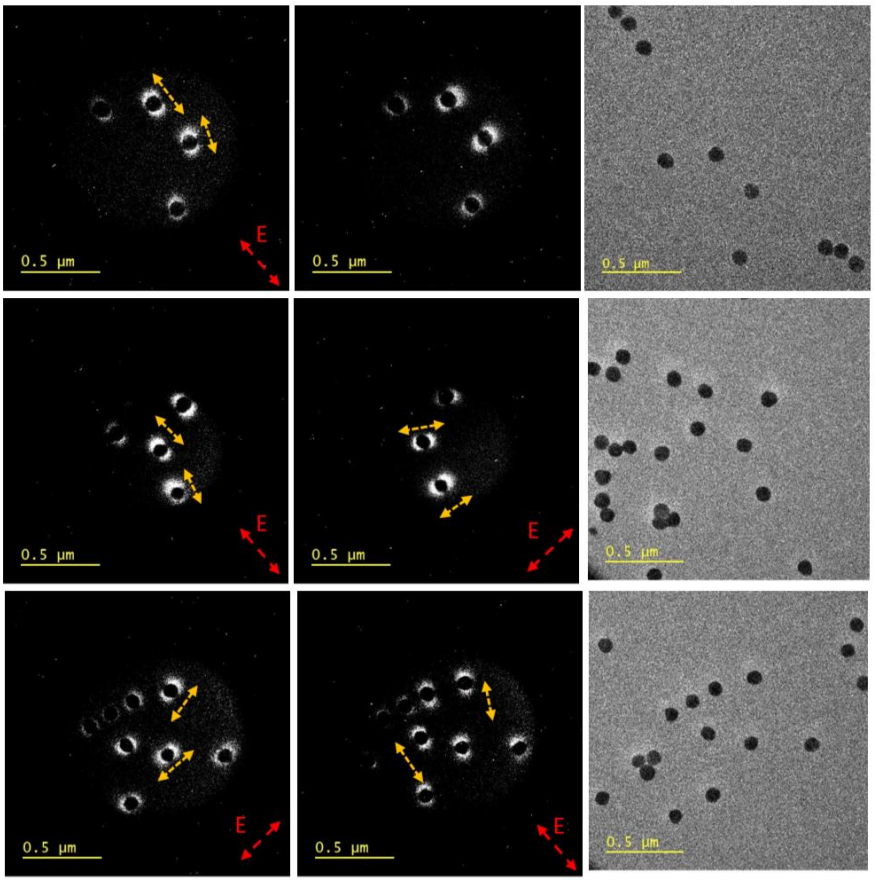

Figure 2-39 PINEM images of the near fields of the Ag NPs created by the pump laser with a linear polarization, which is shown by a red dashed line in the right lower corner. The yellow dashed lines show the difference in directions of dipoles.

Figures 2.40 and 2.41 present PINEM images of silver (Ag) nanoparticles (NPs) deposited on a SiO substrate, illuminated by a 515 nm pump laser operating at 80 mW. The red dashed lines indicate the laser polarization direction, while the yellow dashed lines represent the dipole

direction for specific nanoparticles. As evident from the images, Ag NPs exhibit similar behavior to Au NPs, with some nanoparticles showing noticeable deviations in dipole angles. Figure 2.41 presents additional Ag NPs, where in some cases the angular deviation is visible, while in others the dipole directions closely align with the laser polarization.

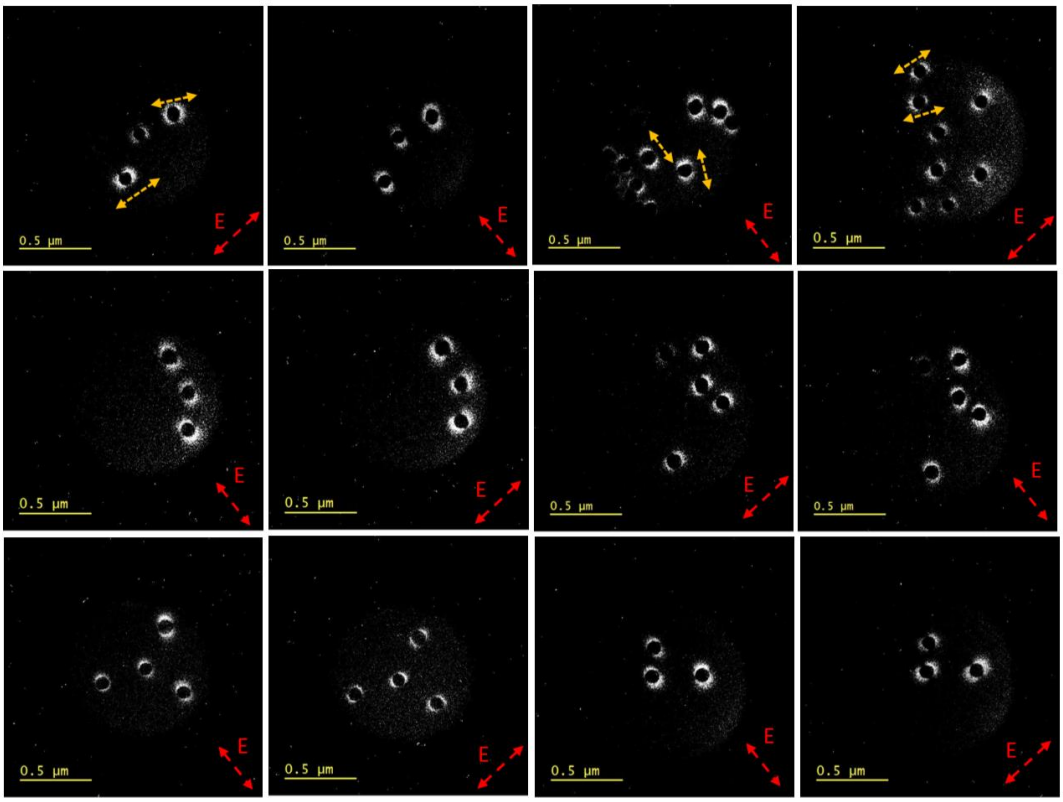

Figure 2-40 PINEM images of the near fields of the Ag NPs. The dashed colored lines are plotted for the same purpose as Figure 2.40.

To further investigate the effect of pump laser polarization rotation on the orientation of near fields around nanoparticles, we selected two Ag nanoparticles on a SiO grid, as shown in Figure 2.42, and captured the PINEM images. Initially, the laser polarization was oriented at approximately 120° (northwest direction), with the half-wave plate fixed at 0°. As the polarization was rotated with 6° steps, the dipole directions rotated counterclockwise. At a rotation angle of 18°, the polarization became nearly circular and remained so until 24°. Beyond this point, it began aligning in the opposite direction, which becomes obvious from the 36° rotation to 60°. At a rotation angle of 66°, the dipoles begin to exhibit a circular pattern, which persists until approximately 72°. By

78°, the dipoles start to realign in a direction similar to that observed at 0°, as expected after a 90° rotation of the half-wave plate (corresponding to a 180° rotation in the actual polarization direction). To confirm the emergence of circular near fields at specific angles, we repeated the experiment using three different Ag nanoparticles on a SiO substrate. The results, shown in Figure 2.43, demonstrate that at angles of 18° and 24°, the PINEM signals of the near fields exhibit a circular pattern.

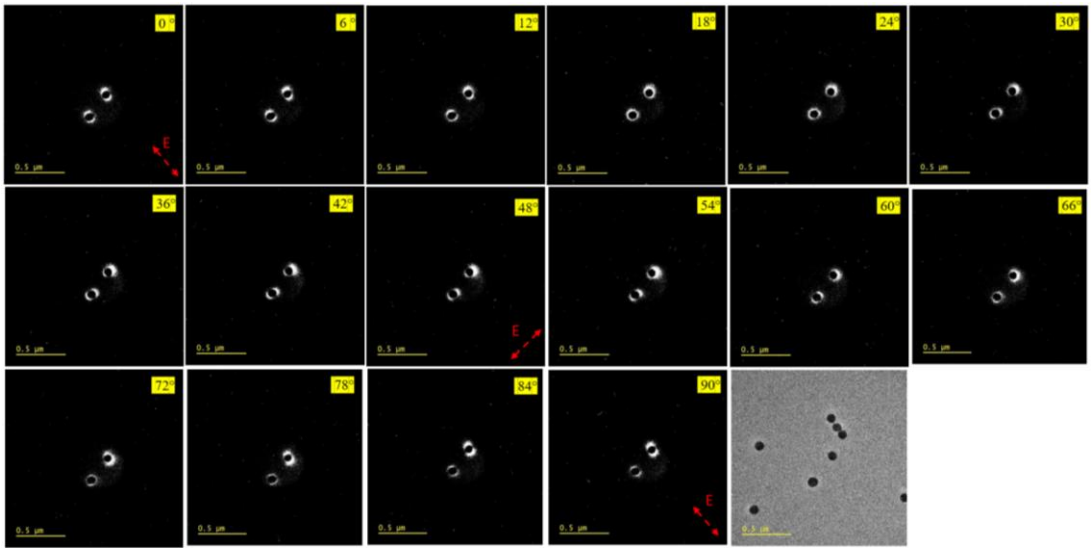

Figure 2-41 Near-field signals of two Ag NPs on the SiO substrate as a function of the polarization rotation of the pump laser, captured by the PINEM technique. The rotation angles are 0° to 90° with steps of 6°.

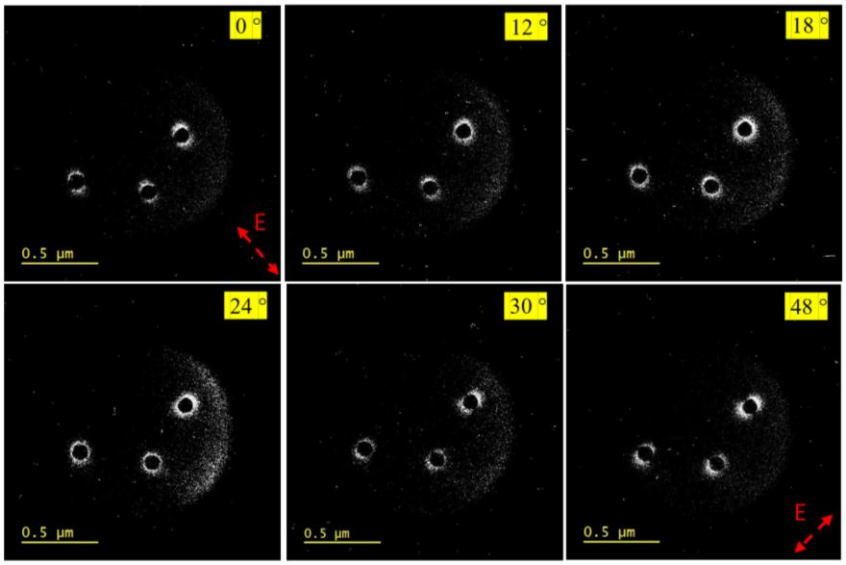

Figure 2-42 Near-field signals of three Ag NPs on the SiO substrate as a function of the polarization rotation of the pump laser. The rotation angles are 0° to 48°.

These experiments on Ag nanoparticles show results consistent with those observed for Au nanoparticles. The main findings include variations in the dipole orientations of the nanoparticles and the appearance of circular PINEM signals at specific polarization angles. In Section 2.3.3, we statistically analyzed the dipole directions and discussed the influence of the SiO and graphene grids. Here, we focus on understanding the unexpected emergence of circular PINEM signals at certain angles, despite the pump laser having linear polarization. Initially, high-resolution TEM images of silver nanoparticles (Ag NPs) with a diameter of approximately 100 nm were captured, as shown in Figures 2.44 and 2.45. The images confirm that the nanoparticles are single crystals, with distinct lattice planes clearly visible in Figures 2.44c, 2.44d, and 2.45c.

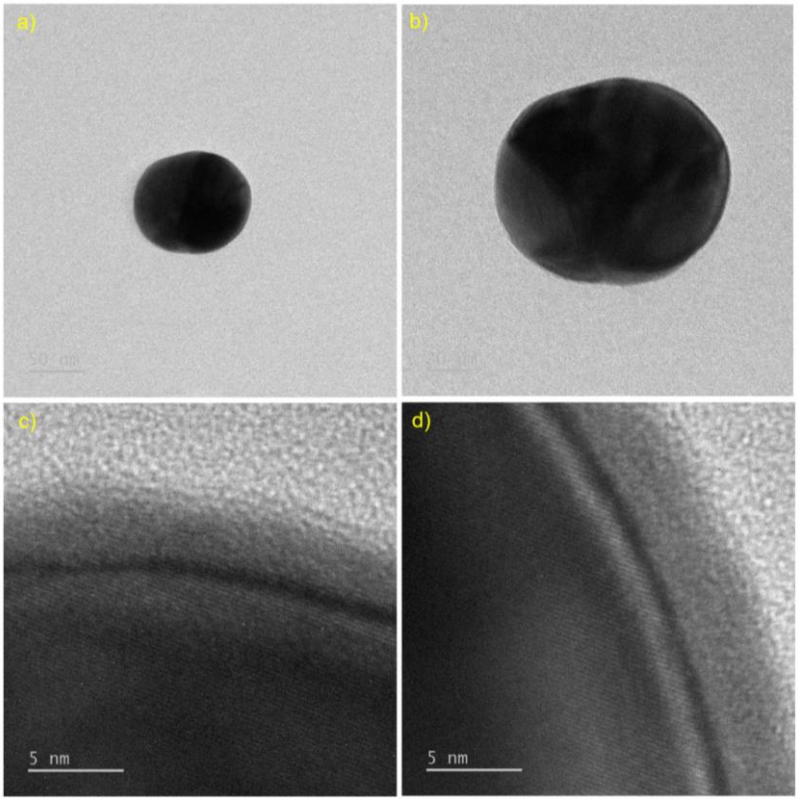

Figure 2-43 a,b) TEM images of an Ag nanoparticle with a 100 nm diameter. c,d) HRTEM images of the two edges of the same NP. The nanoparticles appear as single crystals, exhibiting well-defined lattice fringes.

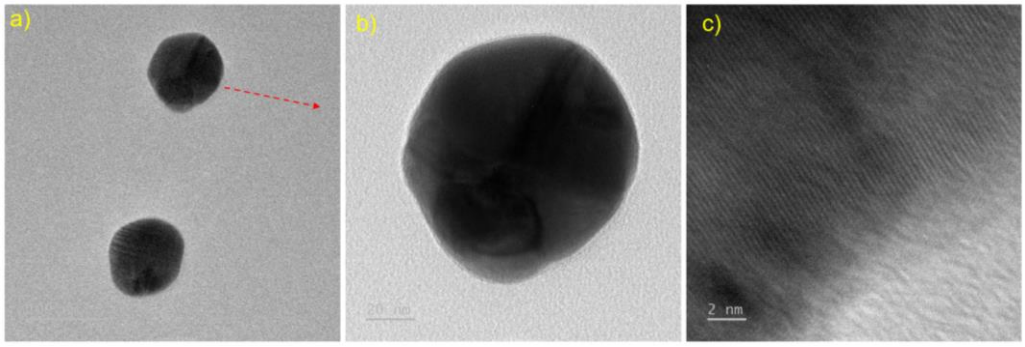

Figure 2-44 a,b) TEM images of two Ag nanoparticles with a 100 nm diameter. c) HRTEM images of the edge of the upper NP in part a. The nanoparticles appear as single crystals with well-defined lattice fringes.

2.3.5 Modeling the circular near fields of metallic NPs

To explore the origin of circularity at angles where the half-wave plate changes the direction of the linear polarization of the pump laser, we begin by examining the equations governing the interaction between the pump laser and the nanoparticles. In analogy with Equation (2.4), we consider:

$$E_z(x,y,z;t) = E_0 a^3 \frac{(\vec{p}.\vec{r})z}{r^5} e^{-iwt} \tag{2.9}$$

where $\vec{p}$ is the polarization, $r = \sqrt{x^2+y^2+z^2}$, E_0 is the amplitude of the incident field, a is the radius of the NP, and w is the frequency of the laser. By setting $E_0 = 1, a = 1$, the equation simplifies to

$$E_z(x,y,z;t) = \frac{(p_x x + p_y y)z}{r^5} e^{-iwt} \tag{2.10}$$

Considering the linear relation $\vec{p} = \chi.\vec{E}$ and defining the susceptibility tensor, the result is

$$\begin{bmatrix} p_x \\ p_y \end{bmatrix} = \begin{bmatrix} \chi_{xx} & \chi_{xy} \\ \chi_{yx} & \chi_{yy} \end{bmatrix} \begin{bmatrix} E_x \\ E_y \end{bmatrix} \tag{2.11}$$

And if we define the incident field as $E = E_0[\cos(\varphi)\hat{x} + \sin(\varphi)\hat{y}]$, and $E_0 = 1$, then

$$\begin{bmatrix} p_x \\ p_y \end{bmatrix} = \begin{bmatrix} \chi_{xx} & \chi_{xy} \\ \chi_{yx} & \chi_{yy} \end{bmatrix} \begin{bmatrix} cos(\varphi) \\ sin(\varphi) \end{bmatrix} \tag{2.12}$$

Thus,

$$p_x = \chi_{xx}\cos(\varphi) + \chi_{xy}\sin(\varphi)\ ,\ p_y = \chi_{yx}\cos(\varphi) + \chi_{yy}\sin(\varphi) \tag{2.13}$$

Now, assume a specific form of the susceptibility tensor:

$$\chi = \begin{bmatrix} \chi_{xx} & \chi_{xy} \\ \chi_{yx} & \chi_{yy} \end{bmatrix} = \chi_0 \begin{bmatrix} 1 & i \\ -i & -1 \end{bmatrix} \tag{2.14}$$

Then,

$$p_x = \chi_0\cos(\varphi) + i\chi_0\sin(\varphi),\ p_y = -i\chi_0\cos(\varphi) - \chi_0\sin(\varphi) \tag{2.15}$$

For the case $\varphi = 90°$, this simplifies to $p_x = i\,\chi_0, p_y = -\chi_0$ indicating a phase difference of $\Delta\phi = 90°$, which corresponds to a circular near-field. Figure 2.46 presents the theoretical PINEM signals corresponding to the near fields around a gold nanoparticle, modeled using the susceptibility tensor given in Equation (2.14).

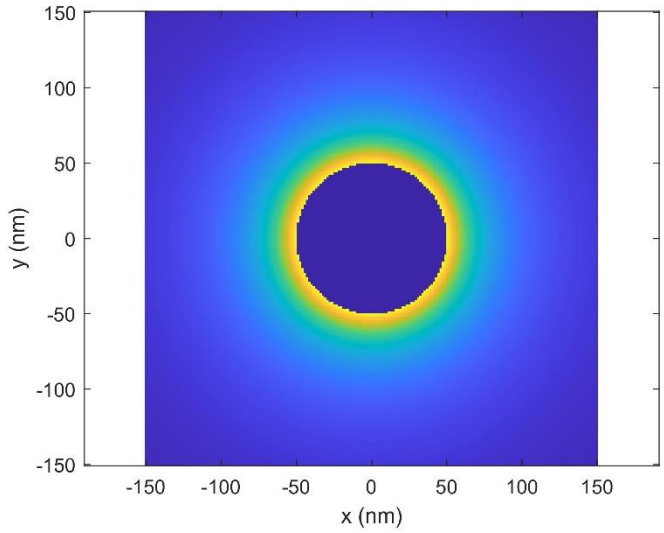

Figure 2-45 The theoretical PINEM signal of near fields around a gold nanoparticle, which has the susceptibility tensor of (2.10).

Similar behavior occurs at $\varphi = 0°,\ 90°, 180°, 270°,\ 360°$ angles where the direction of linear polarization of the pump laser changes. To produce the circular pattern, two conditions must be met:

1) $|p_x| = |p_y|$,

2) A phase difference of exactly ±90° between p_x and p_y : $\frac{p_y}{p_x} = \pm i$.

We now proceed to examine these conditions. For the case (2.10), starting from the second condition gives:

$p_y = \pm ip_x \Rightarrow -i\cos(\varphi) - \sin(\varphi) = \pm i[\cos(\varphi) + i\sin(\varphi)]$

For $p_y = + ip_x \Rightarrow -i\cos(\varphi) - \sin(\varphi) = i\cos(\varphi) - \sin(\varphi) \Rightarrow \varphi = 90°, 270°$

For $p_y = - ip_x \Rightarrow -i\cos(\varphi) - \sin(\varphi) = -i\cos(\varphi) + \sin(\varphi) \Rightarrow \varphi = 0°, 180°, 360°$

Therefore, the condition in Equation (2.14) produces circular near-fields only at angles where the polarization direction of the pump laser changes, i.e., at 0°, 90°, 180°, 270°. In our setup, these angles correspond to approximately 24°, 72°, 114°, and 160° on the half-wave plate. Figure 2.47 shows the half-wave plate angles at which the laser polarization changes from upward to downward or from leftward to rightward. The initial polarization angle on the camera is 120°, corresponding to a half-wave plate rotation of 0°. As the half-wave plate rotates to 24°, for instance, the polarization angle on the camera becomes: 120°+2×24°=168°.

In summary, at specific angles where the amplitudes of p_x and p_y become equal and satisfying a phase difference of ±90°, the conditions for generating circular patterns in the near-field are fulfilled.

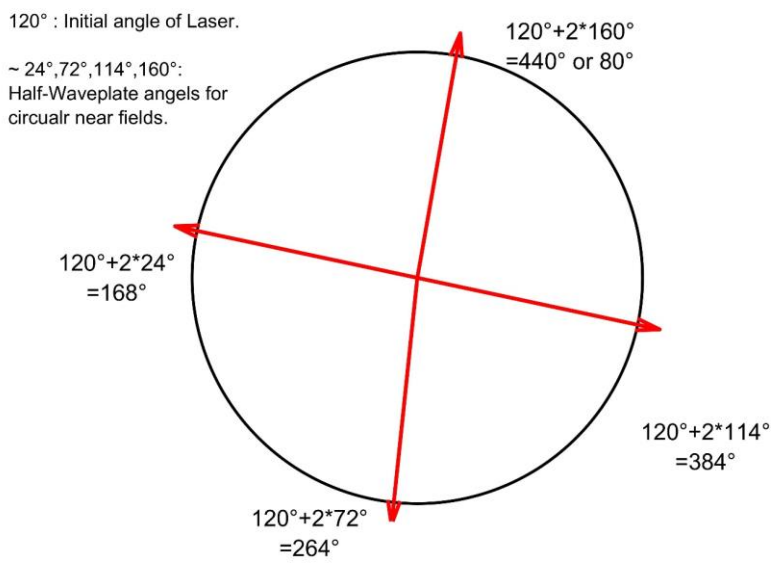

Figure 2-46 The angles on the camera correspond to the half-wave plate angles where the pump laser of the UTEM setup changes the direction from upward to downward and from leftward to rightward.

The discussed susceptibility tensor (2.14) corresponds to a chiral material. Chirality can be an intrinsic material property, such as in magneto-optically active or structurally chiral systems. However, extrinsic chirality arises when the material itself is achiral, but symmetry is broken through geometry or external excitation. Various forms of asymmetry—including particle shape, crystalline structure, anisotropy, or substrate configuration—can induce polarization-dependent optical responses. Moreover, interference between distinct plasmonic pathways can lead to a near-field distribution that is uniform (symmetric) at specific polarization angles and becomes asymmetric at others [105], [106], [107].

2.4 Conclusion

In this chapter, we explored light–matter interactions at the nanoscale with femtosecond temporal resolution, utilizing the PINEM technique to analyze near-field behavior surrounding nanomaterials. Despite employing a linearly polarized pump laser, the observed dipole orientations in some metallic nanoparticles (Au and Ag) were not strictly aligned with the laser's electric field direction.

A statistical comparison revealed that nanoparticles on silicon monoxide (SiO) substrates exhibited more frequent and pronounced deviations in dipole orientation than those on graphene. The interplay between defect-rich SiO substrates and nanoparticle surface characteristics critically shapes particle–substrate interactions. Localized surface charges arising from substrate defects influence adhesion and charge transfer, while the crystallographic facets of nanoparticles further modulate coupling through their unique atomic arrangements. These combined effects lead to selective binding, anisotropic behavior, and dipole misalignment in the near field, ultimately altering plasmon oscillation dynamics and broadening dipole orientation distributions observed on SiO surfaces.

A similar trend was observed for Ag nanoparticles on SiO. Angular distributions extracted from more than 100 Au nanoparticles on SiO yielded a Gaussian profile with a full width at half maximum (FWHM) of 19°, compared to 9° for those on graphene, underscoring graphene's suitability for near-field investigations via PINEM.

Additionally, varying the pump laser polarization revealed circular near-field distributions at specific angles (18°, 66°, 114°, and 162°), suggestive of a recurring angular periodicity of approximately π/4. To produce the circular pattern, two conditions must be met:

1) $|p_x| = |p_y|$,

2) A phase difference of exactly ±90° between p_x and p_y : $\frac{p_y}{p_x} = \pm i$.

Circular near-field patterns arise at specific angles where the amplitudes of p_x and p_y are equal and exhibit a phase difference of ±90°, thereby satisfying the necessary conditions for circular polarization. In summary, even achiral materials can exhibit chirality through geometric or excitation-induced asymmetries, resulting in polarization-dependent responses and near-field symmetry breaking via plasmonic interference. Furthermore, interference among distinct plasmonic pathways can give rise to a near-field distribution that exhibits symmetry at certain polarization angles, while becoming asymmetric at others.

3 Study of the high-pressure phase of Silicon (Si) using the Poly algorithm

3.1 Introduction

3.1.1 Background and Motivation

The rapid advancement of technology necessitates the development of new materials with enhanced properties. As a versatile material, Silicon emerges as a prominent candidate due to its extensive applications in electronics and various other industries. The distinct phases of silicon offer unique applications, prompting extensive efforts to synthesize these phases through a range of techniques, with a particular focus on the application of high pressure. Our understanding of the structure and properties of materials under high pressure has been largely enabled by diamond anvil cell experiments, which have provided insights into several material phase transitions and metastable states [108-110]. However, these devices are naturally limited by the strength of the diamond, resulting in a maximum achievable pressure of 640 GPa [111]. Recently, a new approach was developed to expose materials to pressure levels beyond the limit of the diamond anvil cell and preserve the high-pressure phases for further studies. The method is based on focusing high-energy ultrashort laser pulses inside the bulk of transparent material to induce a microexplosion in a confined geometry [112-114]. The creation of these phases presents a significant challenge in phase identification, as the affected region often consists of polymorphic nanomaterials with dimensions smaller than the resolution limit of X-ray diffraction (XRD). Although selected area electron diffraction (SAED) can capture diffraction patterns, the d-spacing information often exhibits ambiguity in phase determination, as individual Bragg spots may correspond to multiple phases. This chapter describes a new phase identification algorithm called Poly, intended for spotty selected-area electron diffraction patterns collected from polymorphic nanomaterials. We have developed this new approach to determine the predominant high-pressure phases produced in laser-shock-affected regions of Silicon.

3.1.2 Problem Statement and Research Objectives

Phase identification of nanomaterials, particularly polymorphs, is a challenging process with significant potential for error. The common approach in laboratories, XRD analysis, can not give reliable information due to several reasons. The size of the studying regions is small, and XRD averages the diffraction signal over the entire sample. In heterogeneous nanomaterials, where polymorphs exist in localized regions, XRD may fail to resolve these small-scale variations. Different polymorphs of the same material may have very similar crystal structures, resulting in overlapping diffraction peaks. Improving the quantitative phase analysis (QPA) of polymorphic nanomaterials requires developing new diffraction data analysis approaches. In 2015, Rapp et al. demonstrated the formation of novel silicon phases by irradiating silicon samples with ultrafast laser pulses [1]. The laser was focused beneath a transparent amorphous silicon dioxide (SiO_2) overlayer, which served to confine the resulting microexplosion and create voids in the sample. SAED analyses of the laser-modified regions confirmed the formation of multiple metastable silicon polymorphs. However, the corresponding d-spacing values exhibited significant overlap among several phases, leading to ambiguity in the phase identification of many Bragg reflections. For the laser-irradiated silicon, the volume near the void surface is polycrystalline and contains a mixture of high-pressure phases. Perhaps the most straightforward approach to perform QPA in this case is to azimuthally average the SAED pattern and input the data positions into Powder X-ray Diffraction Quantitative Phase Analysis (PXRD QPA) software. However, this reduces the information content of the pattern and is not able to distinguish the case when two phases have different unit cell symmetries but similar powder peak positions.

With this motivation, we have developed a new approach for phase identification of polymorphic materials from individual parallel-beam electron diffraction patterns like those routinely collected in SAED measurements. This leverages the correlations of angles between observed Bragg spots and those predicted from an assumed phase. It then scores this correlation in a spot-wise manner, which allows for QPA of patterns from mixed-phase polycrystalline samples.

3.1.3 Literature review

3.1.3.1 Silicon and its high-pressure phases

Silicon (Si) is the second most abundant element in the Earth's crust (approximately 27.7%), typically found in the form of silicon dioxide (SiO_2) in sand and rocks located in Group 14 (IV-A) of the periodic table with an electron configuration of $1s^2\ 2s^2\ 2p^6\ 3s^2\ 3p^2$. It is a metalloid, meaning it has properties of both metals and nonmetals. Silicon is situated in Period 3, in group 14, between carbon (C) and germanium (Ge). Its atomic number is 14, and it is known for its semiconducting properties, making it essential in electronics and material science. Si has a diamond cubic crystal structure, and its lattice constant is approximately 5.43 Å (angstroms) [115].

Table 3-1 The unit cell lattice parameters and Laue group of the silicon high-pressure phases, which are considered [116].

Phase	a (Å)	b (Å)	c (Å)	α	β	γ	Lauegroup	Crystal Family
β-Sn-Si	4.680	4.680	2.580	90°	90°	90°	$I4_1/amd$	Tetragonal
bc8-Si	6.658	6.658	6.658	90°	90°	90°	$m\bar{3}$	Cubic
hd-Si	3.850	3.850	6.364	90°	90°	120°	$P6_3/mmc$	Hexagonal
r8-Si	5.650	5.650	5.650	110°	110°	110°	R-3	Trigonal
VIII-Si	8.627	8.627	7.500	90°	90°	90°	$P4_12_12$	Tetragonal
IX-Si	7.482	7.482	3.856	90°	90°	90°	P_222	Tetragonal
bt8-Si	6.648	6.648	6.461	90°	90°	90°	4/m	Tetragonal
st12-Si	5.650	5.650	6.764	90°	90°	90°	4/mmm	Tetragonal
m32-Si	5.763	11.039	9.321	90°	79.98	90°	$P2_1/c$	Monoclinic
m32*-Si	9.390	13.305	6.626	90°	134.8	90°	$c2/m$	Monoclinic
t32-Si	9.408	9.408	6.646	90°	90°	90°	$P\bar{4}2_1c$	Tetragonal
t32*-Si	9.403	9.403	6.655	90°	90°	90°	$P4_32_12$	Tetragonal

During the decades, there have been attempts to calculate and produce the possible high-pressure phases of Si, and some of them have been achieved. Table 3.1 shows twelve phases of Si.

3.1.3.2 Microexplosion and other methods to create the high-pressure Si phases

In this approach, the laser energy is deposited into the bulk of transparent material in a very short time-scale < 1 ps (1 ps = 10^{-12} s), shorter than it can be dissipated by electronic heat conduction and electron-ion collision time. Deposition of only 1 μJ of laser pulse energy focused into a sub-micron-sized focal volume immediately leads to an energy density of 1 $\mathrm{MJ/cm^3}$ (1 $\mathrm{MJ/cm^3}$= 1 TPa), which is higher than the strength of any material. The following fast plasma-solid transformation promotes the formation of metastable phases, which can only be formed from the thermodynamically non-equilibrium high-entropy state of warm dense matter [1], [117]. Following the rapid heating of the confined sub-micron volume, a highly localized shock wave is created that expands and dissipates its energy into the bulk. At the front of the shock wave, pressures have been estimated to reach 10 TPa and temperatures above 10^5 K [1], [112,114]. This microexplosion is followed by highly non-equilibrium quenching conditions with ultrafast pressure release and ultra-high cooling rates (~10^{14} K/s), which gives access to novel material states in local free energy minima far from equilibrium. Such novel phases remain trapped in a localized region in the pristine crystal that preserves them for later characterization. In this way, laser-shock-affected areas are created, and new high-pressure phases have been studied [1,112,117]. For example, super-dense Aluminum has been formed from sapphire [117] and phase transformations in olivine ($(\mathrm{Fe,Mg})_2\mathrm{SiO_4}$) [118] have been reported using this approach.

In 2015, Rapp et al. produced new phases in silicon by irradiating samples with 170 fs laser pulses of 790 nm wavelength [1]. The laser was focused on a silicon surface buried under a transparent amorphous silicon dioxide (SiO_2) layer, which acted to confine the microexplosion. Selected area electron diffraction (SAED) measurements made on the affected area showed that the laser irradiation led to the formation of several new silicon metastable polymorphs. Laser fluences of 48 and 95 $\mathrm{J/cm^2}$ were found to result in the metastable phases of st12-Si and bt8-Si in the laser-shock-affected area, as well as an indication of the potential existence of two more new structures, namely, t32-Si and t32*-Si.

The presence of these phases was also confirmed by Raman spectroscopy conducted on similarly prepared samples [119]. This has been followed by theoretical studies of numerous other high-pressure phases [120,121]. Based on DFT simulations, the t32-Si phase can have a small quasi-direct band gap of 1.28 eV, which is useful in photovoltaic devices [122]. Therefore, producing new phases of Si, such as t32-Si and t32*-Si, and distinguishing them from other high-pressure silicon structures is potentially important for future energy applications.

3.1.3.3 Phase identification methods and algorithms in materials and nanomaterials

The challenge with performing quantitative phase analysis (QPA) of polymorphic nanomaterials using SAED measurements is that in many cases, patterns contain overlapping diffraction patterns produced from nanocrystalline phase mixtures. The common approach to identifying phases using SAED patterns is only suitable for single crystals, as it involves orienting crystals along a zone axis and comparing the measured pattern to that calculated from unit cell information [123-125]. Another common approach to perform QPA on nanocrystalline materials is to azimuthally average the SAED pattern and use software designed for powder diffraction to identify the observed peaks [126]. However, this reduces the information content of the pattern and is not able to distinguish the case when two phases have overlapping peak positions. Other approaches that have been reported to perform QPA on nanomaterials in a TEM include: studying the local Fourier transform of high-resolution images [127], correlating with dark field imaging to remove dominant phases , and using a series of precession diffraction measurements [128-130]. However, each of these methods has limitations on the sample crystallinity or requires specialized instrumentation. Meanwhile, SAED patterns contain rich information about the structure of the sample that can be collected using any TEM. Furthermore, the ability to disentangle the information in overlapping diffraction patterns resulting from polycrystalline materials has been recently demonstrated by the development of multiple crystal indexing algorithms for X-ray diffraction measurements, such as triplet methods [131-133], Grainspotter , and FELIX [134] .

3.1.3.4 Polycrystalline nanomaterials and ambiguity in phase identification

Nanomaterials are materials that have at least one dimension in the nanometric range. They exhibit unique physical and chemical properties due to their reduced grain size and increased surface area compared to bulk materials. Approaches such as bottom-up (e.g., chemical synthesis) or top-down (e.g., ball milling, microexplosion) are used to create nanomaterials, and most of these methods result in multiple small crystalline grains with random orientations. Therefore, these nanomaterials are called polycrystalline nanomaterials, as they are composed

of various grains with different nanocrystal orientations. [46,135]. Figure 3.1 illustrates the differences between polycrystalline nanomaterials, single crystals, and amorphous nanomaterials. In light of this, it is essential to use precise characterization methods in nanomaterial production. As discussed in the previous section, distinguishing the phase of polycrystalline nanomaterials is not straightforward. For example, in the case of a silicon (Si) sample irradiated with a laser using the microexplosion technique to create high-pressure phases of Si, Rapp et al. employed the SAED pattern of the region of interest [1].

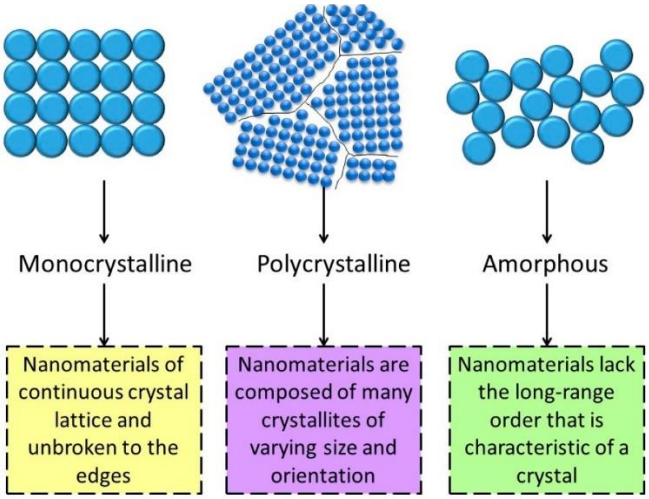

Figure 3-1 Nanomaterials Classifications based on their crystallinity [136]**.**

By analyzing the SAED pattern and the d-spacing information of the different phases of Si [137], they were able to correlate Bragg spots to specific phases. The problem arose when they observed that the d-spacing of certain Bragg spots corresponded to the d-spacing of multiple phases of Si, leading to ambiguity in phase identification. In simpler terms, when probing a region of polycrystalline nanomaterials, the analysis of the SAED pattern requires precise methods to reduce such ambiguities.

3.2 Methods

3.2.1 The details of the spot-wise phase identification algorithm: Poly

Our algorithm calculates a score for each observed diffraction spot reflecting its level of agreement with an assumed known phase. Its logic and organization follow the accumulation approach described by Morawiec for indexing and crystal orientation determination [138]. A flowchart of the data processing steps of the algorithm is shown in Figure 3.2. In step 1, the spots are found in the diffraction image using the approach detailed in section 3.2.4. The center of the pattern is found, and each spot position is transformed into a vector in reciprocal space in step 2, using the relationship

$$\boldsymbol{g_i} = [x_i/d\,,\ y_i/d\,,\ 0], \tag{3.1}$$

where x_i and y_i are the coordinates of the spot relative to the center in the image, and d is the pixel-to-reciprocal space conversion factor determined from detector distance calibration images. Then, a table of angles (γ_{ij}) between all pairs of **g** vectors ($\boldsymbol{g_i}, \boldsymbol{g_j}$)) is calculated.

Step 3 involves calculating the full set of reciprocal vectors, denoted by the variable ***h***, from an assumed crystal structure, using the following equation,

$$\boldsymbol{h} = h\boldsymbol{a}^* + k\boldsymbol{b}^* + l\boldsymbol{c}^*. \tag{3.2}$$

In this relationship, h, k, and l are the Miller indices, and **a***, **b***, and **c*** are reciprocal space basis vectors defined as:

$$\boldsymbol{a}^* = \frac{\boldsymbol{b}\times\boldsymbol{c}}{\boldsymbol{a}\cdot(\boldsymbol{b}\times\boldsymbol{c})};\ \boldsymbol{b}^* = \frac{\boldsymbol{c}\times\boldsymbol{a}}{\boldsymbol{a}\cdot(\boldsymbol{b}\times\boldsymbol{c})};\ \boldsymbol{c}^* = \frac{\boldsymbol{a}\times\boldsymbol{b}}{\boldsymbol{a}\cdot(\boldsymbol{b}\times\boldsymbol{c})}, \tag{3.3}$$

where a, b, and c are unit cell lattice vectors in real space. As a result, a list of all Bragg reflections having magnitudes up to a cut-off defined by the experimental SAED limit is generated. The forbidden reflections are removed from the list based on the space group of the associated phase. In our case, it was not necessary to include spots arising from dynamic diffraction, as we are studying small domains of high-pressure silicon phases in a deformed area of the silicon substrate. However, this framework allows dynamic diffraction spots to be included in this spot vector list generation step. Then, in step 4, the full list of reciprocal vectors is grouped according to families. A family is defined as a set of reciprocal vectors that are related by the symmetry

operations of the Laue group, irrespective of their magnitudes [138]. For example in the case of the phase t32-Si which is tetragonal with $P\bar{4}2_1c$ Laue group [139], only considering the vector $[100]$ and space group operators: xyz and $y\bar{x}\bar{z}$, a family is generated composed of the vectors $[100]$, $[010]$, $[0\bar{1}0]$, $[\bar{1}00]$, and any parallel vectors like [n00] and [0n0], where n is an integer. In step 5, all angles between h vectors are calculated. These angles (η_{mn}) are indexed according to the associated families m and n. Then, duplicate angles with the same family indices are removed, resulting in a list of unique angles between pairs of families.

In step 6, we identify potential ***h*** vectors for an observed ***g*** by comparing their magnitudes following

$$|h - g| < \varepsilon_1, \tag{3.4}$$

where ε_1 is a user-defined threshold. Then, the pairs of g vectors are selected and the list of angles between potential ***h*** vectors η_{mn} is compared to the angle γ_{ij} using the relationship

$$\left|\eta_{mn} - \gamma_{ij}\right| < \varepsilon_2, \tag{3.5}$$

where ε_2 is a separately defined threshold for angles. We estimated these threshold parameters from the width of a Gaussian fit to the observed Bragg spots, as is explained in section 3.3.2 for experimental data.

In step 7, a vote table is generated with votes for g vectors organized in rows and those for families organized in columns. If Equation (3.5) is satisfied, a vote is added to the table elements with indices (i,m), (i,n), (j,m), and (j,n). In this manner, votes are accumulated in the table considering all pairs of g vectors and potential families. Then, in step 8, the highest score for each g vector is selected and saved for later comparison. This also identifies the reflection families that correlate the most with the observed g vector.

To validate the calculated score, the algorithm conducts a null hypothesis test in step 9 to determine if the score is similar to that from a set of random spots without any crystallographic relationship. The parameters for this test were determined by generating a set of diffraction patterns with random spot positions, and then using poly to calculate the average (M) and standard deviation (Δ) of spot scores in the random data set for an assumed phase. These values were normalized by the number of spots in the pattern to allow for later comparison with an experimental score. Then, a k-score was calculated from the experimental scores as follows:

$$k = \frac{|\bar{x} - M|}{\Delta}, \tag{3.6}$$

Where $\bar{x}$ is the score of a spot from step 8 divided by the number of spots in the pattern. If the k-score of a spot is greater than 2, we reject the null hypothesis and consider the score further in the analysis. After applying this k-value filter to all scores, the final scores of a spot for different phases are compared.

This comparison is done in a spot-wise manner, allowing for the poly algorithm to identify diffraction patterns containing multiple crystals of different phases. In the next section, the performance of this algorithm is demonstrated on simulated patterns for multiple crystals in random orientations.

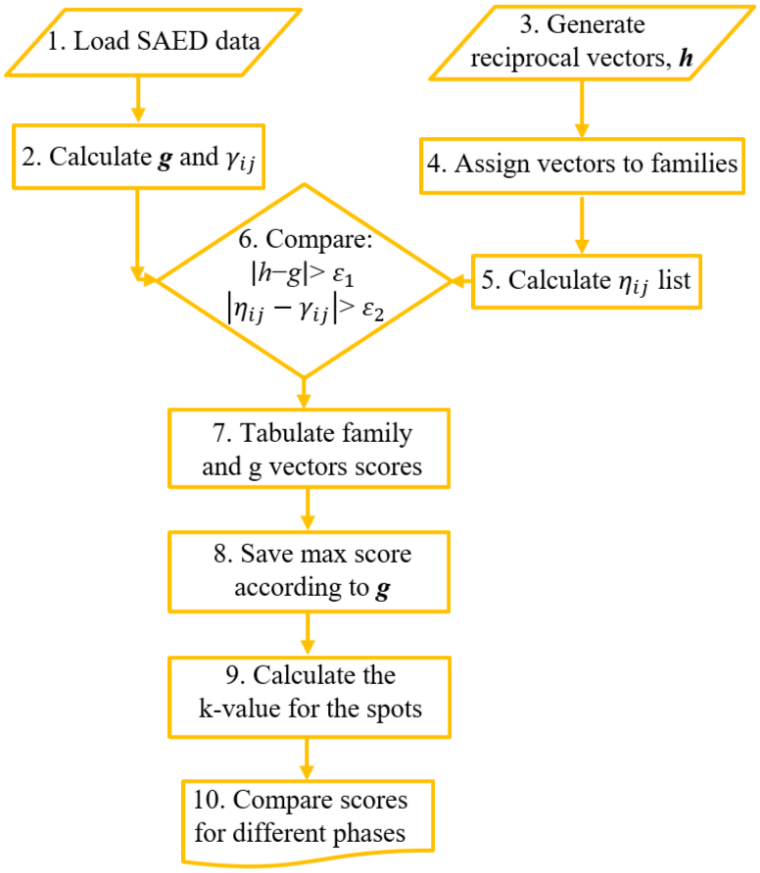

Figure 3-2 Flowchart of the phase identification algorithm, Poly.

3.2.2 Simulation methods of diffraction patterns, specifically, Si

To evaluate the accuracy of the phase identification program Poly, we generated simulated diffraction patterns following the workflow outlined in Figure 3.3. In Step 1, for a specific phase of Si, we use Laue group reflection conditions to identify the allowed Miller indices (hkl). For example, Equation (3.7) shows the conditions for the phase Si-bt8 [140].

$$\begin{aligned} &hkl: h+k+l=2n \\ &0kl: k+l=2n \\ &h0l: h+l=2n \\ &hk0: h,k=2n \\ &h00: h=2n \\ &0k0: k=2n \\ &00l: l=4n \end{aligned} \tag{3.7}$$

In Step 2, using the lattice parameters of the given phase and Equation 3.2, we calculate the magnitude of the reciprocal space vector for each (hkl) value.

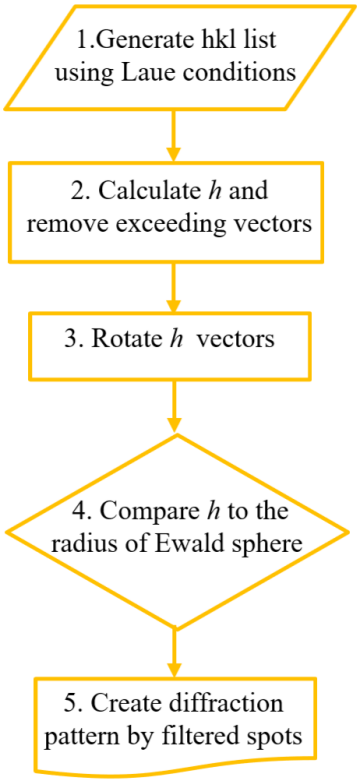

Figure 3-3 Flowchart of the diffraction simulation algorithm

As we focus on a specific region of the diffraction pattern if a magnitude of a vector exceeds the determined value, we remove the relevant hkl values from the list. To ensure the simulated

diffraction pattern resembles the experimental one, in step 3, we apply Euler's three-dimensional rotation Equations [141] to rotate the vector, generating diffraction patterns along the zone axis, off-zone axis, or other orientations.

$$R_x = \begin{bmatrix} 1 & 0 & 0 \\ 0 & \cos\theta & -sin\theta \\ 0 & \sin\theta & cos\theta \end{bmatrix},$$

$$R_y = \begin{bmatrix} cos\varphi & 0 & sin\varphi \\ 0 & 1 & 0 \\ -sin\varphi & 0 & cos\varphi \end{bmatrix} \quad (3.8)$$

$$R_z = \begin{bmatrix} cos\psi & 0 & cos\psi \\ cos\psi & -sin\psi & 0 \\ 0 & 0 & 1 \end{bmatrix}$$

After generating and selecting the reciprocal space vectors, in step 4 we compare their magnitudes to the radius of the Ewald sphere (1/λ) ,[142] which, in our case, corresponds to an electron wavelength of 0.0025 nm for a 200 keV electron beam in the TEM. Finally, in step 5, the Bragg spots whose reciprocal vectors intersect the Ewald sphere form the simulated diffraction pattern.

3.2.3 SAED patterns of the Silicon sample irradiated by laser (microexplosion)

To synthesize high-pressure phases of silicon, Rapp et al. [1] employed the microexplosion method, followed by focused ion beam (FIB) milling to prepare the samples for transmission electron microscopy (TEM) analysis, as illustrated in Figure 3.4. Selected area electron diffraction (SAED) patterns were then acquired using TEM. Representative patterns, shown in Figures 3.5 to 3.7, were collected from different regions of the sample and at various time intervals. For instance, patterns 901, 679, 759, and 864 were recorded after 34, 48, 78, and 92 days, respectively. The temporal evolution of the sample's structure is analyzed and discussed in detail in Section 3.3.3.

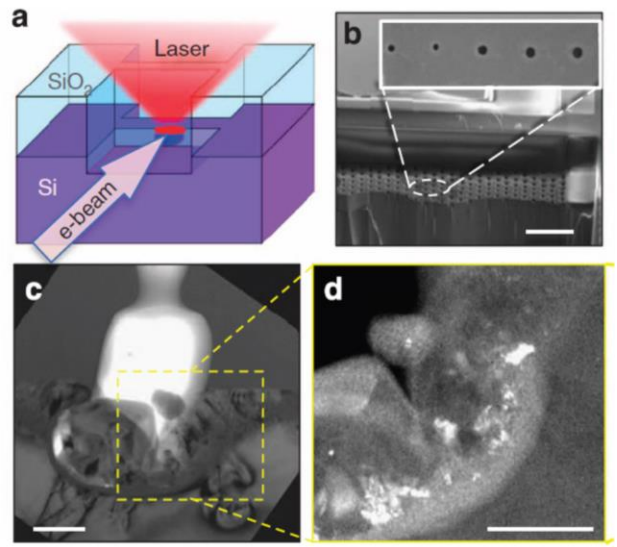

Figure 3-4 a. Schematic picture for microexploitation technique on Si b. SEM image of the sample c. affected area d. the area which contains high-pressure phases of Si [1]**.**

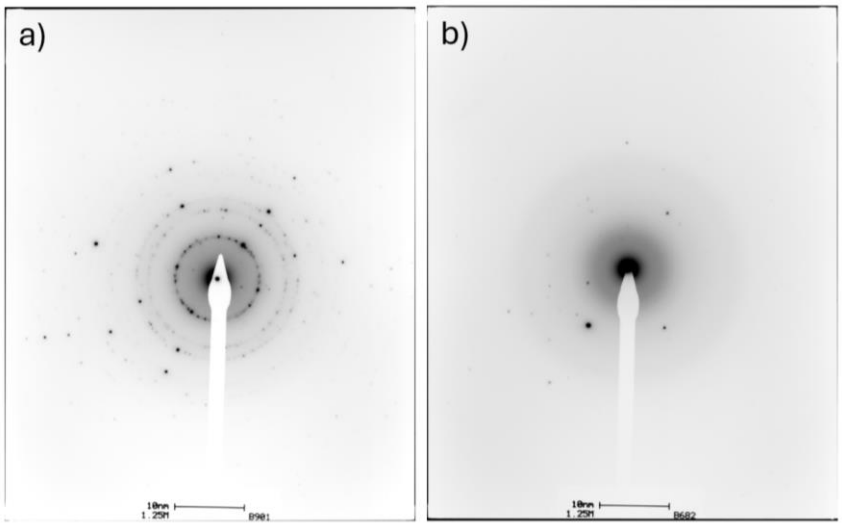

Figure 3-5 SAED of the Si sample labeled 901 and 682.

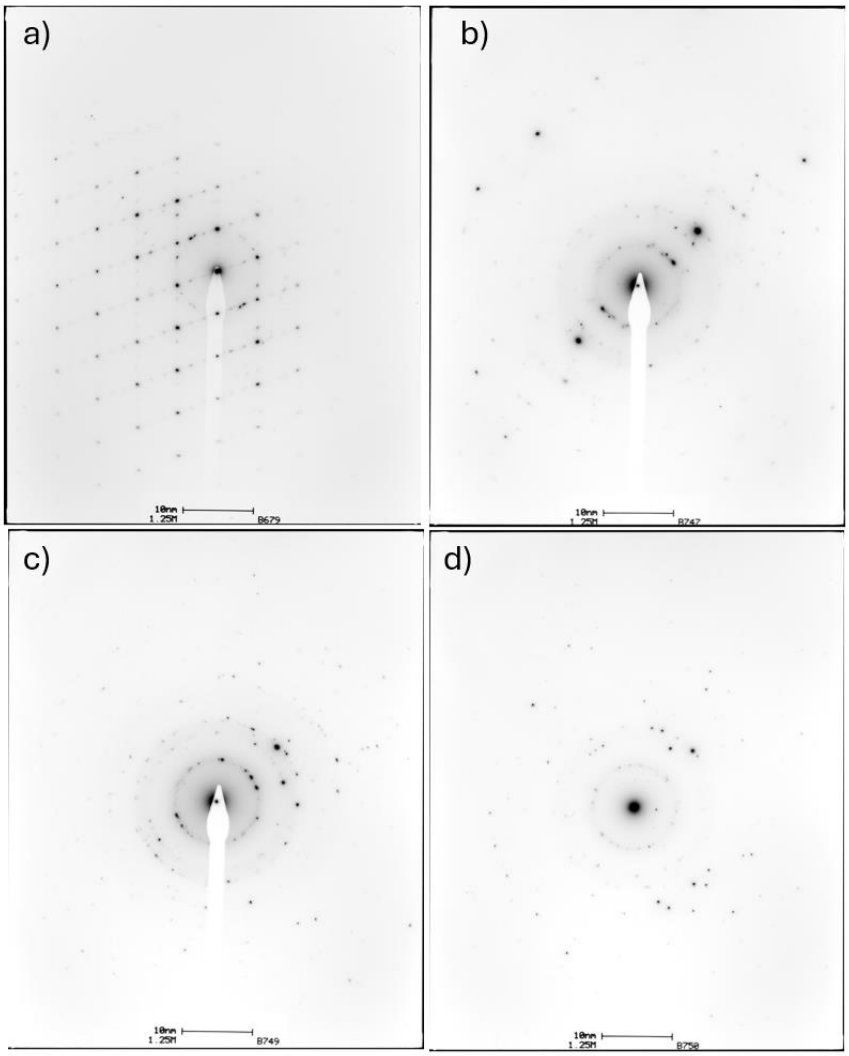

Figure 3-6 SAED of the Si sample labeled 679, 747, 749, and 750.

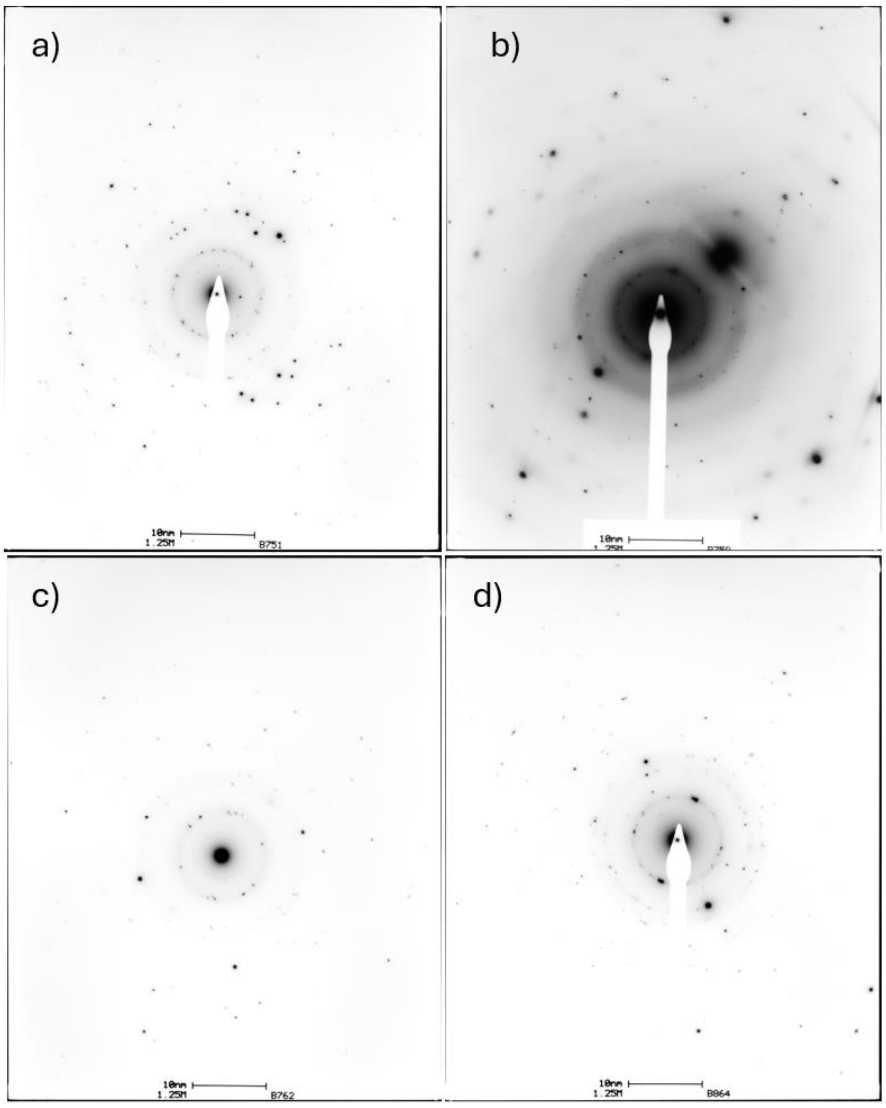

Figure 3-7 SAED of the Si sample labeled 751,759,762, and 864.

3.2.4 Spot-finding process for SAED pattern

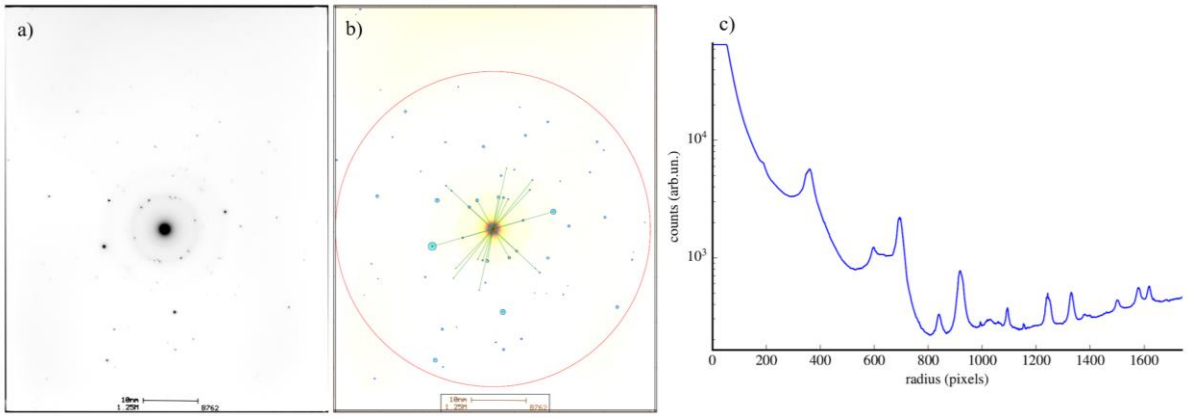

Figure 3-8 a) A typical SAED pattern. b) The algorithm found spots (light blue), pairs (connected by green lines), and the reciprocal space origin (red cross). c) The radial profile of the scattered intensity was obtained employing the calculated reciprocal space origin. The integrated region corresponds to the area enclosed by the red circle in Figure 3.8b.

Here we describe the spot-finder algorithm that was used to process the measured SAED images. It served to identify the diffraction spots and measure attributes like their size, circularity, and location. After loading an SAED image, like that shown in Figure 3.8a, preprocessing was performed using routines from the Open Source Computer Vision Library (OpenCV) [143]. To reduce sharp intensity fluctuations, a Gaussian filter operation was performed using the Gaussian Blur function of OpenCV with a kernel size of 5×5 pixels and σ = 1.1. The region in the black rectangles in Figure 3.8b was excluded from the image.

Then, intensity thresholding was performed to create a binary image that was used to identify candidate spots. Local adaptive thresholding was applied to overcome the large change in background level found in the image as a function of distance from the center. As seen in Figure 3.8c, the background was found to change by more than an order of magnitude across the image. To account for this, the OpenCV adaptive threshold function was used, assuming a threshold value of $\mu - 10$ where μ is the mean intensity over a given region of 751×751 pixels. Then, to remove thin-intensity clusters, morphological erosion was performed with a kernel size of 5×5 pixels.

The next step was spot finding, which started with processing the binary image. A spot was defined as a group of bright connected pixels satisfying the following size and shape criterion: the size condition was defined as a minimum of 10 pixels and a maximum of half the number of pixels

defining the image width, while for the shape the number of pixels along one direction must be less than twice the number along the other. For pixels at the coordinates $\boldsymbol{p}_i = (x_i, y_i)$ with the intensity values (Ii), the integrated intensity (I) and the center of the intensity ($\boldsymbol{p}_c$), were defined following

$$I = \sum_i I_i, \tag{3.9}$$

$$\boldsymbol{p}_c = \sum_i I_i \boldsymbol{p}_i \tag{3.10}$$

where I and $\boldsymbol{p}_c$ are integrated and the center of the intensity respectively and the summations run over each pixel in the cluster. The moment of inertia (k_c) relative to the center of intensity and the circularity (γ) of the data were respectively expressed as

$$k_c = \sum_i I_i \ \ \|\boldsymbol{p}_i - \boldsymbol{p}_c\|^2, \tag{3.11}$$

$$\gamma = 1 - \frac{\sum_{i \notin C} I_i}{\sum_{i \in C} I_i} \tag{3.12}$$

where the circularity is related to the likeness of intensity distribution and a circle of radius $r = \sqrt{I/\pi}$.

After finding the spots in the SAED pattern, the last step was the identification of the reciprocal space origin. The first guess of the center position was found by calculating the center of mass of the spots that were more than 10% away from the center of the image. The center of the diffraction pattern was then refined by looking for Friedel pairs in the image. Pairs were found by starting from a spot at pi then searching for a spot within a circle at $(-x_i, -y_i)$ with a radius of 5 pixels. If a spot was found to fall within the projected circle, it was documented as a pair of the spot at pi.

The statistical weight of each pair was defined according to different considerations that are summarized in Table 3.2. If the spot belonged to more than one pair because of peak splitting, the pair was deleted. Otherwise, the weight was given by the sum of the value calculated according to each row in the table. Once the weighting scheme was defined, the reciprocal space origin was located by performing a weighted average of each pair's mean position, $\overline{\boldsymbol{p}_n}$:

$$\boldsymbol{p}_O = \frac{\sum_n w_n \overline{\boldsymbol{p}_n}}{\sum_n w_n}. \tag{3.13}$$

Finally, the spot list was created, defining the position with respect to p_O, the integrated intensity and the circularity. Weighting schemes are detailed in Table A2.

Table 3-2 Weighting scheme. Different features contributing to the definition of the weighting scheme are obtained as the sum of the values in each row of the second column.

	Attribute	Definition
1	pairs lying on parallel lines	w = 1
2	integrated intensity similarity	w = min$\{l_0, l_1\}$/max$\{l_0, l_1\}$
3	average circularity	W=$(\gamma_0 + \gamma_1)/2$

3.3 Results and Discussions

3.3.1 Testing Poly on simulated diffraction patterns of Si

We simulated SAED patterns of the bt8-Si and st12-Si phases, which have distinct unit cells and space groups (Table 3.1), yet have many similar Bragg peak scattering vector magnitudes, which makes identification by existing approaches challenging. The pattern simulation proceeded by generating a list of allowed ***h*** vectors following Equation (3.2) and considering the ***h*** vectors with magnitudes less than 6 1/nm. This value maintains enough simulated Bragg spots for analysis, optimizing the operation time for the Poly. It also covers the same diffraction spots analyzed in the experimental data by Rapp et al. Then, a different orientation was created by rotating the h vectors according to a random set of Euler angles. The pattern was generated by finding all h vectors that satisfied the Ewald sphere condition, considering a wavelength of 0.0025 nm, corresponding to 200 keV electrons. An incident vector $\boldsymbol{S_0}$ with a form of [0,0, $1/\lambda$] was defined. Then, the magnitude of the vector S=h-$\boldsymbol{S_0}$ was compared to the Ewald sphere radius using

$$|S - 1/\lambda| < \varepsilon_3, \tag{3.14}$$

where ε_3 is a user-defined threshold assumed to be $2\pi/100\ \mathrm{nm} = 0.063$ 1/nm. This value was determined by comparing the number of spots in simulated patterns to that found in the later experimental measurements. The patterns, including more than 10 Bragg spots, were kept for

later analysis. The intensities of Bragg spots were not calculated because they are not considered in the poly algorithm.

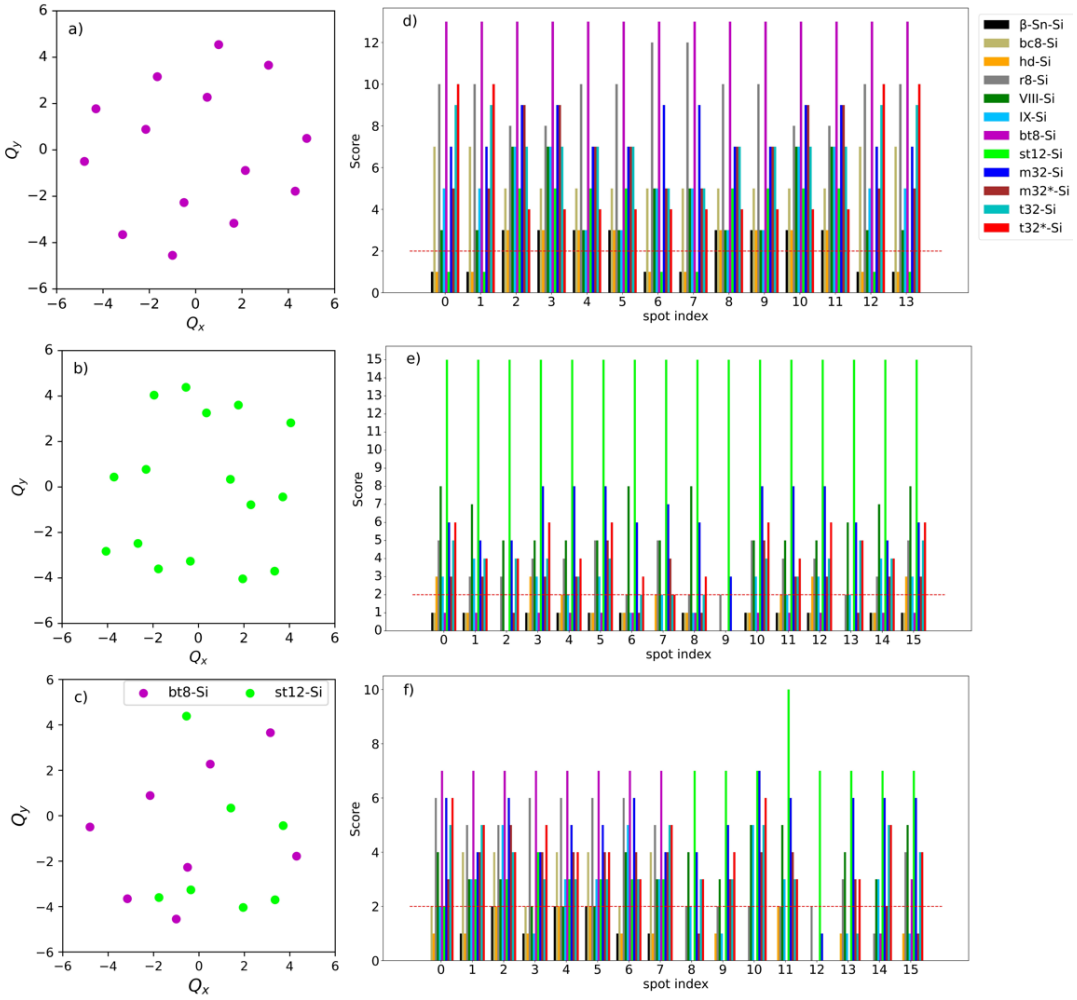

Figure 3-9 Simulated SAED patterns are shown for a) a randomly oriented bt8-Si crystal and b) a randomly oriented st12-Si crystal. c) – A mixed-phase SAED pattern was simulated using a selection of spots from those in a) and b). d-f) Spot-wise similarity scores are compared assuming twelve Si phases in the shown diffraction patterns when analyzing the patterns (a-c) with the poly algorithm. The spots are colored according to the related phase with the highest scores.

Figure 3.9a shows an example simulated SAED pattern for the bt8-Si phase. The poly algorithm described in the preceding section was first used to calculate similarity scores for the spots, assuming the known phase, the results of which are shown as violet bars in Figure 3.9d. The assumed values for the thresholds in Equations (3.4) and 3.5 were ε_1=0.1 1/nm and ε_2 = 0.2°. Then the scores from the set of eleven candidate high-pressure phases of Si were considered, which are compared in the bar chart in Figure 3.9d. The lattice parameters and space groups

assumed for each phase are listed in Table 3.1. The highest scores were used to color the spots in Figure 3.9a. As shown in the color bar, a higher score for bt8-Si is indicated by violet spots, while a better agreement with st12-Si is shown in green.

In general, for a pattern of N spots, a spot can have N-1 angles with others, and therefore the highest score possible for a spot is N-1. This value indicates that all angles with other spots agree with the assumed structure. For Figure 3.9a, 14 spots were simulated, and all spots obtained the theoretical maximum score of 13 when assuming the bt8-Si phase, which affirms the accuracy of the Poly algorithm. When other phases were assumed, lower scores were found, which shows that Poly correctly identifies the phase of the spots.

An example pattern simulated for the st12-Si phase is shown in Figure 3.9b and was analyzed using Poly, assuming st12-Si and the other eleven phases of Si as before. The scores are plotted in Figure 3.9e. Again, in this case, the theoretical limit score of 15 was achieved when the st12-Si phase was assumed. The scores for st12-Si were found to be significantly higher than others, showing less ambiguity in the phase identification. Therefore, the Poly algorithm also shows good efficiency in phase identification for the case of st12-Si.

To simulate an SAED pattern of a polycrystalline sample, we then randomly selected some spots from the two patterns in Figure 3.9a and Figure 3.9b and merged them into a single pattern in Figure 3.9c. This was then analyzed as before, and the scores are shown in Figure 3.9f. Spots with indices from 0 to 7 were taken from the bt8-Si pattern, while those from 8 to 15 were taken from the st12-Si. In Figure 3.9f, it is seen that each spot was correctly identified by receiving a higher relative score for the phase that matches the originally simulated pattern. Figure 3.9c visually indicates the ability of the algorithm to identify the phase of the spots in this polycrystalline-like pattern.

These results show that Poly has a good capability of identifying a specific phase of Si from others. Furthermore, it works in a spot-wise manner and can correctly classify spots into different phases, which is applicable to polymorphic samples. One drawback of the Poly algorithm is that it requires a predefined unit cell. However, we have found that slight deviations, which may be caused by defects and strain, can be accommodated by adjusting the threshold parameters $\varepsilon 1$ and $\varepsilon 2$. Finally, the algorithm will not work in the case of identifying spots from phases with similar lattice constants and space groups. This case is expected to lead to similar scores for those phases because of equivalent d-spacing and angular relationships. Simulations like those presented can be used to test if multiple phases in the list of candidates are distinguishable by the algorithm. Still, in the event of a spot receiving similar high scores for multiple phases, we have found it is

best to regard this as a subset of potential matches and compare this subset to how the scores are distributed for other spots in the pattern. As will be shown, this approach serves to significantly reduce the list of candidates and identify dominant phases in a SAED pattern.

3.3.2 Data treatment results for the Si sample irradiated by laser

To analyze a diffraction pattern, at first, the film-recorded diffraction pattern was digitized, and then the spots were found in the pattern using the algorithm detailed in section 3.2.4 (Spot-finding process for SAED pattern). The locations of the found spots are shown as red circles overlaid with the diffraction pattern shown in Figure 3.10a. The center of the diffraction pattern was refined using Friedel pairs in the found spot list and by determining the intersection of lines connecting them. Then, the detector distance was refined using a histogram of spot vector magnitudes and by identifying the first three major peaks as the first diffraction rings of the low-pressure silicon diamond cubic structure. This was used to transform the spot list into reciprocal space coordinates, resulting in the g vectors plotted as the blue dots in Figure 3.10b.

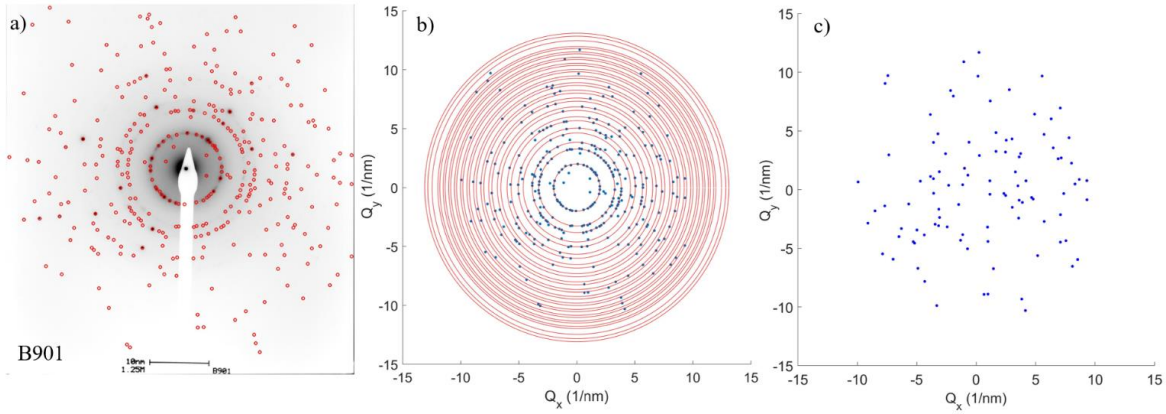

Figure 3-10 a) Experimental SAED pattern of the Si sample that was irradiated by the laser. Detected spots are shown by red circles. b) Detected spots are overlaid by the diffraction rings corresponding to the cubic phase of Si. c) The spots remaining after filtering out the cubic phase of Si are shown.

To calculate the uncertainty in the locations of spots in the SAED pattern, we used a two-dimensional Gaussian fit for each spot so that the standard deviation of the fit provided the uncertainty in the x and y coordinates of the spots. Using these values, the uncertainties in the angles between pairs of spots were calculated. The values for the uncertainty in angles are in the order of 0.2°, therefore, we defined the threshold $\varepsilon_2 = 0.2°$ for the following reported analysis.

After finding the location and uncertainty for each spot, we removed the spots that were found to have a scattering vector magnitude (g) that agreed with the cubic phase of Si. The result of filtering is shown in Figure 3.10c. Spots with g < 6 1/nm were considered for further analysis. This spot list was then analyzed using Poly, assuming the high-pressure phases described in Table 3.1.In the next section, the results of the analysis for pattern b901 are presented in Figures 3.11a to 3.11e and summarized in Table 1.

3.3.3 Phase identification of Si sample using Poly

We used Poly to analyze a dataset of 10 SAED patterns measured from different affected regions around voids created with an incident laser fluences of either 48 or 95 J/cm2. Samples were prepared by a focused-ion beam to produce thin cross-sections of the voids suitable for TEM measurements. The time between the focused-ion beam sample preparation and the SAED measurement also varied between 34 to 94 days, which we will refer to as the “measurement delay”. Figure 3.11 shows the results of analysis for four patterns that were found to have a significant number of spots that could be identified by the algorithm. The spots in the diffraction patterns are color-coded in Figures 3.11a-d according to the phase that achieved the highest score for each spot, while the full score distributions are shown in the bar chart in Figures 3.11e-h. The red line in the score distribution indicates a similarity score threshold that was introduced to identify spots that did not seem to have a significant agreement with any phase. If the spot received a score less than this threshold, it was designated as a poor match and shown as empty circles in the patterns. A list of experimental parameters and the number of spots matching each of the high-pressure silicon phases are given in Table 3.3. The patterns measured with a SAED measurement delay of less than 50 days (b901 and b679) were found to predominantly have spots that had the highest similarity score to the t32-Si and t32*-Si phases. As seen in the score distributions, the poly algorithm attributed similar scores for each of these phases. This is because the unit cell parameters are very similar (Table 3.1), making it hard for poly to distinguish between them. Interestingly, a higher number of t32-Si and t32*-Si spots were found in b679 than in b901. This seems to correlate with the laser fluence used for void creation, as the fluence for b679 was 95 $\mathrm{J/cm^2}$, while that of b901 was 48 $\mathrm{J/cm^2}$.

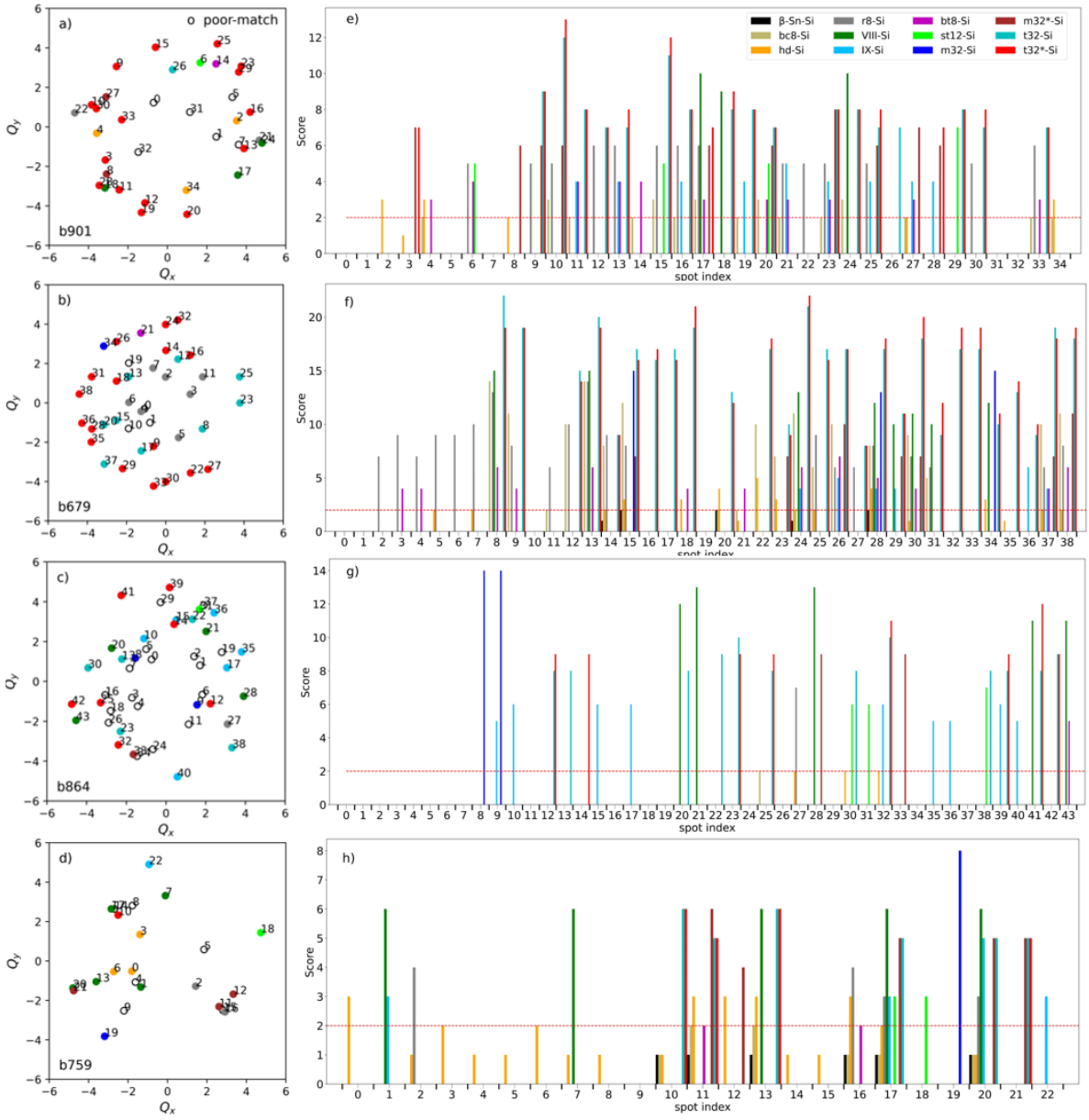

Figure 3-11 The experimental SAED patterns of the Si samples were extracted from Figure 3c for pattern a and from other patterns in b-d, considering g < 6 1/nm, and were analyzed by g and γ_{ij} information using the poly algorithm. The spots in a-d are colored according to the highest scores in the e-h bars. The empty black spots achieved scores less than the similarity threshold for Si phases. In e-h spot-wise similarity scores, assuming the Si phases in the analysis are compared. The threshold score of 2 is shown as a red dashed line.

Then, it appears that a higher laser fluence increases the fraction of the t32-Si phases created in the shock-affected region of the sample. Spots in these patterns assigned to other high-pressure phases were found in a significantly lower abundance. The phase r8-Si was found in both cases, while the hd-Si and VIII-Si phases were assigned to a few spots in the lower laser fluence

measurement (b901). The original analysis by Rapp et al focused on the presence of the bt8-Si and st12-Si; however, the poly algorithm only found a few spots that matched with these phases. This difference is not surprising, as the original analysis only considered the spot scattering vector magnitude and did not consider the angular correlations as in the present approach. Furthermore, it focused on a few spots closest to the center of the pattern because the phase identification of the spots further from the center became increasingly ambiguous.

Table 3-3 Experimental and analyzed data of four patterns of the Si sample irradiated by a laser.

SAED pattern ID	**b901**	**b679**	**b759**	**b864**
Laser Fluence (J/cm^2)	48	95	95	95
Measurement Delay (day)	34	48	78	92
N of spots	35	39	23	44
hd-Si spots	3 (8%)	0	3(13%)	0
r8-Si spots	2 (6%)	7(18%)	2(9%)	1(2%)
VIII-Si spots	3 (8%)	0	5(22%)	4(9%)
IX-Si spots	0	0	1(4%)	6(14%)
bt8-Si spots	1 (3%)	1(3%)	0	0
st12-Si spots	1 (3%)	0	1(4%)	1(2%)
m32-Si spots	0	1(3%)	1(4%)	2(4%)
m32*-Si spots	2 (6%)	0	3(13%)	1(2%)
t32-Si spots	1 (3%)	9(23%)	0	5(12%)
t32*-Si spots	16(46%)	17(43%)	1(4%)	7(16%)
Poor Match	6 (17%)	4(10%)	6(27%)	17(39%)

Our present analysis does not exclude the presence of the st12-Si and bt8-Si in the sample, as a few spots were indeed identified in the patterns and reasonable scores for these phases are found in the distributions shown in Figure 3.11e and Figure 3.11f. Instead, our analysis suggests that the t32-Si and t32*-Si phases seem to be more abundant in the sample.

The different measurement delays of the patterns in the dataset have also allowed us to study the evolution of the stability of the high-pressure phase created in the affected region of the laser shock volume. Creating the cross-section and thinning the sample near the void removes residual stress and promotes the relaxation of the high-pressure phase to lower-pressure phases. To study this process, Figure 3.12 contains a plot of the fraction of spots identified for each phase versus the measurement delay. It is observed that the number of spots in phase t32/t32*-Si, shown in red and green colors, is decreasing over time. This reduction also occurs in phase r8-Si, albeit with a less steep decline. Based on these analyses, the relaxation time for phases t32/t32*- Si and r8-Si is estimated to be between 50 and 70 days. Conversely, the situation differs for phase XI-Si, with an increase in specified spots from 0% to 14%, suggesting that it is a by-product of the t32/t32*-Si phase relaxation.

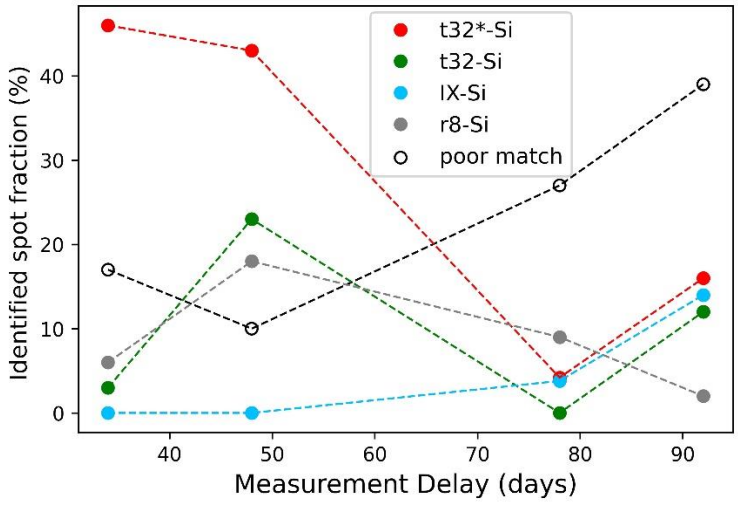

Figure 3-12 The fractions of spots attributed to the phases of silicon found to dominate the patterns shown in Figure 4 are plotted as a function of the delay between the FIB preparation and SAED measurement of each pattern.

It is noteworthy that over time, the occurrence of spots in poor matches is also increasing. While the precise cause is unclear, it could be attributed to an unidentified phase or a lack of sufficient spots in diffraction due to a small crystal size. Another potential explanation is an increased

heterogeneity in the sample microstructure. In poly, the scores of spots depend on the number of spots (N) in a specific phase. If the variety of phases in a region increases, the scores decrease, and the probability of poor matches grows. To achieve more detailed insights in these cases, we plan to conduct nanobeam diffraction experiments to study the performance of poly on smaller affected volumes, which is expected to reduce the number of existing phases in the area and increase the relative scores.

3.3.4 Supplementary Analysis of Poly: Finding the limitations of Poly using different mixtures of phases in simulated polycrystalline diffraction patterns

By testing poly using simulated diffraction patterns, it was shown to work correctly. However, the question remains: under what circumstances could it fail? To address this, we designed three additional tests. In this section, we classify the tests into three groups. First, we examine Poly's accuracy in cases where a phase has fewer Bragg spots. We begin with a mixture of two phases and, at each step, remove some spots from one phase to determine if poly can still identify these spots. Second, we add spots from simulated diffraction patterns corresponding to different orientations of another phase into the mixture until Poly can no longer distinguish between the phases. Third, in each step, we add a simulated diffraction pattern from different phases of Si to determine the point at which Poly fails to identify the phases.

3.3.4.1 Diffraction spot limit: A mixture of the phases Si-t32 and Si-st12, then removing spots from the Si-t32 pattern.

To perform the first test on Poly, we used the simulation steps described in the previous section to generate Bragg spots for the Si-t32 phase. Figure 3.13a shows the simulated SAED pattern containing 20 spots, labeled 0 to 19. Next, we followed the same procedure to simulate 13 spots for the Si-st12 phase, shown in Figure 3.13b. Finally, we combined these two patterns to create a polycrystalline-like pattern, shown in Figure 3.13c, where Si-t32 spots are colored blue and Si-st12 spots are colored red.

Figure 3.13d presents the scores analyzed by Poly for the pattern in Figure 3.13a. As expected, Poly assigned the highest scores to the Si-t32 phase. The score level reaches 19, consistent with the N-1 rule for 20 spots. For the pattern in Figure 3.13b, the scores are plotted in Figure 3.13e, confirming that the spots were correctly assigned to the Si-st12 phase.

The analysis of the combined pattern in Figure 3.13 c is shown in Figure 3.13 f, demonstrating Poly's ability to distinguish spots originating from the Si-t32 and Si-st12 phases. After confirming Poly's capability to handle this mixture, we began removing spots from the target phase (Si-t32) to determine the threshold at which Poly fails to accurately identify the phases.

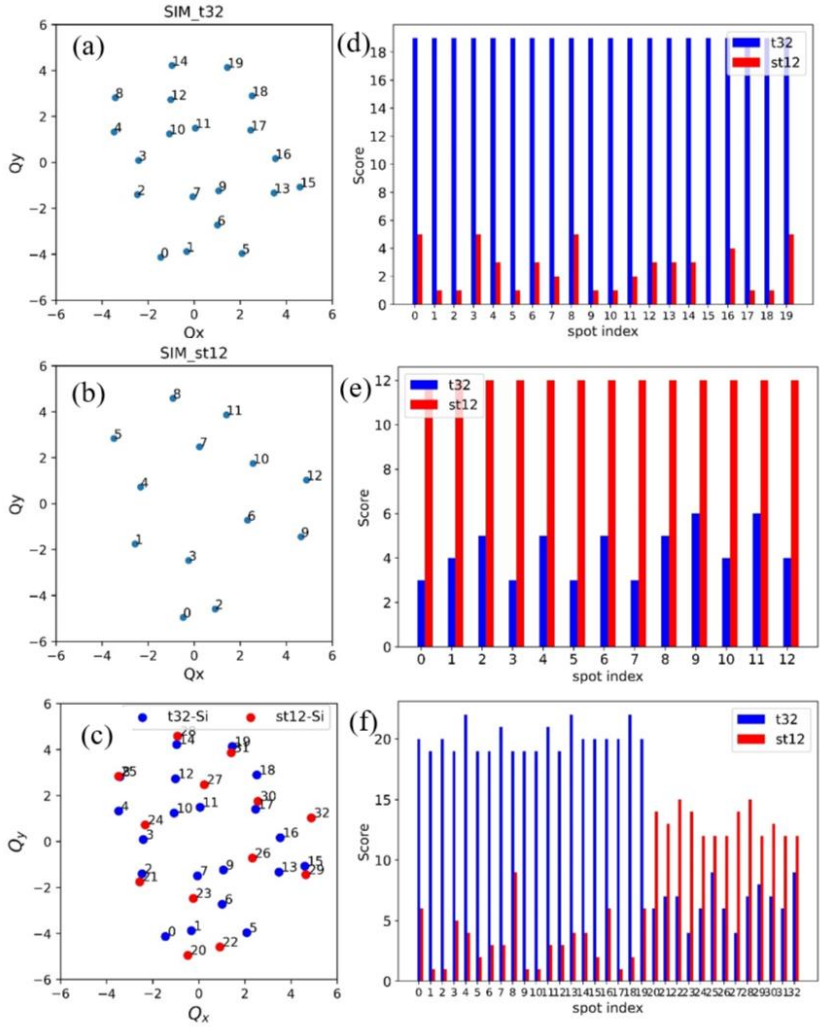

Figure 3-13 A simulated SAED pattern for the Si-t32 phase, which contains 19 Bragg spots. b) A simulated SAED pattern for the Si-st12 phase, which contains 12 Bragg spots. C) The mixture of spots parts a and b. d,e) scores of spots for the phases Si-t32 and Si-st12 achieved by poly. f) scores of spots for the phases Si-t32 and Si-st12 for the mixed pattern achieved by poly.

The results of the Poly analysis for the spot removal procedure are shown in Figure 3.14, where part a represents the initial pattern used for the analysis. It contains 32 spots—20 spots labeled 0 to 19 belong to the Si-t32 phase (colored in blue), while 13 spots labeled 20 to 32 correspond to the Si-st12 phase (colored in red).

In Figure 3.14 b, the scores given by Poly illustrate the phase identification between Si-t32 and Si-st12. The scores for Si-t32 are generally expected to be around 19, following the N-1 rule, where N is the number of spots. However, some spots, such as spot 3, exceed a score of 19 and reach 22. This occurs because certain Si-st12 spots are positioned very close to Si-t32 spots, satisfying the vector conditions for magnitude and angle, which allows them to be mistakenly identified as Si-t32 spots. This is not a critical issue, as these spots would still be considered part of the Si-t32 phase even with slightly lower scores.

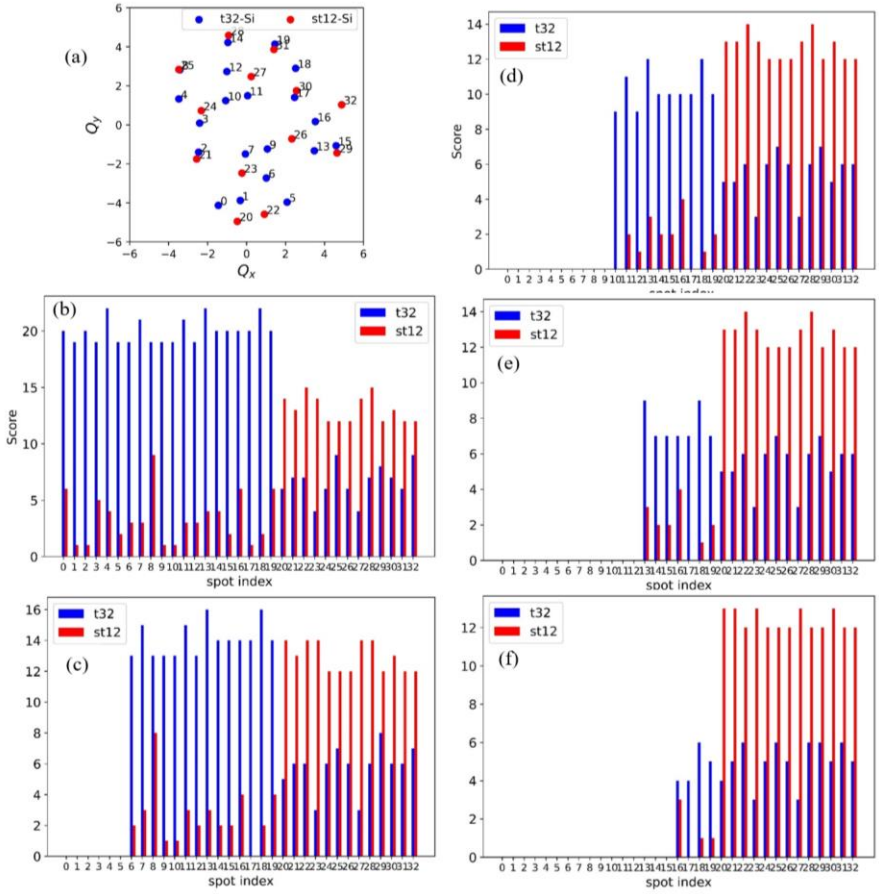

Figure 3-14 a)The mixture of spots same as figure c. In each step, some spots are removed, and poly is used to calculate the scores. b) scores for 32 spots showing that 20 blue spots belong to the Si-t32 phase and 13 belong to Si-st12. c) scores after removing the spots labeled 0 to 5 d) scores after removing the spots labeled 0 to 9 e) scores after removing the spots labeled 0 to 12 f) scores after removing the spots labeled 0 to 15.

Next, we removed six spots (0 to 5) from the Si-t32 phase. The result is shown in Figure3.14 c. It is clear that Poly still identifies both phases; however, some changes have occurred. The scores for the Si-t32 spots have decreased due to the reduced number of spots. Additionally, there is a

slight change (by one score) in the Si-st12 scores, which may be related to the removal of the Si-t32 spots.

In the algorithm, a score table is generated by accumulating votes for each spot. The maximum value in this table determines which phase family the spot belongs to. When a Si-t32 spot is removed, its top-ranking position can occasionally be transferred to a Si-st12 spot. However, this change is minimal (typically one score) and occurs only rarely.

The next step involved removing spots 6 to 9 from the Si-t32 phase. Poly's analysis produced the score results shown in Figure 3.14d. Poly could preserve its efficiency at this step, with the Si-t32 spots showing scores around 10, as expected with 10 spots remaining. The scores for the Si-st12 spots remained stable at around 12, corresponding to the 13 spots.

Figure 3.14e presents the scores after removing spots 0 to 21 from the Si-t32 phase. Remarkably, Poly continued to distinguish the phases accurately. With only eight Si-t32 spots left, the average score for these spots was around 7, which is consistent with expectations. Meanwhile, the scores for the Si-st12 spots remained fairly constant, and they were correctly identified.

In the final step, shown in Figure 3.14f, only four Si-t32 spots remained. Interestingly, Poly was still able to distinguish these few spots from the Si-st12 spots. The scores for the Si-st12 spots remained in the same range, indicating stable phase identification.

Therefore, we can conclude that Poly is capable of handling situations where the number of spots for a specific phase is limited.

3.3.4.2 Crystal limit: Si-t32 pattern, then adding patterns from Si-st12 with different orientations.

In order to investigate the effect of different orientations on poly's result, we developed a test starting with a pattern of Si-t32 and then adding Si-st12 phase patterns with different orientations. This test is similar to the experimental situation in that different grains have the same phases but different orientations. Figure 3.15a shows a mixture of Si-t32 (in blue) and Si-st12 (in red) phase patterns. Figures 3.15b to 3.15f demonstrate adding patterns of Si-st12 to the initial pattern of Si-t32, respectively.

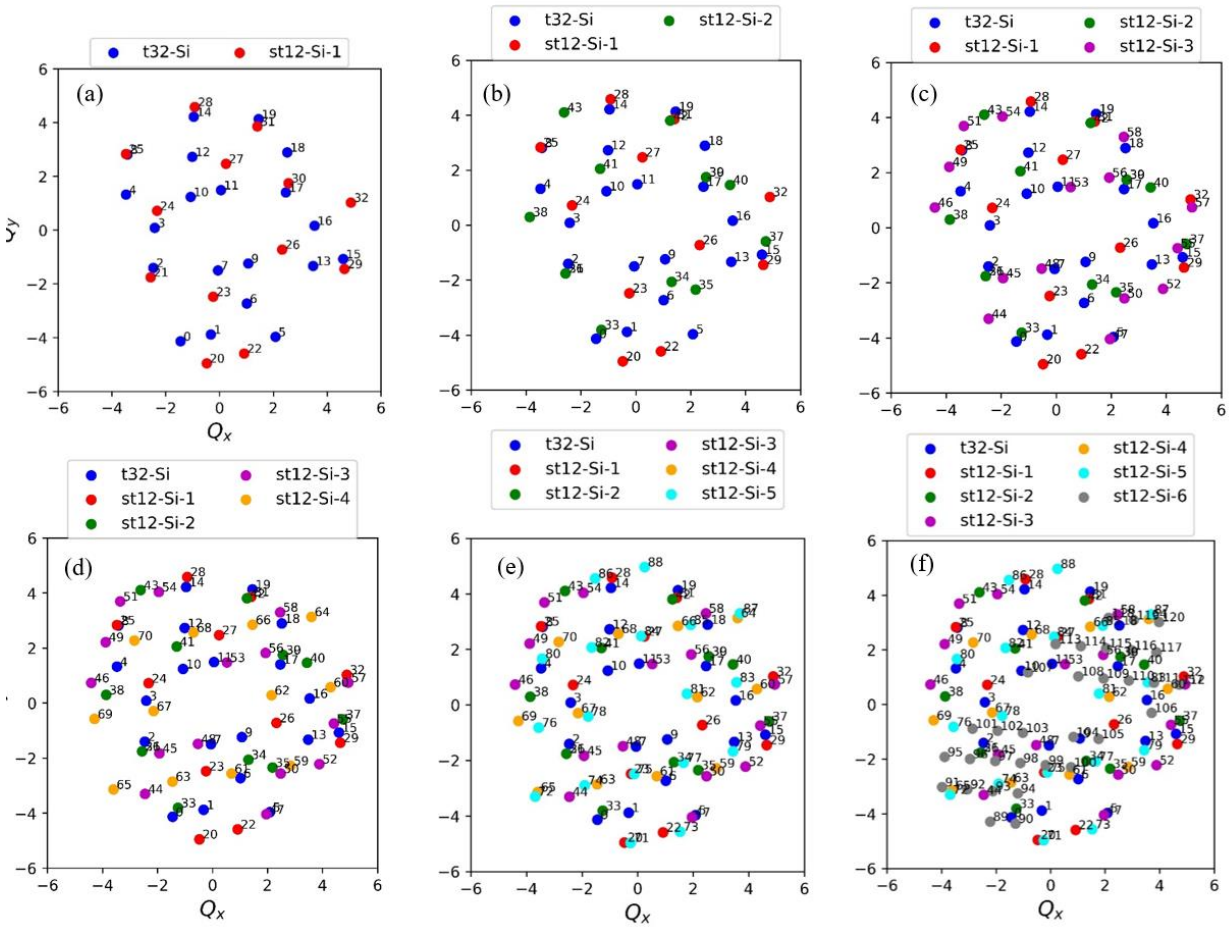

Figure 3-15 a) The mixture of simulated diffraction spots of Si-t32 in blue color and Si-st12 phases in red color. Different sets of spots corresponding to the Si-st12 phase with various orientations are added to the mixed spots in parts b) (green), c) (purple), d) (orange), e) (cyan), and f) (gray) in the final pattern. In part f, there are seven mixed patterns.

The first pattern in Figure 3.15a contains 19 spots with the Si-t32 phase and 12 Si-st12 spots. In the second pattern in part b, there are 11 spots labeled 33 to 43 in green color. The next step adds 15 spots (44 to 58) colored purple. In Figure 3.15d, we added 12 spots with labels 59 to 70 shown in orange. Figure 3.15e contains 18 spots of Si-st12 with labels 71 to 83, which are shown in cyan color. Finally, in Figure 3.15F, 36 spots of Si-st12 are added to the pattern labeled 84 to 120.

We used poly to analyze these patterns, and the results are represented in Figures 3.16 and 3.17. For the first pattern shown in Figure 3.15a with two sets of spots, the result is Figure 3.16a a which is the same as we started in the previous section, and both phases are identified. In Figure 3.16 b, with 43 Bragg spots, it is seen that poly has identified the phases where the average

scores for the phase Si-t32 are around 21 and for the Si-st12 are 15, which makes sense because of the spot counts for each phase. There is a slight increase in scores, which the reason is by increasing the spots, the probability of the vector match increases for both phases, which can use other phase spots.

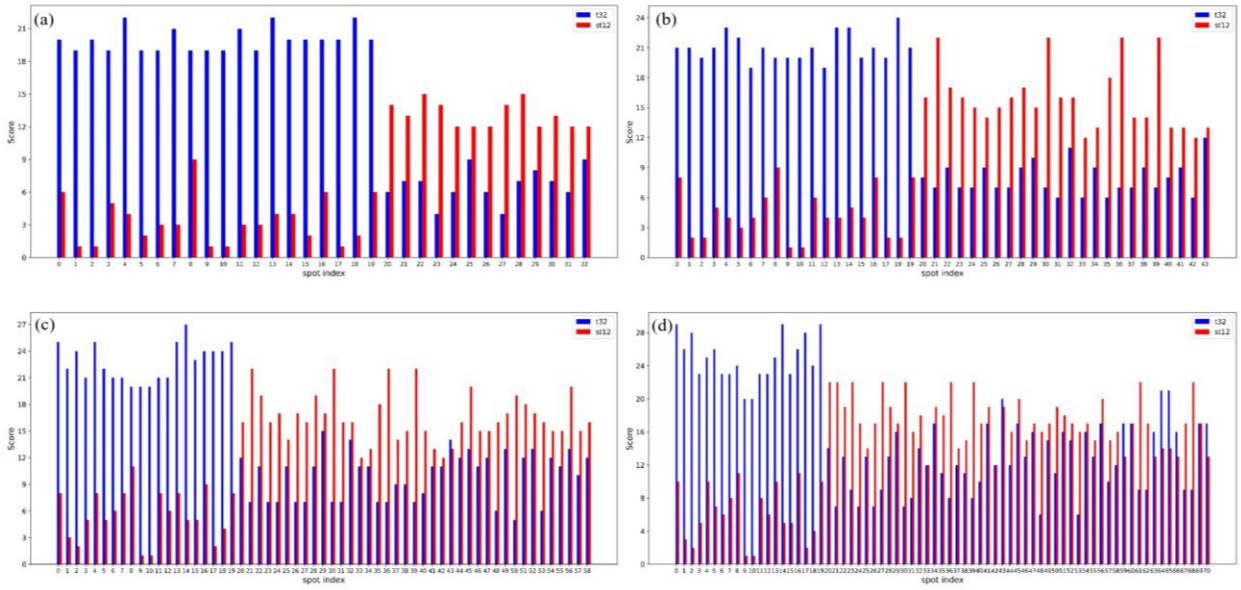

Figure 3-16 The scores of spots obtained from polyphase analysis for the mixed patterns in Figure 3.15. The scores for the Si-t32 phase are shown in blue, while those for the Si-st12 phase are shown in red. a) The initial pattern contains 32 spots, with 20 belonging to the Si-t32 phase and 12 originating from the Si-st12 phase. b) A new set of spots corresponding to a different orientation of the Si-st12 phase is added to the pattern, labeled from 33 to 43. c) Another set of spots from the Si-st12 phase is added to the pattern, labeled 44 to 58.d) In the next step, additional spots are added to the pattern with labels 59 to 70.

In Figure 3.16c, it is demonstrated that the phase Si-t32 is perfectly identified from Si-st12; however, there is a trace of increasing ambiguity in scores, specifically for the Si-st12 phase. To see its trend, we followed the analysis for the next pattern, which is shown in Figure 3.16d. Here, there are 70 spots, and Si-t32 is still distinguished; however, Si-st12 is getting close to the ambiguity. In addition, the average score for Si-t32 is around 25.

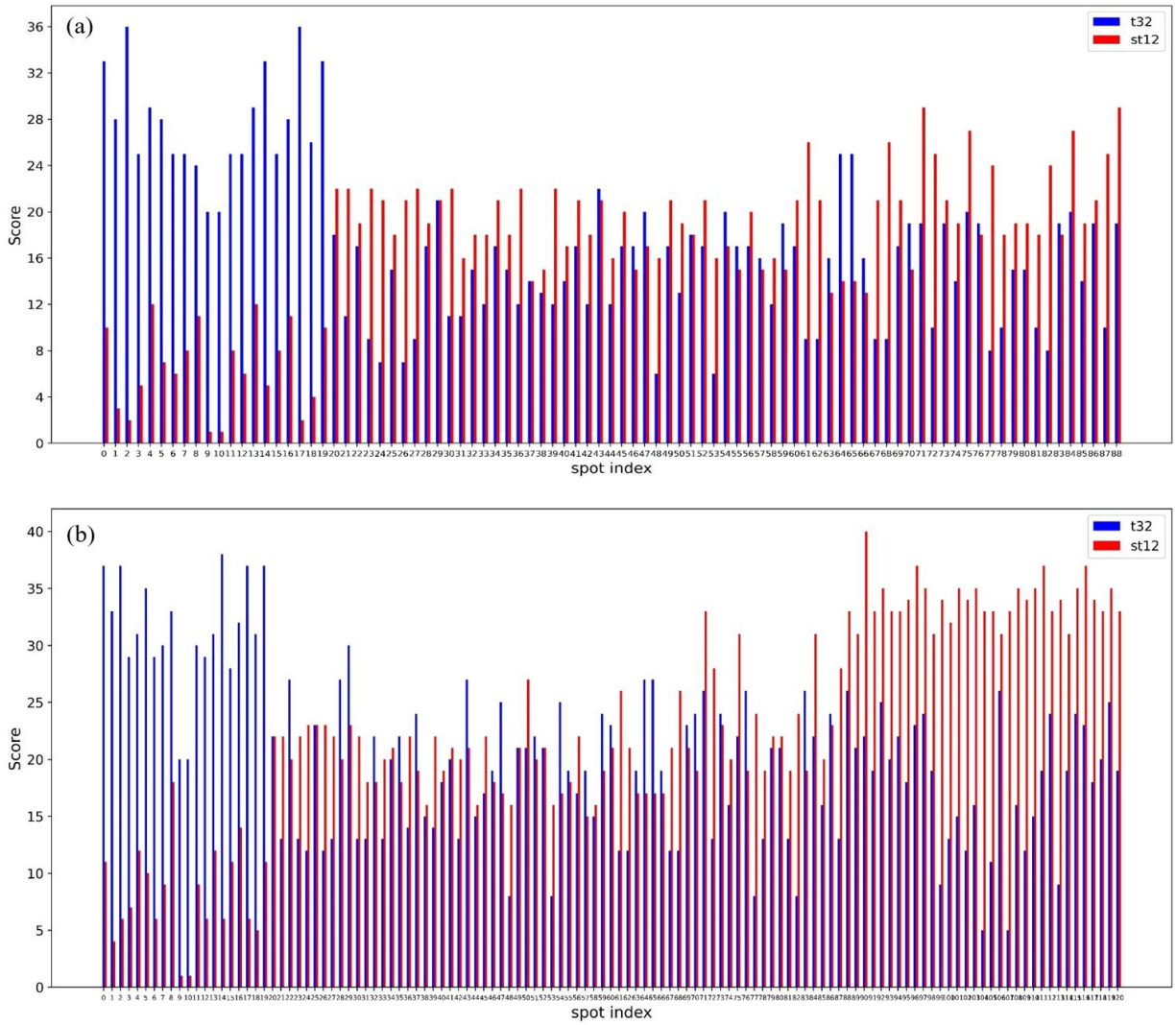

Figure 3-17 The scores of spots obtained from poly analysis for the mixtures in Figures 3.15a to d. The scores for the Si-t32 phase are shown in blue, while those for the Si-st12 phase are shown in red. a) Following the pattern in the figure, this one contains 89 spots. a new set of spots corresponding to a different orientation of the Si-st12 phase is added to the pattern of Figure 3.15d, labeled from 71 to 88. c) The last set of spots of the Si-st12 phase is added to the pattern with labels of 89 to 120.

In the following steps, the total number of spots increases to 88 and 120, respectively. To visualize the results, we plotted them in Figure 3.17. Figure 3.17a displays the scores for the pattern with 88 spots, corresponding to the diffraction pattern shown in Figure 3.15e. Although the Si-t32 phase is identified, the scores associated with the Si-st12 phase continue to increase. This trend overlaps with the scores for Si-t32 (highlighted in blue), thereby increasing the ambiguity in phase identification.

Finally, for the pattern containing 120 spots, the results are presented in Figure 3.17b. The Si-t32 phase remains distinguishable, with an average score of approximately 28. As the number of Si-st12 spots increases, we observe a mixed effect: on one hand, the scores for some Si-st12 spots increase; on the other hand, ambiguity rises for the remaining Si-st12 spots.

This analysis of various orientations demonstrates that Poly can successfully identify phases within a mixture of patterns that include different sample orientations. However, the number of spots included in the analysis can influence the scores and affect the final phase identification.

3.3.4.3 Phase Mixture limit: Si-t32 pattern, then adding patterns from different phases

In this section, we evaluate the performance of the *Poly* algorithm when applied to mixtures of diffraction patterns originating from distinct silicon polymorphs. To begin, we simulated selected area electron diffraction (SAED) patterns for several individual Si phases. Figure 3.18 displays these reference patterns: (a) Si-t32, comprising 20 diffraction spots, also used in the preceding analysis; (b) Si-st12 with 13 spots; (c) Si-bc8 containing 11 spots; (d) Si-hd with 9 spots; (e) Si-IX with 13 spots; and (f) Si-bt8 including 10 spots.

In the first stage, patterns (a) and (b)—corresponding to Si-t32 and Si-st12—were combined, as shown in Figure 3.19a. Here, Si-t32 spots are indicated in blue (labels 0–19) and Si-st12 spots in red (labels 20–32). The Si-bc8 phase was subsequently introduced, represented in green (labels 33–43) in Figure 3.19b. In the third step, the Si-hd phase was added (purple, labels 44–52) as shown in Figure 3.19c. The fourth composite pattern included the Si-IX phase (orange, labels 53–65), presented in Figure 3.19d. Finally, Figure 3.19e incorporates the Si-bt8 phase (cyan, labels 66–75), completing the full six-phase diffraction mixture.

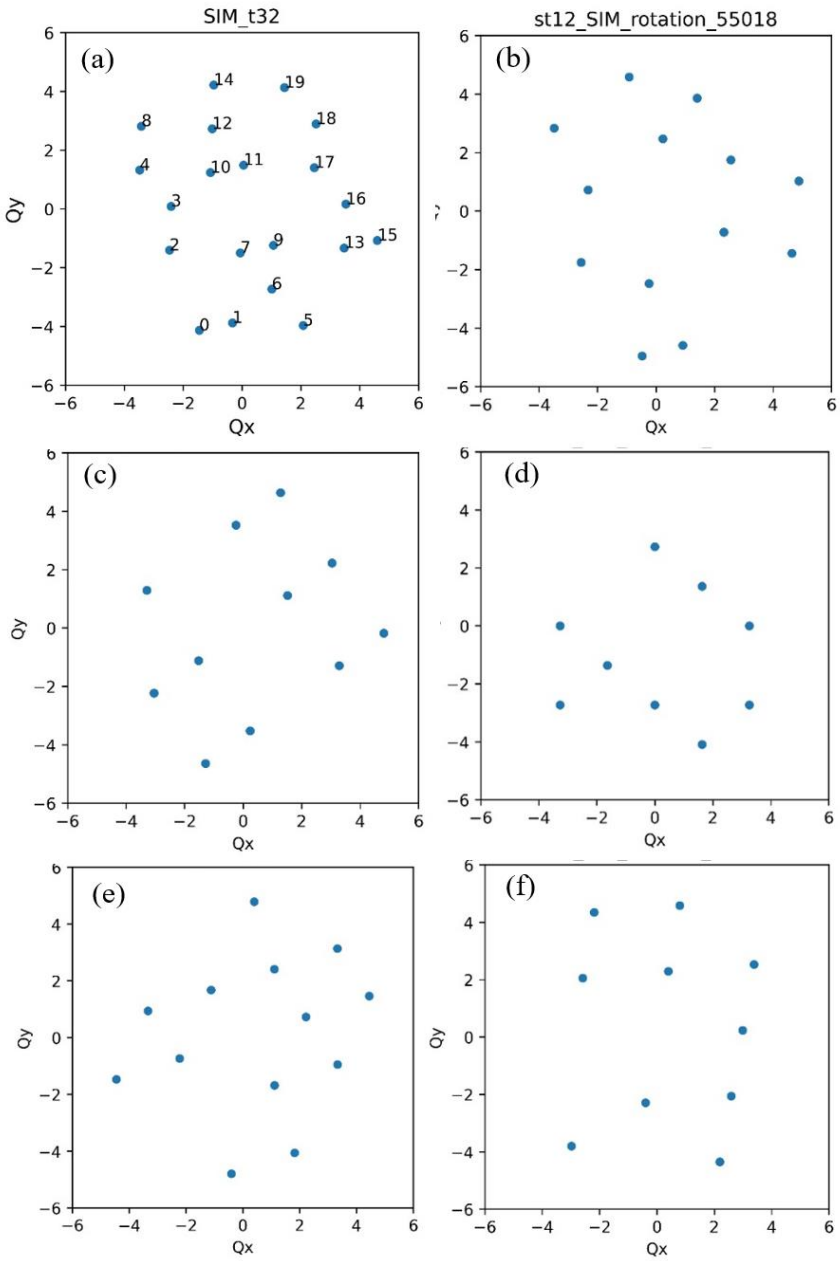

Figure 3-18 Different simulated SAED patterns of the phases a) Si-t32 b)Si-st12, c)Si-bc8, d)Si-hd, e)Si-IX, f)Si-bt8.

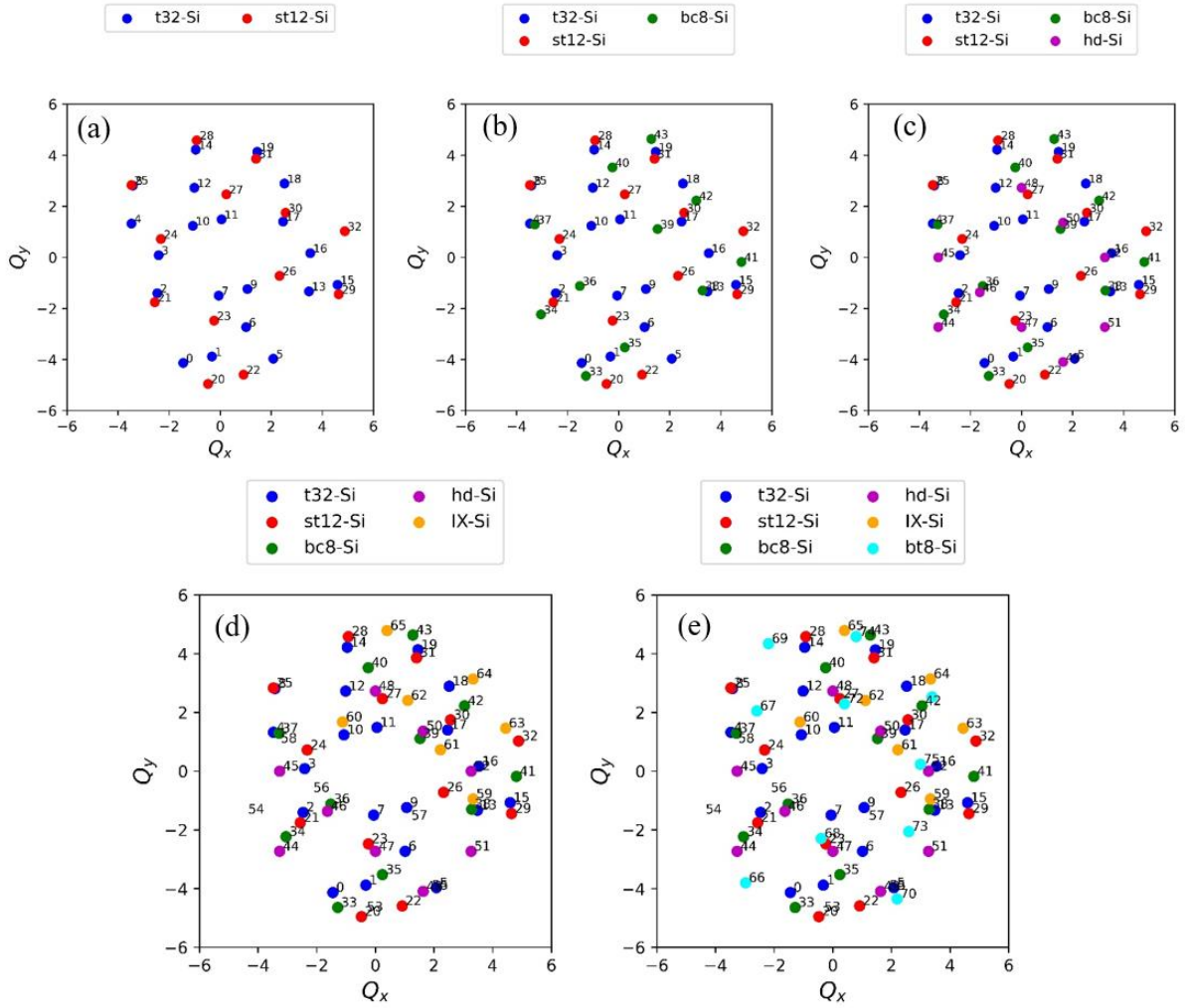

Figure 3-19 a) The mixture of simulated diffraction spots of Si-t32 in blue color and Si-st12 phases in red color. In each step, a new set of spots is added to the initial pattern so that in b) Si-bc8, c) Si-hd, d) Si-XI, and e) Si-bt8 spots are added, respectively.

We employed the Poly algorithm to investigate phase identification across five mixed diffraction patterns. The analysis was carried out by evaluating each pattern against a set of eleven candidate silicon phases, as represented in Figures 3.20 and 3.21. In these figures, each phase is denoted by a distinct color in the plots: Si-t32 (blue), Si-st12 (red), Si-bc8 (green), Si-hd (purple), Si-IX (orange), Si-bt8 (cyan), Si-r8 (gray), Si-m32* (black), Si-VIII (light blue), Si-m32 (dark green), and Si-t32* (brown).

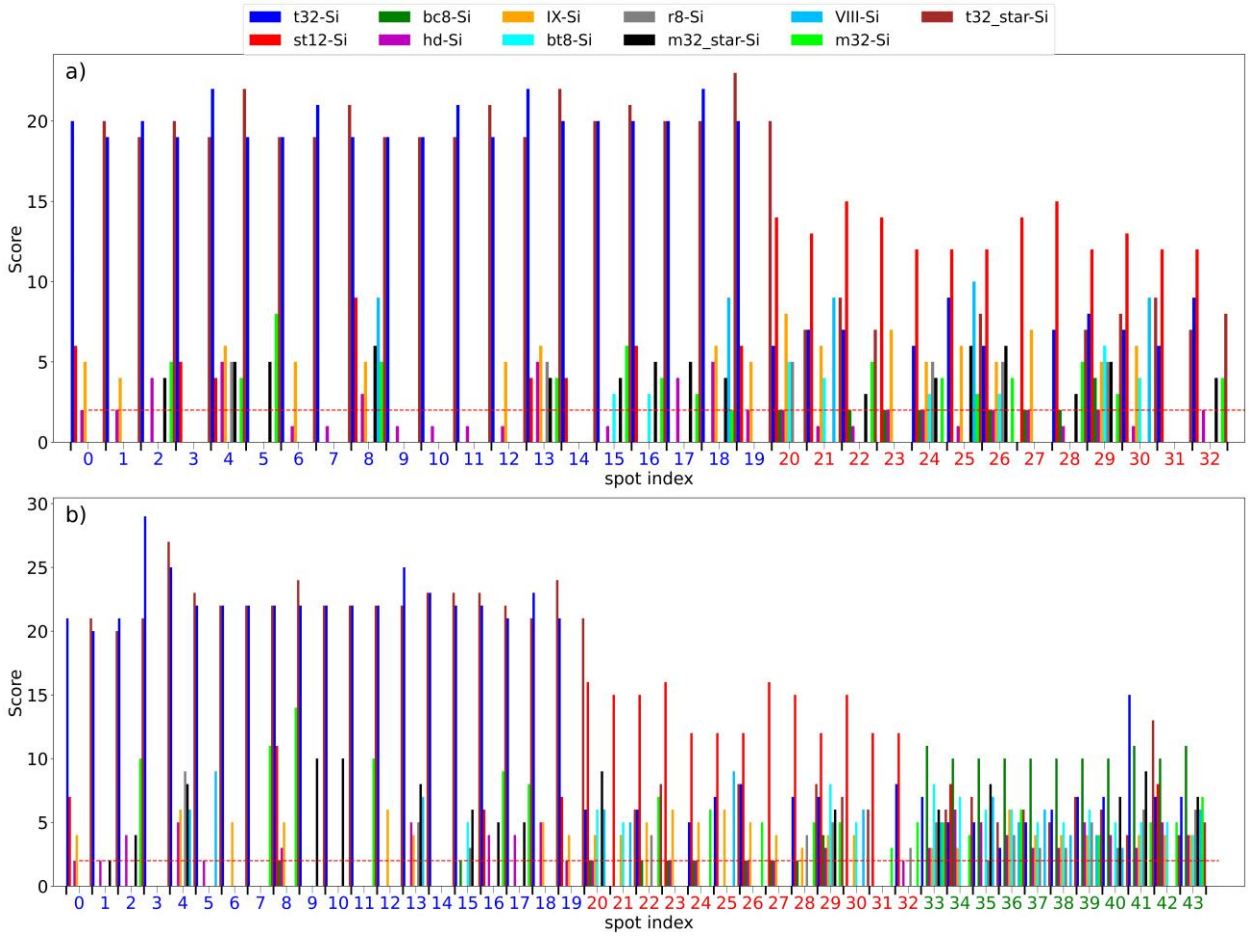

Figure 3-20 The scores of spots obtained from the Poly analysis for the mixtures in Figures 3.19a and b. The scores for the eleven phases are shown in different colors: Si-t32 (blue), Si-st12 (red), Si-bc8 (green), Si-hd (purple), Si-IX (orange), Si-bt8 (cyan), Si-r8 (gray), Si-m32* (black), Si-VIII (light blue), Si-m32 (light green), and Si-t32* (brown). scores correspond to a) pattern a and b) pattern b in Figure 3.19.

Figure 3.20a shows the result of the poly analysis. For the spots labeled 0 to 19, the highest scores correspond to Si-t32 and Si-t32, as expected. The scores for these two phases are very similar because the library information in poly, such as lattice parameters and crystallographic structure, is nearly identical for both phases. This makes it challenging to distinguish between Si-t32 and Si-t32* based solely on the magnitudes and angles of the vectors. The spots labeled 20 to 32 achieved higher scores for the Si-st12, proving that poly is scoring in the right way. Other phases have received some scores, but they are not high enough to be considered as serious candidates. In Figure 3.20b, we plotted the result of the analysis for pattern b. It shows the Si-t32, Si-st12, and Si-bc8 spots are identified correctly. Overall, the highest scores belong to Si-t32 and then Si-st12 and finally Si-bc8, which corresponds to the number of spots in each phase related to the N-1 rule and is rational. An important observation is that patterns containing fewer diffraction spots are more prone to score ambiguously, as their limited information content increases the likelihood of matching with multiple phases.

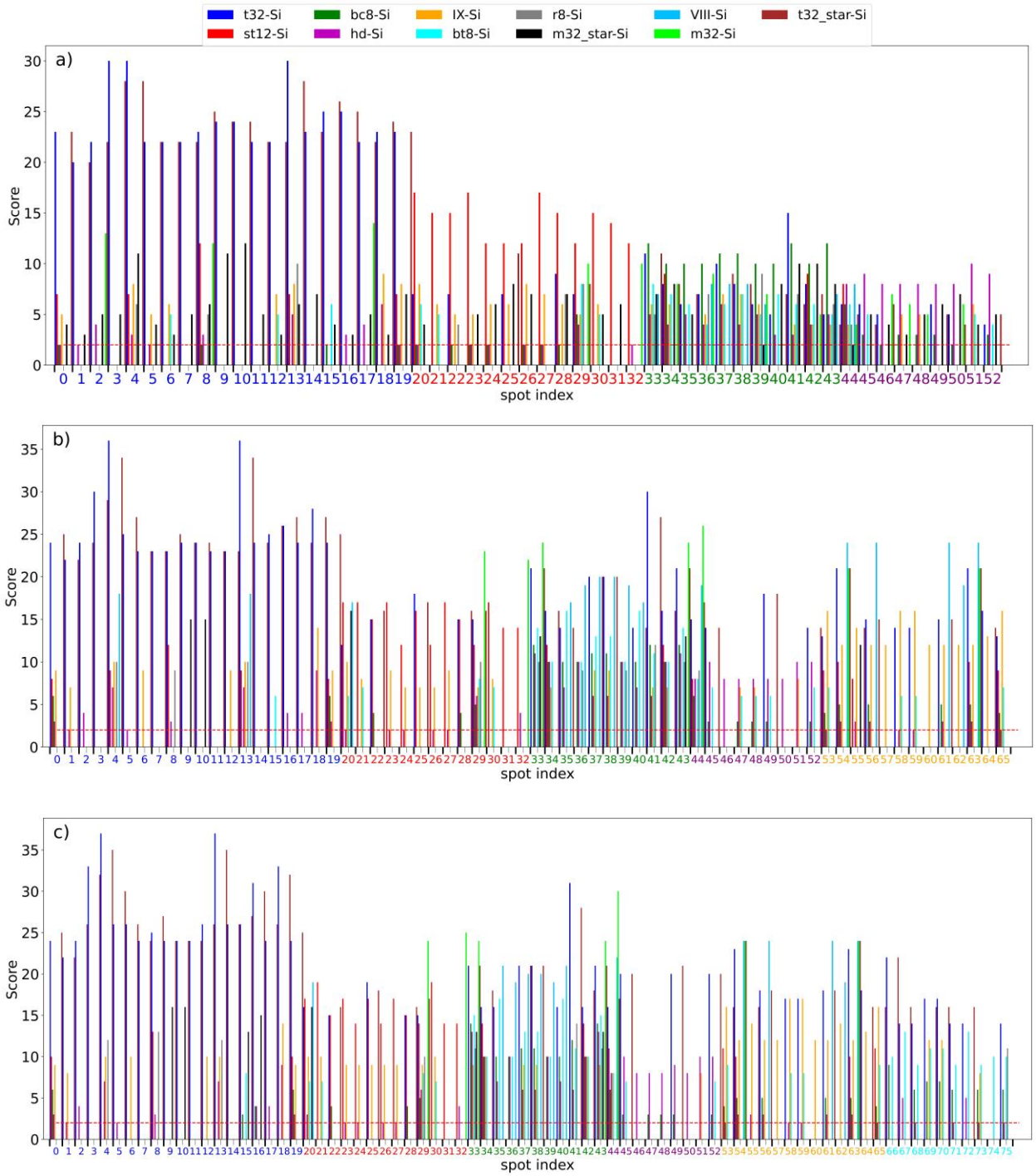

Figure 3-21 The scores of spots obtained from poly analysis for the mixtures in Figure 3.19c to e. The scores for the eleven phases are shown in different colors: Si-t32 (blue), Si-st12 (red), Si-bc8 (green), Si-hd (purple), Si-IX (orange), Si-bt8 (cyan), Si-r8 (gray), Si-m32* (black), Si-VIII (light blue), Si-m32 (light green), and Si-t32* (brown). scores correspond to a) pattern c and b) pattern d, and c) pattern e in Figure 3.19.

Figure 3.21a presents the phase-matching scores for a diffraction pattern composed of mixed spots corresponding to the Si-t32, Si-st12, Si-bc8, and Si-hd phases (refer to Figure 3.21c). In this

case, the algorithm distinctly identifies Si-t32, Si-st12, and Si-hd. However, for the Si-bc8 spots, while the highest scores align with the correct phase, other phases also yield similarly high scores, placing those reflections within a zone of ambiguity. This may be attributed to the addition of Si-hd spots, which increases the structural similarity between Si-bc8 and other phases, complicating their discrimination.

The subsequent analysis includes the incorporation of Si-IX spots, as shown in Figure 3.21d. The corresponding scoring results, depicted in Figure 3.21b, reveal that while Poly continues to reliably identify Si-t32, significant ambiguity emerges for other reflections. When Si-bc8 is added once again, as shown in Figure 3.21c, Si-t32 remains confidently identified, whereas the remaining spots cannot be assigned to specific phases with high confidence.

Notably, this ambiguity becomes pronounced beginning with the dataset in Figure 3.21b, which contains 66 total spots. As demonstrated in prior sections, surpassing a certain threshold in spot density increases the likelihood of overlapping match conditions across phases. The continued reliable identification of Si-t32 is due to its relatively low structural similarity to the other phases, reducing the probability of erroneous spot correlations.

3.4 Conclusion

3.4.1 The Capability of Poly for Phase Identification Tested by Simulated Diffraction Patterns

We developed the poly algorithm to perform spot-wise QPA of nanoscale polymorphic materials. Diffraction patterns of bt8-Si and st12-Si were simulated to test the algorithm.

We used crystallographic information for different phases of Si to simulate SAED patterns. These simulations were performed using Python, leveraging various libraries for processing. The high-pressure Si phases studied included Si-bt8, Si-st12, Si-bc8, Si-r8, Si-hd, Si-IX, Si-VIII, Si-m32, Si-m32*, Si-t32, and Si-t32*.

The analysis of these simulated patterns with Poly demonstrated the algorithm's strong capability to accurately identify phases.

3.4.2 Phase identification of the Si sample irradiated by the laser using Poly

The results demonstrate that the Poly algorithm can reliably match detected diffraction spots from microexplosion experiments with known high-pressure silicon phases. In addition, we analyzed experimental SAED patterns obtained from laser-shock-affected silicon samples, revealing the presence of novel high-pressure phases. A prior study by Rapp et al. reported that microexplosions in silicon generated several tetragonal and monoclinic phases; however, their identification based solely on d-spacing was not quantitative and lacked spot-wise precision. Our analysis using Poly, which incorporates both angular and d-spacing information, enabled the identification of the t32-Si and t32*-Si phases as the dominant components in laser-shock-affected regions of silicon—reported here for the first time. Furthermore, the analysis of a series of patterns acquired at varying time delays indicates that these phases gradually relax into other high-pressure phases within approximately 50 days. Ongoing research aims to further evaluate the capabilities of this spot-wise phase identification approach in other material systems and to apply it to new patterns obtained via nano-beam diffraction. Additionally, Poly is applicable to position-sensitive diffraction patterns collected using 4D-STEM. However, in many such cases, the patterns tend to be highly diffuse. When sharp and well-defined Bragg spots are present, Poly can significantly aid in accurate phase identification.

3.4.3 Limitations of Poly for phase identification

Phase identification procedures, ranging from simple to complex, carry a certain probability of uncertainty due to experimental tool errors, low-quality data, sample-related issues, analysis mistakes, and reference data inaccuracies. In the case of the Poly, we use the magnitudes of the vectors and their angles in the SAED pattern, comparing them to the data library of the sample, specifically Si. It is crucial to identify the weaknesses of the algorithm using the ideal case of simulated SAED patterns. These simulations minimize errors from tools and experiments while providing the initial SAED pattern information needed to evaluate the algorithm. To achieve this, we performed different assessments to test the Poly algorithm. First, as a test for spot limit, a mixed pattern of Si-t32 and Si-st12 phases was created. In each step, we removed some spots from the Si-t32 phase to determine the minimum number of spots required for the phase to remain detectable in the scores. The results showed that Poly could reliably identify the Si-t32 phase with as few as four spots. However, for experimental data, scores at this level will have low reliability.

To assess the effect of different orientations of a specific phase on the efficiency of poly, we conducted a second test, known as the crystal test. The initial SAED pattern contained Si-t32 spots. Gradually, we put additional spots corresponding to the Si-st12 phase in various orientations, step by step. Up to the third step, with a total of 58 spots, Poly successfully identified the phase with a high accuracy. In the fourth step, when the pattern reached 70 spots, the analysis remained reliable for the Si-t32 phase. However, it produced incorrect scores for four spots associated with the Si-st12 phase. Although correlated-scores evaluation of Si-t32 phase scores can still be utilized, we consider this step as the onset of reduced accuracy. Even in steps five and six, poly was still able to identify the phases—particularly Si-t32—but these steps can be considered the critical limit for poly's performance. The third one was the phase mixture test which was done by mixing the spots from different phases of Si. It was shown that, in this case, poly could identify the phases up to a mixture of four phases. This occurred when the number of spots reached 76 while most experimental patterns of Si contained around 35 spots or fewer.

3.4.4 Outlook and Future Work

Poly can serve as a solid starting point for spot-wise phase identification of nanomaterials. Over time, it can be enhanced to handle more complex cases involving ambiguities, such as overlapping diffraction spots or phase mixtures. One potential improvement is introducing a filtering step to exclude high-scoring identified spots, keeping the total number of spots below the threshold. Additionally, correlation scores can be added to assess phase similarity between spots.

From an experimental perspective, modern TEMs equipped with nanobeam (Appendix A Nanobeam measurements) capabilities allow for SAED patterns to be obtained from focused areas of the sample. This reduces the number of coexisting phases in the selected region, significantly improving Poly's accuracy. New SAED measurements of laser-irradiated silicon reveal that, even after a decade, certain phases remain preserved within the material and are amenable to detailed analysis (Appendix A2).

4 Conclusion

We investigated light–matter interactions at the nanoscale using photon-induced near-field electron microscopy (PINEM) with femtosecond temporal resolution, focusing on near-field behavior around metallic nanoparticles. Despite employing linearly polarized pump lasers, dipole orientations in Au and Ag nanoparticles on SiO substrates exhibited significant misalignment, attributed to defect-induced surface charge coupling and facet-dependent interactions. Compared to graphene, SiO substrates showed broader dipole orientation distributions, with Au nanoparticles yielding a full width at half maximum (FWHM) of 19°, versus 9° on graphene—highlighting graphene's superior near-field stability. Additionally, circular near-field patterns emerged at specific polarization angles (e.g., 18°, 66°, 114°, 162°), consistent with conditions for circular polarization—equal amplitude and a ±90° phase difference between orthogonal dipole components. These findings demonstrate that even achiral systems can exhibit chirality through excitation-induced asymmetries, leading to polarization-dependent near-field symmetry breaking via plasmonic interference.

In parallel, we developed the Poly algorithm to perform spot-wise quantitative phase analysis (QPA) of nanoscale polymorphic materials. To validate its capability, we simulated selected area electron diffraction (SAED) patterns for various high-pressure silicon phases—including bt8-Si, st12-Si, bc8-Si, r8-Si, and others—using crystallographic data and Python-based tools. The algorithm accurately identified phases from these simulations and was subsequently applied to experimental SAED data from laser-shocked silicon samples. Unlike previous approaches relying solely on d-spacing, Poly incorporates both angular and spacing information, enabling precise identification of t32-Si and t32*-Si phases—reported here for the first time. Time-resolved analysis revealed that these phases gradually relax into other high-pressure forms over approximately 50 days. Furthermore, Poly shows strong potential for analyzing position-sensitive diffraction data from 4D-STEM, particularly when sharp Bragg spots are present, despite the typically diffuse nature of such patterns.

Overall, these thematic research projects were designed to advance the understanding of light–matter interactions in nanomaterials by integrating transmission electron microscopy with ultrafast laser techniques. The findings offer valuable insights into plasmonic behavior at the nanoscale and enable the discovery of novel high-pressure phases in nanostructured materials, contributing meaningfully to the broader fields of nanoscale characterization and phase transformation science.

References

[1] L. Rapp *et al.*, “Experimental evidence of new tetragonal polymorphs of silicon formed through ultrafast laser-induced confined microexplosion,” *Nat. Commun.*, vol. 6, no. 1, p. 7555, Jun. 2015, doi: 10.1038/ncomms8555.

[2] M. Rahmani and C. Jagadish, “Light–Matter interactions on the nanoscale,” *Beilstein J. Nanotechnol.*, vol. 9, pp. 2125–2127, Aug. 2018, doi: 10.3762/bjnano.9.201.

[3] R. W. Boyd, *Nonlinear optics*, 3rd ed. Amsterdam ; Boston: Academic Press, 2008.

[4] J. J. Sakurai and J. Napolitano, *Modern quantum mechanics*, 2. ed., International ed. Boston, Mass.: Addison-Wesley, Pearson, 2011.

[5] M. O. Scully and M. S. Zubairy, *Quantum optics*. Cambridge ; New York: Cambridge University Press, 1997.

[6] B. E. A. Saleh and M. C. Teich, *Fundamentals of photonics*, Third edition. Hoboken, NJ: Wiley, 2019.

[7] R. Loudon, *The quantum theory of light*, 3rd ed. in Oxford science publications. Oxford ; New York: Oxford University Press, 2000.

[8] P. Törmä and W. L. Barnes, “Strong coupling between surface plasmon polaritons and emitters: a review,” *Rep. Prog. Phys.*, vol. 78, no. 1, p. 013901, Jan. 2015, doi: 10.1088/0034-4885/78/1/013901.

[9] L. Novotny and B. Hecht, *Principles of nano-optics*, Second edition. Cambridge New York Melbourne: Cambridge University Press, 2012. doi: 10.1017/CBO9780511794193.

[10] A. Feist, K. E. Echternkamp, J. Schauss, S. V. Yalunin, S. Schäfer, and C. Ropers, “Quantum coherent optical phase modulation in an ultrafast transmission electron microscope,” *Nature*, vol. 521, no. 7551, pp. 200–203, May 2015, doi: 10.1038/nature14463.

[11] R. Brydson, *Electron energy loss spectroscopy*, 1. publ. in Microscopy handbooks, no. 48. Oxford: Bios in association with the Royal Microscopical Society, 2006.

[12] Z. Zhong-lin Wang, *Elastic and Inelastic Scattering in Electron Diffraction and Imaging*. New York, NY: Springer, 1995.

[13] B. Fultz and J. M. Howe, Eds., *Transmission Electron Microscopy and Diffractometry of Materials*, Third Edition. in SpringerLink Bücher. Berlin, Heidelberg: Springer Berlin Heidelberg, 2008. doi: 10.1007/978-3-540-73886-2.

[14] *Electron Nano-Imaging*. New York, NY: Springer Berlin Heidelberg, 2017.

[15] M. Knoll and E. Ruska, “Das Elektronenmikroskop,” *Z. F*[illegible]*r Phys.*, vol. 78, no. 5–6, pp. 318–339, May 1932, doi: 10.1007/BF01342199.

[16] E. Ruska, “The development of the electron microscope and of electron microscopy,” *Rev. Mod. Phys.*, vol. 59, no. 3, pp. 627–638, Jul. 1987, doi: 10.1103/RevModPhys.59.627.

[17] D. B. Williams and C. B. Carter, *Transmission electron microscopy: a textbook for materials science*, 2nd ed. in Cambridge library collection. New York: Springer, 2008.

[18] S. R. Spurgeon, “Scanning Transmission Electron Microscopy of Oxide Interfaces and Heterostructures”.

[19] “JEM-2100Plus Transmission Electron Microscope User Manual.” JEOL Ltd, 2016.

[20] L. Reimer, *Transmission Electron Microscopy: Physics of Image Formation and Microanalysis*, vol. 36. in Springer Series in Optical Sciences, vol. 36. Berlin, Heidelberg: Springer Berlin Heidelberg, 1997. doi: 10.1007/978-3-662-14824-2.

[21] A. H. Zewail and J. M. Thomas, *4D electron microscopy: imaging in space and time*. London: Imperial College Press, 2010.

[22] A. Feist *et al.*, “Ultrafast transmission electron microscopy using a laser-driven field emitter: Femtosecond resolution with a high coherence electron beam,” *Ultramicroscopy*, vol. 176, pp. 63–73, May 2017, doi: 10.1016/j.ultramic.2016.12.005.
[23] G. P. Lopinski, O. Kodra, F. Kunc, D. C. Kennedy, M. Couillard, and L. J. Johnston, “X-ray photoelectron spectroscopy of metal oxide nanoparticles: chemical composition, oxidation state and functional group content,” *Nanoscale Adv.*, vol. 7, no. 6, pp. 1671–1685, 2025, doi: 10.1039/D4NA00943F.
[24] J. E. Whitten, “Ultraviolet photoelectron spectroscopy: Practical aspects and best practices,” *Appl. Surf. Sci. Adv.*, vol. 13, p. 100384, Feb. 2023, doi: 10.1016/j.apsadv.2023.100384.
[25] W. Xiong *et al.*, “Photoelectron Spectroscopy of CdSe Nanocrystals in the Gas Phase: A Direct Measure of the Evanescent Electron Wave Function of Quantum Dots,” *Nano Lett.*, vol. 13, no. 6, pp. 2924–2930, Jun. 2013, doi: 10.1021/nl401309z.
[26] J. M. Pietryga *et al.*, “Spectroscopic and Device Aspects of Nanocrystal Quantum Dots,” *Chem. Rev.*, vol. 116, no. 18, pp. 10513–10622, Sep. 2016, doi: 10.1021/acs.chemrev.6b00169.
[27] S. V. Kilina, P. K. Tamukong, and D. S. Kilin, “Surface Chemistry of Semiconducting Quantum Dots: Theoretical Perspectives,” *Acc. Chem. Res.*, vol. 49, no. 10, pp. 2127–2135, Oct. 2016, doi: 10.1021/acs.accounts.6b00196.
[28] P. V. Kamat, “Meeting the Clean Energy Demand: Nanostructure Architectures for Solar Energy Conversion,” *J. Phys. Chem. C*, vol. 111, no. 7, pp. 2834–2860, Feb. 2007, doi: 10.1021/jp066952u.
[29] X. Chen and S. S. Mao, “Titanium Dioxide Nanomaterials: Synthesis, Properties, Modifications, and Applications,” *Chem. Rev.*, vol. 107, no. 7, pp. 2891–2959, Jul. 2007, doi: 10.1021/cr0500535.
[30] Y. Lu, Y. Yin, B. T. Mayers, and Y. Xia, “Modifying the Surface Properties of Superparamagnetic Iron Oxide Nanoparticles through A Sol−Gel Approach,” *Nano Lett.*, vol. 2, no. 3, pp. 183–186, Mar. 2002, doi: 10.1021/nl015681q.
[31] S. Cao *et al.*, “Photoelectrochemical sensors based on heterogeneous nanostructures for in vitro diagnostics,” *Biosens. Bioelectron. X*, vol. 11, p. 100200, Sep. 2022, doi: 10.1016/j.biosx.2022.100200.
[32] S. T. Park, M. Lin, and A. H. Zewail, “Photon-induced near-field electron microscopy (PINEM): theoretical and experimental,” *New J. Phys.*, vol. 12, no. 12, p. 123028, Dec. 2010, doi: 10.1088/1367-2630/12/12/123028.
[33] X. Fu *et al.*, “Nanoscale-Femtosecond Imaging of Evanescent Surface Plasmons on Silver Film by Photon-Induced Near-Field Electron Microscopy,” *Nano Lett.*, vol. 22, no. 5, pp. 2009–2015, Mar. 2022, doi: 10.1021/acs.nanolett.1c04774.
[34] S. T. Park and A. H. Zewail, “Photon-induced near-field electron microscopy: Mathematical formulation of the relation between the experimental observables and the optically driven charge density of nanoparticles,” *Phys. Rev. A*, vol. 89, no. 1, p. 013851, Jan. 2014, doi: 10.1103/PhysRevA.89.013851.
[35] M. T. Hassan, H. Liu, J. S. Baskin, and A. H. Zewail, “Photon gating in four-dimensional ultrafast electron microscopy,” *Proc. Natl. Acad. Sci.*, vol. 112, no. 42, pp. 12944–12949, Oct. 2015, doi: 10.1073/pnas.1517942112.
[36] V. Tinnemann *et al.*, “Ultrafast electron diffraction from a Bi(111) surface: Impulsive lattice excitation and Debye–Waller analysis at large momentum transfer,” *Struct. Dyn.*, vol. 6, no. 3, p. 035101, May 2019, doi: 10.1063/1.5093637.
[37] C. Gerbig, A. Senftleben, S. Morgenstern, C. Sarpe, and T. Baumert, “Spatio-temporal resolution studies on a highly compact ultrafast electron diffractometer,” *New J. Phys.*, vol. 17, no. 4, p. 043050, Apr. 2015, doi: 10.1088/1367-2630/17/4/043050.

[38] A. Yurtsever and A. H. Zewail, “4D Nanoscale Diffraction Observed by Convergent-Beam Ultrafast Electron Microscopy,” *Science*, vol. 326, no. 5953, pp. 708–712, Oct. 2009, doi: 10.1126/science.1179314.
[39] J. Hillier and R. F. Baker, “Microanalysis by Means of Electrons,” *J. Appl. Phys.*, vol. 15, no. 9, pp. 663–675, Sep. 1944, doi: 10.1063/1.1707491.
[40] R. F. Egerton, *Electron Energy-Loss Spectroscopy in the Electron Microscope*. Boston, MA: Springer US, 2011. doi: 10.1007/978-1-4419-9583-4.
[41] A. Yurtsever and A. H. Zewail, “Direct Visualization of Near-Fields in Nanoplasmonics and Nanophotonics,” *Nano Lett.*, vol. 12, no. 6, pp. 3334–3338, Jun. 2012, doi: 10.1021/nl301643k.
[42] T. T. A. Lummen *et al.*, “Imaging and controlling plasmonic interference fields at buried interfaces,” *Nat. Commun.*, vol. 7, no. 1, p. 13156, Oct. 2016, doi: 10.1038/ncomms13156.
[43] A. Yurtsever, J. S. Baskin, and A. H. Zewail, “Entangled Nanoparticles: Discovery by Visualization in 4D Electron Microscopy,” *Nano Lett.*, vol. 12, no. 9, pp. 5027–5032, Sep. 2012, doi: 10.1021/nl302824f.
[44] J. C. Brooks-Bartlett and E. F. Garman, “The Nobel Science: One Hundred Years of Crystallography,” *Interdiscip. Sci. Rev.*, vol. 40, no. 3, pp. 244–264, Jul. 2015, doi: 10.1179/0308018815Z.000000000116.
[45] C. Lecomte, “**Crystallography: A Very Short Introduction** . By A. M. Glazer. Oxford University Press, 2016. Pp. 168. Price GBP 7.99. ISBN 9780198717591.,” *Acta Crystallogr. Sect. Found. Adv.*, vol. 73, no. 2, pp. 200–201, Mar. 2017, doi: 10.1107/S2053273316018829.
[46] B. S. Murty, P. Shankar, B. Raj, B. B. Rath, and J. Murday, *Textbook of Nanoscience and Nanotechnology*. Berlin, Heidelberg: Springer Berlin Heidelberg, 2013. doi: 10.1007/978-3-642-28030-6.
[47] C. J. Bradley and A. P. Cracknell, *The mathematical theory of symmetry in solids: representation theory for point groups and space groups*, Repr. in Oxford classic texts in the physical sciences. Oxford: Clarendon Press, 2011.
[48] P. G. Radaelli, *Symmetry in crystallography: understanding the international tables*. in IUCr texts on crystallography, no. 17. Oxford: Oxford university press, 2011.
[49] M. C. Fischer, J. W. Wilson, F. E. Robles, and W. S. Warren, “Invited Review Article: Pump-probe microscopy,” *Rev. Sci. Instrum.*, vol. 87, no. 3, p. 031101, Mar. 2016, doi: 10.1063/1.4943211.
[50] M. Wagner *et al.*, “Ultrafast and Nanoscale Plasmonic Phenomena in Exfoliated Graphene Revealed by Infrared Pump–Probe Nanoscopy,” *Nano Lett.*, vol. 14, no. 2, pp. 894–900, Feb. 2014, doi: 10.1021/nl4042577.
[51] F. Caruso and D. Novko, “Ultrafast dynamics of electrons and phonons: from the two-temperature model to the time-dependent Boltzmann equation,” *Adv. Phys. X*, vol. 7, no. 1, p. 2095925, Dec. 2022, doi: 10.1080/23746149.2022.2095925.
[52] P. Emma *et al.*, “First lasing and operation of an ångstrom-wavelength free-electron laser,” *Nat. Photonics*, vol. 4, no. 9, pp. 641–647, Sep. 2010, doi: 10.1038/nphoton.2010.176.
[53] A. H. Zewail, “Femtochemistry: Atomic-Scale Dynamics of the Chemical Bond,” *J. Phys. Chem. A*, vol. 104, no. 24, pp. 5660–5694, Jun. 2000, doi: 10.1021/jp001460h.
[54] A. Ashoka *et al.*, “Extracting quantitative dielectric properties from pump-probe spectroscopy,” *Nat. Commun.*, vol. 13, no. 1, p. 1437, Mar. 2022, doi: 10.1038/s41467-022-29112-y.
[55] M. A. Lauterbach, “Finding, defining and breaking the diffraction barrier in microscopy – a historical perspective,” *Opt. Nanoscopy*, vol. 1, no. 1, p. 8, 2012, doi: 10.1186/2192-2853-1-8.

[56] I. I. Smolyaninov, “Optical microscopy beyond the diffraction limit,” *HFSP J.*, vol. 2, no. 3, pp. 129–131, Jun. 2008, doi: 10.2976/1.2912559.
[57] A. H. Zewail, “Laser Femtochemistry,” *Science*, vol. 242, no. 4886, pp. 1645–1653, Dec. 1988, doi: 10.1126/science.242.4886.1645.
[58] D. Shorokhov and A. H. Zewail, “4D electron imaging: principles and perspectives,” *Phys. Chem. Chem. Phys.*, vol. 10, no. 20, p. 2879, 2008, doi: 10.1039/b801626g.
[59] A. Feist, K. E. Echternkamp, J. Schauss, S. V. Yalunin, S. Schäfer, and C. Ropers, “Electron-Light Interaction in Optical Near-Fields studied by Ultrafast Transmission Electron Microscopy,” in *CLEO: 2015*, San Jose, California: OSA, 2015, p. FTh1E.3. doi: 10.1364/CLEO_QELS.2015.FTh1E.3.
[60] S. Aseyev, E. Ryabov, B. Mironov, and A. Ischenko, “The Development of Ultrafast Electron Microscopy,” *Crystals*, vol. 10, no. 6, p. 452, May 2020, doi: 10.3390/cryst10060452.
[61] T. LaGrange *et al.*, “Single-shot dynamic transmission electron microscopy,” *Appl. Phys. Lett.*, vol. 89, no. 4, p. 044105, Jul. 2006, doi: 10.1063/1.2236263.
[62] J. E. Evans and N. D. Browning, “Enabling direct nanoscale observations of biological reactions with dynamic TEM,” *Microscopy*, vol. 62, no. 1, pp. 147–156, Feb. 2013, doi: 10.1093/jmicro/dfs081.
[63] R. Srinivasan, V. A. Lobastov, C. Ruan, and A. H. Zewail, “Ultrafast Electron Diffraction (UED): A New Development for the 4D Determination of Transient Molecular Structures,” *Helv. Chim. Acta*, vol. 86, no. 6, pp. 1761–1799, Jun. 2003, doi: 10.1002/hlca.200390147.
[64] P. Baum and A. H. Zewail, “Breaking resolution limits in ultrafast electron diffraction and microscopy,” *Proc. Natl. Acad. Sci.*, vol. 103, no. 44, pp. 16105–16110, Oct. 2006, doi: 10.1073/pnas.0607451103.
[65] K. E. Priebe *et al.*, “Attosecond electron pulse trains and quantum state reconstruction in ultrafast transmission electron microscopy,” *Nat. Photonics*, vol. 11, no. 12, pp. 793–797, Dec. 2017, doi: 10.1038/s41566-017-0045-8.
[66] D. Hui, H. Alqattan, M. Sennary, N. V. Golubev, and M. Th. Hassan, “Attosecond electron microscopy and diffraction,” *Sci. Adv.*, vol. 10, no. 34, p. eadp5805, Aug. 2024, doi: 10.1126/sciadv.adp5805.
[67] R. Shiloh, T. Chlouba, and P. Hommelhoff, “Quantum-Coherent Light-Electron Interaction in a Scanning Electron Microscope,” *Phys. Rev. Lett.*, vol. 128, no. 23, p. 235301, Jun. 2022, doi: 10.1103/PhysRevLett.128.235301.
[68] J. Kuttruff, D. Nabben, A.-C. Zimmermann, A. Ryabov, and P. Baum, “Terahertz control and timing correlations in a transmission electron microscope,” *Sci. Adv.*, vol. 10, no. 26, p. eadl6543, Jun. 2024, doi: 10.1126/sciadv.adl6543.
[69] B. Barwick, D. J. Flannigan, and A. H. Zewail, “Photon-induced near-field electron microscopy,” *Nature*, vol. 462, no. 7275, pp. 902–906, Dec. 2009, doi: 10.1038/nature08662.
[70] M. Liebtrau *et al.*, “Spontaneous and stimulated electron–photon interactions in nanoscale plasmonic near fields,” *Light Sci. Appl.*, vol. 10, no. 1, p. 82, Apr. 2021, doi: 10.1038/s41377-021-00511-y.
[71] S. Tsesses *et al.*, “Tunable photon-induced spatial modulation of free electrons,” *Nat. Mater.*, vol. 22, no. 3, pp. 345–352, Mar. 2023, doi: 10.1038/s41563-022-01449-1.
[72] Y. Kurman *et al.*, “Spatiotemporal imaging of 2D polariton wave packet dynamics using free electrons,” *Science*, vol. 372, no. 6547, pp. 1181–1186, Jun. 2021, doi: 10.1126/science.abg9015.
[73] B. Barwick and A. H. Zewail, “Photonics and Plasmonics in 4D Ultrafast Electron Microscopy,” *ACS Photonics*, vol. 2, no. 10, pp. 1391–1402, Oct. 2015, doi: 10.1021/acsphotonics.5b00427.

[74] O. Kfir, V. Di Giulio, F. J. G. de Abajo, and C. Ropers, “Optical coherence transfer mediated by free electrons,” *Sci. Adv.*, vol. 7, no. 18, p. eabf6380, Apr. 2021, doi: 10.1126/sciadv.abf6380.
[75] A. Ben Hayun, O. Reinhardt, J. Nemirovsky, A. Karnieli, N. Rivera, and I. Kaminer, “Shaping quantum photonic states using free electrons,” *Sci. Adv.*, vol. 7, no. 11, p. eabe4270, Mar. 2021, doi: 10.1126/sciadv.abe4270.
[76] A. Wöste *et al.*, “Ultrafast Coupling of Optical Near Fields to Low-Energy Electrons Probed in a Point-Projection Microscope,” *Nano Lett.*, vol. 23, no. 12, pp. 5528–5534, Jun. 2023, doi: 10.1021/acs.nanolett.3c00738.
[77] A. Konečná, V. Di Giulio, V. Mkhitaryan, C. Ropers, and F. J. García de Abajo, “Nanoscale Nonlinear Spectroscopy with Electron Beams,” *ACS Photonics*, vol. 7, no. 5, pp. 1290–1296, May 2020, doi: 10.1021/acsphotonics.0c00326.
[78] E. Petryayeva and U. J. Krull, “Localized surface plasmon resonance: Nanostructures, bioassays and biosensing—A review,” *Anal. Chim. Acta*, vol. 706, no. 1, pp. 8–24, Nov. 2011, doi: 10.1016/j.aca.2011.08.020.
[79] V. G. Kravets, A. V. Kabashin, W. L. Barnes, and A. N. Grigorenko, “Plasmonic Surface Lattice Resonances: A Review of Properties and Applications,” *Chem. Rev.*, vol. 118, no. 12, pp. 5912–5951, Jun. 2018, doi: 10.1021/acs.chemrev.8b00243.
[80] M. P. Mcoyi, K. T. Mpofu, M. Sekhwama, and P. Mthunzi-Kufa, “Developments in Localized Surface Plasmon Resonance,” *Plasmonics*, Nov. 2024, doi: 10.1007/s11468-024-02620-x.
[81] N. G. Khlebtsov and L. A. Dykman, “Optical properties and biomedical applications of plasmonic nanoparticles,” *J. Quant. Spectrosc. Radiat. Transf.*, vol. 111, no. 1, pp. 1–35, Jan. 2010, doi: 10.1016/j.jqsrt.2009.07.012.
[82] F. Vallee, “7 Optical Properties of Metallic Nanoparticles”.
[83] A.-I. Henry, J. M. Bingham, E. Ringe, L. D. Marks, G. C. Schatz, and R. P. Van Duyne, “Correlated Structure and Optical Property Studies of Plasmonic Nanoparticles,” *J. Phys. Chem. C*, vol. 115, no. 19, pp. 9291–9305, May 2011, doi: 10.1021/jp2010309.
[84] K. L. Kelly, E. Coronado, L. L. Zhao, and G. C. Schatz, “The Optical Properties of Metal Nanoparticles: The Influence of Size, Shape, and Dielectric Environment,” *J. Phys. Chem. B*, vol. 107, no. 3, pp. 668–677, Jan. 2003, doi: 10.1021/jp026731y.
[85] L. Wang, M. Hasanzadeh Kafshgari, and M. Meunier, “Optical Properties and Applications of Plasmonic-Metal Nanoparticles,” *Adv. Funct. Mater.*, vol. 30, no. 51, p. 2005400, Dec. 2020, doi: 10.1002/adfm.202005400.
[86] J. Z. Zhang and C. Noguez, “Plasmonic Optical Properties and Applications of Metal Nanostructures,” *Plasmonics*, vol. 3, no. 4, pp. 127–150, Dec. 2008, doi: 10.1007/s11468-008-9066-y.
[87] Y. Xie *et al.*, “SERS-Based Local Field Enhancement in Biosensing Applications,” *Molecules*, vol. 30, no. 1, p. 105, Dec. 2024, doi: 10.3390/molecules30010105.
[88] R. Lv *et al.*, “When a Semiconductor Utilized as an NIR Laser-Responsive Photodynamic/Photothermal Theranostic Agent Integrates with Upconversion Nanoparticles,” *ACS Biomater. Sci. Eng.*, vol. 5, no. 6, pp. 3100–3110, Jun. 2019, doi: 10.1021/acsbiomaterials.9b00438.
[89] M. Gullans, D. E. Chang, F. H. L. Koppens, F. J. G. de Abajo, and M. D. Lukin, “Single-Photon Nonlinear Optics with Graphene Plasmons,” *Phys. Rev. Lett.*, vol. 111, no. 24, p. 247401, Dec. 2013, doi: 10.1103/PhysRevLett.111.247401.
[90] K. Wang *et al.*, “Coherent interaction between free electrons and a photonic cavity,” *Nature*, vol. 582, no. 7810, pp. 50–54, Jun. 2020, doi: 10.1038/s41586-020-2321-x.
[91] N. Müller, S. el Kabil, G. Vosse, L. Hansen, C. Rathje, and S. Schäfer, “Spectrally resolved free electron-light coupling strength in a transition metal dichalcogenide,” 2024, *arXiv*. doi: 10.48550/ARXIV.2405.12017.

[92] J. H. Gaida *et al.*, “Lorentz microscopy of optical fields,” *Nat. Commun.*, vol. 14, no. 1, p. 6545, Oct. 2023, doi: 10.1038/s41467-023-42054-3.
[93] S. Ghosh *et al.*, “Extremely high thermal conductivity of graphene: Prospects for thermal management applications in nanoelectronic circuits,” *Appl. Phys. Lett.*, vol. 92, no. 15, p. 151911, Apr. 2008, doi: 10.1063/1.2907977.
[94] D. L. Nika, E. P. Pokatilov, A. S. Askerov, and A. A. Balandin, “Phonon thermal conduction in graphene: Role of Umklapp and edge roughness scattering,” *Phys. Rev. B*, vol. 79, no. 15, p. 155413, Apr. 2009, doi: 10.1103/PhysRevB.79.155413.
[95] A. K. Geim and K. S. Novoselov, “The rise of graphene,” *Nat. Mater.*, vol. 6, no. 3, pp. 183–191, Mar. 2007, doi: 10.1038/nmat1849.
[96] I. T. Johansen, “Electrical Conductivity in Evaporated Silicon Oxide Films,” *J. Appl. Phys.*, vol. 37, no. 2, pp. 499–507, Feb. 1966, doi: 10.1063/1.1708203.
[97] J. A. García-Valenzuela, M. R. Baez-Gaxiola, and M. Sotelo-Lerma, “Chemical bath deposition of PbS thin films on float glass substrates using a Pb(CH3COO)2–NaOH–(NH2)2CS–N(CH2CH2OH)3–CH3CH2OH definite aqueous system and their structural, optical, and electrical/photoelectrical characterization,” *Thin Solid Films*, vol. 534, pp. 126–131, May 2013, doi: 10.1016/j.tsf.2013.02.035.
[98] J. E. Sipe and A. I. Shkrebtii, “Second-order optical response in semiconductors,” *Phys. Rev. B*, vol. 61, no. 8, pp. 5337–5352, Feb. 2000, doi: 10.1103/PhysRevB.61.5337.
[99] L. A. Golovan and V. Yu. Timoshenko, “Nonlinear-Optical Properties of Porous Silicon Nanostructures,” *J. Nanoelectron. Optoelectron.*, vol. 8, no. 3, pp. 223–239, Mar. 2013, doi: 10.1166/jno.2013.1473.
[100] “https://www.emsdiasum.com.”
[101] “https://myscope.training/.”
[102] “PhD thesis, ‘Towards atomically resolved magnetic measurements in the transmission electron microscope A study of structure and magnetic moments in thin films,’” 2020.
[103] “https://www.copperpodip.com/.”
[104] C. Huck *et al.*, “Strong coupling between phonon-polaritons and plasmonic nanorods,” *Opt. Express*, vol. 24, no. 22, p. 25528, Oct. 2016, doi: 10.1364/OE.24.025528.
[105] L. A. McCarthy *et al.*, “Chiral Plasmonic Pinwheels Exhibit Orientation-Independent Linear Differential Scattering under Asymmetric Illumination,” *Chem. Biomed. Imaging*, vol. 1, no. 1, pp. 30–39, Apr. 2023, doi: 10.1021/cbmi.2c00005.
[106] T. Oshikiri, Q. Sun, H. Yamada, S. Zu, K. Sasaki, and H. Misawa, “Extrinsic Chirality by Interference between Two Plasmonic Modes on an Achiral Rectangular Nanostructure,” *ACS Nano*, vol. 15, no. 10, pp. 16802–16810, Oct. 2021, doi: 10.1021/acsnano.1c07137.
[107] E. Petronijevic *et al.*, “Demonstration of extrinsic chirality in self-assembled asymmetric plasmonic metasurfaces and nanohole arrays,” *Sci. Rep.*, vol. 14, no. 1, Jul. 2024, doi: 10.1038/s41598-024-68007-4.
[108] C.-M. Sung, “New modification of the diamond anvil press: A versatile apparatus for research at high pressure and high temperature,” *Rev. Sci. Instrum.*, vol. 47, no. 11, pp. 1343–1346, Nov. 1976, doi: 10.1063/1.1134543.
[109] W. J. Evans, C.-S. Yoo, G. W. Lee, H. Cynn, M. J. Lipp, and K. Visbeck, “Dynamic diamond anvil cell (dDAC): A novel device for studying the dynamic-pressure properties of materials,” *Rev. Sci. Instrum.*, vol. 78, no. 7, p. 073904, Jul. 2007, doi: 10.1063/1.2751409.
[110] P. F. McMillan, “New materials from high-pressure experiments,” *Nat. Mater.*, vol. 1, no. 1, pp. 19–25, Sep. 2002, doi: 10.1038/nmat716.
[111] L. Dubrovinsky, N. Dubrovinskaia, V. B. Prakapenka, and A. M. Abakumov, “Implementation of micro-ball nanodiamond anvils for high-pressure studies above 6 Mbar,” *Nat. Commun.*, vol. 3, no. 1, p. 1163, Oct. 2012, doi: 10.1038/ncomms2160.

[112] S. Juodkazis *et al.*, “Laser-Induced Microexplosion Confined in the Bulk of a Sapphire Crystal: Evidence of Multimegabar Pressures,” *Phys. Rev. Lett.*, vol. 96, no. 16, p. 166101, Apr. 2006, doi: 10.1103/PhysRevLett.96.166101.
[113] E. G. Gamaly *et al.*, “Laser-matter interaction in the bulk of a transparent solid: Confined microexplosion and void formation,” *Phys. Rev. B*, vol. 73, no. 21, p. 214101, Jun. 2006, doi: 10.1103/PhysRevB.73.214101.
[114] E. G. Gamaly, A. Vailionis, V. Mizeikis, W. Yang, A. V. Rode, and S. Juodkazis, “Warm dense matter at the bench-top: Fs-laser-induced confined micro-explosion,” *High Energy Density Phys.*, vol. 8, no. 1, pp. 13–17, Mar. 2012, doi: 10.1016/j.hedp.2011.10.003.
[115] J. S. Kasper and S. M. Richards, “The crystal structures of new forms of silicon and germanium,” *Acta Crystallogr.*, vol. 17, no. 6, pp. 752–755, Jun. 1964, doi: 10.1107/S0365110X64001840.
[116] R. Doostkam, L. Gelisio, A. Yurtsever, L. Rapp, A. V. Rode, and K. R. Beyerlein, “Studying novel high-pressure phases in laser-shock-affected silicon using poly: an algorithm for spot-wise phase identification,” *J. Appl. Crystallogr.*, vol. 58, no. 1, pp. 128–137, Feb. 2025, doi: 10.1107/S1600576724011178.
[117] A. Vailionis, E. G. Gamaly, V. Mizeikis, W. Yang, A. V. Rode, and S. Juodkazis, “Evidence of superdense aluminium synthesized by ultrafast microexplosion,” *Nat. Commun.*, vol. 2, no. 1, p. 445, Aug. 2011, doi: 10.1038/ncomms1449.
[118] R. Buividas *et al.*, “Phase Transformation in Laser-Induced Micro-Explosion in Olivine $(Fe,Mg)_2$ SiO_4,” *Adv. Eng. Mater.*, vol. 16, no. 6, pp. 767–773, Jun. 2014, doi: 10.1002/adem.201400091.
[119] L. A. Smillie *et al.*, “Exotic silicon phases synthesized through ultrashort laser-induced microexplosion: Characterization with Raman microspectroscopy,” *Phys. Rev. Mater.*, vol. 4, no. 9, p. 093803, Sep. 2020, doi: 10.1103/PhysRevMaterials.4.093803.
[120] S. Wippermann, Y. He, M. Vörös, and G. Galli, “Novel silicon phases and nanostructures for solar energy conversion,” *Appl. Phys. Rev.*, vol. 3, no. 4, p. 040807, Dec. 2016, doi: 10.1063/1.4961724.
[121] V. E. Dmitrienko and V. A. Chizhikov, “Infinite family of b c 8 -like metastable phases in silicon,” *Phys. Rev. B*, vol. 101, no. 24, p. 245203, Jun. 2020, doi: 10.1103/PhysRevB.101.245203.
[122] B. Haberl, T. A. Strobel, and J. E. Bradby, “Pathways to exotic metastable silicon allotropes,” *Appl. Phys. Rev.*, vol. 3, no. 4, p. 040808, Dec. 2016, doi: 10.1063/1.4962984.
[123] J. Simbrunner *et al.*, “Automatic indexing of two-dimensional patterns in reciprocal space,” *Phys. Rev. B*, vol. 104, no. 19, p. 195402, Nov. 2021, doi: 10.1103/PhysRevB.104.195402.
[124] S. Zaefferer, “A critical review of orientation microscopy in SEM and TEM,” *Cryst. Res. Technol.*, vol. 46, no. 6, pp. 607–628, Jun. 2011, doi: 10.1002/crat.201100125.
[125] J. L. Lábár, “Consistent indexing of a (set of) single crystal SAED pattern(s) with the ProcessDiffraction program,” *Ultramicroscopy*, vol. 103, no. 3, pp. 237–249, Jun. 2005, doi: 10.1016/j.ultramic.2004.12.004.
[126] S. Honglong, Z. Guling, Z. Bin, L. Minting, and W. Wenzhong, “A method for structure analysis of nanomaterials by electron diffraction: Phase identification and unit cell determination,” *Microsc. Res. Tech.*, vol. 76, no. 6, pp. 641–647, Jun. 2013, doi: 10.1002/jemt.22211.
[127] Y. Wang *et al.*, “Precise Identification of the Active Phase of Cobalt Catalyst for Carbon Nanotube Growth by *In Situ* Transmission Electron Microscopy,” *ACS Nano*, vol. 14, no. 12, pp. 16823–16831, Dec. 2020, doi: 10.1021/acsnano.0c05542.

[128] P. Moeck *et al.*, “Precession electron diffraction and its utility for structural fingerprinting in the transmission electron microscope,” in *AIP Conference Proceedings*, Albany (New York): AIP, 2009, pp. 299–303. doi: 10.1063/1.3251238.
[129] A. S. Eggeman, “Scanning transmission electron diffraction methods,” *Acta Crystallogr. Sect. B Struct. Sci. Cryst. Eng. Mater.*, vol. 75, no. 4, pp. 475–484, Aug. 2019, doi: 10.1107/S2052520619006723.
[130] P. A. Midgley and A. S. Eggeman, “Precession electron diffraction – a topical review,” *IUCrJ*, vol. 2, no. 1, pp. 126–136, Jan. 2015, doi: 10.1107/S2052252514022283.
[131] R. Ohba, I. Uehira, and T. Hondoh, “Computer-Aided Spot Indexing for X-Ray Laue Patterns,” *Jpn. J. Appl. Phys.*, vol. 20, no. 5, p. 811, May 1981, doi: 10.1143/JJAP.20.811.
[132] S. I. Wright and B. L. Adams, “Automatic analysis of electron backscatter diffraction patterns,” *Metall. Trans. A*, vol. 23, no. 3, pp. 759–767, Mar. 1992, doi: 10.1007/BF02675553.
[133] Y. Meng and J.-M. Zuo, “Improvements in electron diffraction pattern automatic indexing algorithms,” *Eur. Phys. J. Appl. Phys.*, vol. 80, no. 1, p. 10701, Oct. 2017, doi: 10.1051/epjap/2017160444.
[134] K. R. Beyerlein *et al.*, “FELIX: an algorithm for indexing multiple crystallites in X-ray free-electron laser snapshot diffraction images,” *J. Appl. Crystallogr.*, vol. 50, no. 4, pp. 1075–1083, Aug. 2017, doi: 10.1107/S1600576717007506.
[135] B. Bhushan, *Springer Handbook of Nanotechnology*, 4th ed. in Springer Handbooks Ser. Berlin, Heidelberg: Springer Berlin / Heidelberg, 2017.
[136] A. Barhoum *et al.*, “Review on Natural, Incidental, Bioinspired, and Engineered Nanomaterials: History, Definitions, Classifications, Synthesis, Properties, Market, Toxicities, Risks, and Regulations,” *Nanomaterials*, vol. 12, no. 2, p. 177, Jan. 2022, doi: 10.3390/nano12020177.
[137] R. Hull, Ed., *Properties of crystalline silicon*. London: Institution of Electrical Engineers, 2006.
[138] A. Morawiec, “Indexing of diffraction patterns for determination of crystal orientations,” *Acta Crystallogr. Sect. Found. Adv.*, vol. 76, no. 6, pp. 719–734, Nov. 2020, doi: 10.1107/S2053273320012802.
[139] M. I. Aroyo, Ed., *International Tables for Crystallography: Space-group symmetry*, 2nd ed., vol. A. Chester, England: International Union of Crystallography, 2016. doi: 10.1107/97809553602060000114.
[140] A. Looijenga-Vos and M. J. Buerger, “Space-group determination and diffraction symbols,” in *International Tables for Crystallography*, 1st ed., vol. A, Th. Hahn, Ed., in International Tables for Crystallography, vol. A. , Chester, England: International Union of Crystallography, 2006, pp. 44–54. doi: 10.1107/97809553602060000506.
[141] H. Goldstein, C. P. Poole, and J. L. Safko, *Classical mechanics*, 3. ed., [Nachdr.]. San Francisco Munich: Addison Wesley, 2008.
[142] J. Als-Nielsen and D. McMorrow, *Elements of modern X-ray physics*, Second edition, Reprinted with revisions and Corrections. Chichester, West Sussex: Wiley, a John Wiley & Sons, Ltd Publication, 2017.
[143] *Itseez. “Open Source Computer Vision Library” (2015).*
[144] J. Lee, K. Lee, D. Kim, T. Park, H. Kim, and H. Jeon, “Epitaxial $CoSi_2$ formation using an oxynitride buffer layer,” *J. Mater. Res.*, vol. 24, no. 8, pp. 2705–2710, Aug. 2009, doi: 10.1557/jmr.2009.0320.
[145] “https://www.thorlabs.com/.”

Appendix A. UTEM Calibration and Optimization Studies

1 Nanobeam measurements

The JEOL JEM-2100 TEM is equipped with nanobeam microscopy and diffraction capabilities. In the software, several nominal spot sizes are available, ranging from 35 nm to 1.5 nm. To calibrate these settings for future use, we measured the actual spot size of each nanobeam. Figures A.1 and A.2 present the Nano beam (NB) spot sizes captured in Image mode on the camera for the corresponding nominal spot size settings in the software.

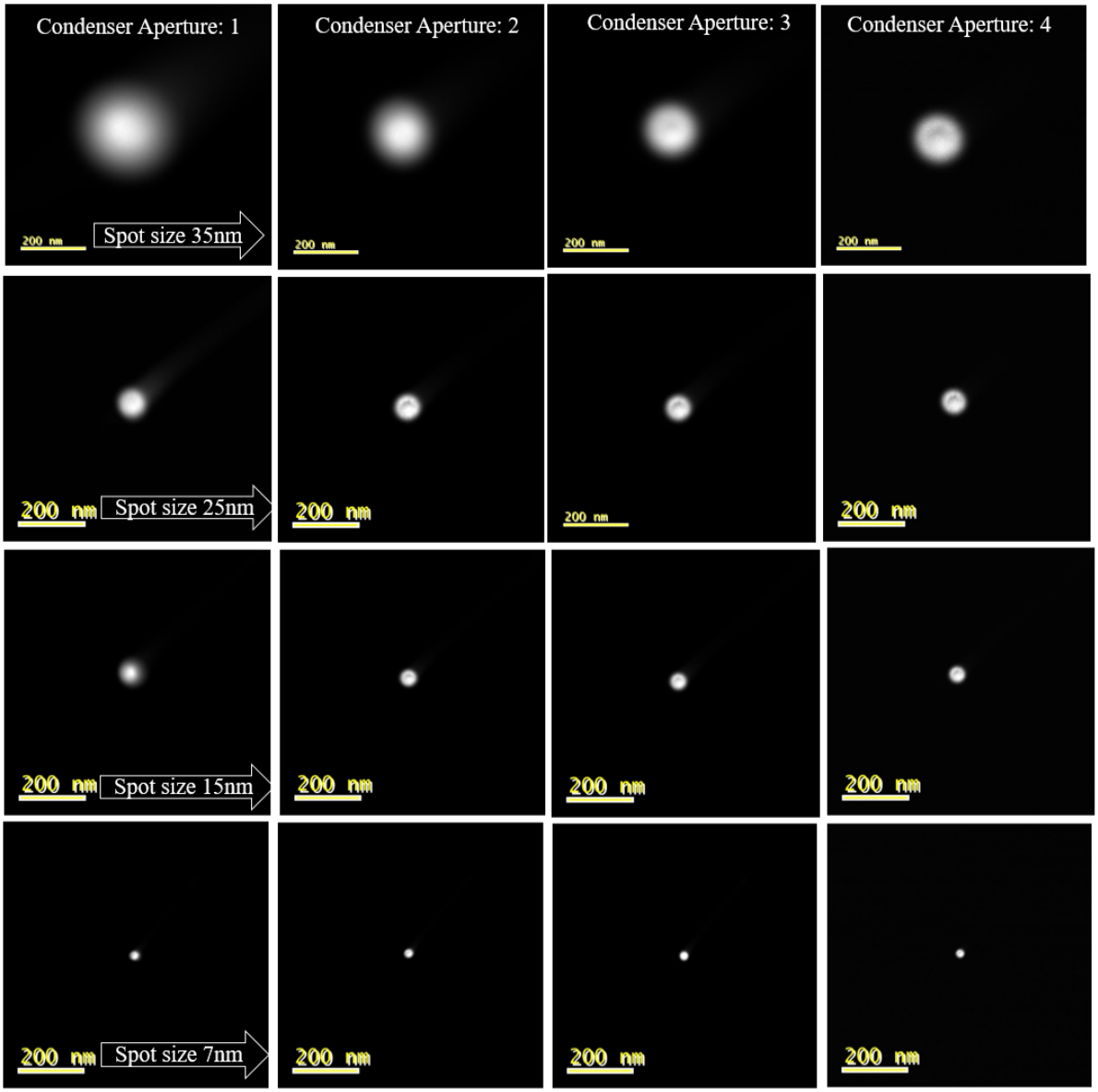

Figure A.1. NB Spot sizes corresponding to the spot sizes set in the software (4, 3, 2, and 1.5 nm).

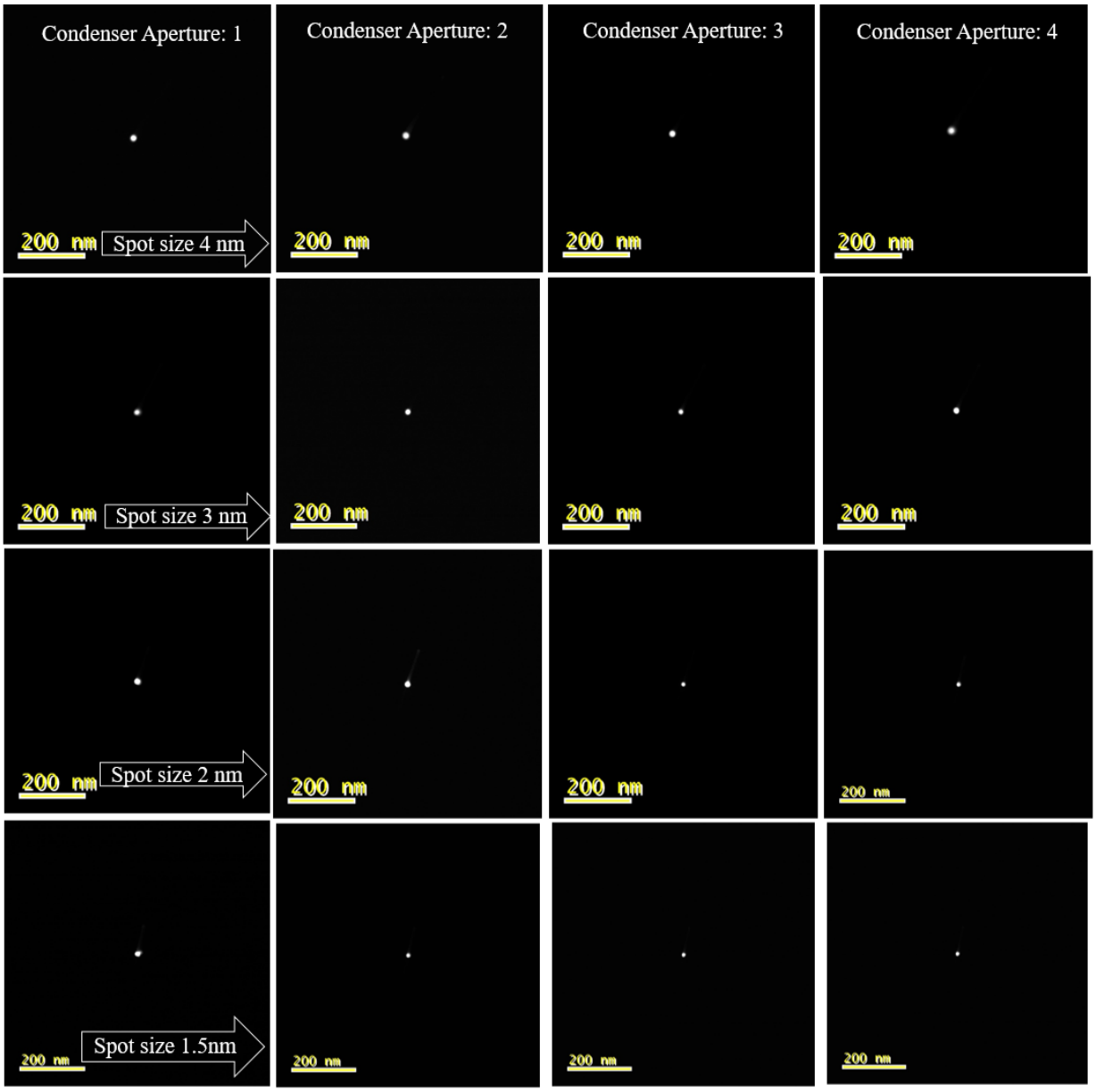

Figure A.2. NB spot sizes corresponding to the nominal spot sizes set in the software (4, 3, 2, and 1.5 nm).

Table A.1 presents the measured values corresponding to the nominal spot sizes set in the software.

Table A.1 Nano beam size on the camera in different nominal spot sizes

Nominal Spot size	Aperture 1	Aperture 2	Aperture 3	Aperture 4
35 nm	195 nm	133	129	122
25 nm	66	64	63	62
15	51	43	42	40
7 nm	23	22	21	20
4 nm	17	15	14	13
3 nm	14	12	11	10
2 nm	11	9	8	7
1.5 nm	10	8	7	6

The size of the Bragg spots in diffraction mode using a nano-beam was measured. Figure A.3 shows the Bragg spots originating from a single-crystal Si thin film sample. Table A.2 presents the measured values corresponding to the nominal spot sizes set in the software.

It is worth noting, however, that the smallest nano-beam setting—corresponding to a nominal spot size of 1.5 nm and condenser aperture 4—produces a spot size of approximately 6 nm on the camera. In practice, this setting is not usable. The reason is that in nanobeam diffraction (NBD), the CL3 lens (beam controller lens) must first be adjusted in image mode to define the desired probe size. After switching to diffraction mode, only the intermediate lens (IL1) can be modified to focus the diffraction pattern. For very small CL3 settings, it is not possible to achieve a properly focused diffraction pattern using IL1 alone.

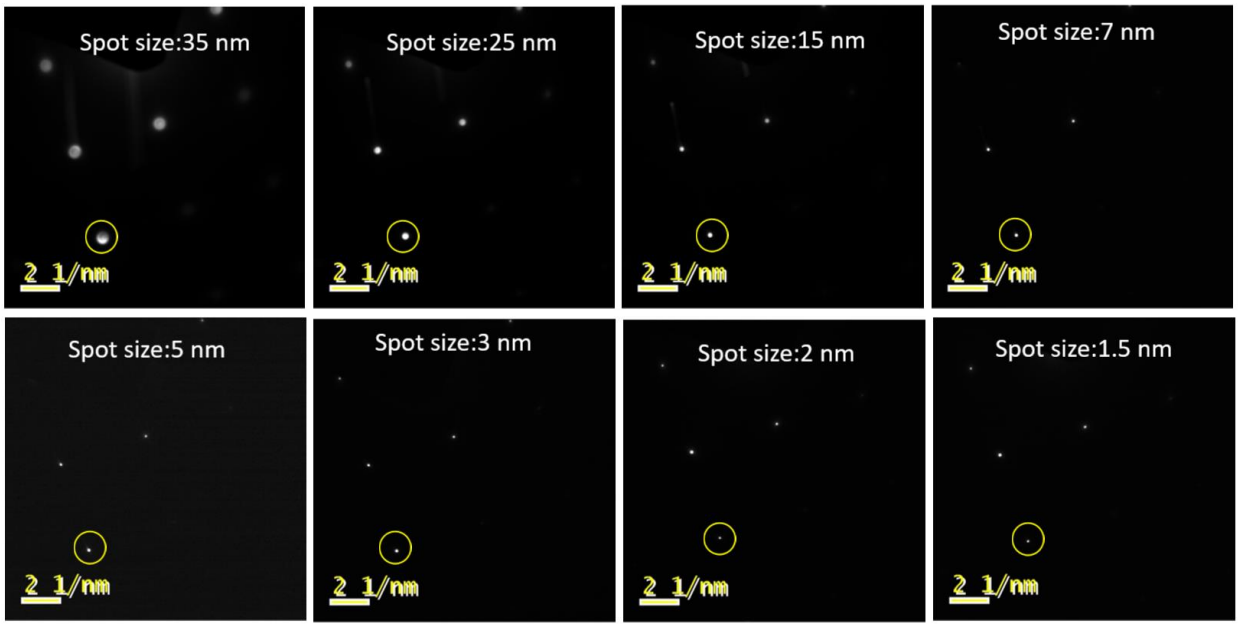

Figure A.3. Bragg spot sizes corresponding to the nominal spot sizes set in the software (35 nm to 1.5 nm).

Table A.2 Bragg spot size with nano-beam diffraction

Nominal Spot size	Aperture 1	Aperture 2	Aperture 3	Aperture 4
35 nm	6.92 nm	2.03	1.52	0.52
25 nm	6.91	1.98	1.55	0.48
15	6.80	2.04	1.76	0.49
7 nm	6.60	2.07	1.91	0.49
4 nm	6.70	2.11	2.03	0.50
3 nm	6.65	2.13	2.05	0.50
2 nm	6.55	2.15	2.00	0.49
1.5 nm	6.64	2.16	2.04	0.50

Nanobeam diffraction (NBD) was performed on a sample of platinum (Pt) nanorods, as shown in Figure A.4a. First, the region of interest was selected by adjusting the nanobeam in image mode (Figure A.4b). Then, by switching to diffraction mode and adjusting the IL1 lens, the diffraction pattern was obtained. The experimental parameters were as follows: camera length–2 cm, nanobeam size–25nm, condenser aperture 3, α3 (convergence angle), and IL1 setting, 68CC.

To ensure that the diffraction pattern included contributions from both nanorods, the beam was next adjusted individually onto the left and right nanorods. Two separate nanobeam diffraction (NBD) patterns were acquired, as shown in Figures A.5b and A.5c. The diffraction pattern from the left nanorod is presented in Figure A.5e, and that from the right nanorod is shown in Figure A.5f.These NBD patterns, when compared to Figure A.5d-which originates from both nanorods-demonstrate that the overall pattern is a combination of the individual diffraction patterns from each nanorod. This confirms that the nanobeam was correctly focused on the regions of interest.

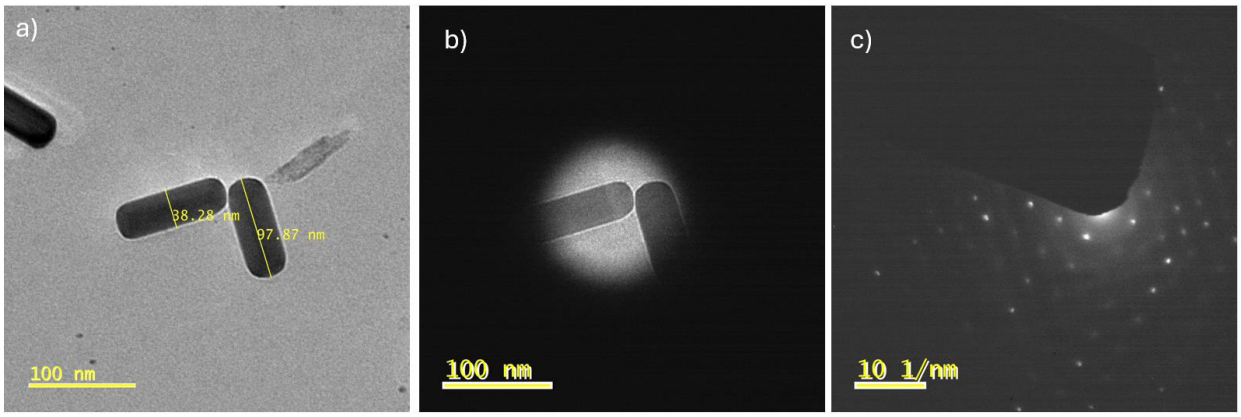

Figure A.4. a) Platinum nanorods, b) Nano beam on the interest region, c) nanobeam diffraction (NBD) pattern.

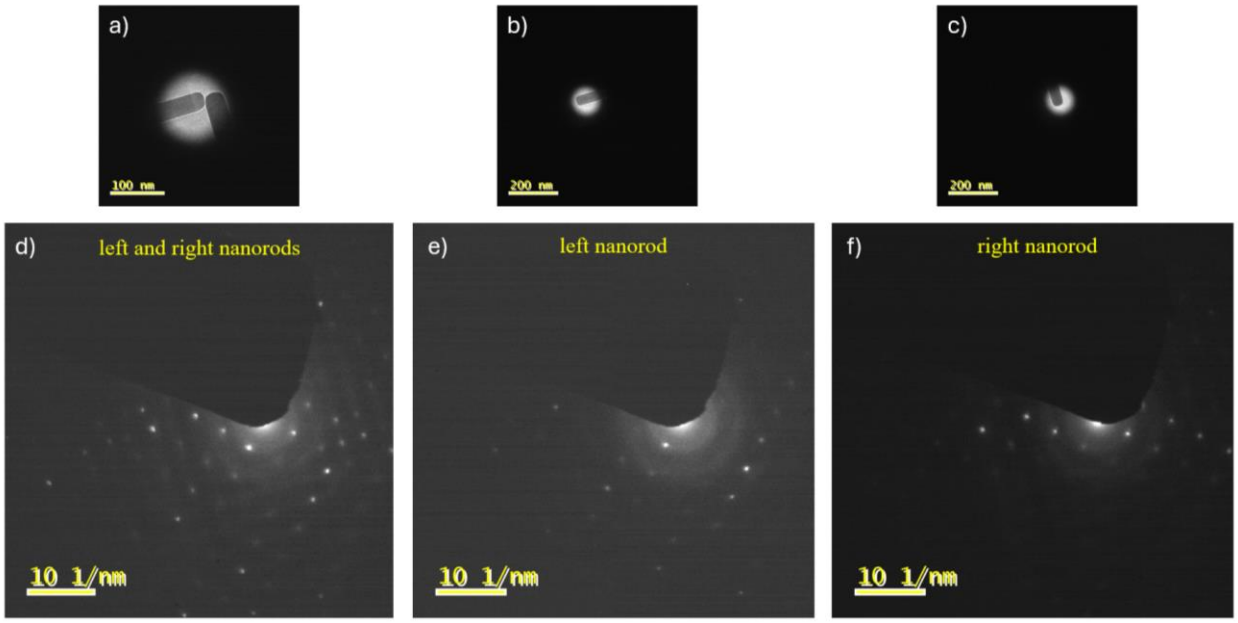

Figure A.5. (a) Nanobeam positioned over the region of interest containing two platinum nanorods; (b) nanobeam focused on the left nanorod; (c) nanobeam focused on the right nanorod. (d–f) Corresponding nanobeam diffraction (NBD) patterns for the regions shown in (a–c), respectively.

2 New SAED of the Si sample irradiated by laser for microexplosion

For the sample fabricated by Rapp et al. and studied in Chapter 3, a new diffraction pattern was acquired using nanobeam diffraction (NBD). Figure A.6 shows the sample and the region containing nanopolycrystalline material. Figures A.6b and A.6c were captured using an optical microscope, while the remaining images were obtained with a scanning electron microscope (SEM).

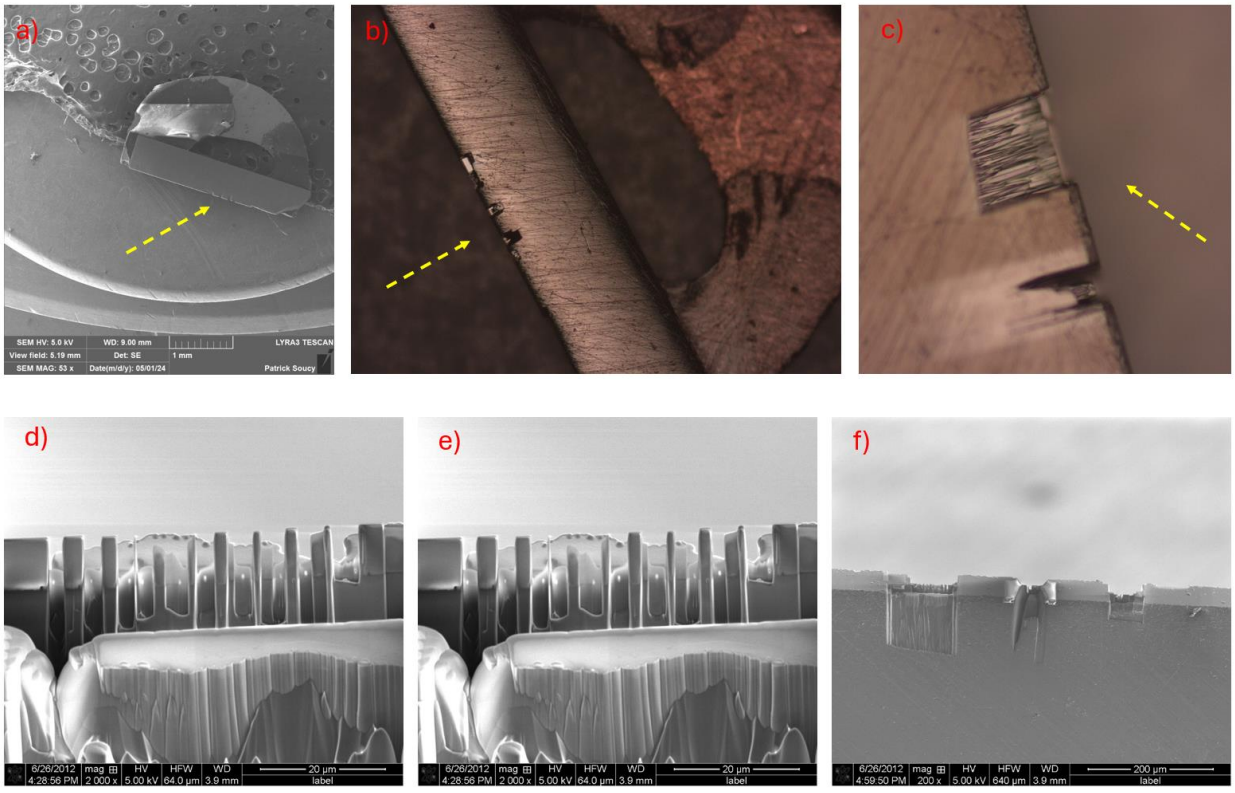

Figure A.6. Si Sample irradiated by a laser for microexplosion, and the region that includes nanopolycrystalline. b,c) are captured by an optical microscope, while the rest are captured by a scanning electron microscope (SEM).

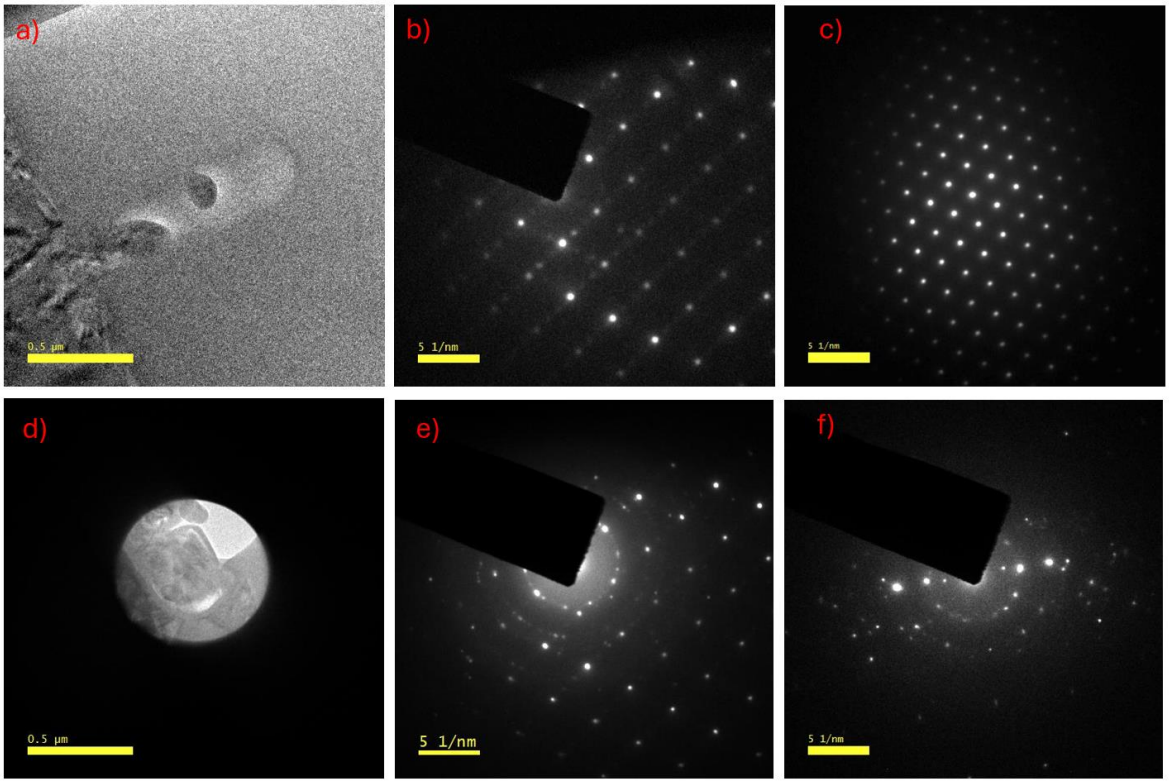

Figure A.7. (a) Laser-affected region in the Si sample; (b, c) nanobeam diffraction (NBD) patterns acquired from the non-affected region, showing a crystalline pattern; (d) polycrystalline region; (e, f) NBD patterns obtained from the polycrystalline region.

3 Camera Calibration for diffraction mode

A single-crystalline Si thin film was used to calibrate the camera in diffraction mode. Figure A.8 shows the thin film sample and its corresponding diffraction pattern. The camera was calibrated by measuring the distances of three diffraction spots from the center and applying the calibration Equation (A.1).

$$g d_{hkl} = L\lambda \tag{A.1}$$

where g is the distance of the Bragg spot from the center in reciprocal space (in units of 1/nm), d_{hkl} is the interplanar spacing, L is the camera length, and λ is the electron wavelength, which is approximately 0.0025 nm at 200 keV [17]. We used the following equation [17] to calculate the d-spacing for the cubic phase of Si:

$$d_{hkl} = \frac{1}{g} = \frac{0.543}{\sqrt{h^2+k^2+l^2}} \tag{A.2}$$

where 0.543 nm is the lattice parameter of silicon, and h,k,l are the Miller indices. Then, using Equation (A.1), the microscope can be calibrated for SAED by using a known d_{hkl} value and the corresponding measured g.

The measured and calculated d-spacing values are presented in Table A.2. Figure A.9 shows other proofs to ensure the indexing was correct. Figure A.4.10 shows the calibration part in the Gatan Microscopy Suite (GMS) software.

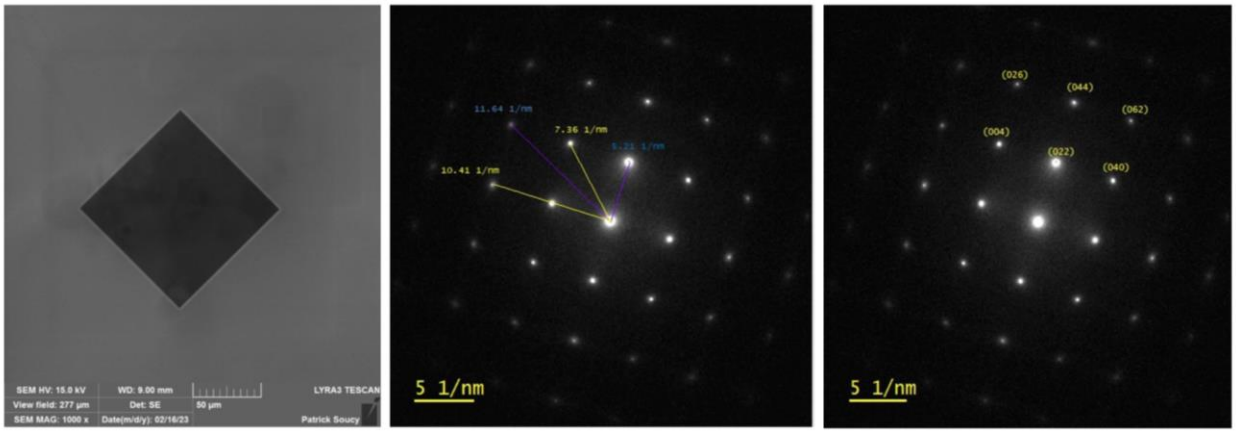

Figure A.8. A Thin film of Silicon sample and its SAED patterns with indexed spots.

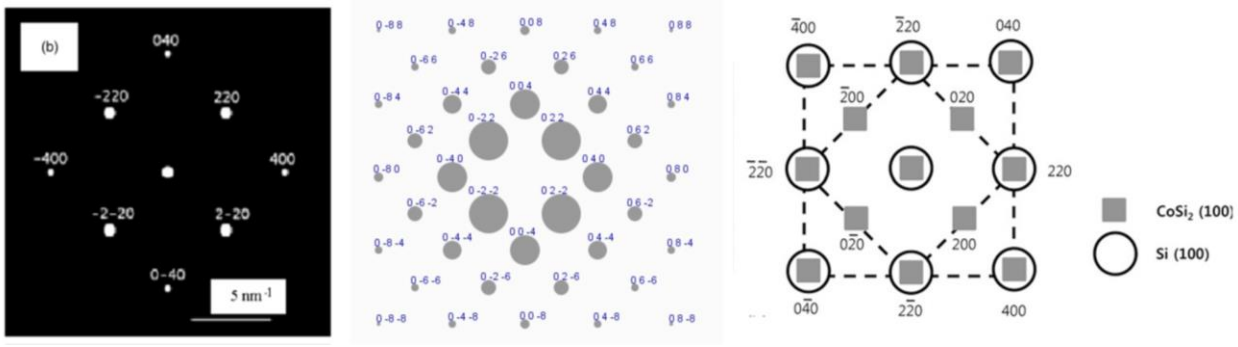

Figure A.9. Indices of Si found in other resources [144]**.**

Table A.2 The measured and calculated d-spacing for the Bragg spots of the crystalline Si thin film.

	The Bragg Spot	Experimental d-spacing	Theoretical d-spacing
1	d_{022}	$\frac{1}{5.21}$=0.192 nm	$\frac{0.543}{\sqrt{8}}$=0.192 nm
2	d_{040}	$\frac{1}{7.36}$=0.136 nm	$\frac{0.543}{\sqrt{16}}$=0.136 nm
3	d_{044}	$\frac{2}{10.41}$=0.096 nm	$\frac{0.543}{\sqrt{32}}$=0.096 nm
4	d_{062}	$\frac{1}{11.64}$=0.086 nm	$\frac{0.543}{\sqrt{40}}$=0.086 nm

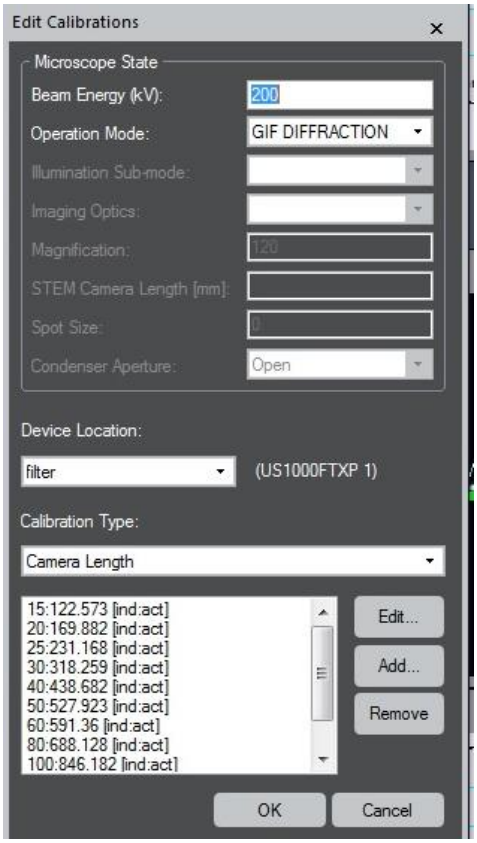

Figure A.10. Calibration part in Gatan Microscopy Suite (GMS) software.

4 Near fields of Silica NPs

We employed the PINEM technique to investigate the near fields around silica nanoparticles. Figures A.11a–e show the nanoparticles imaged using all electrons in photoelectron mode, while Figures A.11f–j present the corresponding PINEM images of the same regions.

Due to the wide band gap of silica (~10 eV), which significantly exceeds the photon energy of the pump laser (515 nm, ~2.4 eV), no clear interaction signal was observed from the nanoparticles. In Figure A.11f, it is evident that the edge of the copper grid produces a detectable near-field signal, whereas the silica nanoparticles do not exhibit any measurable PINEM response.

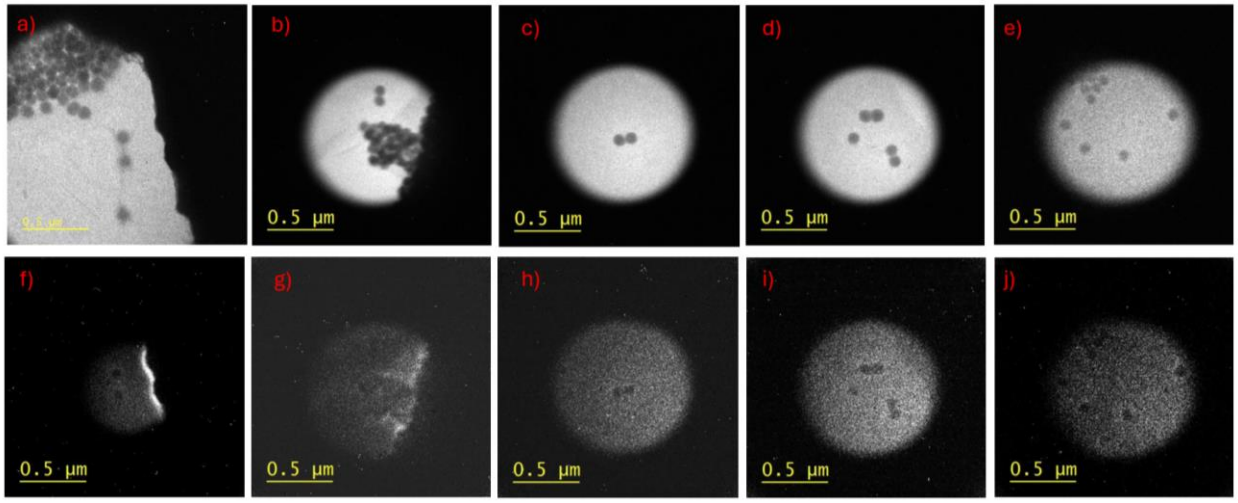

Figure A.11. (a–e) Silica nanoparticles imaged using all electrons in photoelectron mode; (f–j) corresponding PINEM images of the same nanoparticles shown in (a–e), respectively.

5 ZLP measurement

To investigate whether the electron energy distribution changes with beam spreading, we measured the EELS spectrum at different photoelectron beam diameters: 20 nm, 400 nm, 600 nm, 800 nm, and 1000 nm. The beam diameter was determined using the full width at half maximum (FWHM) of the beam intensity profile. The results showed that the electron energy distribution remains approximately constant across the different beam sizes shown in Figure A.12.

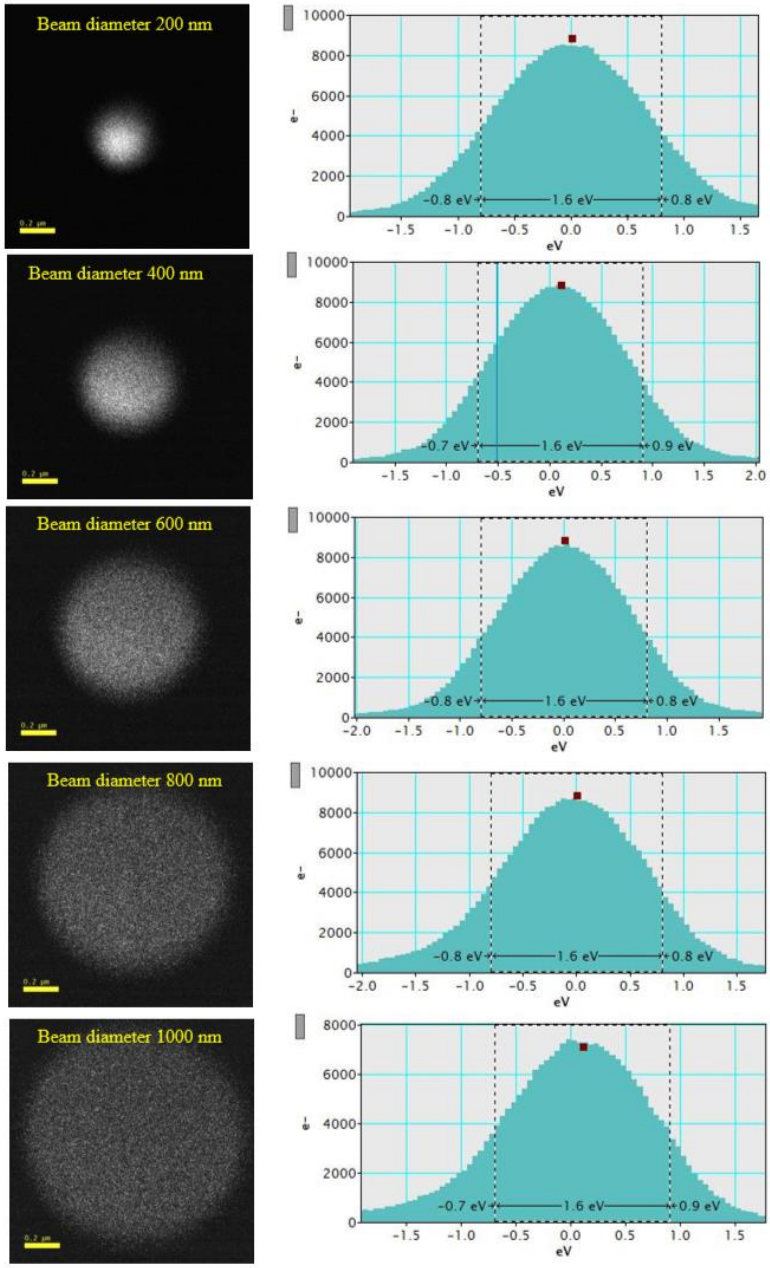

Figure A.12. Photoelectron beams of varying sizes (left) with their corresponding EELS spectra shown on the right.

6 Pump Laser linearity

To verify whether the pump laser beam remains linearly polarized after passing through the half-wave plate and before entering the TEM column, we used a polarizer to measure the extinction ratio, defined as the ratio of maximum to minimum transmitted power (Max/Min). Figure A.13 illustrates the setup configuration positioned just before the TEM column. For a pump laser power of 70 mW, the extinction ratio was 175 when the half-wave plate was set to 0° (70 mW / 0.4 mW), and 100 when it was set to 18° (70 mW / 0.7 mW).

At other angles, the extinction ratio remained high, indicating that the beam retained a high degree of linear polarization across different orientations of the half-wave plate.

Figure A.13. Schematic diagram illustrating the experimental setup used to evaluate the linearity of the pump laser [145]**.**

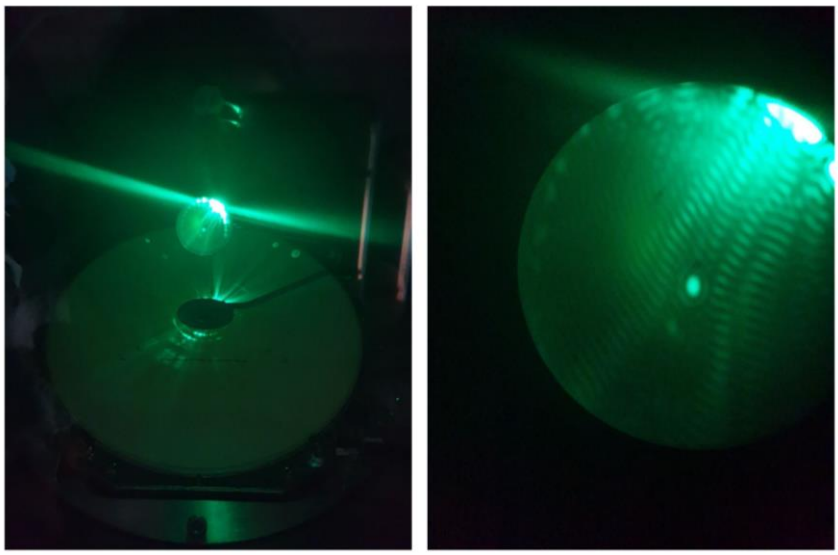

Figure A.14. Pump laser on the screen of TEM after transmission through the sample.